Eur. Phys. J. Spec. Top. (2026) 234:6473–6652
https://doi.org/10.1140/epjs/s11734-025-02016-w

THE EUROPEAN PHYSICAL JOURNAL SPECIAL TOPICS

Review

CLIC readiness report

Erik Adli[1,2,a], Gerardo D'Auria[1,3], Nuria Catalan Lasheras[1], Vera Cilento[1,4], Roberto Corsini[1], Steffen Doebert[1], Mick Draper[1], Angeles Faus-Golfe[1,5], Edward Fraser Mactavish[1], Alexej Grudiev[1], Andrea Latina[1], Lucie Linssen[1], John Andrew Osborne[1], Yannis Papaphilippou[1], Aidan Robson[1,6], Carlo Rossi[1], Daniel Schulte[1], Steinar Stapnes[1], Igor Syratchev[1], Rogelio Tomas Garcia[1], Walter Wuensch[1], T. Abe[7], H. Abramowicz[8], C. Adolphsen[9], D. Aguglia[1], A. Ahmad[10], M. Aicheler[11,12], B. Aimard[13], A. Aksoy[14,15], D. Alesini[16], T. Alexopoulos[17], F. Alharthi[18,19], M. Ali[20], N. Alipour Tehrani[1], M. Almanza Soto[21], F. Andrianala[22,1], F. Antoniou[1], R.J. Apsimon[23,24], D. Arominski[1], K. Artoos[1], A. Aryshev[7], Y. Ashkenazy[25], S. Atieh[1], C. Baccigalupi[1], E. Baibuz[11], I. Bailey[23,24], A. Bainbridge[26,24], C. Balazs[27], G. Balik[13], R. Ballabriga Sune[1], P. Bambade[19], D. Banon Caballero[1], T. Barklow[9], M.J. Barnes[1], V. Baturin[28], J. Bauche[1], M. Bellaveglia[16], C. Belver-Aguilar[1], G. Benedetti[29], Y. Benhammou[8], M. Bergamaschi[20,1], A. Bernhard[30], D. Bett[31], M. Bettencourt[1], S. Bettoni[32], C. Blanch Gutierrez[21], O. Blanco Garcia[1], N. Blaskovic Kraljevic[1], L. Bobb[20,33], R.M. Bodenstein[34], M.J. Boland[35], S. Boogert[36,24], G. Boorman[20], M. Bopp[32], M. Boronat[37], A. Bosco[20], I. Božović Jelisavčić[38], R.A. Bozzi[1], D. Bozzini[1], E. Brücken[11], P. Brückman de Renstrom[39], E. Bründermann[30], H.H. Braun[32], R. Brenner[40], L. Brunetti[13], O. Brunner[1], M. Buckland[1,41,42], B. Buonomo[16], H. Burkhardt[1], P.N. Burrows[31,1], H. Bursali[1], G.C. Burt[23,24], S. Calatroni[1], M. Campbell[1], M. Capstick[20], A. Cardelli[16], S. Casalbuoni[30], B. Cassany[43,1], E. Castro[1], M. Cerqueira Bastos[1], I. Chaikovska[19], M. Chefdeville[13], R. Chehab[19], S. Chekanov[44], H. Chen[45], J.B.B. Chen[2], G. Chen[44], A. Cherif[1], E. Chevallay[1], A. Clapp[20], J.A. Clarke[26,24], M. Coman[40], R. Costa[1,40], P. Craievich[32], A. Curcio[1], B. Cure[1], S. Curt[1], Y. Cuvet[1], D. Dannheim[1], M. Davier[19], M.K. Dayyani[46], A. Degiovanni[1], M. Dehler[32], J.P. Delahaye[1], N. Delerue[19], D. Delikaris[1], H. Denizli[47], A.C. Dexter[23,24], L. Diehl[1], D. Dipac[20], F. Djurabekova[11,48], V. Dolgashev[9], M. Dominguez[49], A. Dominjon[13], A. Dorda Martin[1], C. Drancourt[13], P. Drobniak[2], A.V. Edwards[1,23], M. El Majdara[1], T. Ekelöf[40], D. Esperante[21,1], L. Evans[1], L. Faillace[16], W. Fang[50], W. Farabolini[1], V. Fedosseev[1], L. Felsberger[1], J.C. Fernandez-Ortega[21], P. Ferracin[1], M. Ferrario[16], M. Firlej[51], T.A. Fiutowski[51], K. Foraz[1], M. Franzi[9], F. Friebel[1], M. Fukuda[7], J. Fuster[21], N. Fuster[21], A. Gaddi[1], A. Gallo[16], D. Gamba[1], Y. Gao[45], F. Garcia[11], H. Garcia Morales[1], L. Garcia-Tabares[49], C. Garion[1], T. Garvey[32], M. Gasior[1], L. Gatignon[1], D. Gavela[49], E.N. Gazis[17], N. Gazis[17,1], N. Geoffroy[13], A. Gerbershagen[1], J. Gethmann[30], H. Ghasem[46,1], A. Ghigo[16], P.J. Giansiracusa[52], S. Gibson[20], A. Gilardi[1], B. Gimeno[21], A. Giribono[16], C. Di Giulio[16], J. Goldstein[53], D. González[21], S. Gonzalez Anton[1], M. Gonzalez Berges[1], H. van der Graaf[54], E. Granados[1], A. Grau[30], C. Grefe[1,55], E. Gschwendtner[1], Q. Gu[50], T. Guenzel[29], H. Guerin[1], F.G. Guillot-Vignot[1], M. Guinchard[1], H. Guler[19], E. Haeggström[11,48], S.S. Hajari[46], P. Hamel[43], Y. Han[56], D. Harryman[20], B. Heilig[57,58], J. Hewett[9], Y. Higashi[7], T. Higo[7], V. Hill[23,24], S. Hillenbrand[30], J.K. Holma[1], H. Hoorani[10,59], W. Huang[45], D. Huang[50], X. Huang[50], S. Huang[21], K. Huitu[11,48], E. Huttel[30], M. Idzik[51], Y. Levinsen[1,60], U. Iriso[29], A. Irles[21], M. Jacewicz[40], J. Jacquemier[13], S. Jamison[23], A. Jeff[1], E. Jensen[1], A. Jeremie[13], C. Jing[44], M. Jonker[1], W. Kaabi[19], G. Kačarević[38], J. Kalinowski[61], O.A. Kałuzińska[1,62], P. Karataev[20], O. Karpenko[28], Y. Karyotakis[13], I. Kassamakov[11,48], M. Kemp[9], L. Kennedy[1,31], W.A. Khan[10], V. Khan[1], R.B. Kieffer[1], J. Kimari[11,48], J. Klamka[61], R. Koitermaa[63], R. Koitermaa[11], N. Kokkinis[1], P. Koppenburg[54], I. Kopsalis[17], V. Korchevnyuk[1], A. Korsback[1], A. Korsun[19], P. Korysko[31,1], S. Kourkoulis[17], J.W. Kovermann[1,64], C.-I. Kozsar[1], E. van der Kraaij[1,65], M.A. Krawczyk[1], I. Kremastiotis[1], N. Krumpa[26], B. Krupa[39], M. Krupa[1], Y.P. Kuang[45], K. Kubo[7], M. Kucharczyk[39], S. Kulis[1], S. Kuroda[7], A. Kurtulus[1,66], A. Kyritsakis[63], A. Kyritsakis[11], K. Lasocha[1], Y. Lebedynskya[28], S. Lebedynskyi[28], F. LeDiberder[19], T. Lefevre[1], S. Lehti[11], T. Lesiak[39], A. Levy[8], I. Levy[8,67], B. Li[45], Y. Li[45], A. Liedl[16], C.A. Lindstrøm[2], B. List[68], X. Liu[1], W. Liu[44], X. Llopart Cudie[1], X. Lu[44], T. Lucas[32], O.J. Luiten[69], A. Lyapin[20], L. Ma[56], A. Magazinik[1], H. Mainaud Durand[1], S. Mallows[1], E. Manosperti[1], C. Marchand[43], R. Margraf-O'Neal[44], E. Marin Lacoma[1], T. Markiewicz[9], C. Marrelli[1],

E. Adli, G. D'Auria, N. Catalan Lasheras, V. Cilento, R. Corsini, S. Doebert, M. Draper, A. Faus-Golfe, E. Fraser Mactavish, A. Grudiev, A. Latina, L. Linssen, J.A. Osborne, Y. Papaphilippou, A. Robson, C. Rossi, D. Schulte, S. Stapnes, I. Syratchev, R. Tomas Garcia and W. Wuensch are Editors.

[a] email: erik.adli@cern.ch (corresponding author)

S. Marsh[1], Z. Marti[29], V. Martin[70], P. Martinez Reviriego[1], G. Mcmonagle[1], K. Mekala[61,71], X. Meng[45], L.M. Mether[1], S. Michizono[7], W.L. Millar[1], W.L. Millar[23,24], V. Mitsou[21], M. Modena[1], K. Moffeit[9], P.B. Moniz Cabral[1], E. Moradpur-Tari[63], P. Morales Sanchez[1], M. Moreno Lacer[21], J. Moroń[51], A.-S. Müller[30], V. Musat[31,1], I. Musienko[28], E. Musumeci[21], P. Mutsaers[69], V.V. Mytrochenko[19], E. Nanni[9], M. Nanut Petrič[1], J.M. Nappa[13], Z. Nergiz[15,72], N. Nikiforou[1], M. Nonis[1], K. Nordlund[11,48], Y. Nosochkov[9], J. Ögren[1], T. Okugi[7], J. Olivares Herrador[1,21], L. De Oliveira[1], C. Oliver[49], M. Olvegård[40], S. Oras[63], C. Orero[21], M. Oriunno[9], K. Österberg[11,48], K.Y. Oyulmaz[47], K. Papke[23,24], M. Parodi[1], A. Pastushenko[1,73], M. Patecki[1], B. Pawlik[39], F. Peauger[1], L. Pedraza-Motavita[21], M. Pedrozzi[32], P. Peiffer[30,74], D. Pellegrini[1], K. Pepitone[1], F. Perez[29], A. Perez Fontenla[1], I. Peric[30], T.H.B. Persson[1], N. Pienimaki[1], L. Piersanti[16], P. Piot[44], S. Pitman[1], S. Pittet[1], F. Plassard[1], J. Plouin[43], M. Pont[29], I. Popov[25], R. Pöschl[19], S. Poss[1], J. Power[44], V. Del Pozo Romano[1], D. Protopopescu[6], P. Pushkarna[52], R. Raboanary[22], J.Y. Raguin[32], R.P. Rassool[52], S. Redford[1], S.F. Rey[1], O. Rey Orozco[1], L. Rivkin[32,75], T. Rizzo[9], E. Rodriguez Castro[1], P. Roloff[1], I. Ruehl[1], A. Ruiz-Jimeno[37], G. Rumolo[1], D. Saez de Jauregui[30], E. Said[1], A. Sailer[1], A. Saressalo[11], J. Sauza Bedolla[1], A. Schloegelhofer[1], H. Schmickler[1], E. Senes[1], A. Senol[47], M. Serluca[13], C. Serpico[1], H. Shaker[29], J. Shao[45], B.J.A. Shepherd[26,24], J. Shi[45], W. Shields[20], E. Sicking[1], F. Simon[30], K.N. Sjobak[2], P.K. Skowronski[1], P. Sobrino Mompean[1], P. Sollander[1], P. Sopicki[39], M.P. Sosin[1], S. Spannagel[1], A. Stella[16], G. Sterbini[1], R. Ström[1], M.J. Stuart[1], X.F.D. Stragier[69], P. Svihra[1,76,77], K.P. Świentek[51], K. Szypula[1], J. Tan[50], C. Tang[45], G. Tangari[1,78], S. Tantawi[9], F. Tecker[1], P. Terlecki[51], N. Terunuma[7], P. Thrane[1], T. Tiirats[63], L. Timeo[1], M. Titov[43], F. Toral[49], U. Uggerhøj[79], J. Uythoven[1], C. Vaccarezza[16], J. Valerian[52], A.L. Vamvakas[1], M. Vicente Barreto Pinto[1,80], I. Vidaković[38], S. Vilalte[13], M. Volpi[52,1], M. Vos[21], G. Vouters[13], N. Vukasinović[38], D. Walsh[26,24], P. Wang[45], Z. Wang[50], Y. Wang[63], Y. Wang[19], P. Wang[1], N.K. Watson[81], B. Weatherford[9], M.A. Weber[1], R. Wegner[1], M. Wendt[1], G. White[9], M. Widorski[1], M. Williams[1], A.G. Winter[81], T. Wojtoń[39], M. Woodley[9], B. Woolley[1], L. Wroe[1], X. Wu[45], A. Yamamoto[7,1], R. Yang[1], Ö. Yavas[15], V. Zadin[63], L. Zawiejski[39], R. Zennaro[32], D. Zerwas[19], H. Zha[45], W. Zhang[31], J. Zhang[44], Z. Zhao[50], Y. Zhao[1], A.F. Żarnecki[61], and P. Zisopoulos[1]

Received: 11 September 2025 / Accepted: 30 September 2025 / Published online: 9 December 2025

Abstract The Compact Linear Collider (CLIC) is a TeV-scale high-luminosity linear e^+e^- collider studied by the international CLIC and CLICdp collaborations hosted by CERN. CLIC uses a two-beam acceleration scheme, in which normal-conducting high-gradient 12 GHz accelerating structures are powered via a high-current drive beam. For an optimal exploitation of its physics potential, CLIC is foreseen to be built and operated in stages. The initial stage will have a centre-of-mass energy of 380 GeV, with a site length of 11 km. The 380 GeV stage optimally combines the exploration of Higgs and top-quark physics, including a top threshold scan near 350 GeV. A higher-energy stage, still using the initial single drive-beam complex, can be optimised for any energy up to 2 TeV. Parameters are presented in detail for a 1.5 TeV stage, with a site length of 29 km. Since the 2018 ESPPU reporting, significant effort was invested in CLIC accelerator optimisation, technology developments and system tests, including collaboration with and gaining experience from new-generation light sources and free-electron lasers. CLIC implementation aspects at CERN have covered detailed studies of civil engineering, electrical networks, cooling and ventilation, scheduling, and costing. The CLIC baseline at 380 GeV is now 100 Hz operation, with a luminosity of 4.5×10^{34} $cm^{-2}s^{-1}$ and a power consumption of 166 MW. Compared to the 2018 design, this gives three times higher luminosity-per-power. The new baseline has two beam-delivery systems, allowing for two detectors operating in parallel, sharing the luminosity. The cost estimate of the 380 GeV baseline is approximately 7.2 billion CHF. The construction of the first CLIC energy stage could start as early as ∼2034-2035 and beam commissioning and first beams would follow a decade later, marking the beginning of a physics programme spanning 20-30 years and providing excellent sensitivity to Beyond Standard Model physics, through direct searches and via a broad set of precision measurements of Standard Model processes, particularly in the Higgs and top-quark sectors. This report summarises the CLIC project, its implementation and running scenarios, with emphasis on new developments and recent progress. It concludes with an update on the CLIC detector studies and on the physics potential in light of the improved accelerator performance. The physics potential includes results from the 3 TeV energy stage, which was studied in detail for the CLIC CDR in 2012 and the CLIC Project Implementation Plan of 2018.

Contents

1 Introduction

The Compact Linear Collider (CLIC) is a high-luminosity linear e^+e^- collider under development by the CLIC accelerator collaboration, hosted by CERN. CLIC uses a novel two-beam acceleration scheme, in which normal-conducting high-gradient 12 GHz acceleration structures are powered via a high-current drive beam. The accelerating structures operate in the range of 72 MV/m to 100 MV/m. The baseline initial stage of CLIC is a 380 GeV machine of 11 km site length, serving two detectors. A higher energy stage of 1.5 TeV with a site length of 29 km and compatible with a single drive beam, is also presented. Intermediate energies remain possible, as well as starting at 250 GeV with fewer accelerating modules.

The CLIC Conceptual Design Report (CDR), published in 2012, focused on a 3 TeV collider, with a first stage at 500 GeV. The accelerator CDR volume [1] (850 pages) and a combined Physics/Detector and Accelerator Report [2] (80 pages) provide detailed descriptions of the accelerator project. The principal focus of the CDR was to demonstrate the feasibility of the CLIC accelerator at high energy (3 TeV) and to confirm that high-precision physics measurements could be performed, despite the luminosity spectrum and the presence of particles from beam-induced background (see also [3]).

After the CDR, and with the discovery of the Higgs boson, the initial stage was changed to 380 GeV. The CLIC accelerator was optimised for three energy stages at centre-of-mass energies of 380 GeV, 1.5 TeV and 3 TeV [4]. A comprehensive technical prototyping programme was carried out over the period 2013-2019. The Project Implementation Plan (270 pages) [5], together with a Physics/Detector and Accelerator Summary Report (95 pages) [6], were submitted for the European Particle Physics strategy update in 2018-2019.

Since the publication of the reports above, the baseline luminosity at 380 GeV has been updated according to new studies. New power estimates performed for the 380 GeV and 1.5 TeV machine show a significant reduction. Technical progress and improvements related to X-band technology and klystron design have been achieved. An interaction region with two beam delivery systems and two detectors has been designed.

This article provides a comprehensive overview of the CLIC project, at the time of the European Particle Physics strategy update in 2025-2026, taking all the latest project developments into account. The CLIC studies have put special emphasis on optimising cost and energy efficiency, and the resulting power and cost estimates are reported.

Section 2 summarises the CLIC design considerations, parameters and performance for the 380 GeV energy stage, presents the interaction region with two detectors and describes the upgrade path to higher energies. Section 2 also summarises key achievements providing evidence that the CLIC performance goals can be met.

Section 3 provides an overview of each collider sub-system.

Section 4 discusses key technical challenges for CLIC; the X-band technology, RF sources and alignment/stability.

Section 5 describes the civil engineering aspects and siting.

Section 6 describes the present plans for the implementation of CLIC, with emphasis on the 380 GeV stage. It reports on schedule aspects, and provides estimates of the energy consumption and of the cost for construction and operation.

Section 7 outlines the CLIC objectives for the period 2026–2033.

Appendix A provides a comprehensive description of systems tests and performance demonstration for CLIC in the CLIC Test Facility 3, FACET, ATF2 and elsewhere.

Appendix C describes a klystron-based version of the 380 GeV CLIC.

Detailed studies of the physics potential and detectors for CLIC, and R&D on detector technologies, are carried out by the CLIC detector and physics (CLICdp) collaboration. CLIC offers a unique combination of high centre-of-mass energies, flexibility over a large energy-range, longitudinal electron polarisation and the clean environment of e^+e^- collisions. This enables a broad and guaranteed physics programme, complementary to HL-LHC. The guaranteed physics reach covers a large number of highly accurate Standard-Model parameter measurements, including the top-quark mass, further top-quark properties, the Higgs couplings, as well as the Higgs self-coupling. CLIC moreover offers a rich potential for extensive exploration of the terascale in the form of direct and indirect searches of BSM effects. The physics potential has been explored in detail [3, 7–13].

The CLICdet detector design has been optimised to fulfill the stringent requirements imposed by the precision physics goals and beam conditions at CLIC [14]. Dedicated R&D on innovative detector technologies for CLIC, as well as technology advances in industry and collaborative R&D together with other particle-physics projects, have enabled significant progress towards reaching the demanding CLIC detector requirements [15, 16]. The CLIC and CLICdp studies are available at: http://clic.cern.

2 CLIC accelerator design and performance

In this section an overview of CLIC at a centre-of-mass energy of 380 GeV is presented. The new baseline includes operation at 100 Hz with two interaction regions and two detectors. An overview of the design considerations, the performance and the performance demonstrations is given. The extension of CLIC to higher energies is presented, as well as the CLIC options for running at 250 GeV.

The baseline presented in this section constitutes a full coherent picture of the machine design and its parameters. A number of on-going studies, may still lead to further performance improvements. These studies include improved beam-delivery systems (see Sect. 3.5), main linac tuning bumps (see Sect. 3.4) and damping ring emittance (see Sect. 3.2).

2.1 CLIC design and performance at 380 GeV

2.1.1 Design overview

The schematic layout of the baseline CLIC complex for 380 GeV operation is shown in Fig. 1 and the key parameters are listed in Table 1.

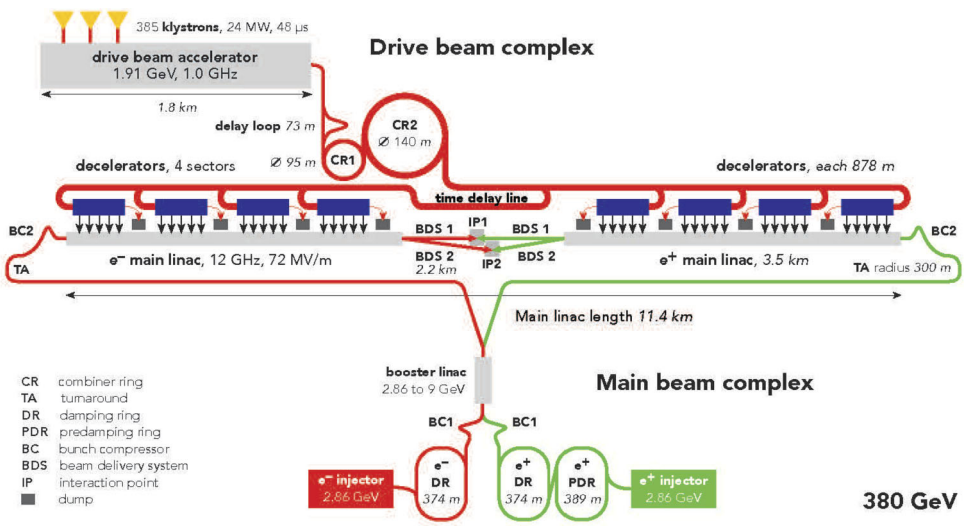

Fig. 1 Schematic layout of the CLIC complex at 380 GeV, with a double beam-delivery system operating with two detectors

Table 1 Key parameters of the baseline machine, a drive-beam based CLIC at $\sqrt{s} = 380$ GeV, running at 100 Hz, operating with two detectors

Parameter	Symbol	Unit	380 GeV, 100 Hz	380 GeV, 50 Hz
Centre-of-mass energy	$\sqrt{s}$	GeV	380	380
Number of interaction points	N_{IP}		2	1
Repetition frequency	f_{rep}	Hz	100	50
Number of bunches per train	n_b		352	352
Bunch separation	Δt	ns	0.5	0.5
Pulse length	τ_{RF}	ns	244	244
Accelerating gradient	G	MV/m	72	72
Total luminosity	$\mathcal{L}$	10^{34} cm^{-2}s^{-1}	4.5	2.3
Luminosity above 99% of $\sqrt{s}$	$\mathcal{L}_{0.01}$	10^{34} cm^{-2}s^{-1}	2.7	1.3
Beamstrahlung photons per particle	n_γ		1.5	1.5
Total integrated luminosity per year	$\mathcal{L}_{\mathrm{int}}$	fb^{-1}	540	270
Power consumption	P	MW	166	105
Main linac tunnel length		km	11.4	11.4
Number of particles per bunch	N	10^9	5.2	5.2
Bunch length	σ_z	µm	70	70
IP beam size	σ_x/σ_y	nm	149/2.0	149/2.0
Final RMS energy spread		%	0.35	0.35

Parameters for an alternative machine, using ca. 40% lower power consumption, running at 50 Hz with a single beam delivery system and one detector, are also given.

The main linac crossing angle is 20 mrad. The crossing angle at the IP depends on the BDS design, and the number of IPs. See Sect. 3.5 for details.

The main electron beam is produced in a conventional radio-frequency (RF) source and accelerated to 2.86 GeV. The beam emittance is then reduced in a damping ring. A second electron beam, accelerated to 2.86 GeV and delivered to a conventional amorphous tungsten target, produces positrons by electron–positron pair production. The positrons are captured by an adiabatic matching device and a capture linac and then accelerated to 2.86 GeV. Their beam emittance is reduced first in a pre-damping ring and then in a damping ring. The ring to main linac system (RTML) accelerates the beams to 9 GeV and compresses their bunch length. The main linacs accelerate the beams to the beam energy at collision of 190 GeV. The beam delivery system removes transverse tails and off-energy particles with collimators and compresses the beam to the small sizes required at the collision point. After the collision, the beams are transported to the respective beam dumps by the post-collision lines.

The RF power for each main linac is provided by a high current, low-energy drive beam that runs parallel to the colliding beam through a sequence of power extraction and transfer structures (PETS). The drive beam generates RF power in the PETS, which is then transferred to the accelerating structures by waveguides.

The drive beam is generated in a central complex with a fundamental frequency of 1 GHz. A 48 µs long beam pulse is produced in the injector and fills every other bucket, i.e. with a bunch spacing of 0.6 m. Every 244 ns, the injector switches from filling even buckets to filling odd buckets and vice versa, creating 244 ns long sub-pulses. The beam is accelerated in the drive-beam linac to 1.91 GeV. A 0.5 GHz resonant RF deflector sends half of the sub-pulses through a delay loop such that its bunches can be interleaved with those of the following sub-pulse that is not delayed. This generates a sequence of 244 ns trains in which every bucket is filled, followed by gaps of the same 244 ns length. In a similar fashion, three of the new sub-pulses are merged in the first combiner ring. Groups of four of the new sub-pulses, now with 0.1 m bunch distance, are then merged in the second combiner ring. The final pulses are thus 244 ns long and have a bunch spacing of 2.5 cm, i.e. providing 24 times the initial beam current. The distance between the pulses has increased to 24×244 ns, which corresponds to twice the length of an 878 m decelerator. The first four sub-pulses are transported through a delay line before they are used to power one of the linacs, while the next four sub-pulses are used to power the other linac directly. The first sub-pulse feeds the first drive-beam decelerator, which runs in parallel to the colliding beam. When the sub-pulse reaches the decelerator end, having delivered most of its energy, the second sub-pulse has reached the beginning of the

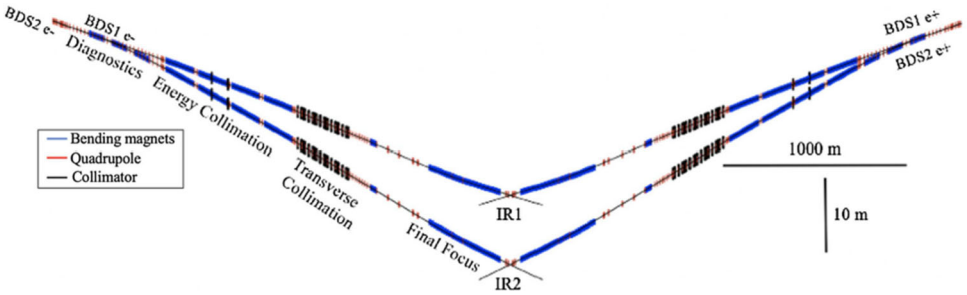

Fig. 2 Schematic layout of CLIC operating with two detectors. From [17]

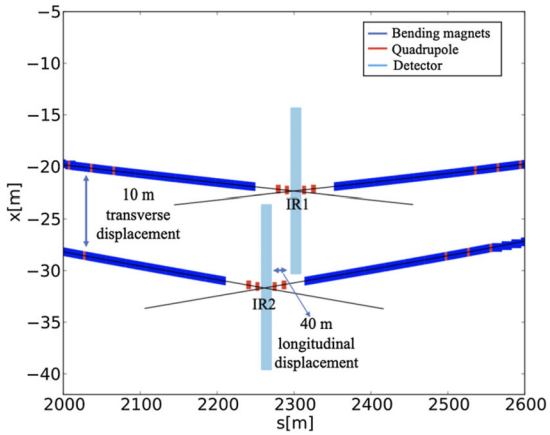

Fig. 3 Zoom at the IRs to have a clear visualization on the longitudinal and transverse separations between the two detectors of about 40 m and about 10 m, respectively. From [17]

second drive-beam decelerator and will feed it, while the colliding beam has meanwhile reached the same location along the linac.

2.1.2 Operation with two detectors

The CLIC baseline is to operate two detectors in parallel, at an average bunch-train repetition rate of 50 Hz. This provides each detector with an average luminosity of about 2.2×10^{34} cm^{-2}s^{-1}. The doubling of machine total repetition rate from 50 Hz to 100 Hz, with respect to the previous baseline [5] is achieved without major design changes. The luminosity delivery can be flexible, if desired a luminosity of (100%) can be provided to a single detector for a given period of time.

The operation of two detectors is achieved with the concept of a dual Beam-Delivery System (BDS) for CLIC that aims to serve two interaction regions (IRs) simultaneously. The dual BDS introduces separate paths for the electron and positron beams to accommodate two detectors with distinct crossing angles. This configuration allows for concurrent data collection at both IRs, enhancing overall experiment throughput and versatility [17].

The 380 GeV stage of CLIC features a dual BDS design achieved by extending the diagnostics section (DS) of the baseline BDS. Eight additional FODO cells, each with a phase advance of 45°, and with a total additional length of 300 m, were added to separate the two IRs longitudinally and transversely. The two BDS paths (BDS1 and BDS2) are optimized for their respective IRs: the crossing angle of IR1 is 18 mrad and the crossing angle of IR2 is 27 mrad (see Sect. 3.5 for details), which is also compatible with potential gamma-gamma collision configurations. A full schematic of the layout is shown in Fig. 2.

To minimize synchrotron radiation effects, the bending angles and magnet strengths in the DS were carefully optimized. The transverse separation between IRs is approximately 10 m, with a longitudinal offset of 40 m to ensure sufficient space for detector placement (see Fig. 3).

The dual BDS maintains robust performance metrics at 380 GeV, with minimal impact on luminosity and beam sizes compared to the single-BDS design. Key results are summarized in Sect. 3.5.4.

2.1.3 Main-beam design considerations and choices

Motivated by an optimal exploration of Higgs and top-quark physics, the baseline for the initial stage of CLIC is 380 GeV. A 10-year operation period at 380 GeV, will be followed by 10 years at a higher energy stage, currently assumed to be 1.5 TeV. Both stages will require only a single drive beam complex. Intermediate energies remain

possible, as well as starting with fewer modules for taking data at 250 GeV. A 3 TeV implementation with two drive beam complexes and a deeper tunnel layout was studied in detail in the CDR [1].

The baseline plan for operating CLIC results in an integrated luminosity per year equivalent to operating at full luminosity for 1.2×10^7 s [18]. This results in integrated luminosities of 4.3 ab^{-1} at 380 GeV and 4.0 ab^{-1} for the 1.5 TeV, see details in Sect. 2.1.7.

The staged approach allows optimal exploitation of the CLIC physics capabilities. For the initial stage, the centre-of-mass energy of 380 GeV gives access to SM Higgs physics and top-quark physics, and provides direct and indirect sensitivity to BSM effects. A top-quark pair-production threshold scan around 350 GeV is also foreseen. A second stage at 1.5 TeV opens more Higgs production channels including $t\bar{t}$H, double-Higgs production, and rare decays, and offers further direct sensitivity to many BSM models. CLIC provides ±80% longitudinal electron polarisation and proposes a sharing between the two polarisation states at each energy stage for optimal physics reach [19]. The energy of the second stage can be optimised in light of new physics information.

Reaching the energy goal requires achieving the target gradient in the accelerating structures. This in turn requires that the structures can sustain the gradient and that the drive beam provides enough power. In addition, to reach the luminosity goal, the colliding beam needs to have a high current and an excellent quality. Thorough studies established a feasible concept for the 380 GeV stage [5]. Based on these the first stage has been designed. The key considerations are:

- The choice of bunch charge and length ensures stable beam transport. The main limitation arises from short-range wakefields in the Main Linac.
- The spacing between subsequent bunches ensures that the long-range wakefields in the Main Linac can be sufficiently damped to avoid beam break-up instabilities.
- The horizontal beam size at the collision point ensures that the beamstrahlung caused by the high beam brightness is kept to an acceptable level for the given bunch charge. This ensures a luminosity spectrum consistent with the requirements of the physics experiments.
- The horizontal emittance is dominated by single particle and collective effects in the Damping Rings and includes some additional contributions from the Ring To Main Linac.
- The vertical emittance is given mainly by the Damping Ring and additional contributions from imperfections of the machine implementation. The target parameters take into account budgets for detrimental effects from static and dynamic imperfections, such as component misalignments and jitter.
- The vertical beta-function is the optimum choice in terms of luminosity. The horizontal beta-function is determined by the combination of required beam size and horizontal emittance.

In summary, the parameters are largely determined by fundamental beam physics and machine design, with the exception of the vertical emittance, which is determined by imperfections. The horizontal beam size is fixed to limit beamstrahlung, therefore if the horizontal emittance is smaller than the target, the horizontal beta-function will be increased to compensate. This means there is no luminosity to be gained by reducing the horizontal emittance.

The most recent beam physics and luminosity considerations for CLIC are presented in [20]. In a machine without imperfections, a vertical emittance of 6 nm is achieved at the interaction point. The impact of static and dynamic imperfections is studied in [20]. The dominant imperfections are the static misalignment of beamline elements and ground motion. Beam-based alignment is used to minimise the impact of static imperfections. The beam-based alignment procedure for CLIC outperforms its requirement, which leads to significantly less vertical emittance growth than budgeted. For the expected alignment imperfections and with a conservative ground motion model, 90% of machines achieve a luminosity of 4.5×10^{34} $cm^{-2}s^{-1}$ or greater, at 100 Hz. This is the value used in Table 1. The average luminosity achieved is 5.6×10^{34} $cm^{-2}s^{-1}$. Future improvements to the technologies used to mitigate imperfections, such as better pre-alignment, active stabilization systems and additional beam-based tuning, will also help increasing this luminosity surplus further. A start-to-end simulation of a perfect machine shows that a luminosity of 8.6×10^{34} $cm^{-2}s^{-1}$ would be achieved.

2.1.4 Beam dynamics and nanobeams

For static imperfections, the vertical emittance growth budgets are the same at 380 GeV and 3 TeV and they correspond to the values described in the CDR [1]. It is required that each system, i.e. RTML, Main Linac and BDS, remains within its emittance budget with a likelihood of more than 90% without further intervention. The key static imperfection is the misalignment of the beamline components with respect to the design. A sophisticated system has been developed and tested that provides a spacial reference frame with unprecedented accuracy, see Sect. 4.10. The Main Linac and BDS components are mounted on movable supports and can be remotely aligned with respect to the reference system. In addition, the main linac accelerating structures are equipped with wakefield monitors that allow the measurement and correction of their offset with respect to the beam. Dispersion-free steering, which has been successfully tested at the SLAC Facility for Advanced Accelerator Experimental Tests (FACET), will further reduce the emittance growth using high-resolution Beam Position Monitors (BPM). In the

BDS, additional tuning is required using optical knobs that move several multi-pole magnets simultaneously to correct the optics properties.

The performance specifications for the alignment systems and instrumentation are kept the same at 380 GeV and 3 TeV and correspond to the CDR description. They are sufficient to achieve the required performance at 3 TeV and most of them could be relaxed for the first energy stage, typically by about a factor of two, to meet the same emittance budget. However, the original, better performances are required for the upgrade to the higher energy stages. No substantial cost saving has been identified by relaxing the specifications for the first stage. Therefore, it has been decided to ensure that the system is consistent with the final energy from the very beginning, thus avoiding the need to upgrade the already existing hardware. This also provides additional margin for achieving the required luminosity.

The tuning procedures for the RTML and the BDS have been improved during the last years. Studies of the static imperfections in the RTML [21, 22], the Main Linac [23] and the BDS [24] show that the target budgets can be met in each system with a margin; in the BDS, the tuning is now also much faster.

Also, for the dynamic imperfections the vertical emittance budgets are the same for 380 GeV and 3 TeV. Key imperfections are the movement of components due to ground motion or technical noise, phase and amplitude jitter of the drive beam, and potentially dynamic magnetic fields.

The level of ground motion is site dependent; measurements in the LEP tunnel showed very small motion [25] while measurements in the CMS detector hall showed much larger motion [26]. With the new design of the final focus system, all relevant accelerator components are mounted in the tunnel of the collider, so one can expect ground motion levels similar to the LEP tunnel. However, for the ground motion studies the level of the CMS detector hall has been used in order to evaluate the robustness of the solutions. The ground motion is mitigated by the design of the magnets, a mechanical feedback that decouples them from the ground, and by beam-based feedback on trajectories. Prototypes of the mechanical feedback have been tested successfully. In the CDR, detailed studies of the 3 TeV stage showed that the performance goal can be met with margin. Studies of the 380 GeV case [27] confirm that ground motion will only use about 10% of the budget allocated to dynamic imperfections.

Dynamic magnetic stray fields may deflect the colliding beams, leading to trajectory jitter and emittance growth, thus reducing luminosity. Their impact is particularly large in the RTML and the BDS. In the latter they are more important at 380 GeV than at 3 TeV due to the lower beam energy. A study in collaboration with experts from the Hungarian Geophysics Institute has commenced to investigate these fields and define the mitigation technologies. The magnetic fields can originate from different sources: natural sources, such as geomagnetic storms; environmental sources, such as railway trains and power lines and technical sources, i.e. from the collider itself. A survey of natural sources showed that they should not affect the luminosity [28] and a measurement station has been established in the Jura mountains near CERN to collect long-term regional data. The study of the environmental and technical sources has started but is not yet complete. Preliminary estimates have been performed using the magnetic field variations that were measured in the LHC tunnel. They concluded that a thin mu-metal shield of the drifts in the RTML and BDS can bring the fields down to a level that does not impact luminosity [27].

Further development of the foreseen technical and beam-based imperfection mitigation systems could allow for a reduction in the emittance budgets and an increase in the luminosity target. Also, new systems could be devised to this end. As an example, the addition of a few klystron-powered, higher-frequency accelerating structures could allow to reduce the energy spread of the colliding beams, which can improve the luminosity and also the luminosity spectrum for specific measurements such as the top-quark threshold scan.

2.1.5 Beam experiments

Beam experiments and hardware tests have provided the evidence that the CLIC performance goals can be met. Some key cases are discussed in the following, while Appendix A contains a more comprehensive overview of performance demonstrations.

Two beam acceleration To test the drive-beam concept, the third CLIC Test Facility (CTF3) [29] was constructed and operated by an international collaboration. It has addressed the key points of the concept:

- The stable acceleration of the initial high-current drive beam in the accelerator.
- The high transfer efficiency from the RF to the drive beam.
- The generation of the final drive-beam structure using the delay loop and a combiner ring.
- The quality of the final drive beam. In particular, feedback has been used to stabilise the drive-beam current and phase to ensure correct main-beam acceleration. CTF3 achieved the drive-beam phase stability that is required for CLIC [27, 30–32].
- The process of RF power extraction from the drive beam and its use to accelerate the main beam, and the performance of the associated hardware. The main beam has been accelerated with a maximum gradient of 145 MV/m.

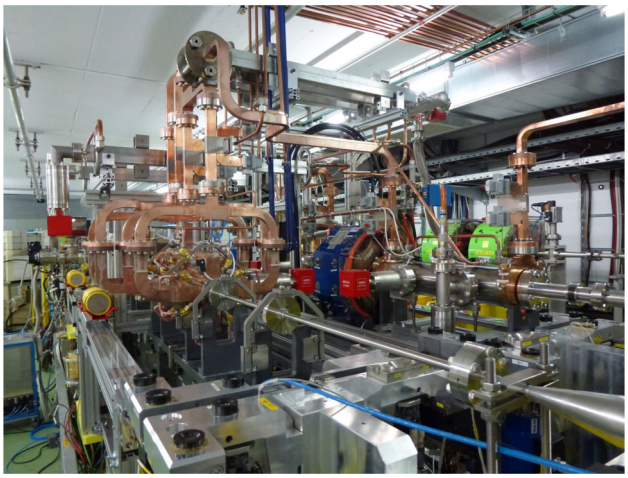

Fig. 4 The two-beam acceleration test stand in the CTF3 facility. The drive beam enters from the middle-right, while the probe (main) beam enters from the bottom-right

CTF3 established the feasibility of the drive-beam concept and the ability to use this scheme to accelerate the main beam. As mentioned in 2.1.5 the results are summarized in [33], and the references therein give more details concerning the points listed above. Figure 4 shows the corresponding two-beam acceleration test stand in the CTF3 facility.

CTF3 has also been instrumental for the development of all the different hardware components that are essential for the scheme – among them the drive-beam gun, the bunch compressor, the drive-beam accelerating structures, RF deflectors, the PETS including a mechanism to switch them off individually, the power distribution waveguide system, fast-feedback systems, drive-beam current and phase monitors, as well as other instrumentation. CTF3 stopped operation after successfully completing its experimental programme in December 2016 and a new facility, CLEAR, is operated [34] in the same location. It re-uses the CTF3 main-beam installations and additional hardware and it runs as a user facility, including for collider R&D [35].

Other beam experiments and hardware tests

- The successful technology demonstration of the CLIC accelerating gradient is discussed in detail in Appendix A. The main performance limitation arises from vacuum discharge, i.e. breakdowns; a rate of less than 3×10^{-7} m^{-1} is required for the target gradient of 72 MV/m. The key parameters for the accelerating structure and the beam have been optimised together. In particular, structures with smaller iris apertures achieve higher gradients for the same breakdown rate, but they reduce the maximum bunch charge for stable beam transport because they produce stronger wakefields.
- The Stanford Linear Collider (SLC) [36], the only linear collider so far, is a proof of principle for the linear collider concept and contributed important physics data at the Z-pole. The SLC achieved collision beam sizes smaller than nominal, but did not reach the nominal bunch charge [37]. Two collective effects led to the charge limitations. They have been fully understood and are not present in the CLIC design.
- The electron polarisation that has been achieved at collision in SLC is similar to the CLIC goal.
- The strong beam–beam effect increases the luminosity in CLIC. This effect has been observed at the SLC, in agreement with the theoretical predictions [38].
- Modern light sources achieve CLIC-level vertical emittances, in particular the Swiss Light Source and the Australian Light Source [39–41].
- CLIC parameters require strong focusing at the IP. This focusing has been demonstrated at two test facilities, FFTB [42] at SLAC and the Accelerator Test Facility ATF2 [43, 44] at KEK. The achieved vertical beam sizes were 40% and 10% above the respective design values for these test facilities. In the super B-factory at KEK the beams will perform many turns through the final focus system, still one aims at beta-functions that are only a factor three larger than in CLIC, and even smaller beta-functions similar to the CLIC values are being discussed [45].
- The use of beam-based alignment, i.e. dispersion free steering [46, 47] to maintain small emittances in a linac has successfully been tested in FACET [48] and FERMI [49].
- The effective suppression of harmful long-range wakefields has been tested with beam in the CLIC accelerating structures [50].
- The novel precision pre-alignment system of CLIC and sophisticated beam-based alignment and tuning ensures the preservation of the beam quality during transport. The alignment system is based on a concept developed for the LHC interaction regions, but with improved performance. Prototypes have been built and successfully tested, see Sect. 4.10.

- Quadrupole jitter has been an important source of beam jitter in the SLC. For CLIC this has been addressed by designing the magnet supports to avoid resonances at low frequencies and by developing an active stabilisation system for the magnets, which demonstrated a reduction of the jitter to the sub-nanometre regime, see Sect. 4.10.
- CLIC requires excellent relative timing at the 50 fs level over the collider complex. CTF3 has demonstrated the phase monitor and correction with fast feed-forward [32]. Modern Free Electron Lasers (FEL) have developed the technology to provide the timing reference over large distances.
- High availability is key to achieve the luminosity goal. The very reliable routine operation of light sources, FELs, the B-factories and the LHC provide concepts to address this issue.

In conclusion, the CLIC parameters are ambitious but are supported by simulation studies, measured hardware performances and beam tests. This gives confidence that the goals can be met.

2.1.6 Operation and availability

The machine protection and operational considerations and strategies at 380 GeV are similar to those at higher energies and are described in the CDR [1]. Machine protection relies on passive protection and the processing of the diagnostics data between two beam pulses to generate a beam permit signal.

Different events can impact both operation and availability and can be roughly categorised as:

- Events that do not require an intervention in the machine and are handled by the control system. These include RF breakdowns in the accelerating structures, which will lead to a small energy error and potentially slight transverse deflection of the beam. Typically this will happen only every 100 beam pulses and will be corrected by the feedback systems.
- Events that require a short stop on the machine but no intervention, such as a false trigger of the machine protection system – e.g. caused by a single event upset. In this case, the machine can be brought back to full intensity in a few seconds.
- Failures of machine components that might compromise the performance but do not require stopping the beam. This includes failures of klystrons or instrumentation. These are mitigated by providing sufficient reserve.
- Failures that require to stop the beam and repair the machine. This is the case for failures of power converters.

Based on an assessment of the complexity of the different systems, an availability goal has been defined for each of them. This allows investigation of individual systems and focus on the key issues.

A number of key potential failures has been studied in detail, in particular of magnet power converters and RF power systems. In the drive-beam accelerator, a reserve of 5% RF units is installed and klystrons operate below their maximum power. If one fails, the power of the others is increased accordingly. Similarly, BPM failures or orbit corrector failures in the main linac compromise the correction of ground motion. However, if 10% of them fail, the effect of ground motion is only increased by 14%. During the technical stops failed klystrons and instrumentation can be replaced. The CLIC lattice design has been optimised to minimise the impact of power converter failures. In particular in the drive beam, the many quadrupoles are powered in groups to minimise the number of power converters and small trims adjust their strength as needed. Compared to individual powering, this strongly increases the mean time between failures, since failures of trims can be mitigated to a large extent. A similar strategy is used for the main-beam quadrupoles.

Detailed studies will be required during the technical design phase covering all components to ensure that the availability goal can be met. Currently, considering key failures, no obstacle to reach the target availability has been identified.

2.1.7 Annual and integrated luminosities, energy flexibility

Estimates of the integrated luminosities are based on an annual operational scenario [18]. After completion of CLIC commissioning, the tentative plan for the operation of CLIC includes a yearly shutdown of 120 days. In addition 30 days are foreseen for the machine commissioning, 20 days for machine development and 10 days for planned technical stops. This leaves 185 days of operation for the experiments. The target availability for the experiments during this period is 75%. Hence the integrated luminosity per year corresponds to operation at full luminosity for 1.2×10^7 seconds [18].

The baseline is to run for 10 years at 380 GeV at 100 Hz, and 10 years at 1500 GeV at 50 Hz. A luminosity ramp-up of three years (10%, 30%, 60%) is assumed for the first stage and two years (25%, 75%) for the subsequent stage. This results in integrated luminosities of 4.3 ab^{-1} at 380 GeV and 4.0 ab^{-1} for the 1.5 TeV.

Prior to data-taking at the first stage, commissioning of the individual systems and one full year of commissioning with beam are foreseen. These are part of the construction schedule.

The beam parameters can be adjusted to different physics requirements. In particular, the collision energy can be adjusted to the requirements by lowering the gradient in the main linacs accordingly. For a significantly reduced

gradient, the bunch charge will have to be reduced in proportion to the energy to ensure beam stability. However, at this moment the only operation energy different from 380 GeV that is required is around 350 GeV to scan the top-quark pair-production threshold. In this case, the bunch charge can remain constant. The RF phases of the accelerating structures are slightly modified compared to the 380 GeV case in order to achieve an RMS beam energy spread of only 0.3%. This allows reaching a luminosity similar to the 380 GeV goal.

Alternatively, when an even smaller beam energy spread would be required, e.g. at the 350 GeV top-quark threshold [9], the beam energy can be lowered at the cost of a reduction in luminosity. One can reduce the bunch charge by 10% and increase its length by 10%. This would keep the wakefield effects in the main linac constant. This configuration reduces the luminosity by around 20%, but reduces the beam energy spread to 0.2%. Similarly, it is possible to reduce the beamstrahlung by increasing the horizontal beam size, in cases where the improved luminosity spectrum is considered more crucial than the luminosity.

Furthermore, gamma-gamma collisions at up to ∼315 GeV are possible with a luminosity spectrum interesting for physics [51].

Z-pole running Occasionally operating the fully installed 380 GeV CLIC accelerator complex at the Z-pole can be motivated by detector calibration purposes. In this scenario the main linac gradient needs to be reduced by about a factor four. The bunch charge is reduced by a similar amount, but the normalized emittances and bunch length remain the same. The beam size at the interaction point increases with the square root of 1/E in the transverse planes. Together this leads to a luminosity reduction roughly proportional to E^3, resulting in an expected luminosity of about 6.9×10^{32} $cm^{-2}s^{-1}$ for 100 Hz operation at 91 GeV.

Alternatively, an initial installation of just the linac needed for the 91 GeV Z-pole, and an appropriately adapted beam delivery system, would result in a luminosity of 1.1×10^{34} $cm^{-2}s^{-1}$ for 100 Hz operation. Or, one could operate with a short linac (approximately 1 km of main linac on each side), before the full 380 GeV machine is installed, quite feasibly using a klystron driven linac. In this scenario the bunch parameters remain unchanged, except for the beam energy, and hence the beam size, at the interaction point. In this case, the luminosity scales, roughly, with the energy. The Z-pole operation could also be set up before one moves to the next energy stage. Hence, at the Z-pole, between 7.5 fb^{-1} and 135 fb^{-1} can be achieved per year for an unmodified and a modified collider, respectively. As for all other CLIC energies, ±80% longitudinal electron polarisation is available at the Z-pole.

2.2 CLIC at 250 GeV

A 250 GeV option can be implemented by using the 380 GeV design as basis, removing 35% of the two-beam modules in each sector, and reducing the drive-beam energy correspondingly. The lower number of modules and the lower-energy drive beam linac give significant initial cost savings if the 250 GeV is run as a first stage. The upgrade to 380 GeV is then straight-forward; installing the missing modules, and extending the drive beam accelerator. This initial missing-module approach is therefore the most practical and economic option for operation at 250 GeV.

The luminosity of the 250 GeV machine is assumed to scale with the energy, thus a factor (250/380) lower than that of the 380 GeV machine, yielding about $3.0 \times 10^{34}\,cm^{-2}s^{-1}$ at 100 Hz.

2.3 Extension to higher energy stages

The CLIC 380 GeV energy stage can be efficiently upgraded to higher energies. This flexibility has been an integral part of the design choices for the first energy stage.

With a single drive beam complex and running at 100 Hz, the machine can be upgraded to 550 GeV. With a single drive beam complex and running at 50 Hz, the machine can be upgraded 1.5 TeV, and possibly to 2 TeV. A detailed description of the 3 TeV stage is documented in the CLIC CDR [1]. Two drive beam complexes are required for the 3 TeV machine. A 3 TeV machine would need a different tunnel layout to one presented in Sect. 5.

A design for 1.5 TeV has been worked out in detail, and its parameters are given in Table 2. The table also contains numbers for a 250 GeV and 550 GeV CLIC. The power and luminosity at the latter two energies are scalings, based on the 380 GeV and 1500 GeV designs.

In the 380 GeV stage, the linac consists of modules that contain accelerating structures that are optimised for this energy. At higher energies these modules are reused and new modules are added to the linac. First, the linac tunnel is extended and a new main-beam turn-around is constructed at its new end. The technical installations in the old turn-around and the subsequent bunch compressor are then moved to this new location. Similarly, the existing main linac installation is moved to the beginning of the new tunnel. Finally, the new modules that are optimised for the new energy are added to the main linac. Their accelerating structures have smaller apertures and can reach a higher gradient of 100 MV/m; the increased wakefield effect is mitigated by the reduced bunch charge

Table 2 Key parameters for 380 GeV and 1.5 TeV stages of CLIC

Parameter	Unit	380 GeV	1.5 TeV	250 GeV	550 GeV
Centre-of-mass energy	GeV	380	1500	250	550
Repetition frequency	Hz	100	50	100	100
Nb. of bunches per train		352	312	352	352
Bunch separation	ns	0.5	0.5	0.5	0.5
Pulse length	ns	244	244	244	244
Accelerating gradient	MV/m	72	72/100	72	72
Total luminosity	10^{34} cm^{-2}s^{-1}	4.5	3.7*	∼3.0	∼6.5
Lum. above 99% of $\sqrt{s}$	10^{34} cm^{-2}s^{-1}	2.7	1.4	∼2.1	∼3.2
Total int. lum. per year	fb^{-1}	540	444	∼350	∼780
Power consumption	MW	166	287	∼130	∼210
Main linac tunnel length	km	11.4	29.0	11.4	∼15
Nb. of particles per bunch	10^9	5.2	3.7	5.2	5.2
Bunch length	µm	70	44	70	70
IP beam size	nm	149/2.0	60/1.5	∼184/2.5	∼124/1.7

Parameters for energy options at 250 GeV and 550 GeV are also given; for these options the power and luminosity are scalings, based on the 380 GeV and 1.5 TeV designs.

*The luminosity for the 1.5 TeV machine has not been updated to reflect recent alignment studies [20]. If the same method is applied, the luminosity at 1.5 TeV is expected to reach 5.6×10^{34} cm^{-2}s^{-1}.

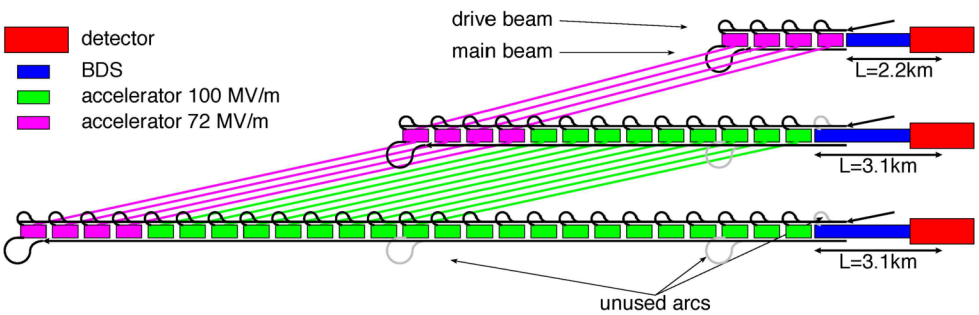

Fig. 5 The concept of the CLIC energy staging for the baseline design. For higher energies, the lower gradient structures are reused for the low energy part of the linac, in addition 100 MV/m structures are installed for the main linac extension

and length. The beam delivery system has to be modified by installing magnets that are suited for the higher energy and it will be extended in length. The beam extraction line also has to be modified to accept the larger beam energy but the dump remains untouched. The concept for upgrading from a 380 GeV stage to a 1.5 TeV stage is shown schematically in Fig. 5.

In the following only the baseline is discussed. The design of the first stage considers the baseline upgrade scenario from the beginning. For the luminosity target at 380 GeV, the resulting cost increase of the first stage is 50 MCHF compared to the fully optimised first energy stage alone (without the constraints imposed by a future energy upgrade beyond 380 GeV). To minimise the integrated cost of all stages, the upgrades reuse the main-beam injectors and the drive-beam complex with limited modifications, and reuse all main linac modules.

In order to minimise modifications to the drive-beam complex, the drive-beam current is the same at all energy stages. The existing drive-beam RF units can therefore continue to be used without modification. In addition, the RF pulse length of the first stage is chosen to be the same as in the subsequent energy stages. This is important since the lengths of the delay loop and the combiner rings, as well as the spacings of the turn-around loops in the main linac, are directly proportional to the RF pulse length. Hence, the constant RF pulse length allows the reuse of the whole drive-beam combination complex. For the upgrade from 380 GeV to 1.5 TeV, only minor modifications are required for the drive-beam production complex. The drive-beam accelerator pulse length is increased in order to feed all of the new decelerators, and also its beam energy is increased by 20%. The energy increase is achieved by adding more drive-beam modules. The pulse length increase is achieved by increasing the stored energy in the modulators to produce longer pulses. The klystron parameters in the first energy stage have been chosen to be

compatible with the operation using longer pulses and higher average power. The remainder of the drive-beam complex remains unchanged, except that all magnets after the drive-beam linac need to operate at a 20% larger field, which is also foreseen in the magnet design. An upgrade from 1.5 TeV to 3 TeV would require the construction of a second drive-beam generation complex.

The impact of the upgrades on the main-beam complex has also been minimised by design. The bunches of the main-beam pulses have the same spacing at all energy stages, while at higher energies the number of bunches per train and their charge is smaller. Therefore the main linac modules of the first stage can accelerate the trains of the second and third stage without modification. Since the drive-beam current does not change, also the powering of the modules is the same at all energies. The upgrade to 1.5 TeV requires an additional 9 decelerator sectors per side and a 3 TeV stage would need another 12. An upgrade from 380 GeV to 550 GeV requires an additional 2 decelerator sectors per side.

Still some modifications are required in the main-beam complex. The injectors need to produce fewer bunches with a smaller charge than before, but a smaller horizontal emittance and bunch length is required at the start of the main linac. The smaller beam current requires less RF, so the klystrons can be operated at lower power and the emittance growth due to collective effects will be reduced. The smaller horizontal emittance is mainly achieved by some adjustment of the damping rings.

The preservation of the beam quality in the main linac is slightly more challenging at the higher energies. However, the specifications for the performance of alignment and stabilisation systems for the 380 GeV stage are based on the requirements for a 3 TeV stage. They are therefore sufficient for high energy stages and no upgrades of these systems are required.

The collimation system is longer at higher energies to ensure the collimator survival at the higher beam energies. Similarly the final focus system is slightly longer to limit the amount of synchrotron radiation and emittance degradation in the indispensable bending of the beams. The systems have to be re-built using higher field magnets. However, the integration into the existing tunnel is possible by design. The extraction line that guides the beams from the detector to the beam dump will also need to be equipped with new magnets.

3 System overview

In this section, we review each of the major accelerator subsystems, give an overview of each system's functioning, and show the important parameters.

3.1 Main-Beam Injectors

The CLIC Main Beam Injectors (MBIs) consist of a polarised electron source, a conventional electron source, and an unpolarized positron source. The polarised low-emittance electron source is a photo-injector followed by a dedicated electron injector linac accelerating the beam to 2.86 GeV, which provides the high-brightness electron beams for the collider. The polarised beam passes through a spin rotator before and after the damping ring (DR), followed by a bunch compressor and the booster linac, which brings the beam to 9 GeV energy. The electron source for positron production is a conventional thermionic gun that delivers a low-quality unpolarized beam to the tungsten target of the positron source. The generated positrons are focused and re-accelerated to 2.86 GeV in a dedicated positron linac. The large phase space of the positrons is reduced to the required emittance in a pre-damping ring (PDR) followed by a damping ring (DR). The bunch compressor and the booster linac are shared with the electron beam. The injector complex is located in a central complex on the surface, parallel to the main linac tunnel. This allows the injector installations to be retained for upgrades to higher energies. A schematic view of the injector complex is shown in Fig. 6.

The injector linacs use a 2 GHz RF system and FODO lattices. Two compressed RF pulses, spaced by 5 µs, accelerate the positron and the electron beam in the common booster linac, allowing individual beam loading compensation. The beam dynamics of the injector linacs and the bunch compressor have been optimised and updated. Details can be found in [22].

The CLIC polarised electron source uses a DC-photo injector followed by a 2 GHz bunching and accelerating system. The spin-polarised electrons are generated using a polarised laser impinging on a strained GaAs cathode. Such cathodes have been used at several accelerator laboratories and demonstrated the CLIC requirements in terms of lifetime and charge extraction [52]. The electrons are accelerated in a pre-injector up to 200 MeV before being injected into the electron injector linac, which boosts their energy to 2.86 GeV. A spin rotator orients the spin vertically before injection into the DR.

The CLIC positron source consists of a 2.86 GeV electron beam impinging on an amorphous tungsten target – the hybrid target considered in previous design stages was given up. Recent improvements in positron capture efficiency allowed the energy of the driver beam to be reduced from 5 GeV to 2.86 GeV, which saves cost and

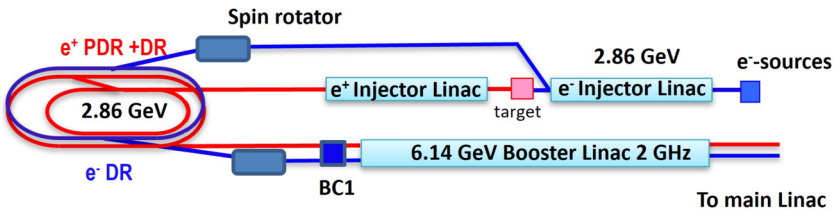

Fig. 6 Schematic layout of the Main-Beam Injector complex. Electrons in blue and positrons in red. BC1 and the Booster Linac are common for electrons and positrons

Table 3 Beam parameters at the entrance of the Pre-Damping Ring for polarized electrons and for positrons at 2.86 GeV

Parameter	Unit	Polarized electrons	Positrons
E	GeV	2.86	2.86
N	-	6×10^9	6×10^9
n_b	-	352	352
Δt_b	ns	0.5	0.5
t_{pulse}	ns	176	176
$\epsilon_{x,y}$	mm mrad	<25	7071, 7577
σ_z	mm	<4	3.3
σ_E	%	<1	1.63
Charge stability shot-to-shot	%	1	1
Charge stability flatness on flat top	%	1	1
f_{rep}	Hz	50	50
P	kW	45	45

electrical power [53]. This also led to significantly less peak-power-deposition density (PEDD) in the amorphous target, which ensures a longer target lifetime. The positrons are captured after the target with an adiabatic matching device and accelerated into a 2 GHz capture linac, bringing the positrons to 200 MeV energy. Recent simulations and updates to the system showed that the positron yield from the target to the Pre-Damping Ring (PDR) could be increased significantly compared to the CDR and PIP results, to ≈1 e^+/e^- [54].

Several changes have been implemented in the DR complex relative to the systems described in the CDR [55]. The updated scheme consists of changing the RF frequency from 1 to 2 GHz in all damping rings, removing the need for the Delay Loop. The electron PDR considered in previous design stages is no longer needed because the electron injector can deliver an emittance smaller than 25 mm mrad and can be injected directly into the DR. In contrast, with its high incoming emittance, the positron beam continues to require a PDR. Thus, the positron bunch train is delayed 20 ms relative to the corresponding electron beam, and is therefore synchronous with the subsequent electron bunch train given the 50 Hz train repetition frequency. Finally, the yield in the positron production chain has been increased significantly, and a single positron production target is sufficient instead of two parallel targets as in the CDR. The different linacs of the injector complex are now housed in one big tunnel with the damping rings stacked on top of each other, on one end to optimise the need for tunnels and buildings.

The beam parameters at the entrance to the rings have changed slightly from the CDR and can be found in Table 3. The bunch charge is increased, and the number of bunches is slightly higher. The bunch spacing is now 0.5 ns, so the train length is shorter. The injectors have been designed to provide about 15% more intensity than required at the input of the DR providing a margin for unexpected beam losses. Two adjacent RF pulses in the booster linac accelerate the electron and positron beams. The time interval between the first electron and positron bunches is 5 µs, which corresponds to the difference in path length due to the civil engineering footprint of the collider. A summary of the main components of the injector linacs can be found in Table 4. A detailed description of the designs of the RF accelerating structures used in the injector complex can be found in [56].

3.2 Damping Rings

The Damping Rings (DRs) are a fundamental part of the CLIC injector complex and are required to damp the large emittance of the injector linac beams, particularly for positrons, in all three dimensions to obtain the desired luminosity. The normalised transverse emittance of the incoming beam is to be reduced to 500 nm and 5 nm in horizontal and vertical directions, respectively, at an energy of 2.86 Gev, corresponding to geometric emittances of around 90 pm rad and 0.9 pm rad. These transverse emittances, combined with the longitudinal emittance specification of 6 keV m (i.e. ultra-short bunch lengths of below 2 mm), while individually achieved in light sources

Table 4 Main parameters and components of the Injector Linacs

A RF unit consists of a modulator, a klystron, a pulse compressor and two accelerating structures. Spare units are added to the number of RF units.

LINAC	Integrated Voltage (GeV)	Charge (nC)	Gradient (MV/m)	RF-units No.	Length (m)
Electron Injector Linac	2.86	1	15.6	30+1	250
Positron Linac	2.86	1	14.5	32+1	280
Booster Linac	6.14	0.83	16.7	62+2	550
Bunch Compressor BC1	0.5	0.83	14	5+1	50

in operation, are unprecedented in combination with a high bunch population of 5.7×10^9 (a margin for the bunch charge was put in the design since only 5.2×10^9 are needed for collision). The generation and preservation of this high bunch brightness is subject to a number of collective effects (intra-beam scattering, space-charge, coherent instabilities including e-cloud for positrons and fast-ion for electrons) and drives both the optics of the rings and the various mitigation measures for vacuum design and feedbacks [57–61]. After the publication of the CDR [55] and in view of a CLIC staged approach [7], an effort was made to revise the DR system, adapting its performance to the different stages of the collider and in particular to the 380 GeV first stage.

A schematic view of the DR complex with the e^- and e^+ DR and the positron PDR (red) is shown in Fig. 6. In the original design, four rings were foreseen: a PDR and a main DR for each particle species. Now, only three are needed. In the positron line, the PDR is necessary due to the large input emittance coming from the positron source, which requires dynamic and momentum acceptances incompatible with the design of a high-focusing ultra-low emittance main DR. In addition, the storing time of 20 ms, corresponding to the high repetition rate of the collider, 50 Hz, is not long enough to allow the large injected emittances to damp to the required output value. In the case of the electrons, a combination of a high-brightness source and a careful emittance preservation in the injector linac could allow for a transverse input normalised emittance value of around 10 µm, which is lower in the horizontal but higher in the vertical plane, with respect to the actual performance of the PDR. A careful Dynamic Aperture (DA) optimisation of the DRs in the vertical plane confirmed that such an emittance could be accommodated in the main rings, thereby making the electron PDR obsolete. The possibility exists of replacing the positron PDR with a booster ring, which could simultaneously dampen and accelerate the beam, thereby reducing the positron linac cost.

In the CDR [1], the injected bunch train structure in the DRs was composed of two trains with twice the nominal separation (1 vs 0.5 ns), separated by half the DR circumference. The two-train structure of 1 GHz was chosen to reduce the transient beam loading effects in the RF cavities of the DRs. These trains were damped simultaneously and then extracted in a single turn from the main DR. A delay and recombination loop was located downstream of the rings, and served to combine the two trains into one, through an RF deflector, thus providing the required 2 GHz bunch structure. However, it was apparent [62] that an RF system with a frequency of 2 GHz has no higher technological difficulties than a system with an RF frequency of 1 GHz. In addition, using 2 GHz avoids the complexity of the RF deflector for the train recombination and reduces the impedance that might affect the transverse emittances. The RF option with a frequency of 2 GHz was then chosen as the baseline. A design optimisation of the RF system, including low-level RF, was further studied using a novel concept which significantly reduced the DR power consumption [63, 64].

The DRs design is based on a racetrack shape composed of Theoretical Minimum Emittance (TME) arc cells, FODO cells, straight sections, and Super-Conducting (SC) damping wigglers. The DR design was revised based on recent developments in the low-emittance rings community for both beam dynamics and technology. This resulted in a new DR arc cell employing a novel concept of a TME with a longitudinally varying bend [60, 65–67]. This dipole with a varying field along the longitudinal position and including a small transverse gradient can further reduce the horizontal emittance while keeping the same space constraints of the TME arc cell. A variable dipole prototype based on permanent magnet technology was designed and built at CIEMAT [68], achieving all specifications, including field quality. Furthermore, using a novel wire technology with Nb_3Sn, higher fields can be reached in the SC wigglers [69, 70] for roughly the same period length. These two considerations enabled the reduction of the DR circumference by approximately 13%, while maintaining their performance. The parameters for the new design are found in Table 5. This design achieves normalised emittances within the required targets for all collider flavours and even higher bunch charge with some margin. The damping times are short enough to enable operation at 100 Hz, without requiring the storage of more trains and operating in staggered mode. Finally, the lattice design was revised, significantly reducing chromaticity and increasing the dynamic aperture [60]. Additional work was undertaken in collaboration with the light-source community for beam tests of critical hardware, such as the SC wigglers [71, 72] and the kicker system [73–77]. In particular, a variable bend concept spin-off was further developed through EU funds with the involvement of industry, for building another prototype with slightly pushed parameters, which could reduce the horizontal emittance of the already upgraded ELETTRA storage ring by an additional factor of two [78].

Table 5 Design parameters for the improved design of the CLIC DRs, for the case of $f_{\mathrm{RF}} = 2$ GHz and $N_b = 5.7 \times 10^9$

Parameters, Symbol [Unit]	Variable dipole
Energy, E [GeV]	2.86
Bunch population, N_b [10^9]	5.7
Circumference, C [m]	373.7
Number of arc cells/wigglers, N_d/N_w	90/40
RF Voltage, V_{RF} [MV]	6.50
RF Stationary phase [^{o}]	63.0
Harmonic number, h	2493
Momentum compaction, α_c [10^{-4}]	0.88
Damping times, (τ_x, τ_y, τ_l) [ms]	(1.19, 1.23, 0.61)
Energy loss/turn, U [MeV]	5.8
Horizontal and vertical tune, (Q_x, Q_y)	(51.18, 14.55)
Horizontal and vertical chromaticity, (ξ_x, ξ_y)	(−67, −75)
Wiggler peak field, B_w [T]	3.5
Wiggler length, L_w [m]	2
Wiggler period, λ_w [cm]	4.9
Normalized horiz. emittance with IBS, $\gamma\epsilon_x$ [nm-rad]	472
Normalized vert. emittance with IBS, $\gamma\epsilon_y$ [nm-rad]	4.6
Longitudinal emittance with IBS, ϵ_l [keVm]	5.8
IBS factors hor./ver./long.	1.24/1.26/1.02

The magnetic field is varying along the dipoles [60].

Table 6 Beam parameters assumed at the entrance and required at the exit of the CLIC RTML

Parameter	Unit	Entrance	Exit
Bunches per train		352	
Particles per bunch		5.2×10^9	
Beam energy	GeV	2.86	9
Bunch length (σ_z)	µm	1800	∼70
Energy spread (σ_E/E)	%	0.12	< 1.7
Horizontal emittance ($\epsilon_{n,x}$)	nm· rad	700	< 800
Vertical emittance ($\epsilon_{n,y}$)	nm· rad	5	< 6

3.3 Ring To Main Linac sections

3.3.1 Overview

The Ring To Main Linac (RTML) sections transport the electron and the positron beams from their respective damping ring at ground level to the main start points of the main linacs underground. While transporting the beam and matching the geometric layout of the beamlines, the RTML must preserve the ultra-low beam transverse emittances from the damping rings, increase the beam energy from 2.86 GeV to 9 GeV, and compress the bunch length from 1.8 mm to ≈70 µm. Table 6 summarises the beam parameters assumed at the entrance and required at the exit of the CLIC RTML. The layout and total lengths of the electron and positron RTMLs are different, as the two lines have to accommodate different tunnel requirements and guarantee the correct arrival time of the beams at the linacs start and, therefore, at the Interaction Point (IP). The electron line comprises eight subsystems: the Spin Rotator (SR), the two Bunch Compressors (BC1 and BC2), the Booster Linac (BL, which is shared between electrons and positrons), the Central Arc (CA), the Vertical Transfer (VT), the Long Transfer Line (LTL) and the Turn-Around Loop (TAL). The positron RTML comprises the same subsystems as the electron line, except for the Spin Rotator, which is absent and labelled as Transport Line (TL) in the tables of this section. A sketch of the whole RTML showing all subsystems is visible in Fig. 7.

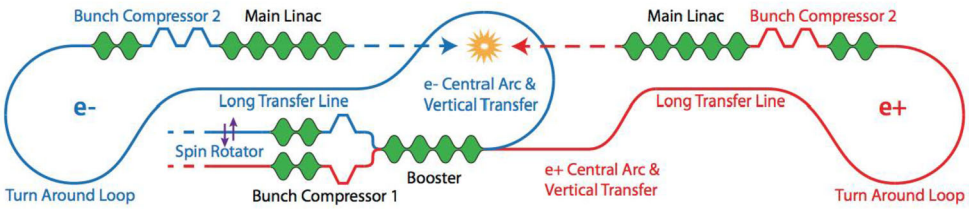

Fig. 7 Sketch of RTML section, all subsystems are visible (dimensions not-to-scale)

Table 7 Main parameters of the two types of RF structures used in the RTML

Parameter	Unit	"CLIC L-band"	"TD-31" X-band
Section		BC1 & BL	BC2
RF frequency	GHz	1.999	11.994
Structure length	m	1.5	0.275
Number of cells		30	33
Phase advance per cell	deg	120	120
Working RF phase	deg	90	90
First iris radius	mm	20	4.062
Last iris radius	mm	14	2.6
Average iris radius	mm	17	3.331
First iris thickness	mm	8	2.525
Last iris thickness	mm	8	1.433
Average iris thickness	mm	8	1.979

Table 8 Optimal voltages and bending angles for BC1 and BC2

Parameter	Symbol	Unit	BC1	BC2
Total voltage	V	MV	450	650
Bending angle	θ	°	3.95	1.55

3.3.2 Design choices

The electron RTML starts with the tunable spin rotator (SR), which enables the arbitrary orientation of the beam polarisation. Its design is unchanged from the CDR and is documented in [79] and in the CDR. Since the axis of the SR extraction runs parallel to the ML, the electron beam depolarisation between the SR and the end of the ML is minimal (the small bending angle introduced by the Beam Delivery System (BDS) leads to negligible depolarisation).

Bunch compressors 1 and 2, located respectively at the beginning and end of each RTML, have been adapted from the 3 TeV CLIC design to the single-bunch parameters of the 380 GeV energy stage. The bunch length is compressed from 1.8 mm to 235 µm in BC1 and from 235 µm to 70 µm in BC2. Due to the flexibility of the original design, it was possible to adjust the magnetic chicanes and the operating parameters of the RF systems without changes in the layout [80].

In contrast, the RF systems of the two bunch compressors, 2 GHz for BC1 and 12 GHz for BC2, have been significantly redesigned and improved compared to previous documents [22]. The BC1 RF has been updated to use the same L-band RF structure as the Booster Linac (BL), the so-called "CLIC L-band" structure. The BC2 RF has been updated to use the "TD-31" X-band structure designed and optimised for the klystron-based version of the CLIC ML [5]. The RTML's structures parameters are summarised in Table 7. The integrated voltage and required bending angles in the RF section and magnetic chicanes of BC1 and BC2 are reported in Table 8. An optimisation of the booster RF system aimed at minimising cost while maximising efficiency leads to having the two-electron/positron pulses separated by 5 µs [56].

3.3.3 Beam performance

One of the main challenges of the RTML is to meet the tight emittance budgets summarised in Table 9 while providing isochronous transport. Compared to the CLIC CDR parameters [55], the increased bunch charge and

Table 9 Budget for the normalised emittance growth at the end of the RTML

Emittance budget$^{(\star)}$	Unit	$\epsilon_{n,x}$	$\epsilon_{n,y}$
Perfect machine	nm.rad	< 800	< 6
Static imperfections	nm.rad	< 820	< 8
Static and dynamic imperfections	nm.rad	< 850	< 10

$^{(\star)}$ 90^{th} percentile.

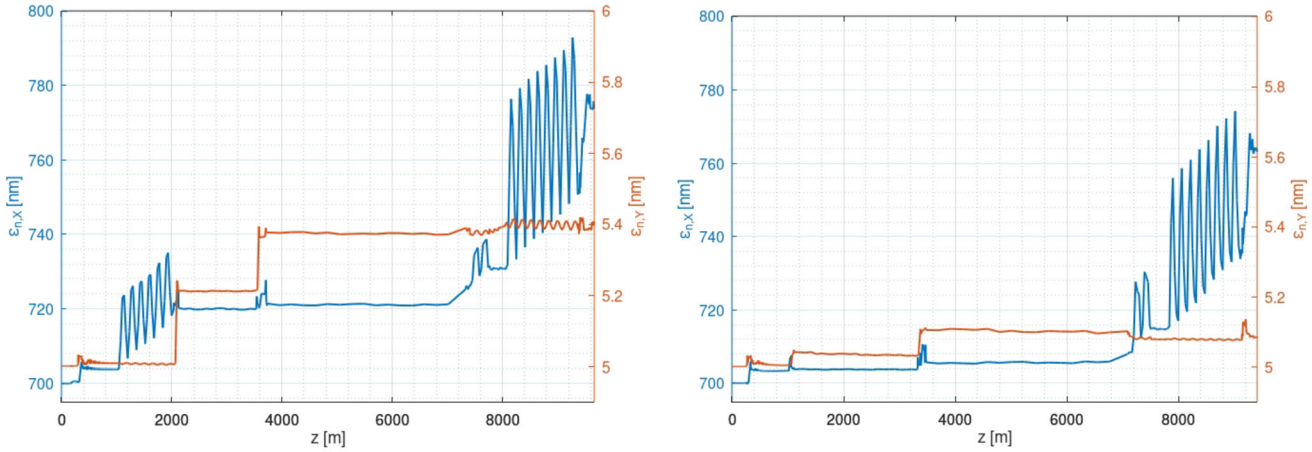

Fig. 8 Design emittance growth along the RTML beamline for electron (left) and positron lines (right)

bunch length of the 380 GeV energy stage affect the two main effects that drive the RTML design: The increased charge induces stronger emission of synchrotron radiation in all bending magnets; the increased bunch length enhances the wakefield effects in the accelerating structures, especially the transverse component. On the other hand, the increased bunch length reduces the emission of the coherent component of the synchrotron radiation, which is the most harmful. These effects have been considered and carefully balanced throughout the whole RTML, leading to the so-called "design" emittance growth. The design of the arc cells is the same as described in the CDR and is common to both CA and TAL. It consists of highly focused double-bend achromatic cells with sextupoles for chromaticity correction, making the arcs particularly sensitive to imperfections. The design emittance growth along the RTML beamline due to all these effects is shown in Fig. 8. From the plot, one can notice that the electron line shows a larger design emittance growth due to the presence of the central arc, as can be seen in the figure.

The design's complexity makes the RTML extremely sensitive to static and dynamic imperfections due to the high bunch charge and bunch length. Beam-based alignment (BBA) techniques are therefore mandatory to preserve the ultra-low emittances from the DR to the Main-Linac entrance and then to the IP, under the effects of misalignments and other static imperfections. Table 10 summarises the static imperfections considered, which therefore constitute pre-alignment requirements. Notice that all the tabulated numbers have already been achieved and exceeded in existing machines, like light sources.

The BBA procedure designed for the RTML involves a few iterations of orbit correction and dispersion-free steering (DFS) in all subsystems [46], followed by an iteration of emittance tuning bumps.

In the Central Arc and Turnaround Loops, the test beam for DFS is obtained by reducing the magnetic strength of all magnets by 5%. The correction is applied piecewise to short bins along each subsystem, with a short overlap between successive bins.

The emittance tuning bumps are implemented using the first five sextupoles of both the CA and the TAL, which are moved transversely using a Simplex algorithm aimed to minimise the transverse beam emittance at the Main Linac entrance, removing the effects of coupling and optics mismatch. This tuning relies on repeated emittance measurements in the dedicated measurement station located at the RTML end, with an assumed resolution of 10%.

Detailed studies have been carried out to assess the performance of the BBA procedures, taking into account element pre-alignment errors, magnet strength errors, and dynamic magnetic-centre shifts when scaling the magnetic strengths for DFS. Table 10 provides a detailed list of the imperfections considered.

Since the CDR, the BBA procedure has been significantly improved. Indeed, the results of the simulations show that the emittance budgets for the 380 GeV and the 3 TeV stages of CLIC could be fulfilled. That is, more than

Table 10 Static imperfections considered

Imperfection	Unit	Value
Magnet and BPM positron error	µm	30
Magnet and BPM tilt error	µrad	100
Magnet and BPM roll error	µrad	100
Quadrupole strength error in CA & TAL	%	0.01
Quadrupole strength error in other sections	%	0.1
Other magnet strength error	%	0.1
BPM resolution	µm	1
Magnetic center shift w/ strength scaling	µm / 5%	0.35
Emittance measurement uncertainty	%	10

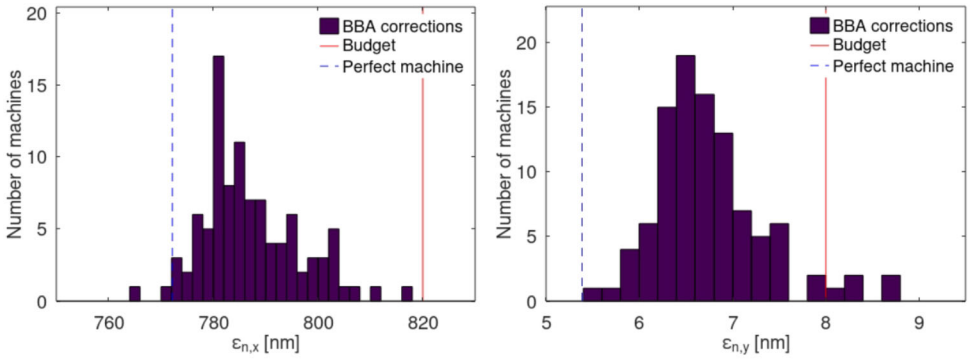

Fig. 9 Emittance at the end of the electron RTML after beam-based alignment and tuning, assuming a 10% emittance measurement resolution. 95% of the corrected machines are below the emittance budget at the RTML exit, which meets the requirement of ≥90%

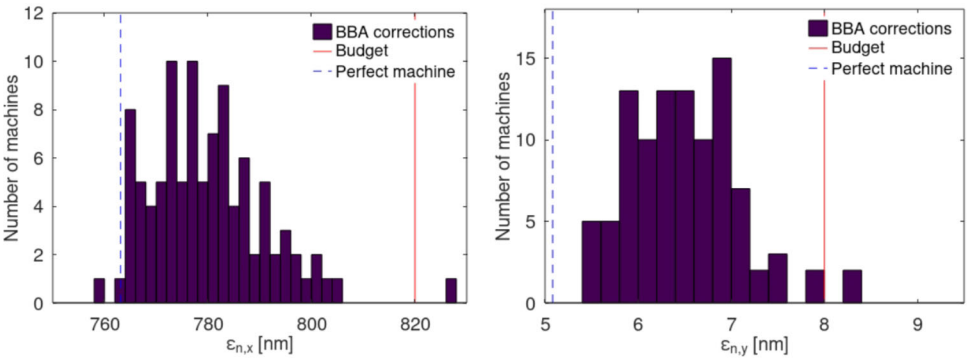

Fig. 10 Emittance at the end of the positron RTML after beam-based alignment and tuning, assuming a 10% emittance measurement resolution. 97% of the corrected machines are below the emittance budget at the RTML exit, which meets the requirement of ≥90%

90% of the simulated machines are corrected to be within the budget both in the horizontal and in the vertical plane, which is the most critical. The distribution of final emittances of 100 random machines is shown in Figs. 9, and 10. These new studies showed increased robustness compared with the CDR results and allowed the relaxation of the pre-alignment tolerances for the components installation in the tunnel.

The emittance growth in the RTML is also sensitive to dynamic effects, such as transverse orbit jitter at injection, element vibrations, and stray magnetic fields. Previous studies showed that the impact of these effects on the emittance growth is within budgets [81, 82]. The transverse orbit jitter seems the most critical among the dynamic effects and results in stringent stability requirements of the DR extraction elements. This led to dedicated R&D for the DR extraction kickers, as documented in [83]. To further minimise the impact of the incoming beam jitter on the RTML, an option for a feed-forward solution via hardware is presented in [84].

3.3.4 Component overview

Tables 11 and 12 summarise the number of elements in the RTML lattice, separated by subsection and type.

Table 11 Number of solenoids, dipole correctors (Steerers), bending dipoles (Dipoles), quadrupoles (Quads), sextupoles (Sexts) and BPMs in each section of the electron RTML

Section	SR	BC1	BL	CA	VTL	LTL	TAL	BC2	Total
Solenoids	4	0	0	0	0	0	0	0	4
Steerers	72	50	75	247	73	21	392	32	962
Dipoles	6	4	0	155	11	0	254	8	438
Quads	72	50	75	243	69	21	407	32	969
Sexts	1	0	0	124	8	0	200	0	333
BPMs	72	50	75	243	69	21	392	32	954

Table 12 Number of dipole correctors (Steerers), bending dipoles (Dipoles), quadrupoles (Quads), sextupoles (Sexts) and BPMs in each section of the positron RTML

Section	TL	BC1	BL	CA	VTL	LTL	TAL	BC2	Total
Steerers	72	50	75	16	60	21	392	32	718
Dipoles	0	4	0	4	10	0	254	8	280
Quads	72	50	75	16	60	21	407	32	733
Sexts	0	0	0	2	6	0	200	0	208
BPMs	72	50	75	16	60	21	392	32	718

Table 13 Key beam parameters in the ML

Particles per bunch	5.2×10^9	Bunches per pulse	352
Bunch spacing	15 cm	Bunch length	70 µm
Initial R.M.S. energy spread	$\leq 2\%$	Final R.M.S. energy spread	0.35%

3.4 Main Linacs

3.4.1 Overview

The two Main Linacs (MLs), one for positrons and one for electrons, accelerate the beams from an initial energy of 9 GeV to the final value of 190 GeV using normal conducting accelerating structures with an RF frequency of 12 GHz and a gradient of 72 MV/m. This choice of frequency and gradient is based on an optimisation of the total accelerator cost. The linac design is identical for electrons and positrons and the linacs are each about 3.5 km long. This includes a total energy overhead of 10% to allow for different operational margins. A key design goal is the preservation of the ultra-low transverse emittances during beam transport. This goal is achieved by careful lattice design, precise pre-alignment of the beamline components, stabilisation of the beam-guiding quadrupoles against vibrations, and beam-based correction methods. The Main-Linac tunnel and the beamline are laser-straight. This avoids the complications resulting from a linac that follows the curvature of the Earth [85].

3.4.2 Beam parameters

Table 13 shows the key beam parameters for the Main Linacs. In the linac, the bunch length remains constant while the transverse emittances increase due to machine imperfections. The beam is accelerated at an average RF phase of 12° in order to limit the final energy spread; this results in an effective gradient reduction of about 2%.

3.4.3 Linac layout and optics

The Main Linac consists of a sequence of 2.343 m-long modules. Three types of modules exist: the most common supports eight accelerating structures (type T0). The other two (T1 and T2) support six or four accelerating structures and a quadrupole of 0.43 m or 1.01 m length, respectively. A single PETS in the Drive-Beam line feeds a pair of accelerating structures.

The ML consists of five lattice sectors, each using FODO optics [86]. The phase advance is about 72° per cell throughout the ML. The quadrupole spacing is constant in any particular sector but varies from sector to sector following an approximate scaling with $\sqrt{E}$ (see Table 14). There is a quadrupole on every module in the first sector (2.343 m spacing). The quadrupole spacing increases along the linac until there is one quadrupole for every four

Table 14 The main parameters of the different ML sectors

Sector number	1	2	3	4	5
Number of quadrupoles	120	150	86	62	156
Quadrupole length [m]	0.43	0.43	0.43	1.01	1.01
Quadrupole spacing [m]	2.343	4.686	7.029	7.029	9.372

Table 15 Key alignment specifications for the ML components and the resulting emittance growth

Imperfection	With respect to	Value	$\Delta\epsilon_y$ [nm]		
			1-2-1	DFS	RF
Girder end point	Wire reference	12 µm	12.91	12.81	0.07
Girder end point	Articulation point	5 µm	1.31	1.30	0.02
Quadrupole roll	Longitudinal axis	100 µrad	0.05	0.05	0.05
BPM offset	Wire reference	14 µm	188.99	7.12	0.06
Cavity offset	Girder axis	14 µm	5.39	5.35	0.03
Cavity tilt	Girder axis	141 µrad	0.12	0.40	0.27
BPM resolution		0.1 µm	0.01	0.76	0.03
Wake monitor	Structure centre	3.5 µm	0.01	0.01	0.35
All			204.53	25.88	0.83

The values after simple steering (1-2-1), Dispersion Free Steering (DFS) and realignment of the accelerating structures using the wakefield monitors (RF) are shown.

accelerating modules in the last sector (9.372 m spacing). This quadrupole spacing balances the contributions to emittance growth from dispersive and wakefield effects along the linac. The total length of quadrupoles is roughly the same in every sector, resulting in an almost constant fill factor (the ratio of the length of the accelerating structures to the total length). The lattice functions between sectors are matched using the last four quadrupoles of the lower energy sector and the first three quadrupoles of the higher energy sector.

At the end of each Drive Beam sector, four of the Main Beam modules are not equipped with accelerating structures but only with drifts. In this section, the used Drive Beam is bent into the dump line, and the new Drive Beam is brought in. The total number of PETS per decelerator is 1,273.

3.4.4 Accelerator physics issues

The main challenge in the main linac is the preservation of the vertical emittance in the presence of static misalignments of the accelerator components. A set of specifications for the imperfections has been developed together with the different subsystem designers [87] and is given in Table 15. The emittance growth resulting from each imperfection is also detailed for the different stages of the beam-based alignment methods. First, a simple one-to-one steering achieves a smooth beam orbit using the BPMs. Dispersion-free alignment is then implemented by changing the gradient in the linac for different beam pulses and identifying a common, energy-independent orbit. Finally, the RF structures are aligned to the beam using the built-in wakefield monitors.

The expected value for the total growth is about 1 nm. The emittance growth has a stochastic probability distribution (Fig. 11). With a probability that 90% of the machines remain below 1.5 nm emittance growth.

In addition, tuning bumps will be used to improve the emittance growth further [88]. Each bump uses quadrupoles and girders that support RF structures. The components are moved transversely to optimise the collider's luminosity, thus mitigating the residual effects of the imperfections globally. With this scheme, all machines remain below an emittance growth of 1 nm.

Good vacuum quality prevents fast beam ion instability and keeps tail generation due to beam-gas scattering low. A vacuum quality similar to that of the 3 TeV design [55] is foreseen; studies with a more refined simulation code indicate that the requirements could be relaxed by a factor of a few [89].

3.4.5 Components

The total number of components is listed in Table 16. The alignment tolerances are listed in Table 15.

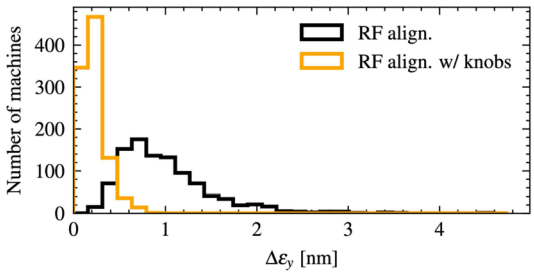

Fig. 11 Probability distribution of the emittance growth for static imperfections for a ML average RF phase of 12°. The distribution after RF alignment and after applying the tuning bumps is shown

Table 16 Key components of the Main Linac

Structures T0	914
Quadrupoles T1	356
Quadrupoles T2	218
Accelerating structures	10,184
PETS	5,092

Table 17 CLIC 380 GeV beam parameters

Norm. emittance (end of linac) $\gamma\epsilon_x/\gamma\epsilon_y$	[nm]	930 / 15
Nominal beta function (IP) β_x^*/β_y^*	[mm]	8.0 / 0.1
IP beam size σ_x^*/σ_y^*	[nm]	149 / 2.0
Bunch length σ_z	[µm]	70
R.M.S. energy spread δ_p	[%]	0.35
Bunch population N_e	[10^9]	5.2
Number of bunches n_b		352
Repetition rate f_rep	[Hz]	100
Luminosity $\mathcal{L}_0$	[10^{34} cm^{-2}s^{-1}]	4.50

3.5 Beam delivery system

The Beam Delivery System (BDS) transports the e^+ and e^- beams from the exit of the linacs to the IP and performs the critical functions required to meet the CLIC luminosity goal. First, the beam is cleaned in the collimation section and then it is focused with the Final Focus System (FFS) while correcting higher-order transport aberrations in order to deliver the design IP beam sizes. The BDS new baseline foresees an L^* of 6 metres with final quadrupoles mounted outside the detector volume [90, 91], directly on the tunnel floor. The Final Focus lattice with $L^* = 6\ m$ has been lengthened by a factor 6/4.3 compared with the previous $\sqrt{s} = 500$ GeV design [92].

3.5.1 BDS optics design

The BDS has been optimized with respect to the beam parameters foreseen for the first CLIC energy stage given in Table 17. The length of the entire 380 GeV BDS is ≈ 1.95 km (with one IR) and the FFS length is 770 m. The BDS, extended to 2.2 km is 878 m shorter than the 3.1 km BDS for the 1.5 TeV design. In order to allow for the energy upgrade inside the CLIC tunnel, the end of the 380 GeV and 1.5 TeV BDS beamlines have been matched such that the axis along which the maine linac (ML) is located is unchanged by the upgrade. The crossing angles quoted in previous CLIC reports omitted the fact that the BDS has a net bending angle of 0.6 mrad (see Fig. 12). Assuming that the two main linacs have a full crossing angle between them of 20 mrad the IP crossing angles are given in Table 18. This small change should have negligible impact on performance. Further studies in collaboration with the civil engineering team should refine these values, considering additional optimizations. The FFS dipoles, quadrupoles and sextupoles have been optimized to match the desired beam parameters at the IP while locally correcting the chromaticity generated by the Final Doublet [93, 94] (QF1 and QD0 quadrupoles). The main optical functions are shown in Fig. 13. A pair of octupoles has been introduced in the lattice to correct the remaining 3$^{\mathrm{rd}}$ order chromatic and geometric aberrations.

To assess beam sizes and luminosity, a beam is tracked from the end of the ML with emittances (930/15 nm) throughout the perfect BDS. Due to the non-uniform energy spread and highly nonlinear properties of the FFS, the rms beam sizes get artificially inflated by the bunch tails. Instead, the quoted beam sizes are computed from Gaussian fits of the core of the beam at the IP.

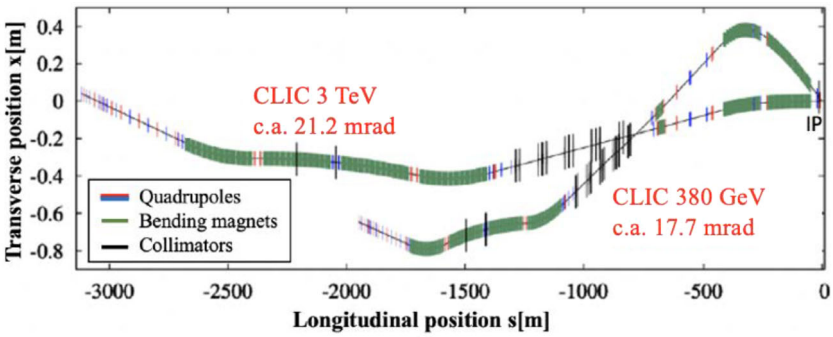

Fig. 12 CLIC 1.5 TeV and 380 GeV BDS layouts with $L^* = 6\ m$

Table 18 Crossing angles at the IP for different CLIC energy stages assuming that the two main linacs are placed at an angle of 20 mrad

Beam Energy / IR	Crossing Angle (mrad)
380 GeV / IR1	17.7
380 GeV / IR2	27.2
1.5 TeV / IR1	21.2

Fig. 13 Optical functions through the FFS with $L^* = 6$ m

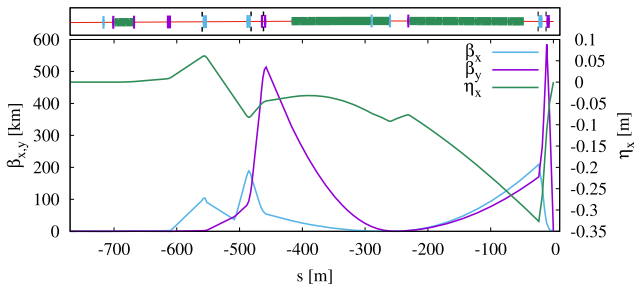

3.5.2 Optimization of the BDS

The CLIC CDR suggests using the BDS designed at 3 TeV as a temporary solution for operation at an intermediate energy of $\sqrt{s} = 1.5$ TeV, proposing a luminosity of 3.7×10^{34} cm^{-2}s^{-1}. However, since the design is not optimized for 1.5 TeV, studies are underway to determine its actual performance at this energy. Early results of the study suggest that the luminosity could improve by up to 20% compared to the original CDR estimate as shown in Table 19. In addition, a 500 m length reduction of a single BDS line is possible, offering an overall 1 km footprint reduction of the facility. The compatibility of the new 1.5 TeV design with the 380 GeV baseline is shown in Fig. 14. Benefiting from a 220 m length reduction in the 1.5 TeV FFS, the 380 GeV CDR FFS was replaced by the shortened design, providing a further upgrade to 5.20×10^{34} cm^{-2}s^{-1} luminosity at 380 GeV.

Studies show that further reductions of up to 800 m are possible, reducing costs by negating the need for one power module at the cost of reduced luminosity. Preliminary results show that with a BDS of length 2.3 km, a luminosity of $4.3{\times}10^{34}$ cm^{-2}s^{-1} can be reached.

3.5.3 FFS tuning

Tuning of the FFS aims to bring the system to its design performance under realistic beamline imperfections [95, 96]. The procedure consists of beam-based alignment (BBA) techniques for correcting trajectory and dispersion, and orthogonal sextupole knobs that aim to correct chosen aberrations at the IP [97], independently. The general steps are described in the tuning procedure [98]:

1. Beam-based alignment (BBA) with all multipoles switched OFF
2. Pre-alignment of sextupoles by powering them one-by-one and monitoring luminosity
3. Sextupole linear knobs (transverse position)
4. Octupole linear knobs (transverse position)
5. Sextupole linear knobs (transverse position), second iteration

The most recent work on the CLIC Tuning can be found in [99].

Table 19 Overview of BDS parameters for different configurations

Energy [GeV]	380	1500	380†	1500†
Final drift $L*$ [m]	6	6	6	6
FFS length [m]	770	770	550	550
BDS length [km]	1.94	3.12	1.72	2.62
Norm. emittance (end of linac) $\epsilon_{n,x}/\epsilon_{n,y}$ [nm]	930/15	660/20	930/15	660/20
Beta function (IP) β_x^*/β_y^* [mm]	8/0.07	8/0.11	6/0.08	6/0.08
Beam size at IP (rms) σ_x^*/σ_y^* [nm]	149/2.0	60/1.5	120/3.9	57/1.2
Bunch length σ_z [µm]	70	44	70	44
Energy spread δ_p [%]	0.3	0.3	0.3	0.3
Bunch population N [$\times 10^9$]	5.2	3.72	5.2	3.72
Number of bunches N_b	352	312	352	312
Repetition rate [Hz]	100	50	100	50
Crossing angle [mrad]	17.7	21.2	20.2	21.2
Total luminosity $\mathcal{L}_{tot}$ [10^{34} cm^{-2}s^{-1}]	4.50	3.70*	5.20	4.71*

The first two columns represent the baseline versions, with the 1.5 TeV baseline based on the 3 TeV CDR design. The last two columns indicate the current optimization status, resulting in reduced length and improved luminosity compared to the baseline.

*These luminosities have not been updated to reflect recent alignment studies [20]. If the same methods are applied, we expect these luminosities to further increase by 50%.

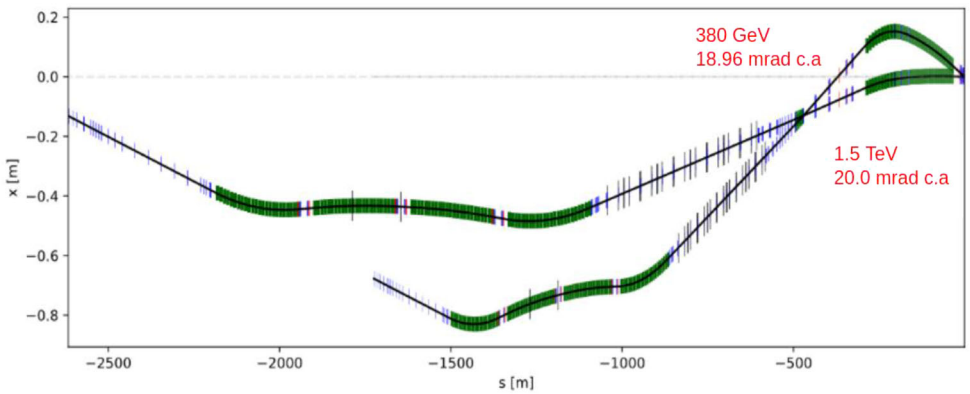

Fig. 14 BDS compatibility with the 550 m FFS at 1.5 TeV and 380 GeV assuming the ML has an angle of 20 mrad

Table 20 Key parameters of the CLIC Dual BDS at 380 GeV

	IR1	IR2
Final drift L^* [m]	6	6
FFS length [m]	770	770
BDS length [m]	2294	2256
Beta function (IP) β_x^*/β_y^* [mm]	8/0.1	8/0.1
Beam size (IP) σ_x^*/σ_y^* [nm]	149/2.0	149/2.0
Total luminosity $\mathcal{L}_{tot}$ [10^{34} cm^{-2}s^{-1}]	2.25	2.21

3.5.4 Details of the dual BDS solution

Additional details of the dual BDS solution, introduced in Sect. 2.1.2, are summarized in Table 20. These results demonstrate that the dual BDS design achieves nearly identical luminosity performance for both IRs, with losses of less than 1.5% due to synchrotron radiation, when the beam is delivered at the same rate to the two detectors. Importantly, the solenoid effects, which are significant at higher energies, are negligible at 380 GeV.

Table 21 Number of components in each section of the BDS1

Component	Diagnostic	Collimation	FFS	Total
Dipoles	0	192	220	412
Quadrupoles	140	160	40	340
Sextupoles	0	48	16	64
Octupoles	0	0	8	8
Multipoles	0	8	0	8
BPMs	0	76	0	76
Ecollimators	0	38	0	38
Rcollimators	0	20	0	20

Table 22 Number of components in each section of the BDS2

Component	Diagnostic	Collimation	FFS	Total
Dipoles	48	192	220	460
Quadrupoles	140	160	40	340
Sextupoles	0	48	16	64
Octupoles	0	0	8	8
Multipoles	0	8	0	8
BPMs	0	76	0	76
Ecollimators	0	38	0	38
Rcollimators	0	20	0	20

3.5.5 Component overview

Tables 21 and 22 summarize the number of elements in the dual BDS lattice, divided into the three main subsystems: Diagnostic Section, Collimation, and FFS. These numbers are shown for BDS1 and BDS2, respectively.

3.6 Machine Detector Interface

The Machine Detector Interface (MDI) is the region within the detector cavern where the beam lines of the accelerator pass through the detector. Key issues are the support of the final beam line components within the detector, luminosity monitoring and feedback, background suppression, and radiation shielding. The MDI includes the positioning of the final focus quadrupoles, QD0, which have very stringent alignment and stabilisation requirements. Luminosity monitoring is integrated within the detector. The spent beams must be transported cleanly away through the experiment onto two beam dumps, via the post-collision lines. Collimators and masking must suppress backgrounds from the incoming beams, from the beam-beam interaction and from the beam dumps. The cavern layout must minimize the exposure of equipment and personnel to radiation.

The CDR studies [55] concentrated on a design in which the final focus quadrupole QD0 was placed inside the detector (with $L^* = 3.5$ m at 3 TeV or $L^* = 4.3$ m at 500 GeV). This imposed significant constraints on the detector acceptance and maintenance scenarios. In particular, the angular acceptance of the calorimetry was significantly reduced. Following the CDR phase, the detector and MDI studies concentrated on a single detector concept, CLICdet [100], incorporating detector technology advances and lessons learned from the CDR. As a result the final focus quadrupole QD0 is now placed on the tunnel floor, just outside the detector (using $L^* = 6$ m for both 380 GeV and 3 TeV designs). The angular acceptance of the detector in the forward region improved significantly and a number of technical systems have become simpler, as further explained below. The peak luminosity decreases only marginally. A blown-up view of the forward region of the detector is shown in Fig. 15.

The placement of the final focus elements outside the cavern, directly on the tunnel floor, requires moving the detector to a garage position prior to opening it for maintenance. This is illustrated in Fig. 16. The new CLIC baseline with a reduced power consumption allows for operating two experiments in parallel. Figure 77 in Sect. 5.1.5 presents a civil engineering concept of the experimental area with two independent caverns, ensuring the stability of the final focus magnets as well as the servicing of each detector away from its beam line.

The crossing angle between the beam lines at 380 GeV is 18 mrad, and 27 mrad respectively for the two detectors. At 1.5 TeV it is 21 mrad. Lower backgrounds from incoherent pairs at 380 GeV allow for a central

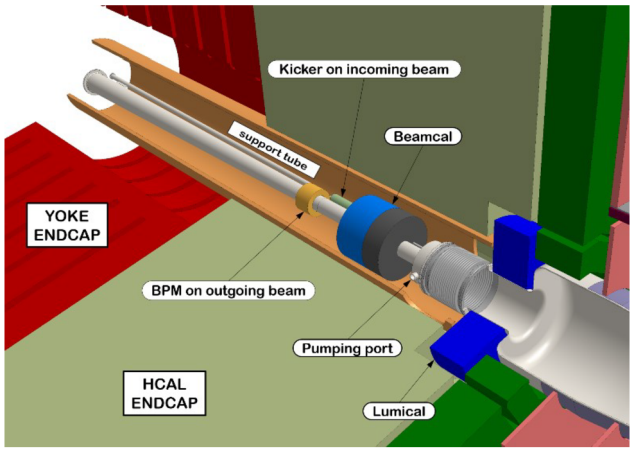

Fig. 15 A blown-up view of the MDI region inside the detector, showing the incoming and outgoing beam line, the forward calorimeters Beamcal and Lumical, the kicker for the incoming beam, and the beam position ponitor (BPM) on the outgoing beam

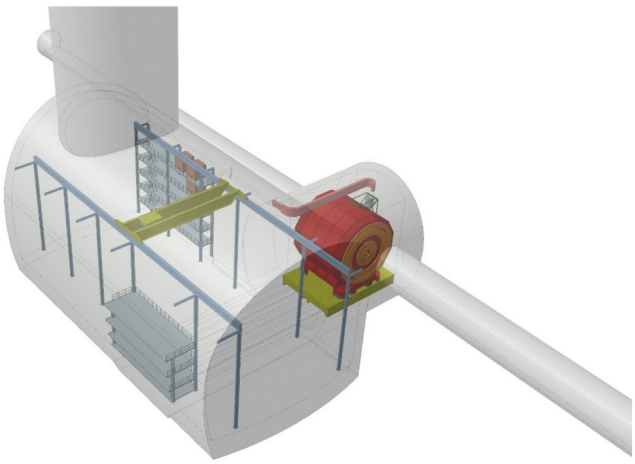

Fig. 16 Cavern layout showing the CLIC detector placed directly the beam line. For maintenance the detector moves sideways to the large cavern

vacuum pipe with a smaller diameter, and thus a smaller radius of the innermost vertex detector layer. However, most of the detector elements - in particular the heavy and expensive calorimeters - will remain unchanged when moving from the 380 GeV baseline to the higher energy stages.

As many of the design constraints, such as beam-beam backgrounds and radiation effects, as well as required fields and gradients are more stringent at 3 TeV, most of the MDI studies have focused on the 3 TeV parameters. This means that parameters are generally more relaxed at the lower centre-of-mass energies.

As indicated above, contrary to the design presented in the CDR, the QD0 quadrupoles are mounted on the tunnel floor. This is motivated by measurements at the CMS cavern and at various tunnel locations. These have shown that tunnel floor movements are almost two orders of magnitude smaller than vibrations inside the detector. In the tunnel sufficient space is available to comfortably house the stabilisation and alignment systems. The alignment of the final focus elements can therefore be based on the same technology as the rest of the linacs and Beam Delivery Systems. Moreover, it has been shown that the luminosity does not change appreciably if the QD0 magnets are split into two or three shorter parts. Compared to the CDR design, the QD0 quadrupoles have a much smaller gradient, 25 T/m, and a larger aperture radius (25 mm). Shorter magnets are lighter, easier to produce and to stabilise. The overall design features could remain the same, but with the lower gradient an alternative solution with classical electromagnets is now under consideration. No anti-solenoid is needed, as the QD0 magnets are outside the detector solenoid field.

The new layout simplifies the Machine Detector Interface inside the detectors considerably. The IP feedback Beam Position Monitors (BPMs) and kickers can stay roughly in their CDR positions. The larger aperture minimises the pumping time and venting of the QD0 is no longer required before moving the detector to its garage position. Therefore, the vacuum sectorisation can be significantly simplified.

3.7 Post-Collision Line

The CLIC Post-Collision Line (PCL) is described in detail in the CDR [55]. This description focused on the 3 TeV design. Accounting for changes and improvements [101–103], the PCL has been re-investigated for the 380 GeV

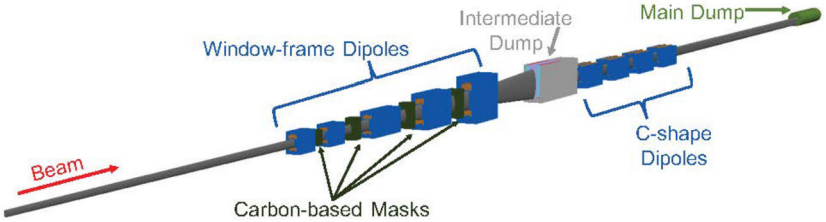

Fig. 17 Post-collision line layout from BDSIM viewer

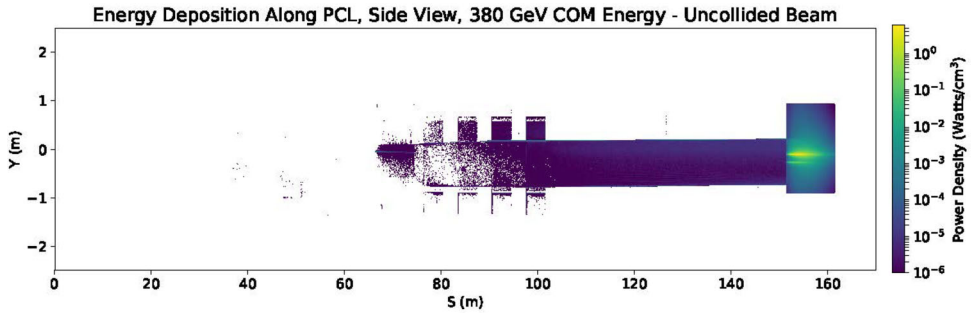

Fig. 18 Energy deposition along the PCL for 190 GeV uncollided electron beam

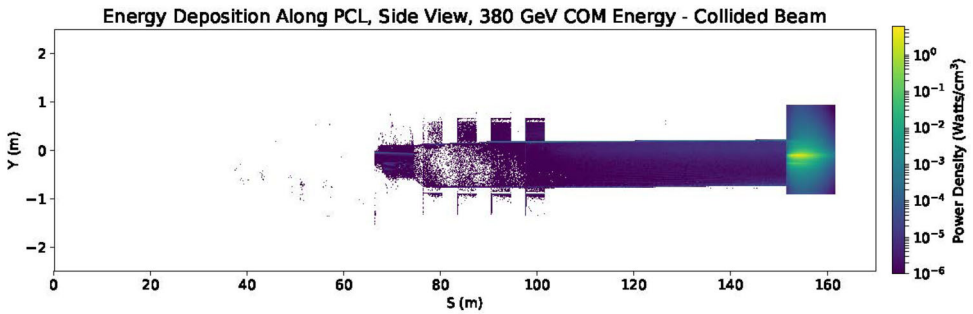

Fig. 19 Energy deposition along the PCL for 190 GeV collided electron beam

design. The lower-energy design is expected to meet the requirements described in the CDR more easily. The investigation confirms that by scaling the dipole magnet strengths down from 0.8 T to approximately 0.1 T and maintaining the other key aspects of the 3 TeV design, the 380 GeV PCL has more margin of meeting the design requirements than the 3 TeV PCL.

The general layout remains essentially the same as that described in the CDR, except for the first dipole magnet pair and the final drift length. Looking at the magnet designs described in [104], the lengths of the pair of magnets were kept at 2 m each, instead of 0.5 m and 3.5 m, as previously stated. This change caused no impact on the overall performance of the PCL and followed the design parameters described in [104]. The final drift is no longer 210 m, but 50 m, as described in [101].

To be sure that the re-investigation provided similar results to those shown in the CDR and previous studies, the model was rebuilt from the ground up using BDSIM [105] and its geometry utility, pyg4ometry [106]. The geometries of the beampipes, the intermediate dump, and the carbon-based masks were based upon the designs listed in [101–103]. For the beam distributions, the data were provided by the CLIC beam-beam interactions studies for both the 3 TeV and the 380 GeV machines [107]. The main dump was based upon the design detailed in [108]. An overview of the full PCL design as visualized in BDSIM can be seen in Fig. 17.

After confirming that this re-built 3 TeV design achieves similar results to those previously reported, investigation of the 380 GeV design began by scaling down the magnet strengths to provide the same angular kick to the nominal 190 GeV beam. The dipole magnets for the 3 TeV design are all set to 0.8 T, which provides a kick angle of 0.64 mrad to the 1.5 TeV electron beam at each dipole. For a 190 GeV electron beam, the same kick angle is provided by a magnet strength of 0.1 T.

Investigation of the energy deposition along the PCL and in the main dump shows no unexpected “hot spots” along the beamline. Figures 18 and 19 show the energy deposited along the PCL for the uncollided and collided 190 GeV electron beams, respectively. The colours correspond to power density per unit volume, including the power from deposited secondary particles. The main dump receives most of the power deposition, and less power is deposited along the PCL than for the 3 TeV design. Table 23 summarises the power deposition in several key elements of the PCL for both the 3 TeV and 380 GeV designs, including both collided and uncollided electron

Table 23 Power deposited (MW) in key PCL elements

	Intermediate Dump	Final Drift	Main Dump
3 TeV Uncollided	2.10×10^{-4}	1.97×10^{-2}	13.6
3 TeV Collided	3.67×10^{-2}	2.96×10^{-2}	10.2
380 GeV Uncollided	5.19×10^{-5}	4.08×10^{-3}	2.91
380 GeV Collided	7.77×10^{-5}	4.23×10^{-3}	2.70

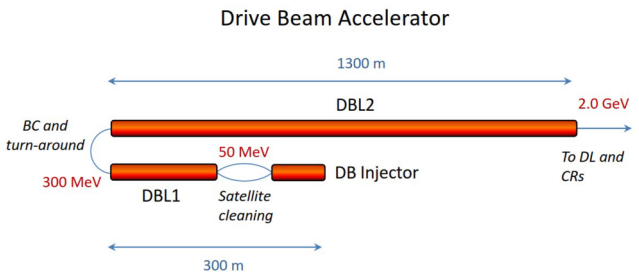

Fig. 20 Schematic layout of the DB Injector and Accelerator

beams. Since the main dump is designed to handle 14 MW of power from the 1.5 TeV electron beam, the 2.91 MW provided by the uncollided 190 GeV electron beam is easily managed, as expected. Furthermore, most energy deposition into the main dump occurs below the vertical centre, around −10 cm. This should allow luminosity monitoring by detecting Beamstrahlung photons, as described in the CDR.

The PCL is capable of achieving the requirements stated in the CDR for both the 3 TeV and 380 GeV designs. Studies indicate no unexpected consequences for scaling down the dipole magnet strengths from 0.8 T to 0.1 T for the 190 GeV electron beam. No major changes to the PCL design are required. Minor changes to the carbon-based masks and the intermediate dump are being investigated to further reduce deposition on the magnets. However, these changes should not affect the overall performance of the PCL. Instrumentation studies for the PCL are in progress. A dedicated redesign of the PCL for 190 GeV could potentially result in cost and real estate savings.

3.8 Drive-Beam Accelerator

3.8.1 Introduction

The Drive-Beam Accelerator (DBA) accelerates the Drive Beam (DB). It consists of an injector generating a 48 µs-long Drive-Beam bunch train with an average current of 4.2 A and a bunch repetition frequency of 499.75 MHz. The two Drive-Beam Linacs (DBL1 and DBL2) accelerate the beam up to 1.91 GeV, and are separated by a bunch compressor. The injector generates electron bunches with a charge of $q_b = 8.4$ nC, an R.M.S. bunch length of 3 mm and a normalised emittance of 100 µm at an energy of 50 MeV. The bunch compressor between DBL1 and DBL2 compresses the bunches to a final length of 1 mm, in a 180° turn-around which reverses the direction of propagation of the beam and minimises the overall footprint. The length of the whole drive beam Linac complex is 1.3 km. The schematic layout is shown in Fig. 20.

Since it is the biggest power consumer in the entire CLIC complex the DBA has been designed to maximise efficiency. The accelerating structures are operated in a fully loaded mode reaching an RF-to-Beam efficiency of 95%. A multi-beam klystron and a solid state modulator have been developed together with industry, efficiencies above 70% and 90% respectively have been obtained. A recent design of a two-stage multi-beam klystron predicts an efficiency of 82% [109]. In addition, the focus of the design was on beam stability. The charge along the bunch train and shot-to-shot has to be stable to 0.1%. The beam energy and phase have to be stable to within 0.2% and 0.05° respectively. These specifications drive the technology choice of the electron source, the modulators, and the RF power source.

The CLIC 380 GeV stage compared with the CDR design [55] has a 20% reduced Drive-Beam energy and a bunch train length which is a factor 3 shorter. In addition, the power per klystron has been increased to 24 MW which reduces the overall length further due to a higher average gradient in the fully loaded accelerating structures.

The baseline emittance of the drive beam at the end of the DBA is $\varepsilon_x = \varepsilon_y = 50$ µm. This is smaller than in the CDR, since recent studies of the Drive-Beam Injector suggest that a small emittance growth can be expected [110]. This is also consistent with the experience at CTF3 and LEETCHEE (Sect. 2.1).

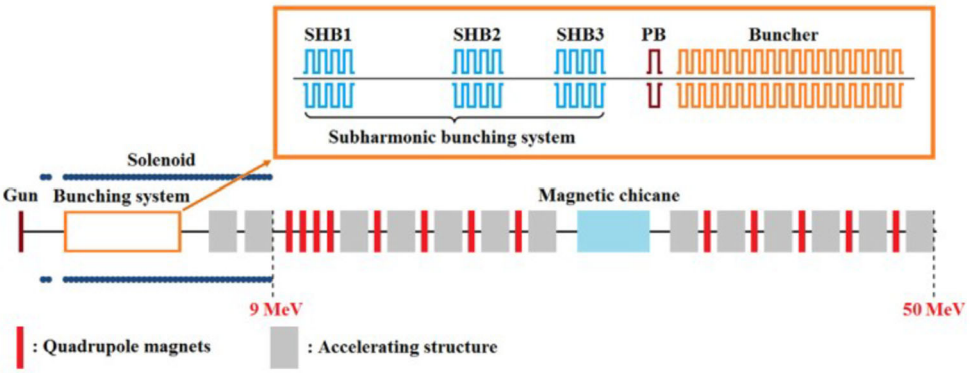

Fig. 21 Schematic layout of the Drive-Beam injector

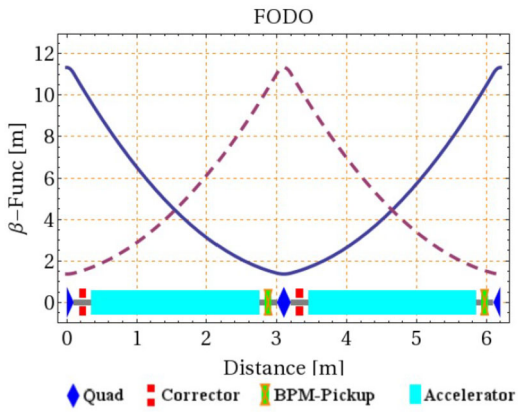

Fig. 22 FODO-lattice for the first DL with one accelerating structure between quadrupoles

3.8.2 Drive-Beam Injector

The Drive-Beam Injector (DBI) has been completely re-designed and optimised relative to the description in the CDR. In particular the capture efficiency has been increased, and the satellite population drastically reduced. The new design is documented in [111–113] and a schematic layout is shown in Fig. 21. The electrons are produced by a thermionic gun at 140 keV. The gun is followed by a sub-harmonic bunching system consisting of three standing wave bunchers at a frequency of 500 MHz (SHB), a 1 GHz Pre-Buncher (PB) and a 1 GHz Travelling Wave Buncher (TWB). Since the beam energy after the TWB is 2.3 MeV two more accelerating structures are embedded in a continuous solenoidal magnetic field to preserve the emittance. At this stage the focusing is done by quadrupoles and 11 more accelerating structures bring the beam energy up to the desired 50 MeV. A magnetic chicane is used to clean up the phase space at low energy. The injector design fulfills all requirements for the DB Linac. At 50 MeV the energy spread is 0.95%, the bunch length is 3 mm and the emittance is below 30 µm. The beam losses in the cleaning chicane are 3.5% and the satellite population is reduced to 2.7%. This low value significantly eases the load of the cleaning system for the satellite bunches described in the CDR.

In the last few years prototypes of the Drive-Beam electron source, sub-harmonic buncher and the RF systems have been built and tested. Results are described in Sect. 2.1.

3.8.3 Drive-Beam Accelerator

The first DBA increases the beam energy from 50 to 300 MeV. It uses a FODO lattice with one accelerating structure between quadrupoles and a phase advance of 106°.

Each FODO-cell is equipped with a Beam Position Monitor (BPM) and corrector magnets for beam-based alignment as shown in Fig. 22. As mentioned, each accelerating structure is operating in fully loaded mode and has an active length of 2.5 m. The input power is 21.5 MW per structure corresponding to an energy gain of 4.9 MeV. The RF-to-beam efficiency is 95%.

After the first linac a 180° turn-around bends the beam into the second DBA. This construction allows the full DBA complex to be located on the CERN Prevessin site. The bend compresses the bunches to a length of 1 mm. Here the electrons are accelerated up to 2 GeV using a FODO cell with 3 accelerating structures between quadrupoles and a phase advance of 101°. A total of 172 quadrupoles and 385 accelerating structures are used in the DBA. Each structure is powered by a modulator and a klystron.

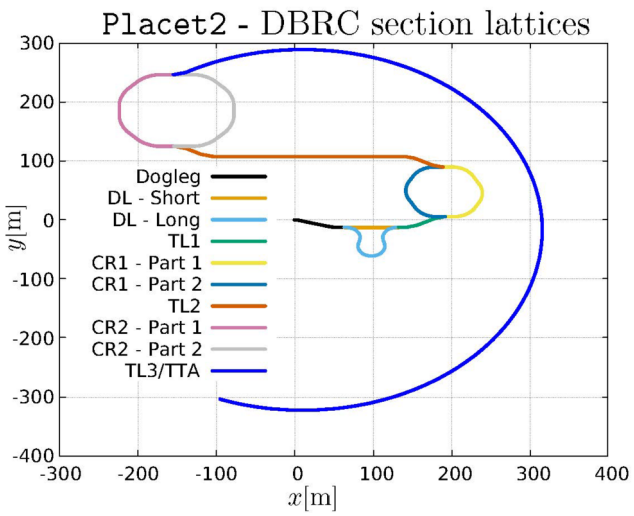

Fig. 23 Schematic view of the full Drive-Deam Recombination Complex, the beamlines that composed the DBRC are denoted by different colours. Figure generated with `Placet2` [120]

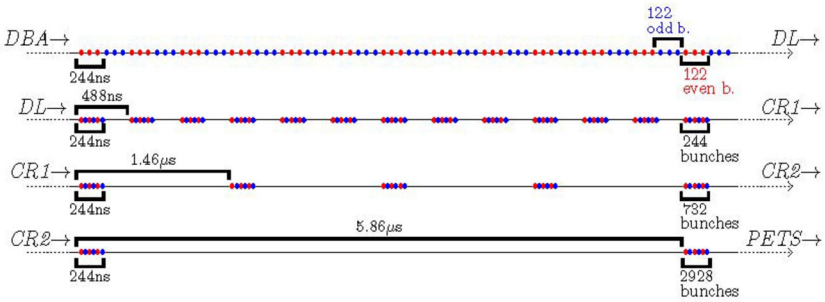

Fig. 24 Train structure in the various stages of recombination [117]

Triplet, Doublet and FODO lattices were studied to optimise the beam stability and emittance growth before the lattice described above was adopted as the baseline [114]. For an RMS misalignment of 100 µm of critical components, such as quadrupoles, accelerating structures and BPMs, the normalised emittance growth remains below 5 µm after beam-based correction, and the total emittance well below the goal of 50 µm. Beam jitter is not amplified significantly.

3.9 Drive-Beam Recombination Complex

3.9.1 Overview

In order to power efficiently the accelerating structures to their nominal gradient of 72 MV/m, the bunches coming out of the DB Linac [115] at a frequency of 500 MHz must be recombined by a factor 24, compressing a 5.86 µs sub-train into a 244 ns pulse with a frequency of 12 GHz. This operation is the function of the Drive Beam Recombination Complex (DBRC), which consists of a Delay Loop (DL), Combiner Ring 1 (CR1), and Combiner Ring 2 (CR2). Each of them recombines 2, 3, and 4 sub-pulses respectively, thereby increasing the bunch frequency by the same amount. Additionally, the DBRC has three transfer lines connecting the DL, CR1, CR2, and the transfer turnaround (see Fig. 23). Further details regarding operation of the DBRC can be found in [55, 116–118]. The drive recombination complex and the beam transport down to the tunnel uses more than 4000 magnets, details about these elements can be found in [119].

3.9.2 System description

The first recombination step separates two 244 ns Drive-Beam sub-trains and interleaves them into a single pulse (see Fig. 24). This is achieved by separating even and odd sub-trains using an RF deflector; the even sub-train is sent through the Delay Loop (DL), the odd sub-train through the straight transfer line. After recombining the two sub-trains, the DB bunch frequency is increased by a factor 2, forming a single 1 GHz pulse.

After the DL, the 244 ns separation between pulses allows the use of combiner rings to further multiply the bunch frequency by a factor 3. In these rings, the time taken by a pulse to complete a full turn is $n \times 244[\text{ns}] + \Delta t_{\text{Rec}}$,

Table 24 Number of main magnetic elements in each ring of the drive beam combination complex

System	Quadrupoles	Sbends	Sextupoles
Delay Loop	96	48	108
CR1	150	48	76
CR2	190	64	176

where Δt_{Rec} is the product of the time between bunches at injection and the ring's frequency multiplication factor. This allows us to interlock several pulses into a single one, multiplying both pulse frequency and current. As shown in Fig. 23, the DBRC has two combiner rings (CR1 and CR2). The frequency multiplication factor of CR1 and CR2 is 3 and 4, respectively. The bunch frequency at CR2 extraction is 12 GHz, which corresponds to the frequency required in the Power Extraction and Transfer Structures (PETS). The injection and the extraction of the recombined pulses into and from CR1 and CR2 rely on transverse RF deflectors and striplines. The number of the main magnetic elements in the delay loop and combiner rings can be found in Table 24. Details on the magnet design can be found in [119].

3.9.3 Performance

The CLIC Test Facility (CTF3) was essential in demonstrating the feasibility of the beam recombination scheme on which the CLIC DBRC is based (see Sect. 2.1). The new design of the DBRC is an improved version of the design presented in [55, 121]. The changes in the lattice design allowed an increase in the energy acceptance of the entire complex, while respecting the transverse emittance budgets, taking account of the effects of Coherent Synchrotron Radiation (CSR) emission [118, 122]. The goal has been set to be close to 1% R.M.S. relative energy spread.

3.9.4 Design updates

Increasing the bunch length at the exit of the Drive-Beam Linac from 1 mm to 2 mm significantly reduces the impact of CSR when the beam circulates through the DBRC. One dogleg has been inserted before the DBRC to lengthen the bunch [123] from 1 mm to 2 mm, and one chicane has been added after the Transfer Turn Around (TTA) to recompress the bunch length from 2 mm to 1 mm (see Sect. 3.8). This compression of the longitudinal phase space is needed for CSR compensation, as well as a longitudinal energy chirp (also known as correlated energy spread) for the phase feed forward to preserve the Drive-Beam-to-Main-Beam synchronization.

In order to increase the energy bandwidth of the system, and accommodate such a correlated energy spread, the design of the CR arc cells has been modified and the original triple-bend achromatic cells have been replaced by a double Chassman-Green cell [123], which had already been adopted for the DL in the CDR design [55].

3.9.5 Longitudinal phase space effects

The development of the tracking code PLACET2 [120] enabled the study of the performance of the DBRC in a fully realistic manner [117], including RF-deflectors (and their impact on the path-length), synchrotron radiation emission and associated energy loss and bunch train recombination.

One of the main issues of the recombination process is a strong parabolic correlation between particle momentum and longitudinal position (see Fig. 25-left). This effect can be corrected by tuning the sextupoles located in dispersive regions (see Fig. 25-right). However, one must consider potential detrimental effects introduced by the sextupoles on the transverse emittances. Optimisation studies to address the issue were performed in [117]. The initial beam emittance is 50 µm. The goal is to reach an emittance after the DBRC of less than 150 µm, as required by the decelerators. Simulations of the full DBRC show that this goal can be reached even with initial emittances of up to 80 µm, while fully correcting the beam's longitudinal aberration [124].

3.9.6 Imperfections

The results of beam-based alignment schemes, like Dispersion-Free Steering (DFS) in CTF3's CR, indicate that misalignment of the element impacts the performance [125]. These studies confirmed that DFS is a promising technique and dedicated studies of its use in the DBRC should be performed. No major problems are expected.

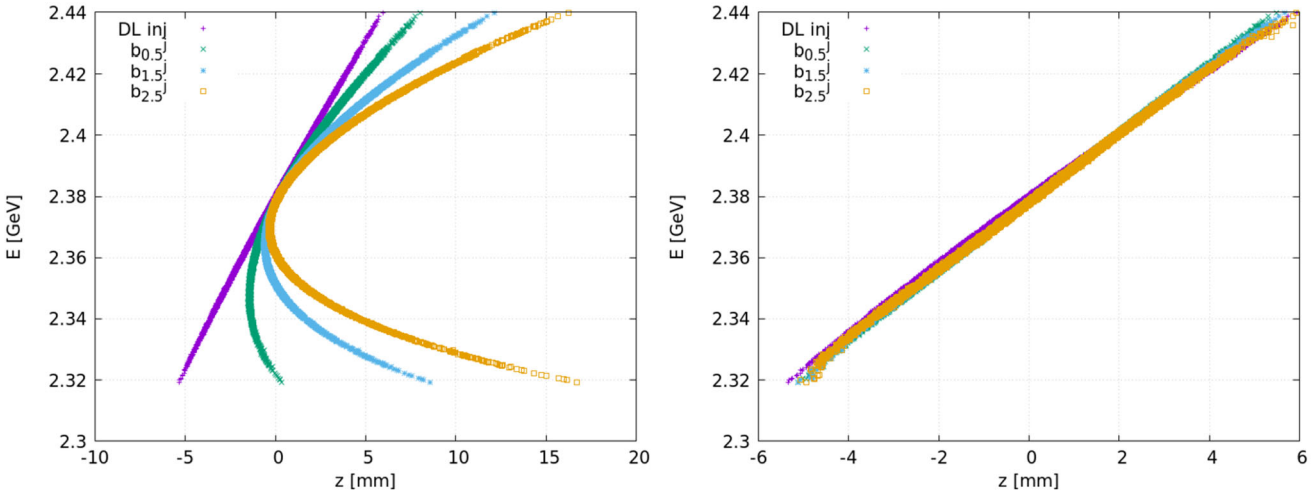

Fig. 25 Longitudinal energy profile before (left panel) and after (right panel) sextupole optimisation. The first layer shows the bunch at the DL injection point (target profile) and the following layers show the bunch after 0.5 $\left(b^j_{0.5}\right)$, 1.5 $\left(b^j_{1.5}\right)$ and 2.5 $\left(b^j_{2.5}\right)$ turns in CR1

Table 25 DB Parameters for Nominal Operation

Drive-Beam parameters [units]	Symbol	Value
Average beam current [A]	I	101
Initial energy [GeV]	E_0	1.91
Minimal final particle energy [GeV]	E_{min}	0.191
Train length [ns]	t_{train}	244
Bunch frequency [GHz]	f_{bunch}	11.994
Bunch-to-bunch distance [mm]	z_{bb}	25.0
Bunch length [mm]	σ_z	1
Bunch form factor [%]	$F(\lambda(\sigma_z))$	96.9
Initial normalized emittance [µm]	$\epsilon_{Nx,Ny}$	150

3.10 Decelerators

3.10.1 Overview

The decelerator lines run in parallel with the two Main-Beam lines for the full length of the Main Linacs. Each linac has four decelerator sectors. In each sector a Drive-Beam train of 101 A, 1.91 GeV, and 244 ns length is decelerated and the kinetic energy of the beam particles is converted to RF power by the Power Extraction and Transfer Structures (PETS) [126].

Four turn-around loops bring the Drive-Beam trains to the start of each decelerator sector; the spacing between them is 878 m. The lengths of the decelerating sectors vary slightly from 900 m to 840 m, such that each decelerator feeds the same number of accelerating structures. This length variation is a result of the variation of the filling factor in the Main Linac due to the limited choices of quadrupole spacings. At the end of each sector an insertion of four module lengths (about 10 m) extracts the used DB into a dump and brings in the new DB with a chicane.

3.10.2 Beam parameters

Table 25 summarizes the main parameters for the decelerator lattice and beam for nominal operation. During a tune-up period, uncombined (0.5 GHz bunch spacing) low-current beams may be used with a shorter train length (as short as required for precise enough BPM resolution).

3.10.3 Drive-Beam dump lines

After leaving ≈90% of its power in the PETS, the spent Drive Beam at the end of each decelerator has to be bent away from the decelerator axis and disposed of at a beam dump. This needs to be done in a way that leaves a sufficient amount of space for injecting the fresh Drive Beam into the next sector, which starts 8 m downstream. The spent beam is characterised by an energy spread of a factor ten, since the bunch is composed of a 2 GeV electron head followed by a long tail of ≈200 MeV electrons. Such a large energy spread requires a dedicated magnet design to bend the spent beam to the 2 m wide dump window located about 15 m away. The peculiar shape of the magnet does not pose a problem from a magnet design point of view. Exotic pole shapes can be manufactured, in particular if the magnet is operated in DC and the yoke is of solid iron. A permanent magnet solution could also be envisaged. The drive beam dump system is described in the CDR, the extraction magnet is found in [127].

4 Components and technologies

4.1 Introduction

This section describes the technological challenges and the solutions implemented in the current design of the accelerator. It starts with the production of the particles and their journey along the accelerator including the various power production schemes and related technologies. Other essential systems are highlighted and discussed, such as Beam Instrumentation, Vacuum, Survey and Stabilisation as well as general machine governing technologies such as Controls, Timing and Machine Protection. Where significant progress has been made with respect to the CDR [55] these differences are pointed out. Tests at system level as well as performance demonstrations are covered in Appendix A.

4.2 Sources and injectors

The injector of the Drive-Beam Accelerator is described together with the Drive-Beam Accelerator in Sect. 3.8. Here we focus on the Main-Beam Injectors which provide longitudinally polarized electrons and non-polarized positrons.

4.2.1 Polarized electron source and pre-injector linac

The CLIC polarized electron source is based on a DC-photo injector followed by a 2 GHz bunching system and a 200 MeV accelerator. After the electron injector linac a spin rotator at 2.86 GeV will be used to orient the spin vertically for injection into the damping ring. The electron injector can deliver an emittance smaller than 25 mm mrad. The source is based on demonstrated technologies and installations. The SLC electron source and the ILC design are used as references. The gun test facility at SLAC has shown the parameters needed for the CLIC source using a commercial strained multi-layered GaAs-cathode [52]. The cathode needs to be operated in a vacuum environment of the order of 10^{-11} mbar. Under such conditions several thousand hours of lifetime have been achieved. The gun has to be equipped with a load-lock system to allow cathode changes and activation under vacuum. Additionally, the gun optics have to be carefully designed to minimize particle losses close to the cathode.

A polarized laser based on flash-lamp pumped TiSa technology is used to illuminate the Ga-As cathodes. The laser has to be tuneable in frequency to be able to tune each cathode individually for maximum polarization. This tuneable bandwidth of approx. 0.7 nm is achieved with a quartz plate inside the laser cavity. The system produces a long pulse of several µs of which a 176 ns long flat pulse is cut out via a Pockels-cell. Experimental results indicate that a polarization above 80% can typically be achieved. Details of the proposed laser system can be found in the CDR and the main parameters of the CLIC polarized electron source can be found in Table 26.

The 176 ns-long electron pulse produced at the cathode will be pre-bunched with a pair of 2 GHz standing wave buncher cavities followed by a five-cell travelling wave buncher. After that, 2 GHz accelerating structures are used to bring up the energy to 200 MeV for injection into the common injector linac. The performance of such a system was simulated and showed an 88% capture efficiency with an emittance of 22 mm mrad [128]. A schematic of the pre-injector for the polarized electrons can be seen in Fig. 26.

Table 26 Laser and electron parameters for the polarized electron source and comparison with experimentally achieved results

	CLIC 2 GHz	CLIC DC/SLAC Demo
Electrons		
Number of electrons per bunch (10^9)	6	1365
Charge/single bunch (nC)	0.96	NA
Charge/macrobunch (nC)	338	300
Bunch spacing (ns)	0.5	DC
RF frequency (GHz)	2	DC
Bunch length at cathode (ps)	100	DC
Number of bunches	352	NA
Repetition rate (Hz)	100	50
QE (%)	0.3	0.3
Polarization	>80%	>80%
Circular polarization	>99%	>99%
Laser		
Laser wavelength (nm)	780-880	865
Energy/micropulse on cathode (nJ)	320	–
Energy/macropulse on cathode (µJ)	113	190
Energy/micropulse laser room (nJ)	1000	–
Energy/macropulse laser room (µJ)	350	633
Peak power per pulse (kW)	2	2
Average power at cathode wavelength (mW)	16	9.5

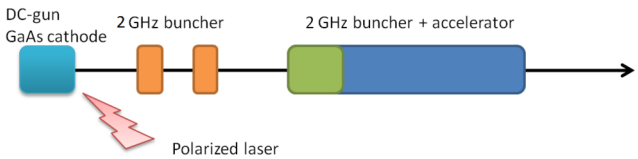

Fig. 26 Schematic view of the polarized electron source and pre-injector

4.2.2 Positron source

The CLIC positron source consists of a 2.86 GeV electron linac, a conventional amorphous target, followed by an adiabatic matching device and a capture pre-injector linac. The amorphous tungsten target generates positrons via pair production. Past experience at SLAC determined a destruction threshold of 35 J/g which should not be exceeded in order to guarantee a lifetime of 1000 days. The newly optimised design for 380 GeV has a peak power deposition density of 33 J/g. Therefore a second parallel target station, as described in the CDR for the 500 GeV case, is not needed. The thickness of the targets and their separation have been optimized together with the incoming beam parameters to maximise the positron yield [53, 54, 129]. Downstream of the target, an adiabatic matching device (AMD) focuses the positrons into the capture linac. The simulations assume a 127 mm long device with an tapered aperture from 6.5 mm to 55 mm and with a magnetic field decaying from 6 T to 0.5 T ($B = B_0 / (1 + \alpha z)$, with $B_0 = 6$ T and $\alpha = 55$ m^{-1}). Several matching devices have been designed [130] and prototypes have been built using both traditional electric discharge machining and innovative additive machining techniques. Figure 27 shows an example of such a prototype.

The positron capture linac and the subsequent acceleration linac to 2.86 GeV have been completely redesigned relative to the CDR. The yield of positrons fitting into the pre-damping ring energy acceptance has been increased significantly, and the longitudinal phase space has been improved, allowing for a lower energy of the positron production drive beam to 2.86 GeV [53, 54, 131]. The positron yield after the target is 8 e^+/e^- and the yield at the entrance of the pre-damping ring reaches 1 e^+/e^-.

The positron driver linac has a length of 250 m and uses a 2 GHz RF system with an accelerating gradient of 15.6 MV/m. The beam optics of the positron injector linac has been designed for the large emittance positron beam. A sequence of FODO lattices has been used with increasing beta-function and quadrupole spacing to minimize the

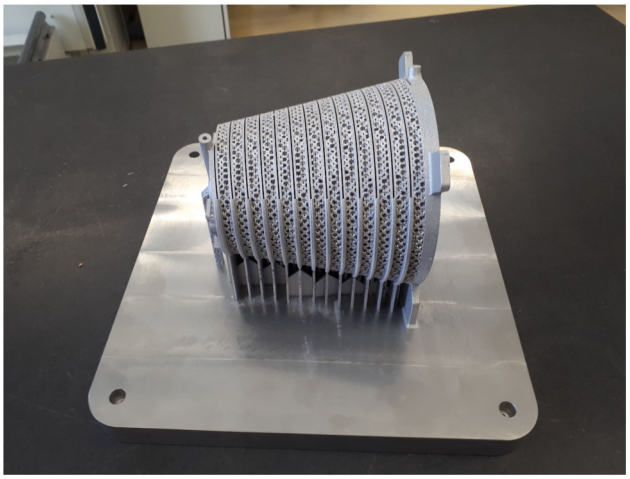

Fig. 27 CLIC adiabatic matching device prototype made of stainless steel by additive machining at CERN. Prototypes in other materials, like copper, could be readily realized elsewhere

number of magnets used. This linac is approximately 280 m long and uses a 2 GHz accelerating structure with a loaded gradient of 14.5 MV/m.

4.2.3 Injector RF system

The whole injector complex uses a 2 GHz RF system for the linear accelerators. The generic unit consists of klystrons with a peak power of 80 MW and a pulse length of 10 µs at 100 Hz repetition rate and a cavity-type pulse compressor. This combination allows the generation of one or a pair of RF pulses with a flat top and amplitude modulation for beam loading compensation. One klystron unit provides power for two accelerating structures installed on a common girder together with focusing and beam diagnostics elements. The electron injector linac and the booster linac use a double RF pulse spaced by 5 µs to accelerate main beam electrons and positron generation electrons in the case of the electron injector linac and positrons and electrons in the case of the common booster linac.

Accelerating structures have been designed with a length of 3 m which will be operated at a gradient between 14 MV/m and 17 MV/m depending on the beam loading for each linac. The aperture of this accelerating structure is larger for the positron linac due to the larger emittance and smaller for the electron linac and booster linac. Details of the main beam injector RF systems can be found in [56].

4.3 The Drive-Beam modules

4.3.1 Introduction

The two Main Linacs take the electron and positron beams from 9 GeV and accelerate them to the collision energy. In the 380 GeV stage, the opportunity is given to study two different accelerator configurations, based on two quite different technologies to feed the Main Linacs with the RF power required for the beam acceleration, the Drive-Beam options and a Klystron-based option. The Klystron-based option is discussed in C. Both have advantages in different areas. The optimisation work performed for the two configurations independently has produced two very different layouts [132], the differences going down to the level of the single accelerating structures. The main components of the accelerators are the RF accelerating structures, which are mechanically assembled two-by-two to form the super-accelerating structures (SAS). They are used to accelerate the beams and are assembled on supporting girders to form what we call the "modules". Modules will be pre-assembled on the surface and then installed in the machine tunnel, so they represent the fundamental building block for the construction of the accelerator, thousands of these are required even at the lowest collision energy.

The implications of the differences between the two configurations are evident in the module architecture and reflected in the accelerator infrastructure. The module nomenclature uses the terms T0, T1, etc., to refer to the number of SAS that are installed on the Main-Beam girder. The Main Beam Quadrupole (MBQ) is not part of the CLIC module and it requires a dedicated support and stabilization system. It will be treated separately (see Sect. 4.12).

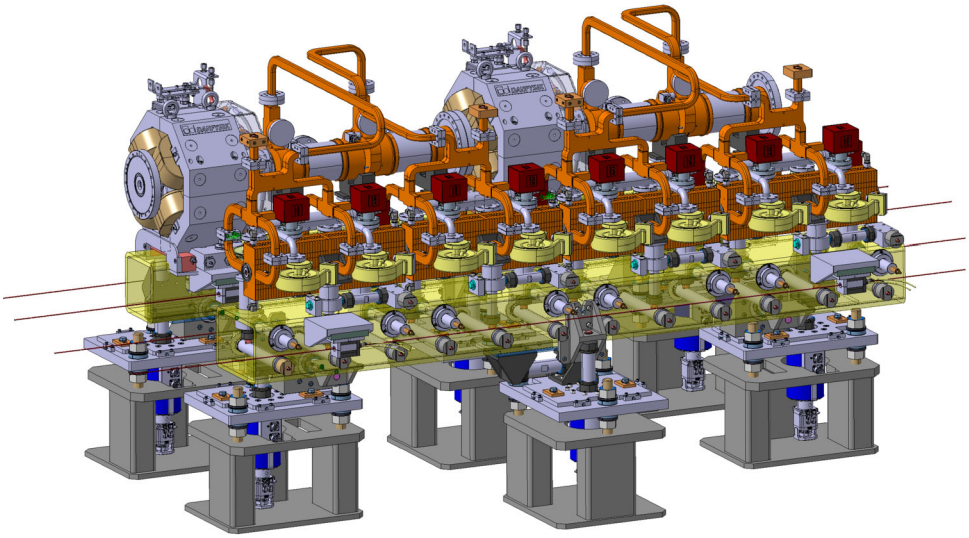

Fig. 28 The Module in the Drive Beam based configuration: the Main Beam girder (front) and the Drive Beam girder (back)

4.3.2 The Drive-Beam-based module

In the Drive Beam (DB) configuration, the RF power is transferred to the Main Linac by the Power Extraction and Transfer Structures (PETS) that are aligned in the Drive-Beam Decelerator, which runs parallel, at a distance of a few cm, to the Main Linac. Each PETS supplies one SAS, and there can be up to four PETS in one module. In the case of the DB configuration, we consider the assembly of the Main Linac and Drive-Beam Linac girders as one module since the two are interconnected by the waveguides transferring the RF power from the Drive beam to the Main beam. The DB-based module is represented in Fig. 28. Details of the design choices can be found in [133]

The optimisation of the accelerating structure geometry, from the point of view of the RF efficiency and of the beam wakefield tolerance, has generated RF structures that are made of 33 cells each and have a length of 0.271 m (see Sect. 4.5). In the case of the DB-based accelerator, the module length is defined by the periodicity of the Drive Beam lattice, so by the interval between Drive Beam Quadrupoles (DBQ). The length of a T0 module including four SAS is 2.343 m. By considering the fraction of RF power entering the accelerating structure that goes into the beam acceleration the RF-to-beam efficiency of the accelerating structures is 39.8%; 59.7 MW peak RF power is required in a pulse length of 244 ns to accelerate the beam with an average gradient of 72 MV/m. In a T0 module with four SAS the average energy gain per module is 156 MeV.

A total number of 2,976 modules are required for the two Main Linacs, which will be filled with 10,184 RF structures; the SAS are on the Main Beam side and the PETS on the Drive Beam side. In the fabrication tests it has been shown that connecting two accelerating structures to form a SAS represents a challenge for the correct alignment of the two structures, which must be within 14 µm R.M.S. with respect to the beam axis. It is our intention to directly assemble the SAS during the fabrication phase of the accelerating structures, when the final alignment can be better kept under control.

The main characteristics of the module in the DB configuration have been summarised in Table 27.

A detailed description of the DB Quadrupoles and their powering architecture can be found in Sect. 4.12. The alignment of the SAS on the supporting girder relies on adjustable supports, the overall alignment strategy for the DB-based accelerator is described in Sect. 4.8. The supporting girder must provide sufficient rigidity and stability. Two materials are being considered, structural steel and Epument, a mineral cast material. The measured static deformation under maximum load is about 15 µm in the case of Epument compared to about 35 µm for structural steel; a choice between the two materials has not been made yet, however cost considerations and simplicity of fabrication would indicate a preference for the structural steel option.

The fact that the PETS and the SAS are tightly connected by waveguides for the RF power transfer has also led to the idea of considering the two components as a single unit with a lighter way of assembling the DB-based accelerator, as shown in Fig. 29. In this scheme the DBQs would be supported separately, also in consideration of the importance that their alignment has on the DB performance. For the time being this solution remains an option that will be further explored.

As opposed to what was established in the CDR, the vacuum system will rely on individual mini-pumps connected to each PETS and SAS, providing ion and getter pumping in the same device; additional pumping will be provided by vacuum pumps connected to the compact spiral loads and to the waveguides. The choice of suppressing the common pumping manifold between the MB and DB sides of the module [55] descends from

Table 27 A summary of the module characteristics in the Klystron-based accelerator

Module and RF Structure Characteristics	Values
Cells / structure	33
SAS length [m]	0.542
SAS / T0 module	4
SAS / T1 module	3
SAS / T2 module	2
Average accelerating gradient [MV/m]	72
Input power / structure [MW]	59.7
RF Frequency [GHz]	12
Module length [m]	2.343
DBQ / module	2

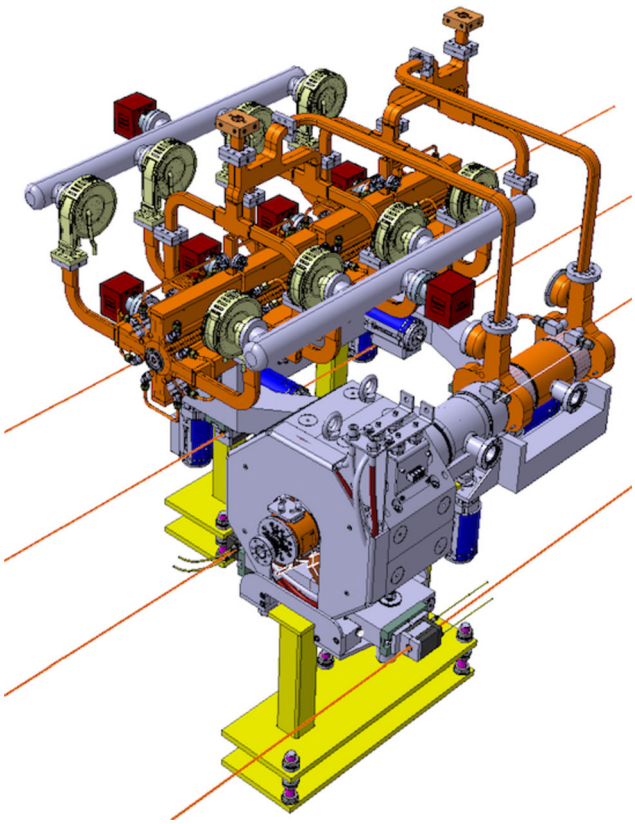

Fig. 29 The RF Unit assembly with PETS and SAS connected to a common supporting frame. The DBQs sit on independent supports

the need to reduce the mechanical coupling and the forces that are exerted between the two girders. A detailed description of the vacuum system is provided in Sect. 4.7.

Due to the tight mechanical tolerances that strongly impact on the Main Beam quality, the thermal stabilisation of the module assumes a critical operational role; most of the power that is dissipated in the module comes from the RF structures and from the RF loads. An extensive study had already been performed at the time of the CDR and here power figures have been reviewed in light of improved efficiencies. In Table 28 a summary of the power dissipated in a T0 module is provided, in the most unfavourable condition of unloaded operation.

A compact spiral load has been specifically developed to dissipate the power transmitted through the accelerating structures. It consists of a 3D printed spiral waveguide built by Electron Beam Melting (EBM) additive manufacturing using pure titanium. It provides −40 dB attenuation at 12 GHz, It can manage up to 200 W average power dissipation and withstand up to 16 MW peak power [134].

Table 28 Power dissipation in the DB module under unloaded conditions (case of a T0 module)

Module Component	Number	Item Dissipation [W]	Total Dissipation [W]
SAS	4	772	3,088
PETS	4	11	42
SAS RF Loads	16	168	2,690
Waveguides	4	60	241
DBQs	2	171	342
Total per module			6,403

Table 29 Specifications for the klystron and modulator for the Drive Beam

Main parameter	380 GeV
Frequency [MHz]	999.516
Number of Klystrons	385
RF Peak Power MW	24
RF Average Power [kW]	58
Pulse Length [µs]	48
Pulse Repetition Rate [Hz]	50
Klystron Efficiency [%]	82
Klystron Perveance [μperve]	2.8
Modulator Voltage [kV]	160-170
Peak Pulse Current [A]	180
Modulator Average Power [kW]	81
Klystron Solenoid Average Power [kW]	5
Klystron Heater Power [kW]	1
Flat-Top Stability [%]	0.1
Pulse-to-Pulse Repeatability [ppm]	50
Rise and fall times (t_{rise}, t_{fall}) [µs]	3,3
Voltage Settling Time (t_{set}) [µs]	5

4.4 Klystrons and modulators

4.4.1 Drive Beam RF power

The Drive-Beam based solutions for CLIC require High Voltage klystron modulators to feed several hundred klystrons. For the CDR [55] different options of RF power sources and klystron configurations were studied. It was found that the most reliable and inexpensive solution would be a multi-beam klystron (MBK) with an output power in the range of 15 to 25 MW [55]. Specifications for the klystron and modulator are summarized in Table 29.

In addition, the amplitude and phase of the RF output power has to be controlled to ±0.2% and ±0.05 degrees respectively, putting constraints on all equipment involved.

4.4.2 Klystrons for the Drive Beam

The Drive Beam is the main power consumer of the facility. Therefore, the efficiency of the RF power source is extremely important. For 380 GeV more than 9 GW of peak power and an average power of 22 MW are needed at an RF frequency of 1 GHz. Increasing the efficiency of the currently available klystrons is therefore essential for CLIC.

For the drive-beam generation complex, two high-efficiency klystron prototypes in L-band technology have been developed in collaboration with industry, with the specifications shown in Table 29, with the goal to obtain an efficiency above 70%. The first prototype, using a Toshiba 6-beam Multi-Beam Klystron (MBK), reached 21 MW

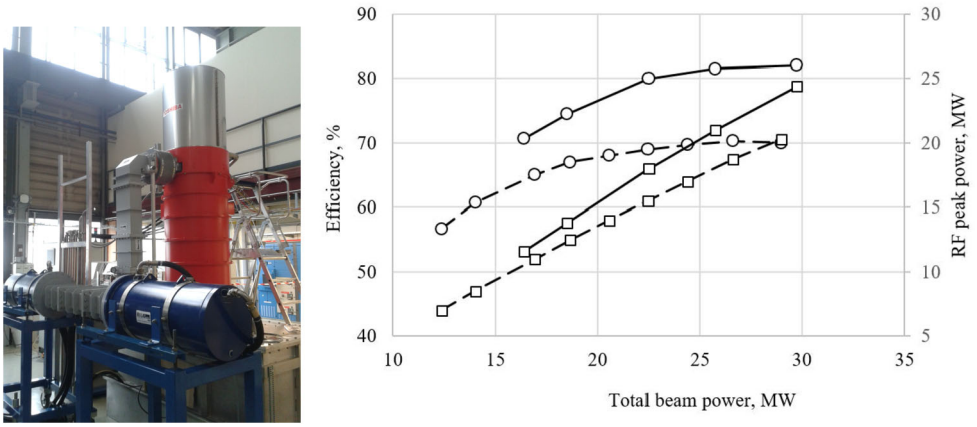

Fig. 30 Left: The 1 GHz klystron test stand at CERN with the Toshiba MBK klystron installed; Right: The simulated klystron efficiency (circles) and the simulated peak RF power (squares)for the new-technology CLIC TS MBK (solid lines), compared to the measured ones for the Toshiba MBK klystron (dashed lines), vs total beam power. From [109]

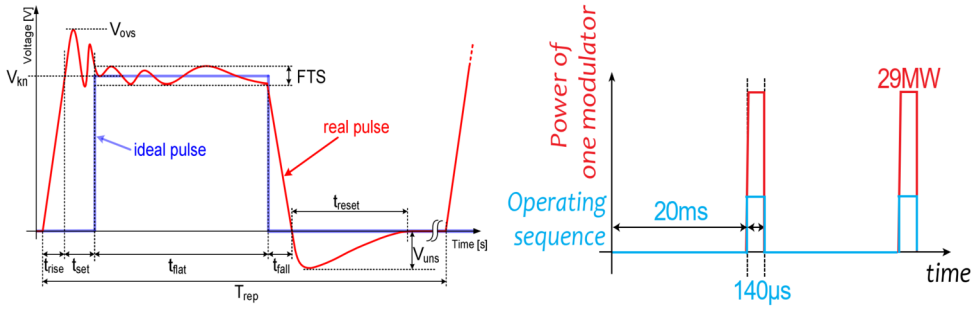

Fig. 31 Left: voltage pulse definition; Right: 3 TeV pulsed power illustration (one modulator)

output power during the factory tests. See Fig. 30 for the Klystron (left) and the measured performance (right). Its efficiency of 71.5% remains remarkable high for a wide range of output power. A second prototype built by another firm, based on a 10-beam MBK, also reached the required peak power and an efficiency of 73%. However, the second prototype does not yet fulfil the requirements concerning stability and average power.

These two innovative prototype MBK commissioned by the CLIC study represent the state-of-the-art of what is available in industry and reach record efficiencies. Based on this experience a large-scale production of such klystrons can be mapped out. Detailed testing of the complete RF power unit including the modulator and the low-level RF system will have to demonstrate the required stability.

Design improvements continue in parallel, and recent developments of new klystron technology (two-stage klystron) [109] and availability of the modern computer tools could allow to boost the efficiency of L-band klystrons from around 70% in the existing the commercial tubes to above 80% in the new designs. In Fig. 30 (right) [109] the performance of the commercial prototype shown is compared to the performance of the new high-efficiency klystron design.

The fabrication of a prototype klystron to realize the new technology is ongoing. It is important to add that this technology is also suitable for ILC and FCC.

4.4.3 Modulator for the Drive Beam

Ther modulator requirements shown in Table 29 fall in an unexplored range where specifications of the fast pulse modulators (voltage fast rise and fall times to minimize power losses) and long pulse modulators (long voltage flat-top) have to be merged. See Fig. 31 (right) for pulse definitions [55].

From the global modulator efficiency of 95%, which includes the electrical efficiency and “pulse efficiency”, defined as the ratio between the ideal and real voltage pulses energies (Fig. 31 (left) pulse rise, fall and settling times have been defined, which shall be minimized to reduce klystron losses. The total power fluctuation (all modulators synchronously operated) is 38 GW (for the 3 TeV case). To obtain a stable voltage distribution network it has been decided to limit the AC power fluctuation to 1%. Details on design challenges are summarized in [135].

4.4.4 General klystron modulator configuration

The search for a suitable klystron modulator configuration has been approached by considering the high power electrical distribution over an approx. 2 km long DB. Global optimization studies [136], considering overall infras-

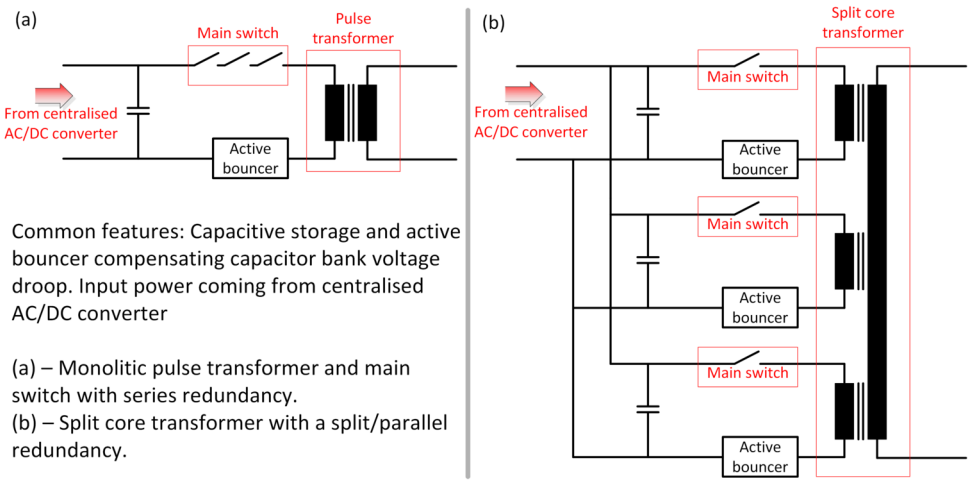

Fig. 32 Principle topology for: (a) serial redundancy and (b) parallel redundancy

tructure cost, operability (modularity), and efficiency, clearly show the need for a medium voltage distribution. The final solution for the 3 TeV option consists of six powering sectors, each with a powering substation, equally distributed along the DB length. Each substation is composed of a set of AC power transformers, AC switchgears and AC bus bars to provide a 10 kV AC network with n+1 redundancy. The 10 kV AC network supplies a modular AC to DC converter, a so-called Modular Multilevel Converter (MMC), which provides 20 kV DC voltage [137]. A novel MMC control has been developed to respect the 1% power fluctuation without the need to synchronize the CLIC RF to the utility grid. All voltage levels result from the global optimization approach in the 3 TeV stage. Each of the six centralized AC to DC converters supplies approx. 180 modulator-klystron sets.

The results of the global electrical distribution and AC to DC conversion impose the modulator configuration, with a medium voltage DC stage and a voltage step-up pulse transformer. Two basic configurations, with series and with parallel redundancies (Fig. 32 (a) & (b)), have been studied [138–141].

The monolithic pulse-transformer-based configuration (Fig. 32 (a)) has been designed and validated via small-scale prototypes [142], whereas a full-scale split-core based configuration prototype has been built and tested. The stringent pulse-to-pulse repeatability requirement [143] drove the choices of the active bouncer configuration (together with the fast rise time) and the design of special acquisition systems for high rate voltage measurements [144].

Preliminary studies show that the proposed 3 TeV powering layout is also an optimal solution for the 380 GeV and 1.5 TeV stages. Since all the equipment up to the Medium Voltage DC distribution is modular, a staged approach minimally influences the cost of each stage; however, an initial extra investment in the modulators (no more than 20%) for 380 GeV is necessary. This allows the modulators to be dimensioned correctly (pulse transformer) for the larger pulse width requirements in the 3 TeV stage.

A full scale modulator prototype based on configuration of parallel redundancy (as seen in Fig. 32 (b)) has been designed and delivered to CERN from ETH Zürich (Fig. 33 left). First tests on an electrical dummy load demonstrated the feasibility of the voltage pulse dynamics up to 180 kV. This modulator represents the new state of the art in fast-pulsed modulators with flat-top medium voltage input.

Following the results (in 2016) of global powering optimisation, the configuration of serial redundancy (as seen in Fig. 32 (a)) is more adapted for CLIC. Therefore a second full-scale modulator prototype based on a configuration of serial redundancy has been constructed

4.4.5 Solenoid focusing magnets

The klystron focusing solenoids are another source of high average power consumption, contributing to approximately 50% of the electrical energy consumed. To make a significant reduction in this power consumption a study to replace the normal-conducting solenoid with a superconducting solenoid has started, where the average power per solenoid is expected to be 1.6 kW.

4.4.6 Low-Level RF (LLRF)

Recent developments in commercially available solid state pre-amplifiers now being used in the high-gradient Test Facilities at CERN show a phase stability of better than 0.05 degrees which is more than sufficient to reach the CLIC requirements. Performances in the operation of the high-gradient Tests Stands and recent X-band linearizers in the Paul Scherrer Institute [145] and in Synchrotron Trieste [146] show that the LLRF used to drive these amplifiers can also achieve the required specifications necessary for CLIC.

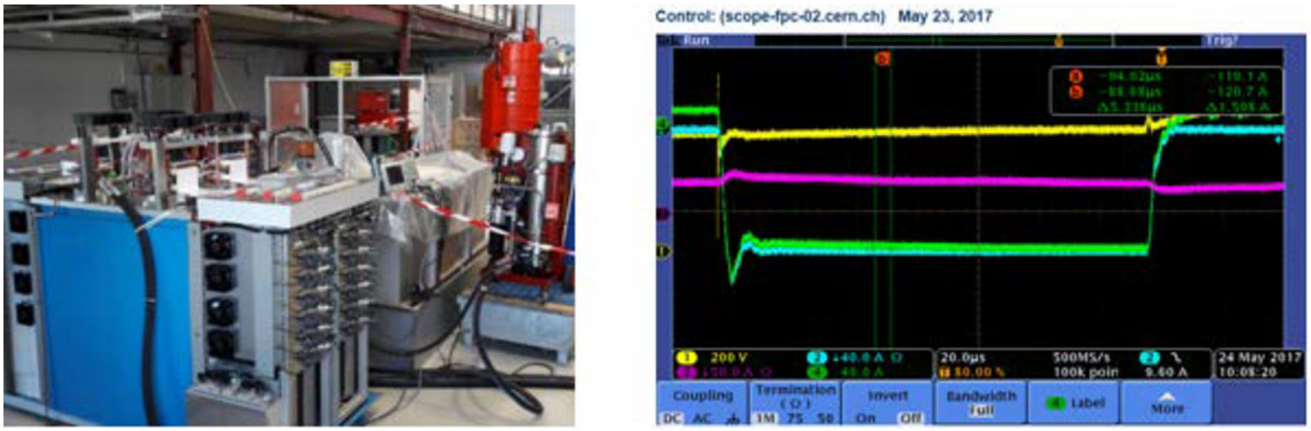

Fig. 33 Left: Photograph of the full-scale modulator prototype installed at the CERN RF test stand. Right: First measured nominal voltage pulses demonstrating the dynamical capabilities

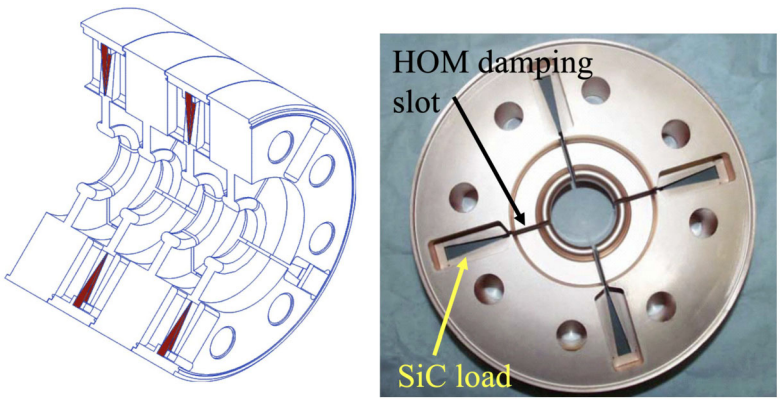

Fig. 34 Cut-away view of the 3 GHz SICA structure geometry (left) and of its cell disk with SiC damping material (right). The CTF3 linac was routinely operated over several years with these structures with high-current electron beams in fully loaded regime

4.5 RF structures

There are ten different RF systems in the accelerator complex including the Main and Drive Beam generation, and the Main Linac. Each of these uses different accelerating, decelerating or deflecting structures. The more relevant ones will be described below.

4.5.1 RF structures of the Drive Beam generation complex

Drive-Beam linac accelerating structure This structure has been designed to maximise efficiency since it is the biggest power consumer in the entire CLIC complex. Therefore the accelerating structures are operated in a fully-loaded mode reaching an RF-to-Beam efficiency of 95%. The main challenge of the system is the handling of long-range wakefields generated by the high current (4.2 A) Drive Beam. The chosen baseline is a disc-loaded travelling wave structure of SICA type (Slotted Iris–Constant Aperture). The required damping is achieved through four slots in each iris to couple to the azimuthal currents generated by transverse modes. The HOM absorbers (SiC loads) are located directly in the iris slot. Other modes are detuned by changing the length of the nose cones in every cell. The structure operates at 1 GHz fed directly by klystrons and is composed of 23 accelerating cells, giving a total active structure length of 2.5 m. The CLIC structure is a scaled version of the 3 GHz SICA structure built and successfully operated in CTF3 (see Fig. 34).

Fabrication of the final structure can be done via conventional precision machining as geometrical tolerances required are of the order of 0.1 mm. For the 380 GeV stage, a higher gradient for the fully-loaded accelerating structures has been adopted, resulting in a reduced overall length.

RF Deflectors The bunch train compression scheme for CLIC relies on the use of fast RF Deflectors (RFDs) for injection into the Delay Line (DL) and in the Combiner Rings (CRs). The three types of deflectors are all based on the travelling wave concept and have different operation frequencies depending on the recombination factor of

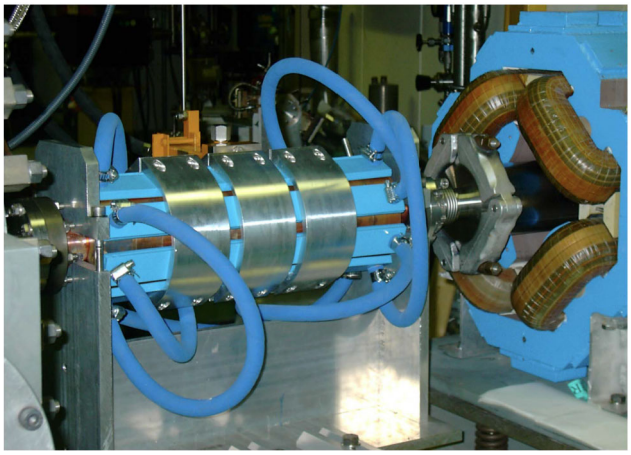

Fig. 35 Photograph of the 3 GHz RF deflectors installed and operated in the CTF3 Combiner Ring

Table 30 Overview of parameters for various RF structures for the Drive Beam generation for 3 TeV (380 GeV numbers in brackets)

	DBA	RFD DL	RFD CR1	RFD CR2
Operating frequency [GHz]	999.5	0.5	2	3
Number of structures	1638 (459)	2	2	6
Active structure length [mm]	240	600	450	150
Number of cells per structure	23			
Pulse length [μs]	150 (48)	140	140	140
Aperture diameter [mm]	98	50	40	40
Filling time [ns]	245	110	80	16
Input peak power [MW]	18	50	50	50
Accelerating gradient unloaded [MV/m]	6.6	11	13	14
Accelerating gradient loaded [MV/m]	3.4	-	-	-

the rings. The frequencies are 0.5 GHz, 2 GHz, and 3 GHz for the DL, CR1 and CR2, respectively. The RF and mechanical designs of a generic RFD exist and have been tested in CTF3 (see Fig. 35).

The various parameters of the above-mentioned structures are summarized in Table 30.

4.5.2 RF structures for the Main Beam

RF system for the damping rings The design of the damping rings is described in Sect. 3.2. There are 3 rings in total: two identical damping rings for production of final electron and positron beams and one pre-damping ring for the positron beams. All three rings require a 2 GHz RF system due to bunch spacing of 0.5 ns only. The combination of the high RF frequency and high energy loss per turn in the wigglers results in a very high transient beam loading effect. Compensation of this effect to the level of the stringent requirements on the low emittance beam stability at the damping rings extraction is the main challenge for the RF system. The design of the RF system is based on the so-called barrel cell cavity (BCC) with ultra-low R/Q $\approx 1\ \Omega$ described in more detail in [63]. There are 24 of these cavities in each of the damping rings and 12 similar cavities in the pre-damping ring. The image of the first prototype of the BCC is shown in Fig. 36. It is a Superconducting RF cavity fabricated by means of high precision machining of the central part out of bulk Nb and welding it together with two extremity pieces to form a cavity.

4.5.3 Main-linac RF structures

Power Extraction and Transfer Structure (PETS) These passive microwave devices, shown in Fig. 37, interact with the Drive Beam to generate RF power along a constant-impedance periodic structure. The power is collected downstream in an RF power extractor that converts the TM01 mode in a 23 mm diameter circular waveguide into a TE10 mode in a rectangular WR90 waveguide. In its final configuration, the PETS comprises eight octants (bars) separated by the 2.2 mm wide damping slots. Each of the bars is equipped with HOM damping loads. A total of sixteen PETS have been manufactured and tested in the two beam lines of CTF3. The performance of the PETS in CTF3 is described in Sect. A.2.

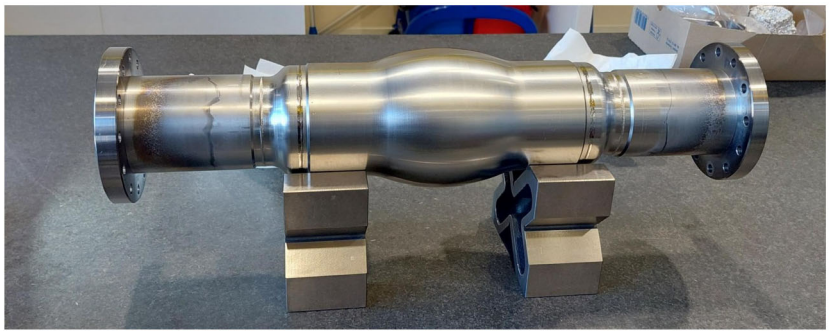

Fig. 36 Photograph of BCC prototype

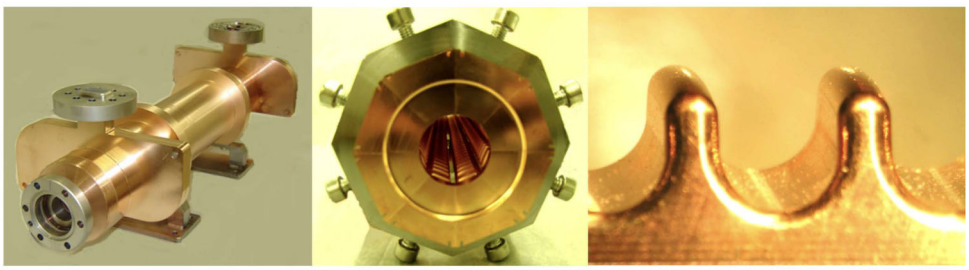

Fig. 37 The assembled PETS body, outside (left) and inside (middle), zoom of the PETS single bar period (right)

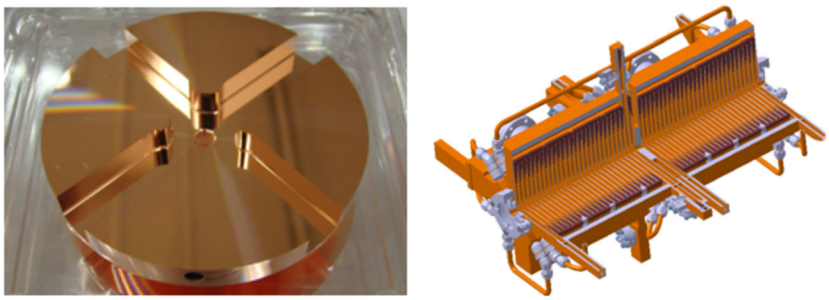

Fig. 38 Photograph of a single disc (left) and an engineering model of a full two-by-two super-accelerating structure (SAS) (right)

Main-Beam Accelerating structure The compactness of CLIC is based on the high gradient achieved in the Main-Beam Accelerator in order to reach 3 TeV in a reasonable tunnel length. The main challenge for these accelerating structures is producing extremely elevated electric fields without excessive vacuum arcing during operation. We use disk-loaded travelling-wave structures working at 12 GHz and with constant gradient to increase RF-to-beam efficiency. See Fig. 38 for an illustration. The very small aperture of the iris generates considerable transverse short-range wakefields which translate into very demanding alignment tolerances of the order of 14 µm per super-structure (as described in Sect. 4.8). Damping of the long-range transverse wakefields is provided by four radial waveguides ending in SiC loads. The continual decrease of the iris radii through the structure ensures as a side effect detuning of the remaining modes. The final optimization of the length, gradient and overall geometry of the structure has been made using a general costing model which takes into account also power and civil engineering costs. Therefore, we have a different structure for each stage of CLIC, as well as for the klystron-based option. The main parameters of all three structures can be found in Table 31. A large number of prototypes corresponding to the 3 TeV stage have been manufactured over the last years. They have been successfully tested in high power conditions in the X-band test facilities at CERN, KEK and SLAC (see Appendix A).

In all cases, the fabrication process is critical to achieve the highest gradient. The structure is made of OFE copper disks machined by turning and milling using single-crystal diamond tools and with tolerances in the micron range. The stack of disks is then bonded in a furnace at 1040 °C with a hydrogen protective atmosphere. Ancillary systems like cooling blocks, manifolds with loads, and the vacuum chamber are brazed separately after this. After RF measurements and bead-pulling, the final unit is then baked for 1-2 days to desorb the Hydrogen and finish cleaning the surface.

Even if the final CLIC prototype accelerating structure has been manufactured and successfully tested, the complexity of assembly and the need for ultra-precision machining made the structure costly and difficult to produce in large numbers. Alternative manufacturing techniques based on vacuum brazing and electron-beam welding of structures made in halves instead of disks are under investigation. In parallel, studies are being launched

Table 31 RF parameters for the Main Linac RF structures working at 11.994 GHz

	Main Beam Accelerator			PETS		Crab
	380 GeV		3 TeV	380 GeV	3 TeV	
	DB	Klystron				
Number of structures	20,592	23,296	143,232	10,296	71,616	2
Active structure length [mm]	272	230	230			
Number of cells	33	28	28	33	34	12
Pulse length [ns]	244			244		∼200
Aperture diameter [mm]	8.2-5.2	7.25-4.5	6.3-4.7	23	23	10
Filling time [ns]	55.8	63.8	66.3	1.52	1.55	
Input peak power [MW]	59.2	40.6	61.1	123.3	127.3	20
Average Q factor	5504	5846	5843	7200	7200	
Accelerating gradient unloaded [MV/m]	92	95	120	-	-	2.55
Accelerating gradient loaded [MV/m]	72	75	100	-	-	

The Main-Beam accelerating structure has been optimized for the 380 GeV initial stage both Drive Beam [147] and klystron based [148] as well as for the 3 TeV stage [149].

together with industry to estimate the necessary modifications in the production flow, production yields, quality assurance needs, costs and learning coefficients for the full CLIC production.

One of the remaining challenges with respect to the Main-Linac accelerating structure is the accuracy required for the integrated wakefield monitor of only 3.5 microns. Laboratory and beam studies in CLEAR are focusing on verifying the geometric accuracy of the cells and wakefield monitors as well as minimizing errors in the electronics, acquisition and signal to noise ratio.

4.6 Beam instrumentation

4.6.1 Overview of the CLIC beam instrumentation requirements

Beam dynamic considerations dictate most of the requirements for beam instrumentation and CLIC is expected to operate with extremely tight tolerances on most beam parameters. Extremely low-emittance beams are generated in the damping rings and must be conserved over kilometres of beam lines requiring a precise control of the beam position over such long distances. Before entering the Main Linac, the bunch length must be shortened and controlled at the femtosecond level. At the interaction point, the beam is finally focused to only a few nanometres in size. After collisions, the highly disrupted beam must be dumped in clean conditions, making sure that the multi-MW of power carried by the particles are safely absorbed.

An overview of CLIC beam instrumentation was presented in the CDR [55] with a collection of technical specifications for the different parts of the 3 TeV stage, together with a description of the possible technologies in use and their expected performance. In the context of a 380 GeV stage, all those specifications and challenges remain valid, and only the total number of devices required is reduced as it scales almost linearly with the beam energy and the overall length of the accelerator complex. The total number of instruments required on the Drive and Main beams for 380 GeV is presented in Table 32.

4.6.2 Main-Beam instrumentation

Main-Beam Cavity Beam Position Monitor The ability of Cavity Beam Position Monitors to achieve nanometre-level resolution was already demonstrated in [150], but an additional challenge in CLIC is the use of dispersion-free steering along the Main Linac, which would require both high spatial resolution and time resolution better than 50 ns. This has launched the development of a lower-Q cavity BPM for the Main Beam, which has been constructed and tested in CTF3 and has demonstrated its capability to measure the beam position, with a 200 ns long train of bunches, with a time resolution better than 20 ns [151]. A picture of the CLIC cavity BPM installed on the CTF3 beam line is shown in Fig. 39.

Table 32 Number of beam instruments for the Drive and Main Beams

Instrument	Main Beam	Drive Beam
Intensity	68	54
Position	4083	7920
Beam Size	68	53
Energy	34	37
Energy Spread	22	37
Bunch Length	35	37
Beam Loss /Halo	4659	7834
Beam Polarization	14	0
Tune	6	0
Beam Phase	4	13
Luminosity	2	0
Total	8995	15985

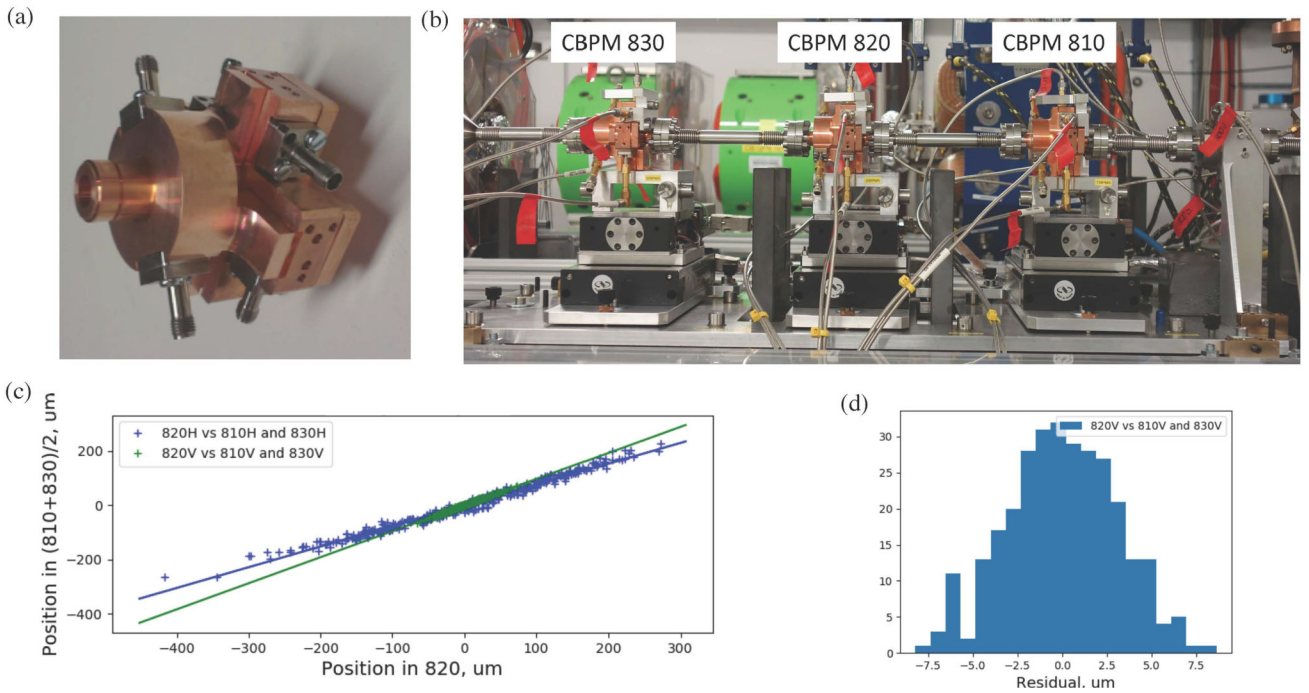

Fig. 39 (a) A picture of the CLIC Cavity BPM; (b) Experimental test-stand installed on the CTF3 beam line with 3 consecutive cavity BPMs, each BPM being installed on movers for remote alignment; (c) Correlation plot of the beam position measured by the central BPM (820) with respect to the positions measured by the two others; (d) The corresponding residual error measured in the vertical plane

Non-invasive short bunch length monitor Bunches as short as 150 fs will be produced and their longitudinal profile must remain under control up to the collision point to guarantee maximum luminosity. The bunch length needs to be measured and controlled accurately with time resolution better than 20 fs. Radio-frequency deflectors [152] have already demonstrated their capability to provide femtosecond resolution but in a destructive way. An R&D program has thus been pursued since 2009 to design and test non-invasive bunch length monitors using laser pulses and bi-refringent electro-optical crystal [153, 154].

Recently, remarkable strides have been achieved through the integration of electro-optical methods using a new scheme, called Diversity Electro-optical sampling [155], which would enable achieving the required time resolution using simpler set-ups.

Measuring very small beam sizes The extremely small transverse emittance generated in the damping rings puts tight requirements on the measurement of transverse beam size, which should achieve micron resolution. In rings, synchrotron radiation [156] provides a great opportunity to measure the small beam sizes. The 3^{rd} generation light source community has been very active over the last 20 years in developing better and better transverse beam diagnostics based on x-ray optics [157] or optical light interferometric techniques [158]. Recently studies using randomly distributed interferometric targets have been performed in an attempt to improve further the performance of SR-based techniques [159] [160].

Other methods were studied in the early 2000's and Laser Wire Scanner (LWS) technology has demonstrated excellent performance in measuring sub-micron beams non-invasively [161]. However, the system's complexity and the need for an expensive high-power laser triggered the study of alternative solutions aiming for better reliability, simplicity and cost saving. A breakthrough was achieved in 2011, with the experimental measurement of the point-spread function of optical transition radiation [162]. This then led to the development of beam size measurement techniques with sub-micron resolution using a simple, cheap and compact optical imaging system [163]. Theoretical considerations on how to use this technique practically for highly relativistic beams was also studied and verified experimentally [164].

4.6.3 Drive-Beam instrumentation

In the framework of CTF3, a full suite of beam instruments has been successfully developed to fulfil the requirements in the Drive Beam complex. These are longitudinal beam diagnostics for measuring the bunch frequency multiplication in the combiner rings [165–168], and also transverse profile monitors for high energy spread beams in the Drive-Beam Decelerator [169–171].

Non-invasive transverse beam profile for low-energy, high-charge beams Compared to CTF3, the CLIC Drive Beam has a considerably higher total charge, corresponding to an average current of 4.2 A over a 48 µs pulse length. This has severe consequences on the technological choices for beam instrumentation. Any intercepting devices would be limited to the observation of a small fraction of the Drive Beam, most likely by reducing the beam pulse length or current. We have launched an R&D program to develop non-invasive transverse beam profile monitors based on the interaction of the particles with a supersonic gas-jet. Given the encouraging results [172–174], this work is being followed up by a large scientific community as it may also be of interest to many other accelerators [175].

Reliable and maintainable beam position monitor system for the Drive-Beam Decelerator With more than 6,000 devices, the BPMs in the Drive-Beam Decelerator will be the largest under-vacuum beam instrumentation system in CLIC. It will also be the biggest cost driver and a critical system that needs to be highly reliable and easily maintainable. Different BPM technologies, such as inductive pick-ups [176] and stripline pick-ups have been tested. We did not find a big difference in cost and performance between these two designs. However inductive pick-ups present several advantages compared to striplines. First, in terms of complexity, inductive pick-ups, based on the measurement of the wall current, have no element under vacuum, whereas striplines sit inside the beam pipe and need to be carefully matched to 50 ohms impedance, which would require longer tuning procedures that would increase the production cost of the system. Moreover, a development made for LHC [177] has shown that inductive pick-ups can be designed and manufactured such that they can be dismounted without breaking the vacuum, which would also enable maintenance and repair to be carried out with minimum downtime and impact on other services.

4.6.4 Technology developments valid for both beams

Non-invasive beam-size monitoring using polarisation radiation Non-invasive transverse beam size monitoring is key to the operation and the optimization of high-beam-charge accelerators. A study addessed techniques based on polarisation radiation, such as diffraction radiation [178]. After the earlier promising measurements [179], a series of experimental investigations was engaged both on the Cornell electron storage ring [180] as well as on the Advanced Test Facility 2 (ATF2) at KEK. The possibility to measure beams with a spot size of a few microns using UV light and very small (<100 µm aperture) diffraction slits was demonstrated recently [181].

This would find application, as an alternative to laser wire scanner in the Main Beam RTML as well as in the Drive Beam complex where the electron beam energy is in excess of 1 GeV.

Looking for a way to overcome background limitation in diffraction radiation from small aperture slits, the Cherenkov Diffraction Radiation emitted in longer dielectric material was investigated. Measurements performed on CESR [182] have shown very promising results, as depicted in Fig. 40. A more extensive study of the effect was initiated in order to measure precisely the resolution of this technique as a non-invasive beam-imaging system.

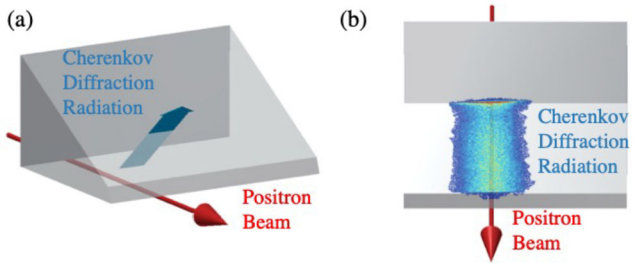

Fig. 40 First detection of Cherenkov Diffraction radiation emitted by a 5.3 GeV positron circulating in the Cornell storage ring;(a): Schematic view of the emission of Cherenkov diffraction radiation in a prismatic dielectric radiator; (b): Corresponding Beam image showing a horizontal beam size of 4 mm

A distributed beam loss monitoring system along the CLIC main linac Along the decelerator, the Drive-Beam energy will be continuously transformed into 12 GHz RF power over some hundreds of meters. The beam energy spread rises up linearly to reach a value of 90% at the end of a decelerator section. The beam optics must be adapted to ensure constant RF power production without consequent beam losses and beam operation relies on the continual monitoring of the beam properties. This is achieved using a beam loss monitoring system with a large number of classical ionization chambers [183] distributed along the main linac. Pursuing an alternative solution providing a better measurement of longitudinal distribution of the losses, simulations and experimental validations have led to the development of a high performance and cost-efficient BLM system [184] based on optical fibre measuring Cherenkov light induced by lost charged particles. In particular, the study has addressed several key features of the BLM system such as the position resolution of the optical fibre detection system when using long electron pulses (i.e. 200 ns) [185] and the crosstalk between losses from the Main and Drive Beams [186].

4.7 Vacuum system

4.7.1 Introduction

Apart from its large size, the vacuum system for the CLIC complex contains a multitude of challenges: synchrotron radiation, electron cloud, sparking and degassing induced by high electrical field, conductance limited system, cryogenic vacuum system, etc. Most of the CLIC complex requires high or ultra-high vacuum. From a general point of view, different technical solutions are chosen:

1. For bakeable vacuum systems operating at room temperature, a solution based on a Ti-Zr-V film coating is used. The thickness of this non-evaporable getter (NEG) coating can be reduced below 1 µm if required. After in-situ activation by heating, it provides a distributed pumping speed for the most abundant gas species released in the vacuum chambers. Also, the desorption yields induced by photon and electron bombardment and the secondary electron yield are reduced drastically when compared to traditional materials. A limited number of lump ion pumps are required to remove noble gas and methane not absorbed by the NEG material.

   For non-bakeable vacuum systems operating at room temperature, vacuum performance is driven by water vapour outgassing. High vacuum can be obtained after a long pumping period. Lumped pumps are used. A combination of NEG pumps with large pumping speed and sputter-ion pumps is recommended to limit the cost of cabling. If low secondary electron yield is required, amorphous carbon (aC) coating can be applied.

   This is the case of the CLIC main linac in which pumps are installed directly on the AS vacuum manifold or the PETS vacuum enclosure. A set of Pirani and Penning gauges are installed on each beam line and in each module to complete the system and provide interlocks [187]. Tests in the module mock-up have demonstrated that after activation of the NEG cartridge, the pressure decreased with time (1/t) and reached 3×10^{-9} mbar along the beam axis after 100 hours of pumping.
2. For vacuum systems operating at cryogenic temperature, the cold surface acts as a cryopump for the impinging gas molecules sticking to it. The pumping speed and saturated vapour pressure of the different gas species depend on the temperature of the vacuum chamber. To reduce secondary electron yield, and therefore the heat load to the cryogenic system, amorphous carbon coating can be applied. Measurements of aC outgassing rates have been carried out in the framework of the HL-LHC project. aC coating will be applied not only in the new triplet areas but also in the half-cells of the arcs presenting high beam induced heat loads

   Unless radiation-hard electronics is developed, vacuum gauge controllers and power supplies have to be installed in a protected area, requiring long high voltage cables. Cost reduction can be achieved by a single power supply used for multiple ion pumps equipped with dispatch boxes and small local cables.

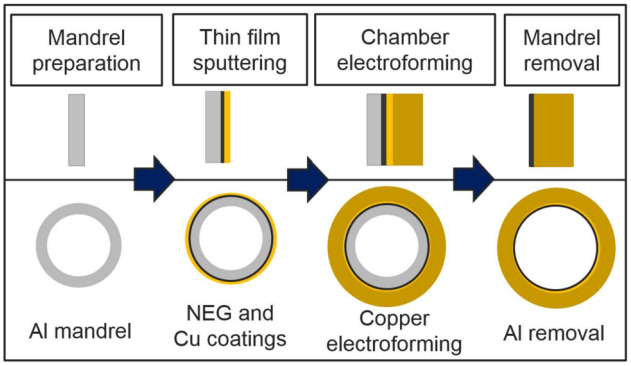

Fig. 41 Electroforming process of low aperture copper vacuum chamber

Fig. 42 Electroformed copper chamber integrating stainless steel flanges

4.7.2 Vacuum developments

Some novel vacuum technologies have been under development to solve particular problems in the CLIC accelerator and are under consideration for other machines and projects.

Low aperture copper vacuum chamber with NEG coating For the low aperture quadrupoles of CLIC, CERN developed copper electroformed vacuum chambers with integrated NEG film coatings [188–191]. This method is based on a sacrificial aluminium mandrel with the required shape on which a thin NEG coating is applied. The vacuum chamber wall in copper is then built up by electrodeposition on top of the NEG film. Finally, the aluminium mandrel is removed by chemical etching. A schematic of the process is shown in Fig. 41. This innovative manufacturing method allows the production of vacuum chambers with very low aperture (down to a few millimetres) while integrating NEG coating, used as a distributed pump and/or low secondary electron yield surface. This procedure can also integrate and join the stainless-steel flanges during the electroforming step. As low as 3 mm diameter coated vacuum chambers were successfully produced using this method (Fig. 42) [192].

Performance of the NEG produced with this method has been assessed. It turned out that the NEG film performance is significantly reduced when the chamber followed a standard activation at 230 °C for 24 hours. Even if the performance is partially recovered in term of activation and CO pumping when an additional temporary copper interlayer is applied between the aluminium mandrel and the NEG film, the H2 pumping speed still exhibits one order of magnitude lower values than expected for standard NEG. Further studies are required to optimize the electroplating parameters and identify possible contaminants in order to recover the full functionality of the NEG film for ultrahigh vacuum applications in accelerators.

Deformable RF bridge Initially proposed for the Drive-Beam interconnections in the Main Linac, the deformable RF bridges have been further developed for the LHC (modules adjacent to collimators) and HL-LHC (interconnection in the triplet areas and modules requiring large transversal displacement). It is based on a deformable thin-walled structure in copper beryllium (Fig. 43), which fulfils different requirements without the need for sliding contacts: longitudinal, angular and transversal movements due to both thermal effects (during bake-out or cool-down) and mechanical misalignments (during assembly, alignment, commissioning and operation phases). Extensive mechanical tests have been done. They show the robustness of the bridge, in particular when subjected to large transverse offset [193, 194]. The first DRF modules have been installed in the LHC during YETS 2023-2024 in critical locations where high beam induced heat loads were observed. So far, after one year of operation, they behave perfectly.

Fig. 43 Deformable RF bridge

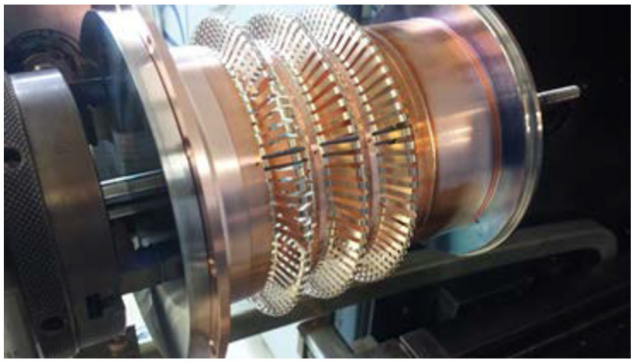

Fig. 44 Error budget for the absolute positioning of the reference axes of components

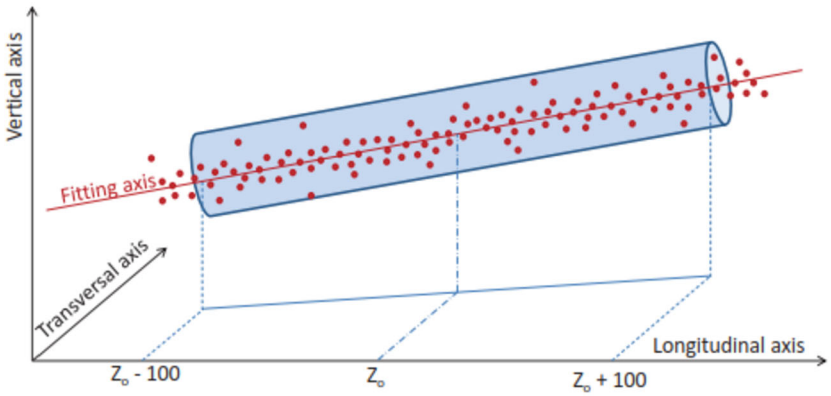

Other novel concepts like Compact Temperature-Controlled UHV Connector based on Shape Memory Alloy [195–197] are being considered for the CLIC machine after successful implementation in the LHC dump for bimetallic connections.

4.8 Survey and alignment

In the updated baseline of CLIC, survey and alignment requirements for 380 GeV are the same as for the 3 TeV layout: an active, remotely controlled pre-alignment for the components of the Main Linac (ML) and Beam Delivery System (BDS); a classical pre-alignment using standard means from large scale metrology, manual jacks and the intervention of technicians in all other areas. The total error budget allocated to the absolute positioning of the reference axes of the major accelerator components (magnetic axis of quadrupoles, electrical zero of BPMs or electro-magnetic axis of RF structures) can be represented by points inside a cylinder over a sliding window of 200 m. Its radius is equal in the ML to 14 µm R.M.S. for MB BPM and RF structures, 17 µm for MB quadrupole and 20 μmfor DB quadrupoles. Further downstream in the BDS its radius is equal to 10 µm R.M.S. over a sliding window of 500 m (see Fig. 44).

Since the CDR [55] deeper studies have been carried out on fiducialisation and initial alignment of components on their common support, leading to a change of strategy for this step; to improve accuracy, efficiency and flexibility. We now have a better knowledge of the sensor configuration needed for each module, following the results obtained on the Two-Beam Test Modules. Two different solutions of supporting and micrometric adjusting have been validated successfully on dedicated test setups. We have also a better knowledge of the accuracy that can be reached on the Metrological Reference Network (MRN) as simulations were confirmed by results on a 140 m long facility.

4.8.1 Determination of MRN

The Metrological Reference Network (MRN) will be installed in the ML and BDS as soon as the tunnel floor is available. It consists of parallel, overlapping stretched wires to provide a straight reference of alignment along the whole length of the tunnel. Wire Positioning Sensors (WPS) are fixed on the same support plate to very accurately define wire-to-wire distances, combined with Hydrostatic Levelling Sensors (HLS) to model the catenary of the wires. This will represent the straight reference of alignment in the tunnel. Simulations have been carried out for

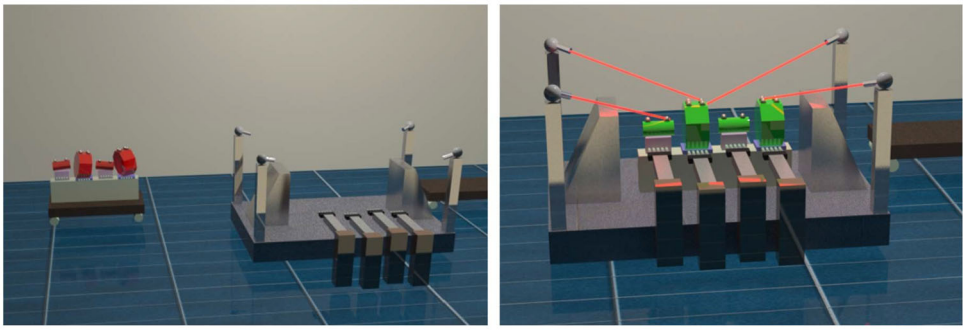

Fig. 45 Automatic initial alignment of the components on their girder assembly

such a MRN [198], considering wires with a length of 200 m and an accuracy of alignment sensors (WPS and HLS sensors) of 5 µm. It was shown that the standard deviation for the position of each component w.r.t. a straight line was included in a cylinder with a radius below 7 µm. This was confirmed experimentally on a 140 m long facility, for the radial position.

4.8.2 Fiducialisation and initial alignment of the components on a common support

In order to facilitate the alignment process in the tunnel, several components are aligned on the same support assembly. In the CDR [55], this was achieved by high-precision manufacturing of the supports and outer surface of the components. As an example, both the outer diameter of RF structures and the V-shaped supports in the girders supporting them, were machined with micrometric accuracy. We initially considered determining the position of the external targets (fiducials) w.r.t. the mechanical axis of the components. A new strategy, however, has been proposed for this fiducialisation and initial alignment of the components on their common support assembly [199], based on results obtained from the PACMAN project [200, 201] and on the development of a 5 DoF adjustment platform [199].

The following sequence is proposed (see Fig. 45):

1. Individual fiducialisation of each component, using techniques developed in the PACMAN project, using a stretched wire which now represents the active access of the component.
2. A 5 DoF adjustment platform is inserted between each component and the girder assembly. All components are roughly pre-aligned on the same girder.
3. The girder is transferred to a measurement marble equipped with Frequency Scanning Interferometry (FSI) heads, to determine with micrometric accuracy the position of the alignment targets of each component in the girder assembly referential frame.
4. Plug-in motors are temporarily connected to the 5 DoF adjustment platforms. Once the position of components is known, the adjustment of each component can take place using these plug-in motors. If all the components are at their theoretical position on the girder, the plug-in motors are disconnected and the girder is stored, being ready for installation. Otherwise, there is an additional iteration of adjustment and position determination.

Such a sequence can be completely automated; it can be performed at the manufacturer's premises, or at CERN in the Metrology lab, or even in the tunnel, provided the FSI heads are installed on a rigid and portable structure. It allows a gain in accuracy and efficiency (an initial alignment can be performed within a few minutes) and allows the possibility of performing alignment checks after transport in the tunnel.

4.8.3 The Support Pre-alignment Network (SPN)

The Two-Beam Test Modules, a full scale mock-up of four CLIC modules, offered the possibility to perform tests on actuators and sensors [201]. This led to a series of modifications for this updated baseline.

Adjustment of girders:

1. The snake configuration, with an articulation point linking two girders, will be kept for the DB side, when there are no discontinuities between girders due to MB quadrupoles (see Fig. 46). In such a configuration, two adjacent girders are interlinked by an articulation point allowing a natural smoothing of the girder and limiting the DoF between girders to three (vertical and horizontal translations and roll rotation). The articulation point will be adjustable, its adjustment being controlled by FSI measurements to an accuracy of less than 5 µm. For such a configuration, three linear actuators, supporting the master cradle, will perform the adjustment [202].

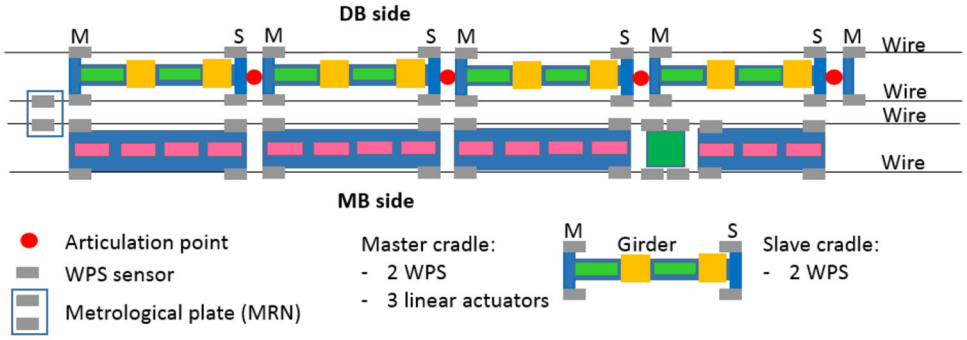

Fig. 46 Sensors configuration for 380 GeV DB option

Table 33 Sensors configuration for 380 GeV DB option

	AS, BPM in µm		MB quad in µm		DB quad in µm	
	(CDR)	(Updated)	(CDR)	(Updated)	(CDR)	(Updated)
Fiducialisation	5 (TBC)		10 (TBC)	10 (TBC)		
Fiducials to pre-ali. sensor interface	5		5			
Pre-alignment sensor accuracy	5	5	5	5	5	5
Sensor linearity	5	5	5	5	5	5
Straight reference	10 (TBC)	7 (rad., vert. TBC)	10 (TBC)	7 (rad., vert. TBC)	10 (TBC)	7 (rad., vert. TBC)
Total error budget	**14**	**11**	**17**	**11**	**20**	**11**

2. For the MB girders and MB quadrupoles, aligned independently, we propose to use cam movers. A configuration of five cam movers was validated for two lengths of quadrupoles: 2 m and 0.5 m, where we showed that the positioning requirements (sensor offsets below 1 µm and roll below 5 µrad) can be met in one movement using feedback from alignment sensors [203–205]. To fulfil the new requirement of micrometric adjustment in the longitudinal direction, we propose to add a sixth cam mover to the system and reorganize the layout of cam movers. The previous prototypes did not meet the MBQ pre-alignment stage stiffness requirement. A new prototype, taking into consideration both the positioning accuracy and stiffness, has been built.

Position determination:

1. Alignment sensors will be installed on girder cradles; cradles and girders being one block, of the same material.
2. The tests performed showed that it was difficult to develop, install and calibrate an absolute inclinometer within a uncertainty of measurement, and that it was far more accurate to use two parallel wires, stretched on both sides of the module, measured by two WPS (one per side of cradle).
3. A redundancy is needed in the configuration of alignment sensors to increase the accuracy of position determination and detect errors. Two additional WPS will be added on the slave cradle of the girder, in case of a snake configuration.

4.8.4 Summary

The collective studies undertaken at several facilities confirm that pre-alignment requirements can be fulfilled in the ML using a combination of WPS and HLS sensors for the determination of the position, linear actuators or cam movers for the adjustment of the component assembly and with a new scenario for the fiducialisation and initial alignment of the components on their assembly, based on the techniques developed in the PACMAN project. The global error budget is summarized in Table 33.

4.9 Ground motion

4.9.1 Introduction

To obtain the desired luminosity of CLIC, very stringent specifications have to be satisfied in term of vibrations [206, 207]. Indeed, a beam with very small emittance is sensitive to all imperfections of the Beam Delivery System

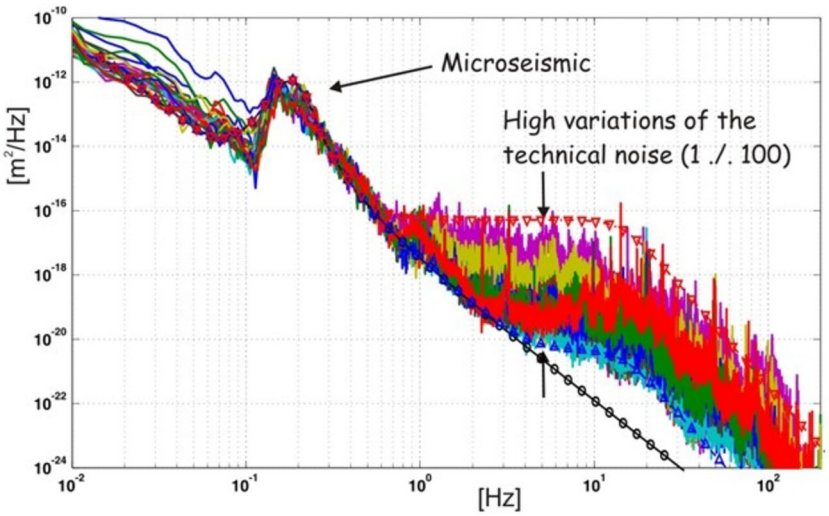

Fig. 47 PSD measurements in the LHC tunnel at different locations [210]

(BDS) and Final Focus System. The Ground Motion (GM) / structural vibrations effects are one of the most critical causes affecting beam brightness and position stability at the Interaction Point (IP). In this section, the GM, its content and its influence on a collider like CLIC are described. The required specific instrumentations and the measurement methods are also detailed.

4.9.2 Ground motion content

Ground motion stems mainly from two sources: the seismic activities (or natural earth motion) and the cultural noise. The seismic activities are basically composed of earthquakes and seismic waves. There are different kinds of seismic waves that move in different ways. The two main types of waves are body waves (can travel through the earth's inner layers) and surface waves (can only move along the surface). Earthquakes radiate seismic energy as both body and surface waves. Seismic activity is a coherent motion and dominates in low frequency range, typically lower than 2 Hz. The second contribution is the cultural noise that results from human activities, whether it is the outside environment like roads, air traffic or internal disturbances like cooling system or vacuum pumps. It is dominant above a few Hertz and is usually not coherent.

Because of the widespread GM issues for large experiments [208], GM collider measurements were already performed worldwide [209]. To consider an environment similar to the foreseen CLIC tunnel, the LHC was selected with measurements at different locations in the tunnel [210] (Fig. 47).

The GM Power Spectral Density (PSD) is basically a steep function of frequency which falls off as $\frac{1}{f^4}$. Above 1 Hz, the cultural noise level depends on the proximity to internal systems or cryogenic pumps for example. Below 1 Hz vibrations are dominated by the earth motion like the micro-seismic peak at 0.17 Hz which is due to incoming sea waves.

At the end, GM induces absolute displacements of about a few dozens of nanometers integrated r.m.s. at low frequency, which is already higher than the requirements for CLIC MBQs and BDS. However, to evaluate the disturbances consequences and the relative motion between the different elements, GM coherence has to be considered. It could be expressed like in equation (1) and a good coherence is equal to:

$$C_{xy}(f) = \frac{|P_{xy}(f)|^2}{P_{xx}(f)\,P_{yy}(f)} \tag{1}$$

Measurements of Fig. 48 show that the motion is coherent over a long distance only in the narrow frequency range around the frequency of the micro-seismic wave (0.17 Hz). Above that frequency, the coherence fades out rapidly and confirms the necessity to manage such vibrations in the mitigation strategy.

From measurements, GM can be simulated and several models are already tuned for different experiments [211] and which could be integrated into a beam dynamic simulation tool like PLACET (Program for Linear Accelerator Correction and Efficiency Tests). The prediction of the GM influence reveals that many accelerator elements, like the quadrupoles, will move independently on a large bandwidth all along the accelerator reducing the performance of the collider [212, 213]. Various control systems and beam controls will be necessary as described in the control section, and all the mechanical design / infrastructure have to be optimized.

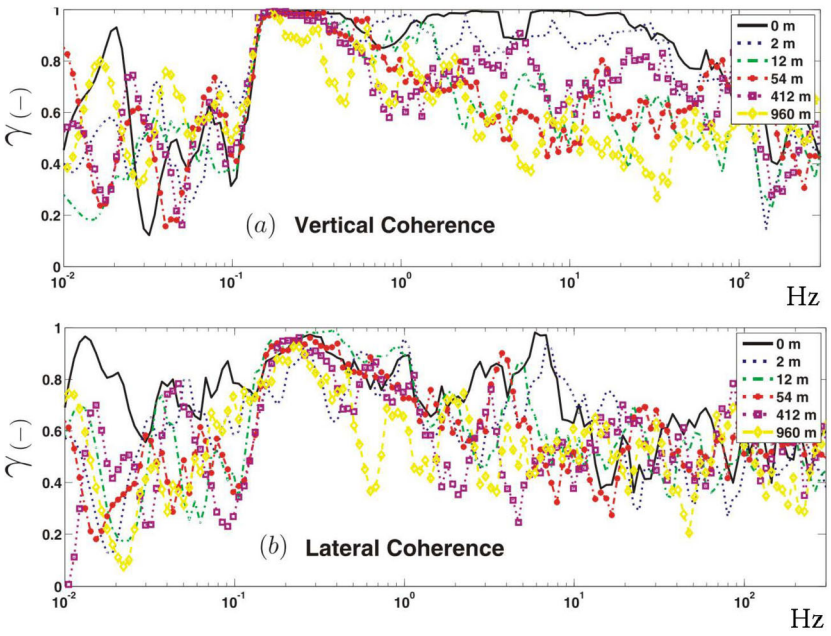

Fig. 48 Coherence measured in vertical and lateral directions [210]

Table 34 Characteristics of common inertial sensors [216–218]

Name	Range [Hz]	Freq. res. [Hz]	Sensitivity [V/(m/s)]	Susp. mass [g]	Size [mm]
GS1	≥1	1	40	700	160 × 75
GS11D	≥4,5	4.5	23	23	33 × 31
L4C	≥1	1	276	1000	76 × 130
STS-2	0.008-50	0.0083	1500		230 × 235
CMG-3ESP	0.03-500	0.03	1000	8	168 × 258
CMG-6T	0.03-100	0.03	2000	2.5	154 × 205
SP500	0.016-75		2000	0.75	$50^2 \times 100$

4.9.3 Available sensors

Given these constraints, it is necessary to be able to measure very low amplitudes of GM and structural vibrations. Consequentially, specific instrumentation is required [214].

To compare the performances of various sensors, the main properties to evaluate are the sensitivity, the resolution and the dynamic range. The sensitivity is the ratio between the real motion *(M)* and its measurement *(V)*, for example the sensor voltage, and could be expressed as $S = \frac{M}{V}$. The noise *(N)* is the part of the signal *(V)* which is not representative of the motion *(M)* and allows to obtain the main critical criteria named resolution *(R)* which is the smallest motion that the sensor is able to measure $R = \frac{N}{S}$. An efficient sensor has very small *(R)* and *(N)* but on a sufficient dynamic range *(DR)* which is a function of the maximal measurable motion taking into account the noise.

In order to evaluate the absolute measurement of the GM (displacement, velocity or acceleration), inertial sensors are the most relevant. The working principle is based on a mass m, linked in the axis direction that one would like to measure via a spring with a stiffness k and a damping c. Among inertial sensors, the geophone is a reliable sensor. In this case, a coil is added around the mass and the motion of the mass inside the coil provides a signal representative of the velocity of the support from a few Hertz to a few hundred Hertz. The limitations of the bandwidth are the characteristics of the mechanical system: the spurious frequencies (high limit) and the fundamental frequency (low limit) [215]. To optimise the measurement in low frequencies, these sensors are managed in a feedback loop: force-balanced accelerometers or broad-band seismometers (Table 34). In this case, the relative displacement of the mass is measured and allows to evaluate the needed coil command to generate a force which compensates the internal mass motion.

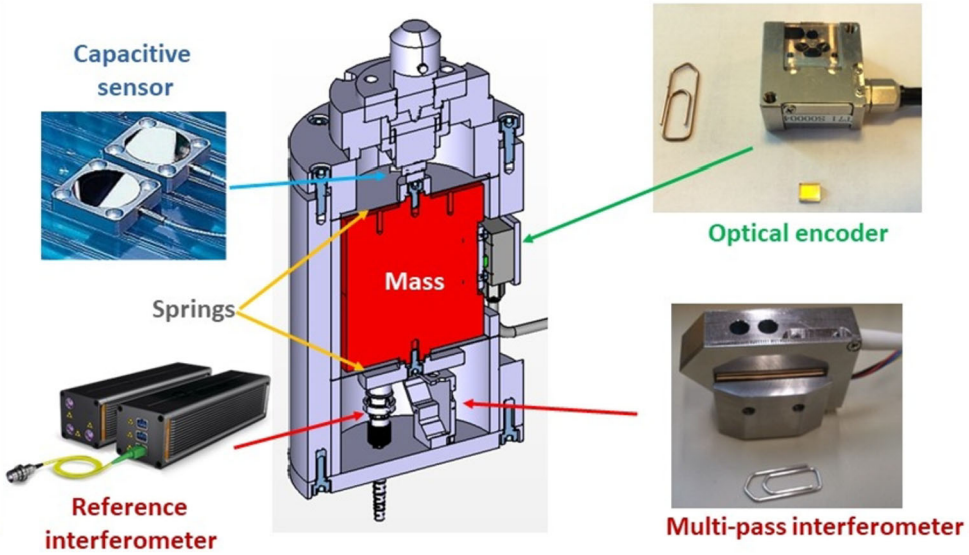

Fig. 49 Comparison measurement technology for the relative motion of the mass [222]

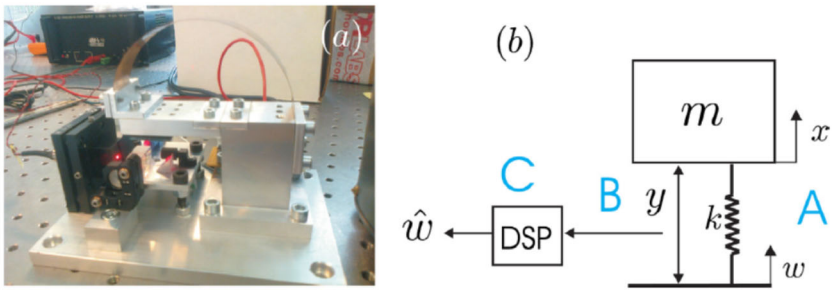

Fig. 50 Picture (a) and schematic (b) of the prototype of the interferometric inertial sensor named NOSE [227]

The last type of sensors is classical broadband accelerometers in which the mass is fixed on piezoelectric transducers [219]. They are well adapted to mechanical structures and infrastructure vibration measurements and could complete in high frequencies the performances of the previously described sensors.

All these sensors are very efficient for GM and / or structural vibrations, but they present two main disadvantages: they are sensitive to radiation and are limited / not dedicated to be integrated into vibration control systems. For these reasons, many specific developments are proceeding to overcome these issues.

4.9.4 Dedicated sensor R&D

Many R&D projects were dedicated to inertial sensors over the past years. The majority were focused on the improvement of commercial geophones for seismic issues [220], but some of them were focused on the application of geophones to the collider environment and its specific aspects [221]. For CLIC, the main recent studies were done at CERN, ULB and LAPP.

The first study was conducted in the innovative doctoral program named PACMAN (Particle Accelerator Components' Metrology and Alignment to the Nanometre scale). One of the topics was to design a new vibration sensor including a comparison of the differential measurement technologies for the internal mass motion [222]. The compared transducers are capacitive sensors [223], optics encoder [224] and interferometers [225] with a multi-pass one [226], as shown in Fig. 49.

Another approach is being carried out by the Université Libre de Bruxelles (ULB) in collaboration with CERN [227, 228]. The classical spring mass of the inertial sensor is replaced by an internal beam - pendulum in cantilever mode and the beam relative motion is measured by interferometry, Fig. 50. Such a setup allows for optimising the Eigen-Frequencies (avoiding as much as possible the spurious ones, increasing the resolution and being efficient in a vibration control system), decreasing the thermal noise and improving the resilience in magnetic environment. In this setup the instrumentation noise is reduced with respect to classic inertial sensors (Fig. 51) and satisfies the vibration control requirements.

Yet another approach has been conducted at LAPP. A specific vibration sensor (patent n° FR 13 59336) has been designed (Fig. 52) [229]. It is based on an internal mass-spring-damper system and a capacitive sensor,

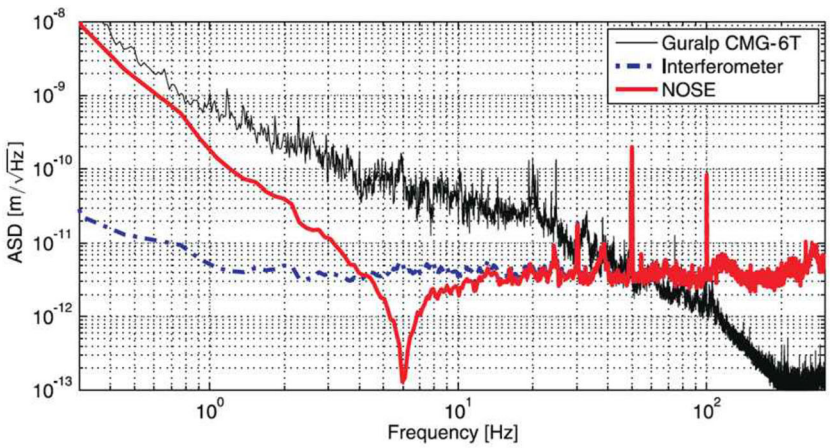

Fig. 51 Measured resolution from experimental sensors: Guralp CMG-6T (two sensors side by side in a quiet environment); estimated resolution of the NOSE prototype, measured by blocking the inertial mass [227]

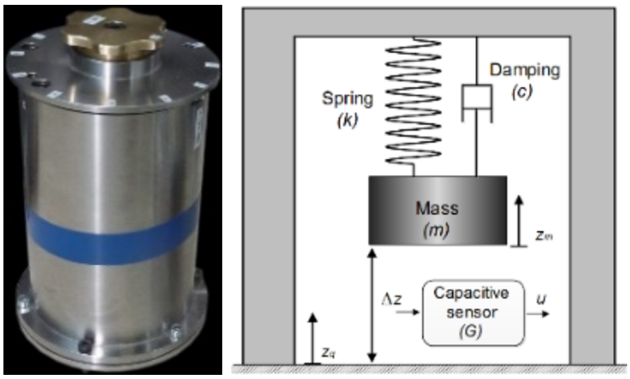

Fig. 52 LAPP sensor image and layout [229]

Table 35 Sensor Bandwidth and Noise Level [229]

Sensor	Bandwidth [Hz] (constructor data)	Effective bandwidth [Hz] (measured)	Noise level R.M.S. @ 4 Hz [nm]
CMG-6T	0.03-100	0.1-0.8 U 4-60	0.1
731-A	0.01-500	8-150	0.5
LAPP	0.1-3000	0.1-100	0.04

which gives the relative motion between this mass and the GM. The GM can be deduced by the sensor's dynamic $L(s) = \frac{u(s)}{z_g(s)}$, through Equation (2).

$$L(s) = G\frac{\frac{1}{{\omega_0}^2}s^2}{1+\frac{2\xi}{\omega_0}s+\frac{1}{{\omega_0}^2}s^2}, {\omega_0}^2 = \frac{k}{m},\ \xi = \frac{c}{2}\sqrt{\frac{1}{m.k}},\ f_0 = \frac{\omega_0}{2\pi} \tag{2}$$

Comparative measurements were performed simultaneously with inertial sensors in a very well adapted environment, which guarantees the quality of the GM coherence. Each sensor's noise, calculated by using the corrected difference method [230], has been characterized by measuring the seismic motion with two sensors of the same model placed side-by-side. The effective bandwidth of each sensor (i.e. the ability of the sensors to measure the seismic level in a specific environment) measured at LAPP is shown in Table 35 and Fig. 53.

Note that this sensor was processed in a dedicated active vibration control system [231]. The control strategy has been optimized by using only one LAPP sensor in a FB loop instead of using up to four sensors for feedback and feedforward. A damping ratio of 8.5 has been achieved at 4 Hz, leading to an r.m.s. displacement of the support of 0.25 nm [232], very close to Final Focus CLIC specification (0.2 nm at 4 Hz).

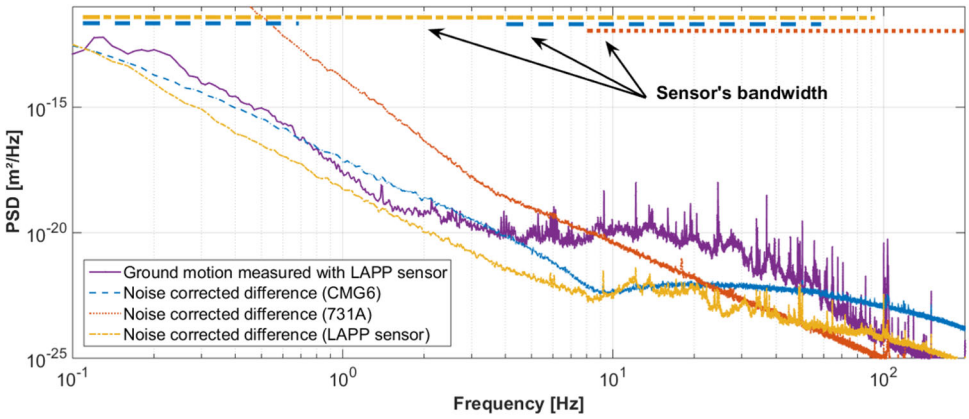

Fig. 53 PSD of the seismic motion measured with LAPP sensor - Experimental measure of the noise of CMG-6T, 731-A, and LAPP sensor [229]

4.9.5 Conclusions

The worldwide GM measurements confirm that the GM mitigation is a critical aspect to the CLIC feasibility. However, the GM spectrum is relatively well known and could be simulated in order to design and develop the control system / beam. Additionally, the outcome of various sensor developments allows for overcoming the limitations of the current commercial sensors in an accelerator environment.

4.10 Stabilisation

4.10.1 Introduction

Dynamic imperfections in the Main Linac, Beam Delivery System (BDS) and Final-Focus (FF) magnets lead to luminosity loss. Ground motion and vibrations that generate motion of the magnets and their field centre create such imperfections. The integrated R.M.S. $\sigma_x(\mathrm{f})$ [233] of the spectral density $\Phi_x(\mathrm{f})$ of absolute displacements of the magnetic field center of the quadrupoles is the first quantity to be observed. As a first approximation, the integrated R.M.S. displacement above 1 Hz shall stay below 1.5 nm in the vertical direction and below 5 nm in the horizontal direction for all Main-Beam Quadrupoles (MBQ). For the FF magnets, the integrated displacement above 4 Hz shall remain below 0.14 nm in the vertical plane.

The magnetic field displacements can be created by ground motion transmitted through the magnet supports and by forces arriving directly on the magnet by e.g. water cooling. Information from several measurement campaigns and models of ground motion are available in Sect. 4.9 and in literature [210, 233–236]. This first quantity $\sigma_x(\mathrm{f})$ is only a measurement at one point over the length of an accelerator. The relative motion between quadrupole magnets at different points is also a significant factor quantified by the correlation or coherence between the different points [210, 233]. The lowest frequency seismic vibrations with a long spatial wavelength move the whole accelerator lattice as a rigid body with little effect on performance if the magnet supports are sufficiently stiff. The higher frequency vibrations in ground motion will have a shorter wavelength that will create relative motion between the lattice components. The propagation from local technical vibrations and their attenuation over distance is also rather well known and was measured near the LHC in operation [237]. An inventory of possible vibration sources acting as direct forces were studied and measured [238–240].

4.10.2 Overall strategy to reach the required stability

The approach to reach the required vibrational stability combines the selection of the site with appropriate geological characteristics and seismic background, the minimization of technical noise sources in and around the CLIC tunnel and finally the use of a mechanical active vibration stabilization system.

By adapting the civil engineering of the tunnel and cavern by, for instance, placing machinery on a separate floor structure [241] or the use of adapted technical concrete, the length of the vibration path and hence the attenuation of the vibrations will be improved. Vibration dampers can be used under the machinery. The depth of the tunnel will reduce the vibrations created at the surface.

Resonant frequencies of poorly damped mechanical structures will be excited by any broad band excitation (ground motion, water cooling, acoustic noise and ventilation) and this can create significant local vibration sources. This was nicely demonstrated at the accelerator test facility ATF2 where beam jitter was reduced significantly after identification of two vibration sources created by poorly supported water pipes [242]. Another demonstration can

Table 36 List of prototypes that reached the requirements

Prototype	Integrated R.M.S. (nm)	R.M.S. Ratio	Set-up	Remark
1. Membrane one d.o.f [207]	0.3 (1 Hz) 0.6 (1 Hz) 0.2 (4 Hz)	Ratio 6 Ratio 10 Ratio 8.5	FF+FB Analogue	Down scaled
2. Tripod [248]	0.9 (1 Hz) 0.7 (4 Hz)	Ratio 2-2.5	FB Digital	Down scaled
3. Two d.o.f. x-y [207]	0.5 (1 Hz)	Ratio 9	FF + FB Analogue Hybrid	Real scale
4. Magnet tripod [207]	0.45 (1 Hz) 0.35 (4 Hz)	Ratio 13.3	FF + FB Analogue Hybrid	Real scale, Measured with nominal magnet field and cooling water flow
5. LAPP [232, 249]	0.25 (4 Hz)	Ratio 8.5	FB Digital	Down scaled

be found in [237] where oscillations of the beam orbit were created by exciting support modes of the Final-Focus magnets. Therefore, the design of all components and supports in the CLIC tunnel shall have natural frequencies as high as possible by careful design. Also a verification with seismometers during the construction phase will help to remove unwanted vibration sources. The most significant consequence is the beam height from the floor that shall be as small as possible. Where possible, the mass of the components shall be reduced and also the position of support points can increase the stiffness of components (Airy points).

4.10.3 Vibration stabilization system studies

From the different measurement campaigns in different particle accelerators [210, 234, 235] and as described in the CDR [55], a vibration isolation system is needed to reach the specified stability levels. A survey of existing vibration stabilization or isolation systems in various fields of precision engineering was performed [243, 244]. Studies were carried out at CERN and at LAPP (Annecy) and ULB (Brussels) and prototypes have been constructed.

The very stringent alignment requirements and the presence of forces acting directly on the MBQ (water-cooling, acoustic noise, vacuum pipes and electrical cabling) as well as the low frequencies for stability, resulted in the choice of active stabilization [245, 246] for the 4,000 Main-Beam Quadrupoles (MBQ). Active stabilization is based on a stiff actuating support that reduces the compliance for the direct acting external forces mentioned above. The use of stiff piezo actuators gives an additional possibility to make fast repositioning of the magnets possible in between beam pulses (every 20 ms) with a high resolution; so-called nano-positioning [247, 248]. Five prototypes were built with increasing complexity, mass and degrees of freedom. The first four prototypes in Table 36 (with references for complete information) all reached the requirements with commercially available piezo actuators and seismic sensors. Prototype 4 is a MBQ (type 1) prototype magnet with nominal magnetic field and water cooling that reached the requirements from a higher vibration back ground (R.M.S. ratio). The last MBQ prototype (Fig. 54) is a complete, fully integrated stabilization system with type 1 MBQ with the same measured transmissibility as prototype 4 but that was not yet tested in a low vibration background (not in Table 36).

The FF magnets are supported by a cantilevered structure in the particle detector and their stabilization require a higher level of integration with the surrounding infrastructure. Different approaches were studied [229, 250] with or without passive components. Prototypes were built with specially developed sensors [232, 249, 251] or using stiff carbon tie rods for active damping [252]. Two prototypes were measured with a low vibration back ground and came very close to the requirements (number 1 and 5 in Table 36).

The success of studies and prototype with respect to integrated r.m.s. displacement will depend on the resolution/noise level and controller stability that can be reached with the combination of sensors, actuating structures, controller and electronics. Some of the studies not reaching the integrated r.m.s objective have however also demonstrated more stable and hence more reliable controllers with for instance the use of collocated force sensors [244, 252] or systems that have components better adapted to the accelerator environment (radiation).

The measured transmissibility or transfer functions of the prototypes were used to estimate the luminosity that can be obtained with the respective stabilization strategies [212, 253, 254]. These studies indicated that the shape of the transmissibility function is more important for the luminosity than the obtained integrated r.m.s. displacement. This understanding has triggered the development of more adapted sensors for the stabilization (see Sect. 4.9) and defined a new luminosity objective for the combined control systems (stabilization and beam).

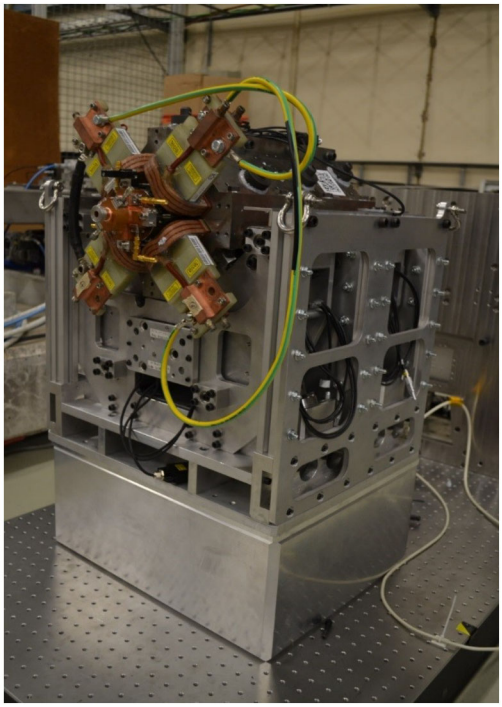

Fig. 54 Main Beam Quad type 1 stabilization prototype

4.10.4 The QD0 stabilisation system

One of the most critical elements in terms of stabilization is the final focusing quadrupole QD0, which is positioned on the tunnel floor, just outside the detector. It focuses the vertical beam size down to about 2.9 nm r.m.s. The distance L* of the downstream end of this quadrupole to the IP has been chosen to be 6 m, the shortest distance compatible with detector space requirements. Any movement of the quadrupole in the transverse plane would affect the transverse position of the beam at the IP by a comparable amount. Therefore, the quadrupole has to be mechanically stabilised to 0.3 nm r.m.s. in the vertical plane for frequencies above 4 Hz. The IP feedback system complements the stabilisation system at lower frequencies. It measures the position of the outgoing beam and applies a calculated kick to the incoming beam in order to optimise luminosity. Bunch-to-bunch correction is not possible, but the latency loop of the system is short enough to allow several iterations during the 156 ns bunch train. An active pre-alignment system ensures that the average position of the QD0 is correct to within 10 µm with respect to the other BDS elements.

An intense R&D program, including the development of custom-made new sensors and an active support, has allowed to reach stabilisation at the 0.25 nm r.m.s. at 4 Hz and above [249]. The result of the measurements is shown in Fig. 55. Therefore, a pre-absorber is no longer needed (or could in the worst case be implemented with existing commercial solutions rather than with a specific development).

4.10.5 Readiness for CLIC

The work described above shows that the required level of magnet field centre stability can be reached on scaled or real size prototypes in a laboratory environment. Most equipment used was commercially available or the components that were developed in house are technologically well within reach. Also the integration with other CLIC systems seems technically possible. The studies and prototypes built by different teams also brought forward the following common factors:

- Piezo actuators combine the required stiffness with the needed sub nano-metric resolution and suitable band width. It is the technology that is commercially most available. Piezo actuators are non linear actuators with hysteresis, this is linearized by special piezo amplifiers.
- High resolution vibration sensors are based on the measurement of an inertial mass with a coil, capacitance measurement, laser interferometer or optical encoders.
- Controller hardware: digital or analogue (hybrid) circuits requiring special care for phase margin in the control (ADC delay, impedance problems).
- Low frequency input and output signals with a high dynamic range.

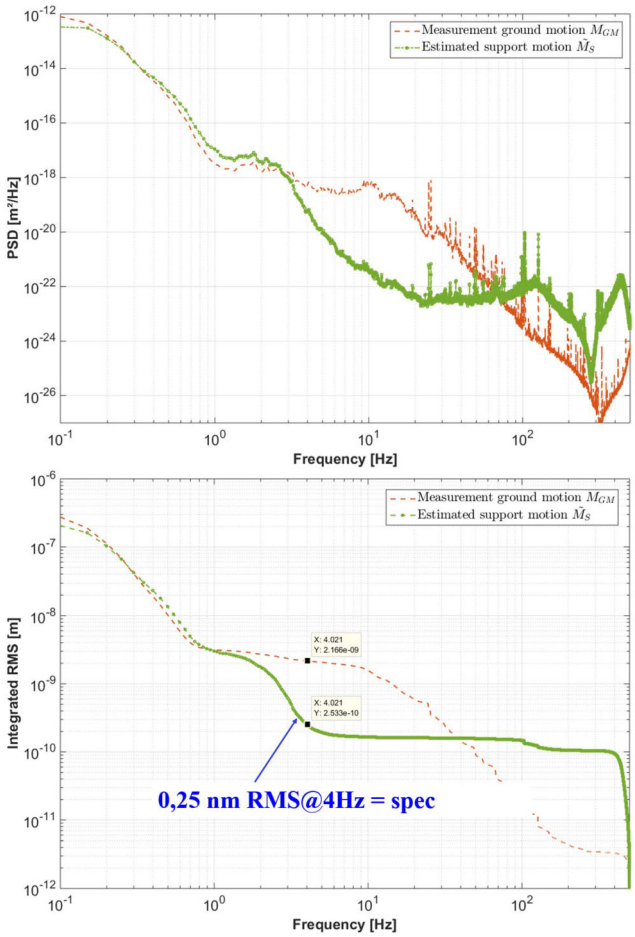

Fig. 55 The measurements of the new stabilisation with and without the QD0 stabilisation system. On the left hand side the PSD, on the right hand side the integrated r.m.s. achieved

Most of these factors call for short cable lengths, i.e. the controller hardware (amplifiers, conditioners and controller) shall be near the stabilization system. This is not evident in an accelerator tunnel with radiation. Complete shielding against radiation in high energy particle accelerators is difficult and would be expensive. It seems, therefore, that we will be required to develop and test radiation hard components and at the same time to develop components that can deal with longer cable lengths.

4.11 Beam transfer

4.11.1 Main Beam: Damping Ring Kicker systems

To achieve high luminosity at the interaction point, it is essential that the beams have very low transverse emittance: the Pre-Damping Ring (PDR) and Damping Ring (DR) damp the beam emittance to extremely low values in all three planes. In order to limit the beam emittance blow-up, due to oscillations at extraction from the DR, the combined flat-top ripple and droop of the field pulse must be less than $\pm$ 0.02%. In addition, the total allowable beam coupling impedance, in each ring, is also very low: 1 $\Omega \times n$ longitudinally and 10 MΩ/m transversally. This section discusses means for achieving the demanding requirements for the DR kickers. Table 37 shows the specifications for the DR extraction kicker system.

To achieve the demanding specifications for low beam coupling impedance, striplines will be used for the DR extraction kickers [73, 83]. Striplines have both an odd and an even mode impedance: the odd mode is when both electrodes are driven to opposite polarity voltages, to extract beam from the DR, whereas the even mode is when the electrodes are at the same potential, e.g. not driven by pulse generators. The characteristic impedance of both odd and even modes should ideally be optimized to 50 Ω. However, for coupled electrodes this is not possible to achieve [73, 83]. Existing designs of stripline electrodes, e.g. [255–257], could not achieve the demanding specifications. Hence a novel electrode shape has been developed for the CLIC DR extraction kicker that achieves the excellent field homogeneity, good matching of both odd and even mode characteristic impedances, and a decrease in the beam-coupling impedance at low frequencies [73].

Table 37 DR Extraction Kicker Specifications

Parameter	DR
Beam Energy (GeV)	2.86
Deflection Angle (mrad)	1.5
Aperture (mm)	20
Field maximum rise and fall time (ns)	1000
Pulse flat-top duration (ns)	∼160 or 900
Flat-top reproducibility	$\pm 1 \times 10^{-4}$
Stability	$\pm 2 \times 10^{-4}$
Field inhomogeneity (%), over 1 mm radius	$\pm 0.01^{*}$
Repetition rate (Hz)	50
Available length (m)	∼1.7
Vacuum (mbar)	$10^{-}10$
Pulse voltage per stripline (kV)	±12.5
Stripline pulse current (A)	±309

To achieve the aforementioned requirements, various shapes of electrodes were studied and optimized. In addition the electrode supports, feedthroughs, and manufacturing tolerances were studied. A novel shape of electrode, called a "half-moon electrode", was selected as the optimum shape [73]. For the DR extraction striplines, manufactured with the optimized half-moon electrodes, the odd mode characteristic impedance is 40.9 Ω. Since an inductive adder will be connected to each electrode with commercial coaxial cable of 50 Ω impedance, and each electrode will be terminated with 50 Ω, there is an impedance mismatch for the odd mode at both the input and output of the electrodes. A mismatched odd mode impedance can significantly influence the striplines performance: predictions for the influence of the odd mode characteristic impedance upon the contribution of each field component, electric and magnetic, to the deflection angle, have been presented in [258]. A new idea has been proposed to match the load side characteristic impedance for both the odd and even modes of excitation of the striplines [73].

The maximum field inhomogeneity allowed is ± 0.01%, over 1 mm radius (Table 37), although a radius of 0.5 mm has also been accepted from beam optics considerations [259]. The magnetic field homogeneity for different frequencies, for the optimized stripline geometry, has also been studied [258].

Stripline kickers are generally assumed to have equal contributions from the electric and magnetic field to the total deflection angle, for ultra-relativistic beams. Hence, the deflection angle is usually determined by simulating the striplines from an electrostatic perspective. However, recent studies show that, when exciting the striplines with a trapezoidal current pulse containing high frequency components, the magnetic field changes during the flat-top of the pulse, due to eddy currents induced in the stripline electrodes, and this can have a significant effect upon the striplines performances [258]. The variation of the magnetic field during the pulse flat-top, and its effect upon the deflection angle, has been presented in [260]. The solution proposed to compensate for this variation is to modulate the pulses created by the inductive adders [261] which will power the striplines.

A first prototype of the extraction kicker for the CLIC DR has been designed and built. The beam coupling impedance of the striplines has been studied analytically, as well as numerically with CST Particle Studio followed by measurements in the laboratory. A new approach for understanding the dipolar component of the horizontal impedance has been derived, when considering both odd and even operating modes of the striplines. This new approach, presented in [262], has been used to understand the differences found between the predicted transverse impedance and the two wire measurements carried out in the laboratory for the prototype CLIC DR striplines.

In order to complete its characterization, the prototype stripline kicker has been installed in one of the medium straight sections, of the ALBA Synchrotron, to be tested with beam [74]. The main purposes of these tests are to measure the beam impedance and DC electric field homogeneity for comparison with predictions from simulations. However, during conditioning of the electrodes, with circulating beam, pressure increased with beam current: this unexpected behaviour of the pressure might be related to ion instabilities and requires further studies. Since the performance of the striplines under these conditions is not compatible with user operation, the striplines have to be removed from the ring during user operation and are only installed for measurements on the striplines – this has limited the time available for measurements, but some initial measurements have been carried out nevertheless [74].

The DR extraction kicker has very demanding specifications: the combined flat-top ripple and droop of the field pulse must be within ± 0.02%. In addition, the flat-top repeatability must be within ± 0.01% (Table 37). An inductive adder has been selected as a contender for achieving the demanding specifications for the DR extraction

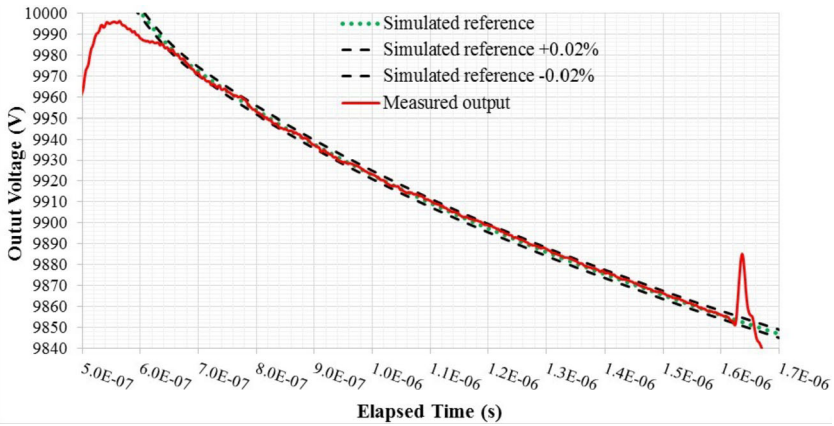

Fig. 56 Simulated optimum waveform for the CLIC DR extraction kicker (green) with ± 0.02% stability margins (black), and an average of 100 measured pulses (red) of the prototype inductive adder

kicker modulator [261, 263–266]. The inductive adder is a solid-state modulator, which can provide relatively short and precise pulses: it is modular and thus the design can be adapted to various requirements.

An inductive adder consists of multiple layers, each of which has a transformer: the transformer usually has a 1:1 turn ratio in order to ensure that it is suitable for fast pulses. The single turn primary totally encloses a magnetic core; hence, the leakage inductance of this geometry is negligible [267]. The secondary winding of each of these transformers is connected in series: hence a step-up voltage ratio of 1:N is achieved by using N-layers, with adequate voltage isolation. The primary circuit typically has many parallel branches: each branch generally contains a single capacitor and a single power semiconductor switch. All the power semiconductor switches and gate drive circuits are referenced to ground and there are no electronics referenced directly to the high-voltage output pulse. In general, the capacitors of all the layers can be charged with a single power supply – this is not, however, necessary and in some applications the capacitors are deliberately charged to different voltages to allow modulation of the output pulse [268]. Each layer has an array of clamp diodes which carry magnetizing current from the core following turn-off of the power semiconductor switches in the layer [264].

An inductive adder has good built-in fault tolerance and redundancy, because if one or more solid-state switches of a layer of the inductive adder stack fails to turn-on, the magnitude of the output pulse of the inductive adder is reduced by, at most, only the voltage of a single layer. Since the inductive adder is of a modular design, extra layers can be added to improve redundancy and/or increase voltage rating. In addition, the modular construction allows for a good scalability, adaptation of individual components to the particular application, and a path for future upgrades.

Considerable research and development has been carried out on the inductive adder for the CLIC DR [261, 263–266]. A significant advantage of the inductive adder over some alternative technologies is the ability to modulate the output [267]. Recent measurements on a prototype inductive adder show that the flat-top stability achieved by applying modulation was ± 0.02% (± 2.2 V) over 900 ns at 10.2 kV output voltage. This pulse meets the stability specifications for the 2 GHz (baseline) and 1 GHz specifications for the DR extraction kicker.

As mentioned above, exciting the striplines with a trapezoidal current pulse results in induced eddy current in the electrodes. This causes the magnetic field to increase in amplitude during the "flat-top" of the current pulse [260]. The solution proposed, to compensate for this variation, is to modulate the pulse created by the inductive adder: a controlled decay-waveform is required [261, 266]. Figure 56 shows a simulated reference controlled decay waveform (green) with error margins for stability of ± 0.02% (black): the measured waveform (red) is within the ± 0.02%, for more than 900 ns, with respect to the simulated reference waveform. This fulfils the 1 and 2 GHz specifications for the CLIC DR extraction kicker system.

As a result of the low source impedance, the source voltage of an inductive adder does not need to be doubled, unlike a matched impedance Pulse Forming Line (PFL) or Pulse Forming Network (PFN). The solid-state switches typically used in the inductive adder are either metal-oxide-semiconductor field effect transistors (MOSFETs) or insulated-gate bipolar transistors (IGBTs). These solid-state switches can be opened when conducting full load current, hence only a portion of the stored energy is delivered to the load during the pulse: therefore a PFL or PFN is not required. In addition, opening of the solid-state switches potentially limits the duration of fault current in the event of a magnet (load) electrical breakdown. Hence the inductive adder is also seen as a promising technology for use in existing CERN kicker systems [269, 270], where a suitable replacement for PFL cable is challenging to purchase these days, as well as for possible future kicker systems at CERN, e.g. for injection systems of the Future Circular Collider [271, 272]. As a result of the use of magnetic cores for the transformer [264], a drawback of the inductive adder is its limitations concerning the available pulse duration: however many kicker magnet applications at CERN require pulse durations of only up to 2.6 µs, which is achievable with the discussed design.

4.11.2 Conclusions and future work

A novel shape of stripline electrodes has been designed to meet the demanding CLIC DR extraction kicker requirements for field homogeneity and low beam coupling impedance: this shape also results in reasonably close values for odd and even mode impedance. Nevertheless, to match the odd mode impedance an additional resistor is proposed to be connected on the output of the striplines, between the electrodes. Detailed studies show that, during field rise and fall, eddy currents are induced in the electrodes, which modifies the deflecting magnetic field. To compensate for this the output pulse of the inductive adder can be modulated – this modulation has been demonstrated. The striplines have been prototyped, and beam coupling impedance measurements carried out. The prototype electrodes have recently been installed in the ALBA synchrotron and initial measurements carried out to characterize the field homogeneity and beam coupling impedance. Detailed characterization of the striplines, in an accelerator, is required to validate the predictions for the longitudinal and transverse beam coupling impedance and field uniformity.

Measurements of the output pulse of the inductive adder show a stability for a flat-top of $\pm 0.02\%$, over 900 ns, for a 10.2 kV pulse. For the controlled decay waveform, the measured stability was $\pm 0.02\%$, with respect to the simulated reference waveform, for 900 ns duration at 10 kV: this stability meets the requirements for the CLIC DR extraction kicker, at approximately 80% of nominal voltage. Tests and measurements are ongoing and the output pulse voltage will be increased to 12.5 kV in the near future. In addition, a second inductive adder has been constructed: the polarity of the output pulse is changed by moving the output connector from one end of the inductive adder to the other. Furthermore, work is ongoing to develop the necessary control system, and an automated way to modify the analogue modulation to achieve the required shape and stability of the deflection waveform. Commercial terminating resistors have proved to be unreliable for the pulse loading. Hence, suitable terminating resistors, for use with the inductive adder, have been designed: these will be manufactured in the near future and tested with the striplines and inductive adder.

The striplines will be tested in the laboratory with pulses of up to ± 12.5 kV, using both inductive adders: long-term testing is required to verify the reliability and response during fault conditions. In addition, it is highly desirable that the striplines and inductive adders are fully tested together with beam: a single bunch could be used to scan through the flat-top and verify the deflection stability and repeatability of the flat-top. Such a flat-top measurement is considered essential to confirm the predictions for the required controlled decay waveform, to achieve a flat-top deflection pulse, and addition as it is not possible to guarantee the absolute precision of the electrical measurements.

4.12 Normal conducting electro-magnets and permanent magnets

4.12.1 Introduction

Even though the size of the initial stage of CLIC at 380 GeV is substantially smaller compared to the 3 TeV final machine, the number of normal-conducting Electro-Magnets (EM) and Permanent Magnets (PM) to be produced will stay well beyond the quantities produced so far for particle accelerators. Therefore the industrialization, cost optimization, quality control, assembly, and installation of such large numbers of magnets will be one of the major challenges of the project. Latter stages concern the Main Linacs and their long transfer lines, but the global layout and beam output energy of the Drive Beam and Main-Beam Injector systems are required for the initial phase. During an intensive R&D design campaign, various magnet types have been designed with numerical methods to assess their feasibility and evaluate their dimensions, power consumption, and cost. More than 15 prototype magnets have been manufactured for the technically most challenging configurations. The outcome of this R&D program is summarized in a magnet catalogue which has been used to select most of the magnetic elements of the new lattices for the various parts of the 380 GeV machine.

4.12.2 Drive-Beam magnets

Quadrupoles in the decelerator Two versions of quadrupoles have been developed in parallel for the Drive Beam: a conventional electro-magnet (EM) version, and a tuneable permanent magnet (PM) version.

A prototype of the EM version is depicted in Fig. 57. The parameters and performance of the EM version have already been presented in the CDR [55] as well as in several other papers [273]. Since the CDR, this design is the baseline and several prototype units have been manufactured, which confirmed the design parameters and achievable tolerances. Some of these magnets have been installed in the CLIC Test Facility (CTF3) for further studies with beam.

As an alternative to the EM version, a PM version has been extensively developed in collaboration with the STFC Daresbury Laboratory in the UK [274–276]. The obvious advantage of this solution is the major savings in

Fig. 57 A drive-beam decelerator quadrupole electro-magnet prototype

electrical power and cooling requirements. However, as the field gradient scales after each Two-Beam module all along the decelerator, up to a factor of 10 for the 3 TeV machine, two types of mechanically tuneable permanent magnets are needed. The first, the High Gradient PMQ, covers the first 60% of the energy range, while the Low Gradient PMQ covers the last 40% of the energy range. The mechanical adjustment of the gradient is piloted with a stepper motor which controls the positioning of the permanent magnet blocks via transfer gearboxes. The challenge resides in the accuracy and stability of the mechanical parts, as well as in the stability of the permanent magnet field.

Prototypes of both High and Low Gradient magnets have been built and measured at STFC Daresbury Laboratory (see Fig. 58), confirming the feasibility of this concept. For the 380 GeV version, the High Gradient type will be sufficient to cover the whole energy range of the decelerator. Since 2014, the STFC Daresbury Laboratory has continued the development of the PMQ designs to further improve their performance, stability while reducing the manufacturing costs by revisiting in particular the motion system, permanent magnet blocks and by reducing the number of components. With these improvements, the design is now considered mature and cost optimized. It has been proposed to change the baseline from the EM version to the PM version for the construction of these magnets. Such a decision is, however, subject to the assessment of the PM material stability in the radiation conditions of CLIC. A survey of results from studies on the radiation damage to PM materials has been carried out [277] and will be used to analyse the criticality of this decision.

Beam transport magnets The lattices of the DB transport complex – which include the combiner rings, delay loop and transfer lines have been reworked to allow standardization of the magnets. About 90% of the new layout is using magnetic elements from the original magnet catalogue. The rest corresponds to some quadrupoles and sextupoles which exceed the current capabilities of the magnets and whose design needs updating. This is also the case for the dipoles in the Turn-Arounds (TA) for which the optics have now adopted combined function magnets. A bespoke magnet design will be developed once the specifications are frozen.

4.12.3 Main-Beam magnets

Main-Beam linacs The Main-Beam Linacs' magnetic lattice foresees the focusing of the e^+ and e^- beams with two types of MBQs electro-magnets which have a similar cross section but different magnetic lengths (see Table 38). The performances in terms of precision of pole shape and quadrants assembly have been achieved in a 2 m long prototype magnet developed for the final energy [278]. Therefore the only remaining challenge expected for

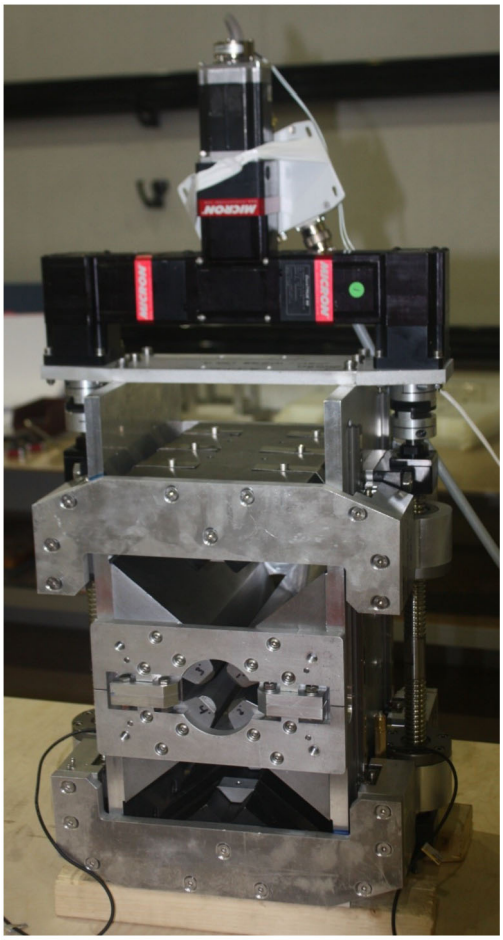

Fig. 58 Prototype of the drive-beam decelerator quadrupole permanent magnet, with optimized design

this type of magnet is the optimization of the production process considering the large quantity of units to be produced.

At the end of each quadrupole a short laminated electro-magnet dipole is attached, and is capable to steer the beam in one plane. A similar approach as for the MBQs has been adopted, with an identical cross section but two different lengths to cope with the increasing energy of the beam along the linac. The evaluation of possible coupling effect between the two magnets is in progress.

Main-Beam transport The Pre-Damping Ring (PDR) and Damping Ring (DR) lattices use mostly electro-magnetic magnets. A special type of dipole with varying aperture along its length is needed in the damping rings to decrease beam emittance. A prototype of this magnet is presently under development with CIEMAT in Spain. This magnet will allow a reduction in the total circumference of the damping ring of 13% for the same performance as the previous version. The concept is being applied to the upgrade of light sources like the ESRF, but the CLIC prototype goes beyond, as it is a tuneable permanent magnet combining dipole and quadrupole components, with an ultra-high field of 2.3 T at its centre (see Fig. 59).

For the Ring to Main Linacs (RTML) beam transport, the main change concerns the number of quadrupoles in the Long Transfer Lines (LTL).

Beam Delivery System (BDS) The baseline QD0 magnet design is based on an hybrid design, combining coils and permanent magnets and described in detail in the CDR [55]. It has in the meantime been validated in the lab by a short, 100 mm long, prototype. It reached a gradient of 531 T, as expected slightly lower than the nominal gradient as the rising fields at the edges are not yet saturated at the centre of this very short magnet. The field quality was within specification as documented in [279–281].

A photo of the prototype is shown in Fig. 60. The optics studies for the Beam Delivery System have shown that the approx. 5 m long quadrupole can be split into two or three shorter magnets without significant loss of luminosity, as long as the coil ends can be kept short.

After the CLIC rebaselining, the installation of the QD0 magnets on the tunnel floor rather than inside the detector, considerably simplifies many aspects of the machine detector interface. Also, the maximum gradient has

Table 38 List of magnet types for both 380 GeV and 3 TeV

	380 GeV		3 TeV	
	No. variants	No. units	No. variants	No. units
Dipoles				
Combined function	3	160	-	-
Bending dipole	3	152	4	1028
Quadrupole	4	796	4	5451
Sextupole	3	644	3	1804
Corrector dipole	1	796	3	3813
Main-Beam Linac				
MBQ Quadrupole	2	1148	4	4020
Corrector dipole	2	1148	4	4020
DBQ Quadrupole	1	5952	1	41400
Damping Rings				
Combined function	1	180		
Bending dipole	1	76		
Quadrupole	6	1240		
Sextupole	2	636		
Skew quadrupole	2	580		
Corrector dipole	2	1228		
Ring to Main Linac Transport				
Bending dipole	5	718	5	708
Quadrupole	9	1674	10	1747
Sextupole	2	541	2	536
Beam Delivery System				
Bending dipole	12	206	12	206
Quadrupole	63	134	63	134
Sextupole	8	30	8	30
Octupole	2	2	2	2
Post Collision Line				
Bending dipole	5	18	5	18
Total	139	18059	130	64917

been reduced from 575 T to 25 T for 3 TeV and considerably smaller for the 380 GeV phase and it is now also conceivable to design it optionally as a conventional quadrupole. The main constraint on the mechanical design of the QD0 magnet stems from the lateral space required for the vacuum pipe of the outgoing beam.

A 254 mm long prototype of the SD0 has been built. The magnet, shown in Fig. 61, is assembled with a core made of cobalt–iron laminates which allows reducing the saturation while carrying the large flux density needed to achieve the required sextupolar gradient 219403 T/m^2. The open frame allows to accommodate the beam pipe of the opposite beam. Further studies on the mechanical design of a long magnet have been performed on a hybrid design of the final sextupole, SD0.

Post-collision Lines The baseline Post-collision Lines (PCL) lattice is composed of five types of dipoles all of which are very large and heavy (up to 90 tons) due to the large aperture required (close to 500 mm for the largest ones).

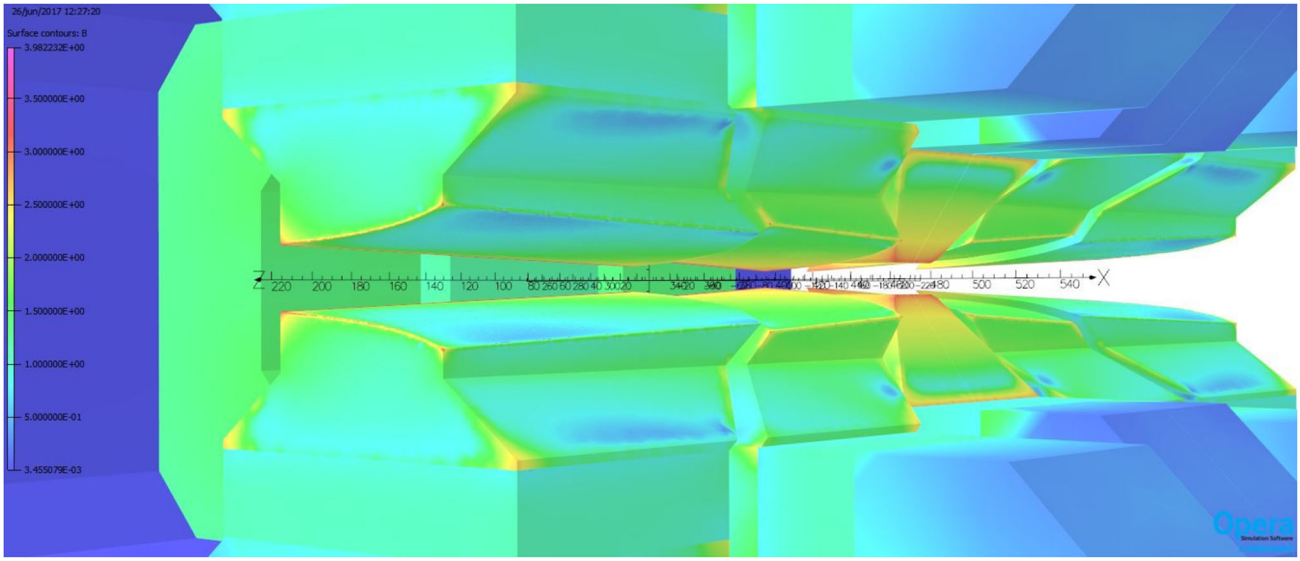

Fig. 59 View of the poles of the longitudinal variable combined magnet

Fig. 60 The short QD0 prototype

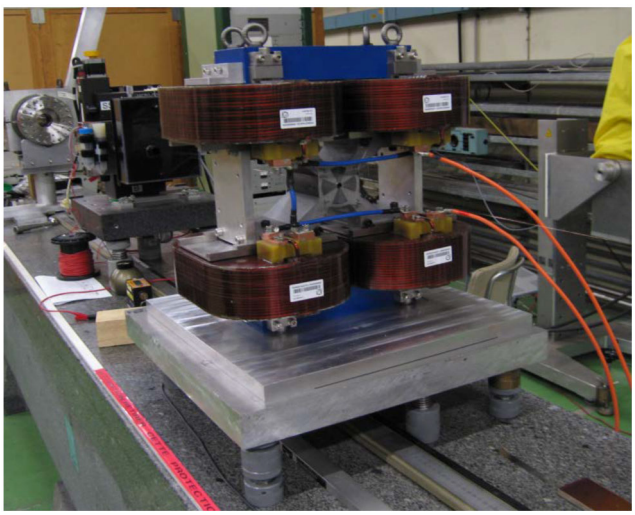

4.13 Super-conducting damping wiggler

4.13.1 Introduction

As shown in Sect. 2.1, to achieve the required luminosity at the collision point of CLIC, the normalized horizontal emittance has to be drastically reduced by means of damping rings. The positron beam enters first a Pre-Damping Ring and afterwards the main Damping Rings. The damping rings will be racetrack shaped rings with 20 wigglers placed in each straight section. The ultra low emittance combined with the fast damping times requires high-fields in the wigglers which can only be achieved with superconducting technology.

The baseline design presented in the CDR was foreseeing Nb-Ti superconducting wigglers with the parameters presented in [71]. To test the wiggler system with beam, one prototype superconducting wiggler magnet has been installed in the ANKA storage ring. The operational parameters for this prototype magnet were slightly different from the today's baseline parameters: $B_w = 3.0$ T, 35 periods, 51 mm period length λ_w and a vacuum cold gap of 13 mm. A detailed analysis was performed and showed that today's baseline parameters are of similar complexity as the parameters of the prototype magnet and are within reach. No large-scale cryogenic infrastructure is foreseen for CLIC, therefore, cooling each wiggler magnet individually with cryo-coolers has been chosen as baseline [71]. To minimize the He inventory, indirect cooling has been chosen and implemented in the prototype magnet.

Fig. 61 Prototype of the hybrid SD0, with PM blocks, Fe-Co core and air-cooled copper coils

Table 39 Main parameters of Nb_3Sn wiggler for CLIC

Period	49	mm
Magnet length	1864	mm
Number of full field poles	72	
Magnetic Field	3.5	T
K	~ 16	
Vacuum gap cold	10	mm
Magnetic gap cold	12	mm
Length flange to flange	2590	mm
Maximum ramping time	< 5	min
Power supply stability	$< 10^{-4}$	
Beam heat load	50	W
Period for LHe refill with beam	> 6	month
Field stability for two weeks	$\pm 10^{-4}$	

In the framework of this programme, wiggler magnets employing Nb_3Sn conductor technology have been designed, small scale demonstrators were built and tested [282, 283]. The present baseline parameters following this technology are presented in Table 39. Nb_3Sn wiggler magnets have the potential to reach smaller period lengths in combination with larger magnetic fields and margins. This very interesting combination of parameters (see Fig. 62) has triggered the construction of small prototypes. The results of tests of these prototypes are promising in terms of magnetic field but the magnets suffered from insulation issues. Therefore, more work would be required to be able to fully exploit the potential of Nb_3Sn wiggler magnets.

4.13.2 Magnet prototype

In a collaboration between CERN, BINP and KIT, a prototype of a superconducting damping wiggler for the CLIC damping rings has been designed, manufactured and installed at the ANKA synchrotron light source [70, 284].

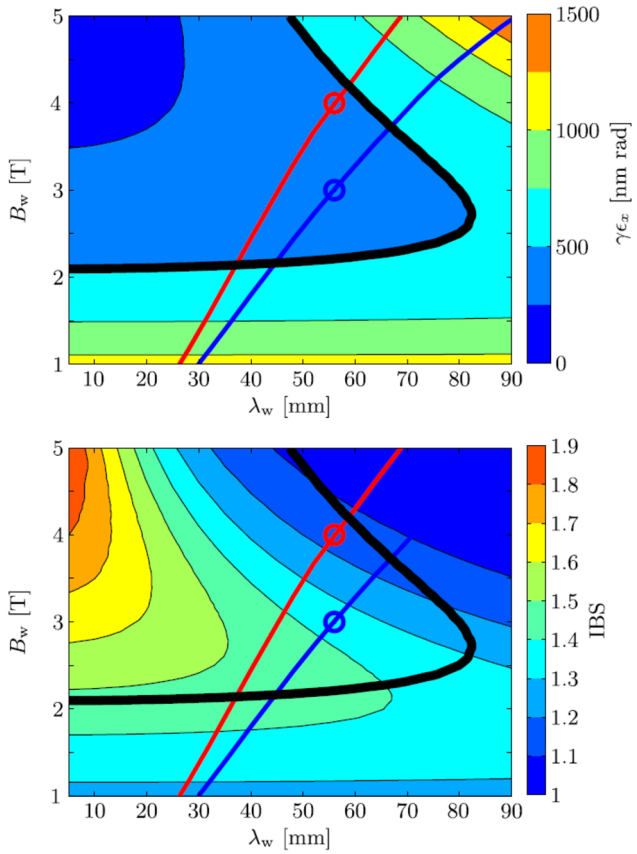

Fig. 62 Equilibrium normalized horizontal emittance YE_x (top) and the effect of IBS ($YE_x = YE_x; 0$). The red and the blue curves show the maximum achievable magnetic flux density for superconducting wiggler magnets with Nb_3Sn and Nb-Ti wire technology, respectively [71]

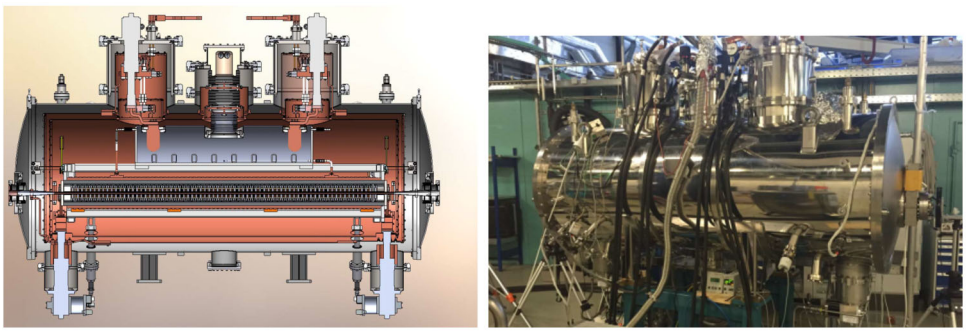

Fig. 63 Cross section of the CLIC damping wiggler prototype (left) and CLIC damping wiggler during testing at BINP (right)

The prototype magnet (see Fig. 63) was used to validate the technical design of the wiggler, particularly the conduction cooling concept applied in its cryostat design, in a long-term study. In this study the expected heat load from the up-stream wiggler's synchrotron radiation in the order of several tens of Watts is also studied by heating the vacuum pipe with a dedicated electrical heater.

4.13.3 Magnet test results

The cryostat design, first tested with the superconducting undulator at APS [285], is based on the continuous recondensation of Helium vapour on plates cooled with the 2nd stage of cryocoolers. This approach led to an under-pressure inside the Helium tank and in turn to temperatures in equilibrium conditions of around 3 K, even during beam operation. Despite this lower than expected temperature, the maximum stable current reached in the magnet coils turned out to be slightly lower than expected from the magnet tests in a liquid Helium bath at 4.2 K [286]. Figure 64 summarizes the quenches of the magnet. The maximum on-axis field amplitude reached during ramping was 3.2 T, both in the bath cryostat and in the wiggler's own cryostat. In the case of indirect cooling, however, holding quenches occur after periods of seconds to several hours in the outer, high current coil sections and basically uncorrelated with the magnet temperature. The physical origin of this instability is not yet

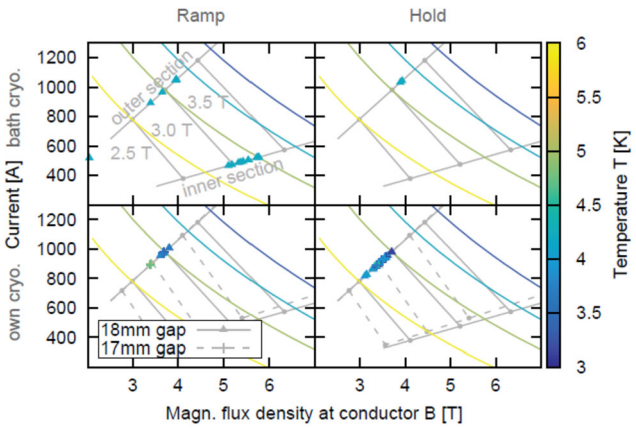

Fig. 64 Quenches of the wiggler marked on the load lines of inner and outer coil sections during current ramps (left) and at constant current (right), in liquid Helium bath (top) and in own cryostat (bottom). Each point marks a quench, colour-coded according to the temperature immediately before the quench. The coloured lines represent the critical condition for different temperature levels, the labelled grey lines depict the corresponding on-axis field for the original (18 mm gap) and the final (17 mm gap) magnet configuration, respectively

satisfactorily explained. The stable field is limited to 2.9 T by this effect, however, the wiggler can routinely be operated at this field level also in the storage ring under beam operation conditions.

4.13.4 Beam test results

Before the installation in the storage ring the field integrals of the wiggler were measured with a stretched wire set-up and minimized by adjusting the current distribution in the wiggler's matching coils. A quite significant horizontal field integral was corrected by additional vertical corrector magnets outside the cryostat. From the closed-orbit measurements a slight readjustment of the field integral compensation settings turned out to be necessary.

The first basic experiments on beam dynamics focused on the wiggler's influence on the closed orbit and betatron tunes in order to confirm the field integral compensation settings, the alignment of the wiggler and the results of the online magnetic characterization. A betatron tune shift due to the vertical focusing strength of the wiggler agrees with the model calculations. The origin of the (unexpected) horizontal tune shift is suspected to be due to sextupolar multi-pole feed-down.

4.14 Controls

4.14.1 Introduction

The CLIC control system will be similar to the control system of the LHC and its injectors (see [287]). Some special consideration has to be given to the Front-End Tier. For all CLIC accelerators excluding the Main Linac tunnel it is proposed to use the "LHC approach" where controls electronics are housed in racks close to the accelerators and connected to front-end computers, via dedicated cabling. These are in turn connected to the CERN Technical Network which is based on gigabit Ethernet. This is the basis of the control system for CTF3 and although the scale of the CLIC project means that the distances and the number of components to be controlled are larger than in CTF3, there should be no fundamental difficulty in controlling the CLIC injector complex.

The equipment in the Main-Linac tunnel can not be controlled in the same way. Here there is high control-signal density (about 100 signals/m). Building the acquisition system for this number of channels in the classical modular approach would simply not be possible in terms of available space and also in terms of cost. In addition, limitations on heat dissipation and the radiation environment in the tunnel, impose a new front-end architecture.

In the scope of the HL-LHC project [288], which is also very demanding in terms of accelerator controls, a project was started; "Distributed I/O Tier and Radiation-Tolerant Fieldbus Project" [289]. This is a variation of what was proposed in the CLIC CDR; where the development of a compact acquisition module, to serve as a dedicated acquisition and control module (ACM) was proposed. For the rest of this discussion, we will discuss only the parts of the CLIC control system which differ significantly from that described in the CDR.

The control system has 3 hierarchical layers of equipment communicating through the CERN Technical Network, a flat Gigabit Ethernet network using the TCP-IP protocol. We will consider only the lowest layer, the hardware layer.

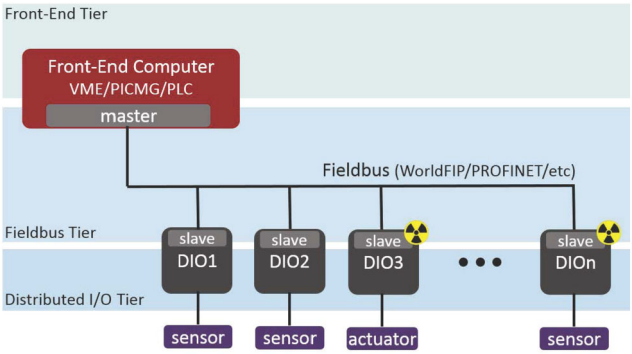

Fig. 65 Hardware layers

4.14.2 Hardware layer

The Hardware layer is where the interaction with the machine components takes place. A Distributed I/O Tier platform (DIOT) and a new high-speed, radiation-tolerant fieldbus, are the areas where the control system as described in the CDR [55] differs substantially from that proposed here.

As Fig. 65 shows, within the hardware layer, one can distinguish three tiers:

- Front-end Tier – a PLC or powerful computer in various form factors (VME, PICMG 1.3, MTCA.4, etc.) running a set of user applications controlling Distributed I/O Tier over a fieldbus.
- Fieldbus Tier – communication link between the Master in the Front-end Tier and a set of slaves in the Distributed I/O Tier
- Distributed I/O Tier – electronics modules that interface directly with the accelerator components in radiation-exposed or radiation-free areas, controlled over the fieldbus. These are usually FPGA-based boards sampling digital and analog inputs, driving outputs and performing safety-critical operations.

Depending on the needs of a given application, equipment groups can either use off the shelf systems (e.g. PLC-based), design custom electronics, or a combination of the two. The specialised needs of the CERN accelerators often demand the development of custom electronics. For these, there is a centralised service in the Front-end Tier in the form of VME crates and PICMG1.3 computers that can host a modular FMC (FPGA Mezzanine Card) kit.

In the Fieldbus Tier the current offering for custom electronics is mainly built around the radiation-tolerant WorldFIP bus. However, the limited (2.5 Mb/s) bandwidth will inflict prohibitive delays on some equipment groups as they try to gather enough diagnostics to find the reasons for a given failure. It is planned to expand the offering by developing a modern fieldbus communication based on 100 Mb/s Ethernet.

A modular standardised hardware kit that can be customized to suit various applications will be developed as part of the DIOT project. Two important principles of the project are staying close to the standards used in industry and designing the modules together with the future users – to benefit from the scrutiny and review of many developers. While the complete kit consists of modules for radiation-exposed and radiation-free areas, in the scope of the HL-LHC and CLIC the focus will be on radiation-tolerant components (Fig. 66):

- The 3U crate with a fully passive, standard, off-the-shelf backplane and power supply that can be exposed to radiation.
- The generic system board that serves as the crate controller, implements crate diagnostics, interfaces with application-specific peripheral boards plugged into other slots of a 3U crate, and features an FPGA that can be programmed by each equipment group.
- A set of communication mezzanines that implement various fieldbus protocols: WorldFIP (2.5 Mbps), Powerlink (100 Mbps), LpGBTx (10 Gbps).

This modular approach will satisfy the needs of the different subsystems. In particular, specific acquisition systems can adopt the whole kit, or use only some of its elements according to their needs. The customisation of the kit is done by developing application-specific add-in modules and implementing FPGA firmware for the system board.

The WorldFIP FMC has been designed [290] and work is ongoing to develop the Powerlink FMC mezzanine. A first DIOT hardware demonstrator which features an off-the-shelf crate has also been developed. The system board for this first prototype is a modified GEFE board designed for control and acquisition of Beam Instrumentation. This kit is being used as a prototyping platform to work on a radiation-tolerant power supply and a set of FPGA cores for uniform diagnostics. These crates will be available to equipment groups for evaluation and development of their application-specific add-in boards [ref DIOT].

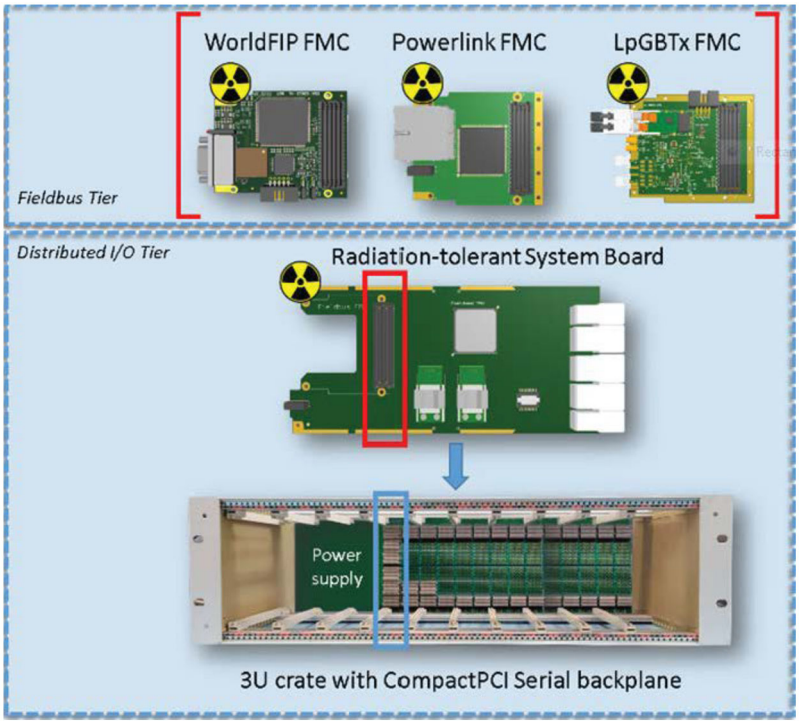

Fig. 66 Radiation-tolerant variant of the Distributed I/O Tier kit

4.14.3 Acquisition and control for the main linac

For each type of CLIC module approximately 200 acquisition channels and 170 control channels are needed to measure and control the properties of the beam, the RF parameters, the module alignment and stabilization, vacuum and the cooling systems. The data rate for acquisition is dominated by the signals coming from beam instrumentation and from RF and is around 6 Mbits/s per "DIO Slave". Given the capacity of current optical fibres, there should be no data transmission bottleneck to and from the "Slaves" to the alcoves.

Owing to the long distance (878 m) between the underground alcoves (see Chap. 5), it is not foreseeable to locate the acquisition and control electronics for the 436 modules of one "sector" in these alcoves. The required space for the electronics for such a large number of modules and the cost for the cabling to and from such a number of modules to the alcoves would be prohibitive.

The proposed solution, therefore, consists of one or two local "DIO Slaves" (DIOS) per CLIC module, located as close as possible to each module. The position of the "DIOS" relative to the module has yet to be decided and depends on the form factors of the chosen hardware platforms. The DIOS should, however, be positioned as far as possible from the beam pipes to limit the amount of radiation to which they are subjected.

The DIOS is responsible for the acquisition and transmission of control signals under the constraints on the radiation hardness and power consumption. In the light of these constraints, a generic approach must be found in order to provide an "open" CLIC module acquisition and control solution that would accommodate the controls requirements for the different CLIC sub-systems.

4.14.4 Digitization and data transmission

The DIOS should perform the following tasks:

- The prompt digitizing of the incoming signals from the CLIC sub-systems
- The execution of commands and configuration actions, as received from the higher level(s) of the CLIC control system
- The execution, for some systems, of pulse-to-pulse feedback loops
- The synchronization of acquisitions and commands with the CLIC timing system
- The time stamping of the acquisitions
- The pulsing of hardware components of the system, in synchronization with the CLIC timing system
- The bi-directional transmission of data via optical link(s) to the next-higher layer of control system.

4.14.5 Remote configuration and diagnostic facilities

The quantities and the underground location of the DIOS represent a unique challenge in terms of operations. Specific aspects should be addressed in terms of operational availability and long-term maintenance and evolution of these systems. The following mandatory services shall be implemented at the level of the DIOS:

- Monitor in real-time, through the communication link, the correct functioning of any internal hardware component of the system.
- In case of malfunction, disable parts of the system in order to allow the operation of CLIC in degraded mode.
- Remotely upgrade firmware and configuration parameters.

4.14.6 Front-end computers

In each alcove there is one, or more, dedicated Front-End Computer (FEC) for each module sub-system: beam instrumentation, RF, cooling, alignment, stabilization, vacuum, and power converters. In addition, there is a dedicated FEC for timing and another FEC dedicated to Machine Protection. The FECs will be the fastest real-time computer available at the time of their installation. For the slower signals (e.g., vacuum and cooling, where real-time processing speed is not so important), Programmable Logic Controllers (PLCs), or their equivalent, may be used. For the FECs to send information, via the middleware services, to the CLIC Control Centre the alcoves must have a connection to the surface. As there is only surface access every fourth alcove, it is necessary to link four alcoves via separate fibres. In the alcove which has access to the surface, dedicated switches take care of the connection to the surface.

4.14.7 Conclusions

The CLIC project comprises several different accelerators, each of which needs a solution for controls. This complex of accelerators resembles the present scheme at CERN for the LHC and its injector chain. Hence a control system as a scaled version of the present LHC system can be envisaged. The basic functionality of a three-tier system has to be provided and the solutions for the front-end computers following the industrial standards available at the time of construction. An exception to this general solution is the acquisition and control of the CLIC modules in the Main Linac and the logging of data coming from the accelerator sub-systems. For this several challenges will have to be addressed as technology develops over the next few years:

- The scale of the CLIC machine requires an unprecedented amount of controls equipment to be installed within a limited space and under radiation constraints. For each of the 2,976 Main-Beam modules (380 GeV stage) one or more DIOS chassis will be installed, each of which holds 10–20 electronics modules. This gives a total of between 30,000 and 60,000 individual electronics modules. A large industrialization and procurement effort will be required to produce and deliver such a quantity of electronic cards.
- The tunnel of the CLIC Main Beam is a very hostile environment for electronics. The DIOS chassis will be installed as close as possible to the modules. This is a new and yet un-tested, concept for an accelerator control system front-end.
- From simulations, the radiation levels in the CLIC Main Beam tunnel are one or two orders of magnitude higher than in the LHC. The DIOT Project, from which comes the DIOS concept, has addressed radiation hardness from the beginning and so this issue should be less limiting than in the CDR.
- Another major challenge is to limit the amount of heat given off by the DIOS into the tunnel. Over the next few years, various low-power solutions will be studied as will the possibility of switching off the electronics between beam-pulses.

4.15 Fine time generation and distribution

4.15.1 Background

The goal of a timing system is to provide a common time reference in a distributed environment. This reference is usually the result of counting ticks of a clock signal from an arbitrary instant. The clock signal, $a(t)$, is ideally of perfect periodicity and stability. Real-world clocks, however, present imperfections [291] in both amplitude and phase as expressed in Eq. (3).

$$a(t) = A\,(1 + \alpha(t))\sin(\omega t + \varphi(t)) \tag{3}$$

where ω is the angular frequency of the clock signal.

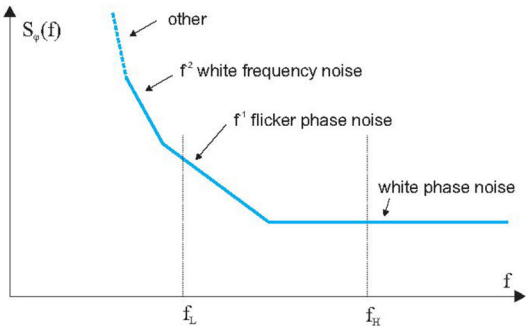

Fig. 67 One-sided PSD of phase noise for a typical oscillator

It is common practice to use the Power Spectral Density (PSD) of signal $\varphi(t)$ to specify jitter requirements. The integral under the PSD curve is the total jitter. In real life, an application is only sensitive to jitter generated between two finite integration limits. Figure 67 shows a typical plot of a one-sided PSD ($S_\varphi(f)$) of the phase noise for an oscillator. Integration limits are set between f_L and f_H. For a machine with a repetition rate of 50 Hz such as CLIC, it is estimated that all perturbations below 5 Hz in Fourier frequency can be dealt with by appropriate inter-pulse feedback strategies. Reasons for establishing an upper limit in integration stem mainly from the inability of some systems to react to such fast variations. These limitations can be in electronics, such as the bandwidth of the input stage of a digital gate, or in electromechanical systems such as an RF accelerating cavity.

4.15.2 CLIC timing requirements

4.15.3 Drive-Beam RF system

In Ref. [292] the jitter of the 1 GHz field in the accelerating cavities of the Drive Beam is specified as 50 fs integrating between 5 kHz and 20 MHz. It is also said that with appropriate feed-forward control in the Main Beam, this figure could be relaxed by a factor of 10. However, the reference phase noise fed to the LLRF system is only responsible for a small percentage of the final jitter in the electromagnetic field. Taking this contribution to be 10% results in a specification of 50 fs for the jitter of the reference clock signal distribution to each one of the 326 accelerating structures in each linac.

4.15.4 Beam instrumentation

Longitudinal profile monitors could be based on distributed lasers and changes in optical properties of bi-refringent materials induced by the Main Beam. These monitors have the task of measuring 150 fs bunches with a resolution of 20 fs [293]. The precision required from the clock signal, which allows the synchronisation of the lasers with the beam, would therefore be in the few tens of femtoseconds, integrated between 5 Hz and a few hundreds of kHz (the bandwidth of the Phase-Locked Loop locking the laser to the reference).

4.15.5 Two-Beam acceleration system

The Two-Beam acceleration scheme in CLIC requires a very precise synchronisation between the Drive Beam and the Main Beam. Figure 68 depicts a possible synchronisation solution. A controller measures the phases of the Drive and the Main Beam with respect to a reference line, and uses that information to control the amplitude of a kicker pulse which modifies the trajectory of the Drive Beam in order to keep it well synchronised with the Main Beam. The required precision of this alignment is around 40 fs [294], so the timing reference precision clearly needs to be better than that. The bandwidth of the kickers, in the several MHz region, would set a natural upper limit for integration of phase noise.

4.15.6 Technical solutions

There are two main types of solutions currently developed and tested for the distribution of precise timing signals in the femtosecond realm [295]. Both types have achieved synchronisations better than 20 fs over distances of several hundreds of metres.

In the Continuous-Wave (CW) variant, a laser modulated in amplitude by the RF or microwave signal to be transmitted. A fraction of the light reaching the destination bounces back from a Faraday Rotator Mirror (FRM)

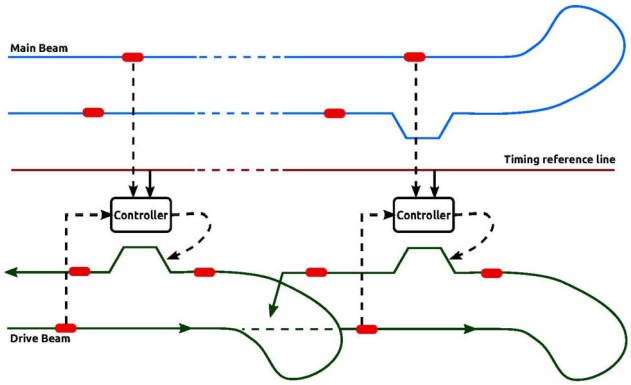

Fig. 68 Timing reference line usage for inter-beam synchronisation (adapted from Ref. [294])

and is, in the process, shifted in frequency using a Frequency Shifter (FS). Another FRM reflects a sample of the light signal as it leaves the source. These two signals, upon mixing together, produce a beat whose phase can be easily measured. The key feature of this system is that the heterodyning process preserves phases, so a phase shift induced in the optical frequency by a change of length in the fibre will show up as exactly the same phase shift at the RF frequency, which is much easier to measure. Once the phase of the beat signal is detected, it can be used to digitally shift the phase of the recovered RF signal at the receiving end of the link. It is important to note that what is really measured in this method is the phase delay, not the group delay of the modulation which is ultimately what we are interested in. In order to compensate for group delay, a first-order correction — based on actual measurements of a given fibre type for a range of temperatures — is applied to the raw phase delay measurements.

In the pulsed variant, a mode-locked laser is synchronised with the external RF signal, which determines its repetition rate. Narrow light pulses come out of the laser and travel through a dispersion-compensated fibre to the receiver, where a fraction of the light is reflected back towards the emitter. An optical cross-correlator measures the degree of coincidence of the two pulse trains and the result is used to control a piezo actuator that changes the fibre length so as to keep a constant group delay. This mechanical actuator is unavoidable because the cross-correlator needs the pulses to overlap, at least partially, in order to give a meaningful reading. On the other hand, the pulsed system controls group delay directly, so no *ad hoc* conversion between phase delay and group delay is needed.

4.15.7 Technical issues

Both types of systems have been successfully deployed over distances of several hundred metres, so the 6 km needed by CLIC Stage 1 is unknown territory. In the case of the CW system, one potential source of concern is the need for a model of phase-group delay corrections vs. temperature. If the temperature is not uniform over the complete length of the fibre, as can easily be the case in CLIC, a solution will need to be found.

Another potential issue is Brillouin scattering, a non-linear effect which is especially strong in optical fibres, due to the large optical intensities in the fibre core. Brillouin scattering in fibres leads to a limit of the optical power which can be transmitted, since above a certain power threshold, most of the light is scattered or reflected. This is especially a problem for narrow-band optical signals, and for long fibre lengths. In the pulsed system, Brillouin scattering is not much of an issue, since the power spectral density, which is the important quantity, is much smaller than for narrowband CW systems.

For the pulsed system, a major difficulty will be the dispersion control of the optical fibres, as the fibre length increases. Additional problems due to non-linearities are not expected to be any more significant than with shorter fibre links.

Finally, one very important difference between the solutions currently deployed and the CLIC scenario is the scale of the project. Current implementations do not scale very well beyond some tens of destinations. This is mainly due to the number of ports typically available in optical components, such as splitters/combiners. For CLIC, one of the challenges will be to explore in detail the real needs of each destination and come up with a strategy for partitioning the system in such a way that a reasonable compromise between performance and cost can be found.

4.16 Machine protection

4.16.1 Introduction

In the CDR [55] there is a detailed discussion of the destructive capacity of the CLIC beams. Although the beam power is impressive (Main Beam: 14 MW and Drive Beam for a single decelerator: 2.9 MW) the energy per pulse

2.8 MJ and 0.58 MJ respectively, is more than two orders of magnitude lower compared to the LHC beam of 300 MJ. Nevertheless, the energy density due to the extremely low beam emittance and spot sizes is very critical. Both beam power and energy density have to be addressed with the machine protection system to allow for safe and reliable operation.

As described in the CDR, the CLIC Machine Protection policy deploys different strategies depending on the time domain of the failures. In the following subsections, the status and implications for each of these strategies is discussed in more detail. The description will start from the interlock protection, which provides real-time protection for equipment failures up about a millisecond before beam passage, and then continues with the strategies to mitigate failures occurring at shorter time scales. Then we discuss the strategies for failures occurring over longer time scales.

4.16.2 Machine interlock system

The CLIC machine interlock system will assure that all equipment failures, detected in time before the next beam is committed, revoke the "next beam permit" and inhibit delivery of otherwise ill-controlled beams.

At CERN, and most notably for the LHC, a lot of experience with interlock systems has been build up. Although there may be many similarities, there is also a substantial number of differences to the CLIC machine. Firstly, whilst the LHC interlock surveys the circulating beams and may demand a beam dump on the next beam passage, in CLIC there is only a single beam passage. Hence, the interlock system only controls the permission for the next pulse. Technically speaking, the CLIC interlock system should be compared with the LHC injection interlock. A second difference is that the CLIC cycle time (20 ms) is by far not comparable with the LHC inter-cycle time (over 20 minutes). Hence, the CLIC interlock system must be able to rearm much faster and rely on automated analysis to determine whether the next cycle can safely be committed. Finally, the CLIC interlock system has to deal with multiple beams (Main Beam, Drive Beam) of various possibly beam intensities (i.e. during the intensity ramp up), that are traversing a multitude of accelerators and transfer lines.

Due to this complexity, the CLIC interlock system must be closely integrated with the beam scheduling system. The beam scheduling system will send out a token with the next pulse configuration that circulates through the CLIC complex. All interlock managing stations in the CLIC accelerator chain have to add their acceptance signature to the token for the next pulse to be executed.

4.16.3 Safe by design

The interlock system intercepts any equipment failure that occurs during the inter-beam period. However, as the interlock system has a finite signal-handling time, the interlock system will only cope with equipment errors that are detected up to 1∼2 ms before the next pulse permit is given. This implies that all the equipment circuits must be designed such that there is enough inertia in the system for the equipment settings to stay within the tolerance required for safe beam passage during 2 ms following the onset of a failure.

This strategy is not new, and is already deployed in many of the CERN transfer lines which carry high-intensity beams.

4.16.4 In-flight protection

The very short pulse length (156 ns for the Main Beam and 244 ns for the Drive Beam) makes it practically impossible to correct real-time errors. Once a pulse has been committed, there are practically no means to intercept safely the beam in the event that beam losses are detected (note that the CDR discusses a few exceptions where theoretically an interlock system may act on the beam in progress). Hence, for so-called "in-flight" failures, the machine protection system has to rely on fixed protections by masks and collimators. Most notably, masks are needed to protect extraction and transfer channels that follow any fast extraction or injection element. The design of the mask will be a challenging task as the charge density of the extracted beam could be high enough to damage the mask.

The interesting concept of reusable surfaces (i.e. where, in case of damage, the collimator surface can be displaced parallel to the beam) which exists in the LHC should also be deployed in CLIC. Furthermore, special attention is given to improving the reliability of the kicker systems through the deployment of inductive adders to pulse the kicker systems.

4.16.5 Beam quality checks and next pulse permit

The strategy to deal with medium term failures is based on the concept of a "next pulse permit". Upon completion of every cycle, the hardware permit of the next pulse will automatically be revoked. Only after a number of

Table 40 Peak energy and total power on the water dump and on the titanium vessel/window for the un-collided and the collided beam scenarios

Statistical uncertainties on the total values are below 0.1%.

	Max [J cm^{-3} per bunch train]		Total power [W]	
	Uncollided	Collided	Uncollided	Collided
H_2O	230 ± 1	9.10 ± 0.01	13.8 M	13.4 M
Ti window	4.35 ± 0.36	83.8 ± 1.0 m	6.24	4.91
Ti vessel (side)	569 ± 18 μ	903 ± 29 μ	8.45 k	9.07 k
Ti vessel (upstr. face)	32.0 ± 13.2 μ	2.15 ± 0.13 m	9.07	45.7
Ti vessel (dwnstr. face)	245 ± 6 m	39.1 ± 6.2 m	1.12 k	944

predefined automated beam quality checks on the actual pulse have successfully passed, will the permit for the next pulse be re-established.

Conceptually this strategy is not new, beam quality checks are also applied in LHC. However, while in the LHC many post-cycle checks are performed under operator/expert supervision, in CLIC this decision has to be executed within the 20 ms cycle, imposing further constraints on the data collection and analysis of the beam instrumentation equipment.

The most important beam quality checks are based on beam losses, beam trajectory information and beam-based feedback/feedforward performance.

The beam quality check will work in close conjunction with the beam scheduling system, which orchestrates the beam intensity ramp-up after a beam interlock. Hence, the next pulse permit decision is not just a go/no-go, but it also encompasses the decision on the beam intensities.

4.16.6 Long-term protection

Long-term protection has to ensure that the machine stays in a healthy state over longer periods. The most important ageing factor of many components is radiation related. Continuous machine optimisation with the aim to reduce radiation losses is important in this context. Radiation levels will be monitored and, where needed, the impact can be reduced by radiation shielding.

4.17 Beam interception devices

4.17.1 Main-Beam Dump

In order to cope with the challenge of absorbing the CLIC Main Beam, a water Beam Dump at the end of the CLIC post-collision line is proposed. It consists of a 10 m long cylinder, filled with water, pressurized at 10 bar, and with a diameter of 1.8 m, surrounded by a 15 mm thick titanium vessel of the same shape. For the present study a circular window has been considered, 30 cm in diameter, 1 mm thick, made of a titanium alloy (Ti-6Al-4V, i.e., ASTM G5, or UNS R56400), and directly cooled by the circulating water inside the dump.

The energy/power deposition by the primary beam on the water dump was calculated using the FLUKA Monte Carlo simulation code [296]. Two different beam scenarios were considered: the 1.5 TeV uncollided electron beam with a transverse Gaussian beam profile centred on the dump axis, with $\sigma_{hor} = 1.79$ mm and $\sigma_{ver} = 3.15$ mm. For the collided beam the secondary particles produced in the electron–positron interactions at 3 TeV centre-of-mass energy were simulated with the GUINEA-PIG package [297] and were transported along the post-collision line up to the dump with the DIMAD tracking code [298].

Table 40 shows the peak energy and total power on the water dump and on the titanium vessel/window for the uncollided and the collided beam scenarios. As expected, the case of uncollided beam is more severe than the one of collided beam.

The induced nuclide production in the dump was estimated; in case of uncollided beam, the short lived radionuclides are (with half-lives in brackets) ^{15}O (2 minutes), ^{13}N (10 minutes) and ^{11}C (20 minutes) are produced with rates of 1.19×10^{15}s^{-1}, 5.51×10^{13}s^{-1} and 3.39×10^{14}s^{-1}, respectively. The long-lived nuclides ^{7}Be (53.6 days) and ^{3}H (12.3 years) have a production rate of 1.14×10^{14}s^{-1} and 3.12×10^{14}s^{-1}, respectively.

Water circulates in the dump in a closed loop, externally cooled. A continuous water flow of at least 25–30 litre/s, at an average speed of 1.5 m/s, is required to remove the power deposited in the innermost part of the dump and maintain the peak temperature of water slightly below its boiling point. A safety factor of at least two should be applied to these values.

In case of inefficient heat removal, the sudden increase of the water temperature is about $\Delta T \sim 55$ K per pulse [108]. Water reaches the boiling point after few bunch trains and the beam must be interlocked. A safety

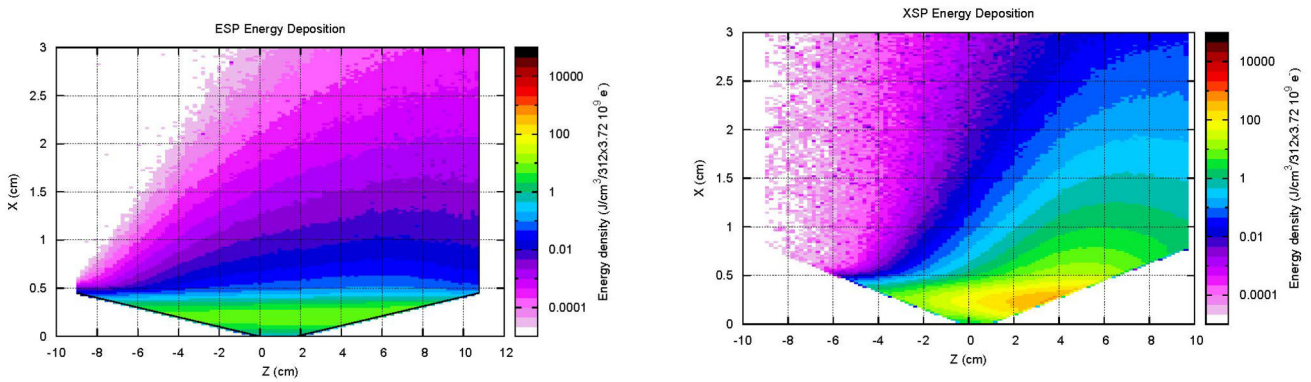

Fig. 69 Energy density map in the case of the accident scenario with 2 mm impact parameter. Left plot shows ESP collimator, right plot XSP collimator

system must be activated to evacuate the vapour pressure generated in the tank. The initial pressurization at 10 bar moves the boiling point of water to 180 °C. allowing a larger margin of manoeuvre, but AUTODYN® [299] simulations show that the pressure wave causes an overstress on the dump walls and window at each bunch train, to be added to the stresses due to the 10 bar hydrostatic pressure. Stiffeners are required, and possibly some type of shock absorbers in critical locations, in order to guarantee the dump structural integrity. The use of gas–water mixtures for a more effective damping of the pressure wave is not *a priori* excluded.

4.17.2 Collimation system

The CLIC collimation system consists of pairs of spoilers and absorbers in order to remove the unwanted halo of the beam. The CLIC collimation system is driven by their cleaning capabilities and its ability to survive a possible accident scenario. The system was simulated by means of FLUKA [296] for a possible beam accident scenario, as well as for normal cleaning operation.

For the accident scenario it was assumed that the full train of 312 pulses with intensity of 3.72×10^9 electrons at 1.5 TeV hits the front face of the energy spoiler (ESP) and, with lower probability, the horizontal or vertical spoilers (XSP/YSP). For the simulation, a shallow depth of the beam was used with an impact parameter of 2 mm assuming a beam spread of 780×22 µm^2 in horizontal × vertical for the energy spoiler ESP and 8×1 µm^2 for the transverse spoiler XSP.

During normal operation all spoilers should see only a fraction of beam (of the order of 10^{-6}). For the sake of simulation, we assumed a beam spread similar to that the accident case.

Figure 69 shows the energy deposition map on a beryllium ESP spoiler for the accident scenario with 2 mm impact parameter. Although the total beam energy is equivalent to 280 kJ, the spoiler stops only a tiny fraction of the beam close to 6 J, about 36.5 MeV out of 1.5 TeV for every primary electron hitting the spoiler. This energy deposition produces a peak energy density of the order of 600 J/cm^3, which will generate, assuming adiabatic conditions, an instantaneous temperature rise of 450 K. The ESP spoiler will survive the accident scenario, since it is practically transparent to the beam, and only a tiny fraction of 2.4×10^{-5} will be stopped on the jaws. The remaining energy will continue downstream, therefore a dedicated study will be required to ensure the protection of the downstream elements that will be exposed on the accidental beam.

In the case of the XSP (Figs. 69 the considerably smaller beam spread as well as the heavier materials used (titanium for the jaws and copper for coating), results in a very high energy deposition with a peak-energy density of 30 kJ/cm^3. Obviously, the jaw material and the coating will not survive this huge energy density therefore a replacement of the spoiler after such a failure scenario would be required.

The main mechanism of secondary particle production on the collimator is the indirect interaction of the electron beam with the spoiler through photo-nuclear interactions from the bremsstrahlung photons. Muons, being minimum-ionizing particles, are those which have a higher probability of reaching the experiments at the interaction point. The correct evaluation of the muon spectrum reaching the experiments will strongly depend on the material present in the flight path of the muons. A possible remedy would be additional shielding after the spoiler in order to allow the charged mesons to interact before they decay.

According to the design parameters, the ESP should be exposed to fractions of 10^{-6} of the full beam, with a very small impact parameter. Assuming an operation of 200 days per year with a pulse train of $312\times3.72\times10^9$ electrons every 20 ms, and a damage threshold for beryllium of 31 eV, the maximum DPA obtained on the ESP spoiler is of the order of 2.5×10^{-6}/year. Using the same parameters, the core of the ESP spoiler will reach a

maximum activity of 200 mSv/h during operation, which very quickly will drop to values below 0.1 mSv/h after one hour of cooling due to the very light and short-lived residual nuclei produced.

4.17.3 Photon absorbers in the damping rings

The twenty wigglers installed in the CLIC damping rings will generate synchrotron radiation with a critical energy of 19 keV with a spectrum emitted in a concentrated light cone with a small opening angle of ∼3.2 mrad. As shown on the plot the maximum energy of these photons is of the order of 50 keV, resulting in an attenuation length of about 19 mm on copper. The total power to be absorbed per wiggler is of the order of 33 kW.

Vertical and horizontal absorbers made of copper are foreseen after each wiggler, based on a 4 wiggler scheme [71]. Ray tracing simulations were performed to estimate the energy density seen by the wiggler absorbers for the original NbTi wiggler. These studies should be updated for the Nb_3Sn version with higher field foreseen in the present DR design.

5 Civil engineering, infrastructure and siting

5.1 Civil engineering

5.1.1 Overview

Since the CLIC PIP was published in 2018, a number of significant changes have been introduced to the civil engineering design. These changes derive from the decision to update the design to have two interaction points, alongside further design optimisation of the 380 GeV Drive-Beam machine. The major changes to the design as a result of these updates are:

- 2 km of tunnel widening on either side of the detector cavern to account for the two incoming beamlines to the two detectors.
- A reduction in size of the surface injector complex, most notably, the combination of the Booster into the Main Beam injector tunnel.
- A decrease in the number of required service buildings.
- An adjusted surface layout avoiding all existing CERN buildings, environmental concerns, and reducing the transfer tunnel lengths.

Information about the previous studies done for a klystron-based alternative can be found in Appendix C. All the updates described in this section have been done for the baseline drive-beam machine.

Figure 70 presents the underground structures schematic for the CLIC civil engineering works at the two proposed energy stages of 380 GeV and the upgrade option of 1.5 TeV. The key features of this layout are:

- 380 GeV Drive-Beam machine with a main tunnel length of 12.1 km.
- 1.5 TeV Drive-Beam machine with a main tunnel length of 29.6 km.
- 3 TeV Drive-Beam option no longer being considered in the Civil Engineering designs.
- A single detector cavern including the two offset detectors.

Tabulated beneath the schematic are the underground component parameters for each energy stage as well as for the Beam Delivery System (BDS) and Detector area.

5.1.2 Study area and siting

The location of the CLIC 380 GeV machine has been optimised whilst still considering the requirements for a higher energy stage. This optimisation took into account the availability of existing CERN sites, the regional geology and local environment. Previous experience from the construction of LEP and the LHC has shown that the sedimentary rock in the Geneva basin, known as molasse, provides suitable conditions for tunnelling. Therefore, boundary conditions were established so as to avoid the karstic limestone of the Jura mountain range and to avoid siting the tunnels below Lake Geneva (see Fig. 71) whilst maximising the portion of tunnel located in the molasse.

Based on the regional, geological and surface data, and using a decision-support web application for future accelerator localisation study (Geoprofiler), a 380 GeV solution has been found that can be upgraded to the higher energy stage of 1.5 TeV. Figure 72 shows the simplified geological profile of the CLIC machine stages. The 380 GeV stage is located entirely in molasse rock and avoids the complex Allondon depression. This solution is optimised

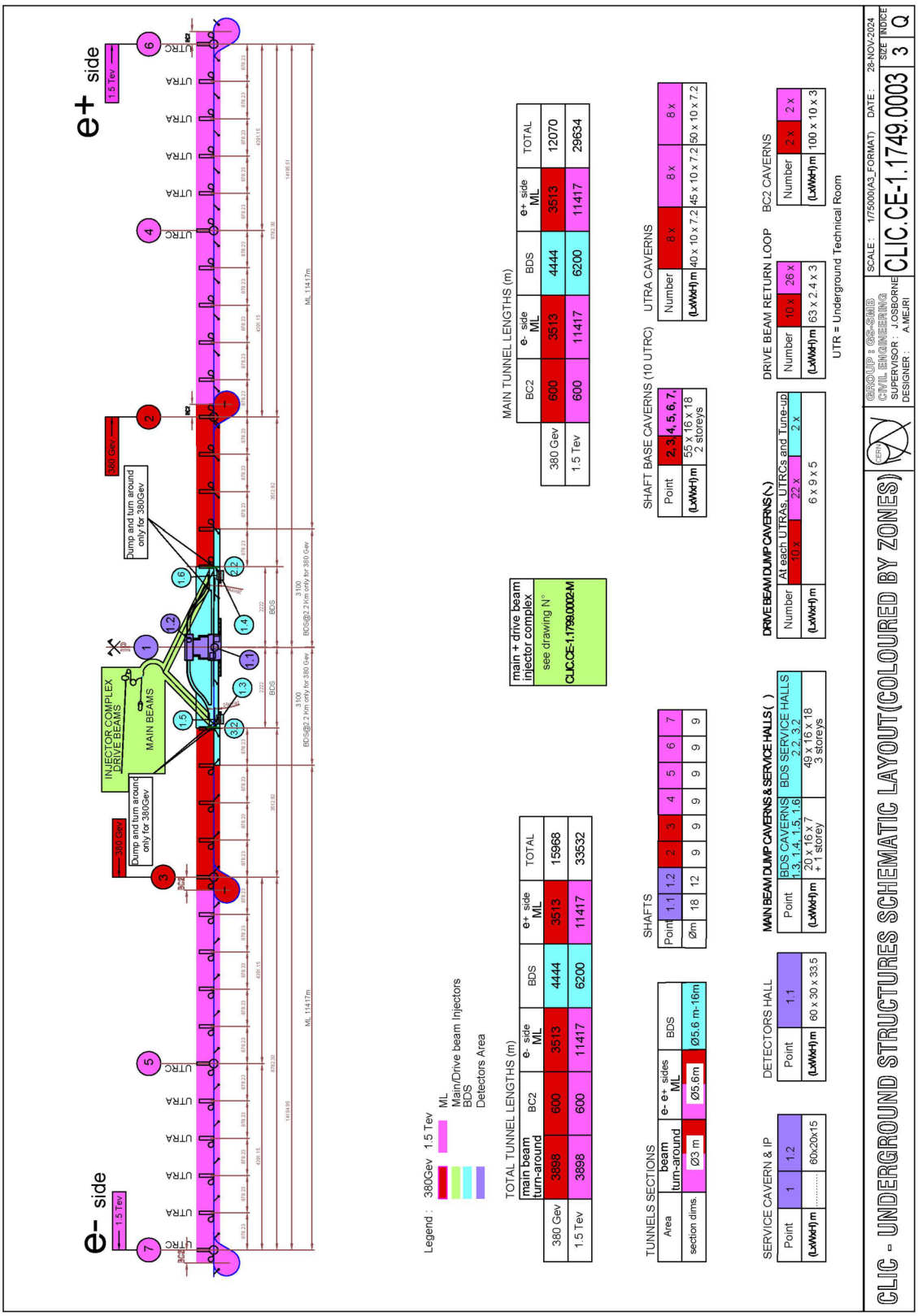

Fig. 70 Schematic layout of the two-stage civil engineering complex

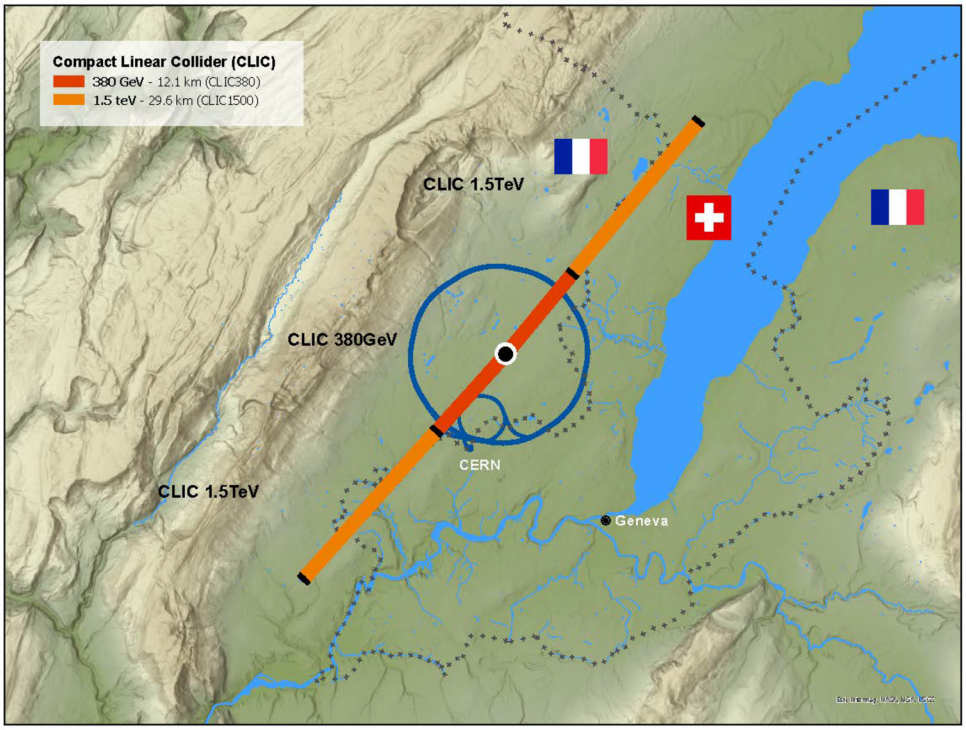

Fig. 71 CLIC siting study area

for 380 GeV and provides an excellent upgrade possibility to the 1.5 TeV stage. A key advantage of this solution is that the interaction point and injection complex are located on the CERN Prévessin site.

Using the Prévessin site and adjacent CERN owned land to house the injection complex and the surface experimental site above the interaction region assists greatly in reducing the needs to acquire land. The only additional land required for the 380 GeV and 1.5 TeV CLIC stages is that for the shaft surface sites. Each surface site requires a 170 m x 140 m plot. Thus, at 380 GeV two sites will be required for the two shafts at the extremities of the tunnel. For the upgrade to 1.5 TeV four sites are required for the additional four shafts.

With the exclusion of the 3 TeV stage, the Gland depression is no longer a geological concern. Thus there is scope at these lower energy stages of 380 GeV and 1.5 TeV to reduce shaft depths, still being housed in good molasse rock without any need for further site investigation to confirm this.

5.1.3 Injector complex

The layout of the Injector and Experimental complexes has been optimised to be completely located on CERN land avoiding all existing CERN infrastructure and the key environmental concern of the river "Le Lion" (see Fig. 73). At 380 GeV the two buildings housing the klystrons and modulators of the Drive-Beam Injector complex have a width of 17 m and a combined length of 1800 m. These buildings are situated on the west side of the Prévessin site. Surrounding these buildings are a series of CV, RF Power Distribution and Water Station buildings.

The Main-Beam Injectors are also located on the CERN site; they consist of several linacs and damping rings. The layout is similar to that presented in the PIP. In 2024, the Main-Beam Injector building has been reduced from a length of 880 m to 500 m and now includes the Booster in the same cut and cover tunnel beneath it. The Main-Beam Injectors have been relocated to the east of the Prévessin site with the damping rings now being stacked. These optimisations reduce the number of required surface structures and the transfer tunnel lengths within the complex significantly.

5.1.4 Main tunnel cross section

A 5.6 m internal diameter tunnel is required to house the accelerating structures and all the necessary services as well as the transport corridor (Fig. 74). It is anticipated that the main tunnels will be constructed using Tunnel Boring Machines (TBMs). For TBM excavation in a sector with "good" conditions, a single pass pre-cast lining is adopted. The tunnel floor is to be cast in-situ in concrete around water supply and drainage channels.

This tunnel section has remained the same since the PIP. The most significant alteration being the introduction of large ventilation ducts that must be routed through the access shaft caverns (UTRCs) and the service alcoves (UTRAs) located every 878.23 m (Fig. 70).

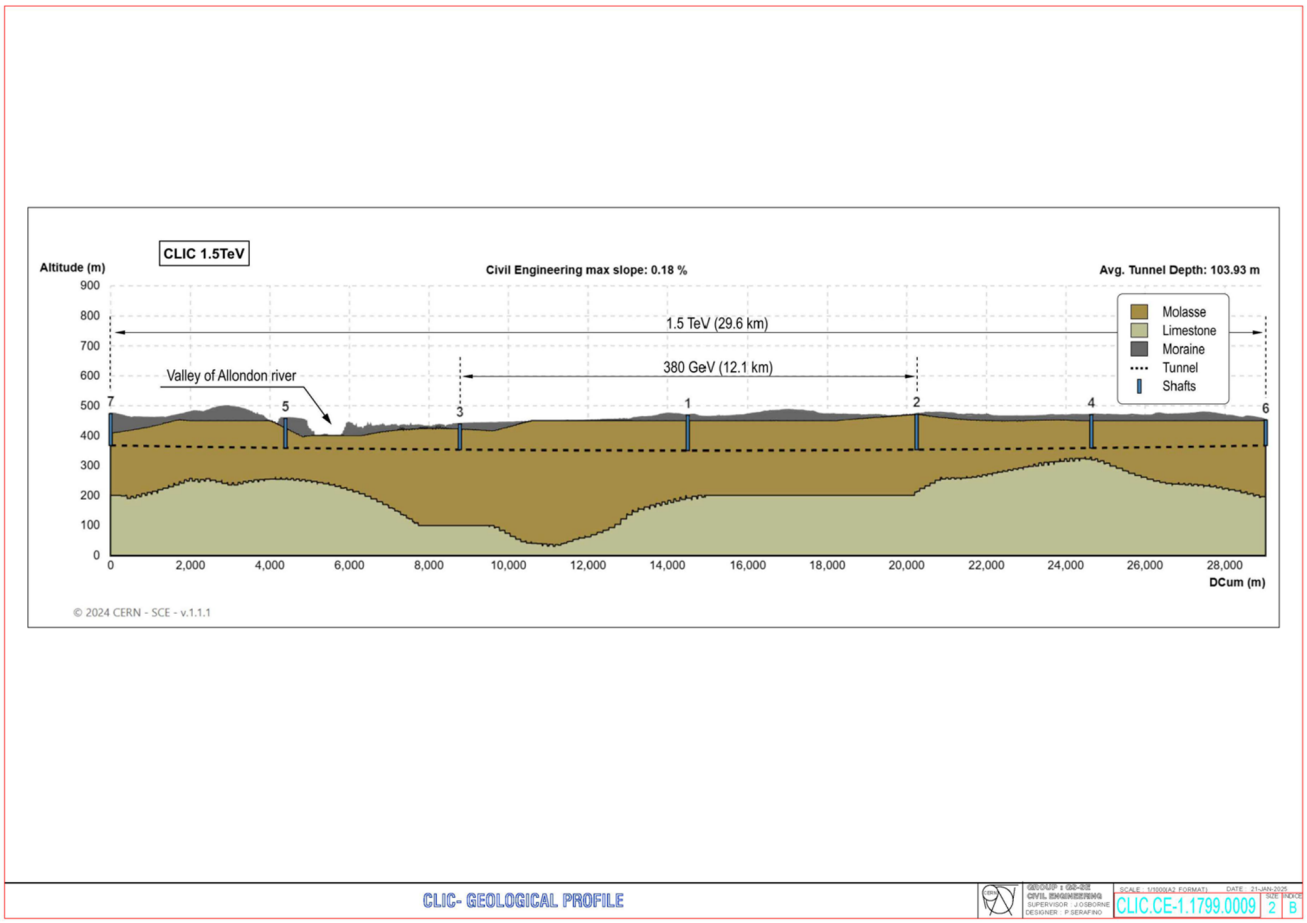

Fig. 72 Geological profile of the two-stage linear collider

Due to the significant change in the cooling and ventilation solution, the UTRCs and UTRAs increased in size. It is necessary to construct caverns that allow large CV ducts to pass from the main tunnel to these auxilliary structures which will be required to house the air handling units; the UTRCs are expected to be 55 m in length and 16 m in width and the UTRAs for the 380 GeV energy stage are expected to be 40 m in length and 10 m in width.

5.1.5 BDS and interaction region

A layout of the interaction region is shown in Fig. 75. It displays the detector and service caverns, which are interconnected by an escape tunnel that leads to a safe area in each of the caverns. The service cavern is accessible via a 12 m internal diameter shaft, whilst the detector cavern has an 18 m diameter centrally located shaft between the 2 detectors. Access to the region is granted via lifts and a stairwell in the service shaft, whilst the experimental shaft is used predominantly for the installation of the detector. The figure further displays the incoming beam lines at 16.5 mrad and 26 mrad alongside the post collision lines which lead into the beam dumps.

In 2024, the IR cavern was replaced directly by the detector hall, with floor parameters of 30 m x 60 m, the detector hall has sufficient space for both detectors and is now connected directly to the BDS. The two tunnels that contain the Beam Delivery Systems, shown in Fig. 76, are each angled at 20 mrad with respect to the Interaction Region. This allows effective extraction of the beams after collision and the separation of the post collision lines from the incoming beam lines. To accommodate for the dual beam line and detector update, a 2 km section on either side of the BDS will undergo tunnel widening linearly from 5.6 m to 16 m at the connection to the detector hall.

Figure 77 presents an alternate design for the Interaction Region. As opposed to tunnel widening, this design requires the beams to split into two parallel tunnels on approach to the IR. Here the two detectors are independent within smaller caverns to assist with the stability of the final focusing magnets. The detectors are connected to separate service caverns which provides an ease of maintenance whilst keeping the other detector operational. Due

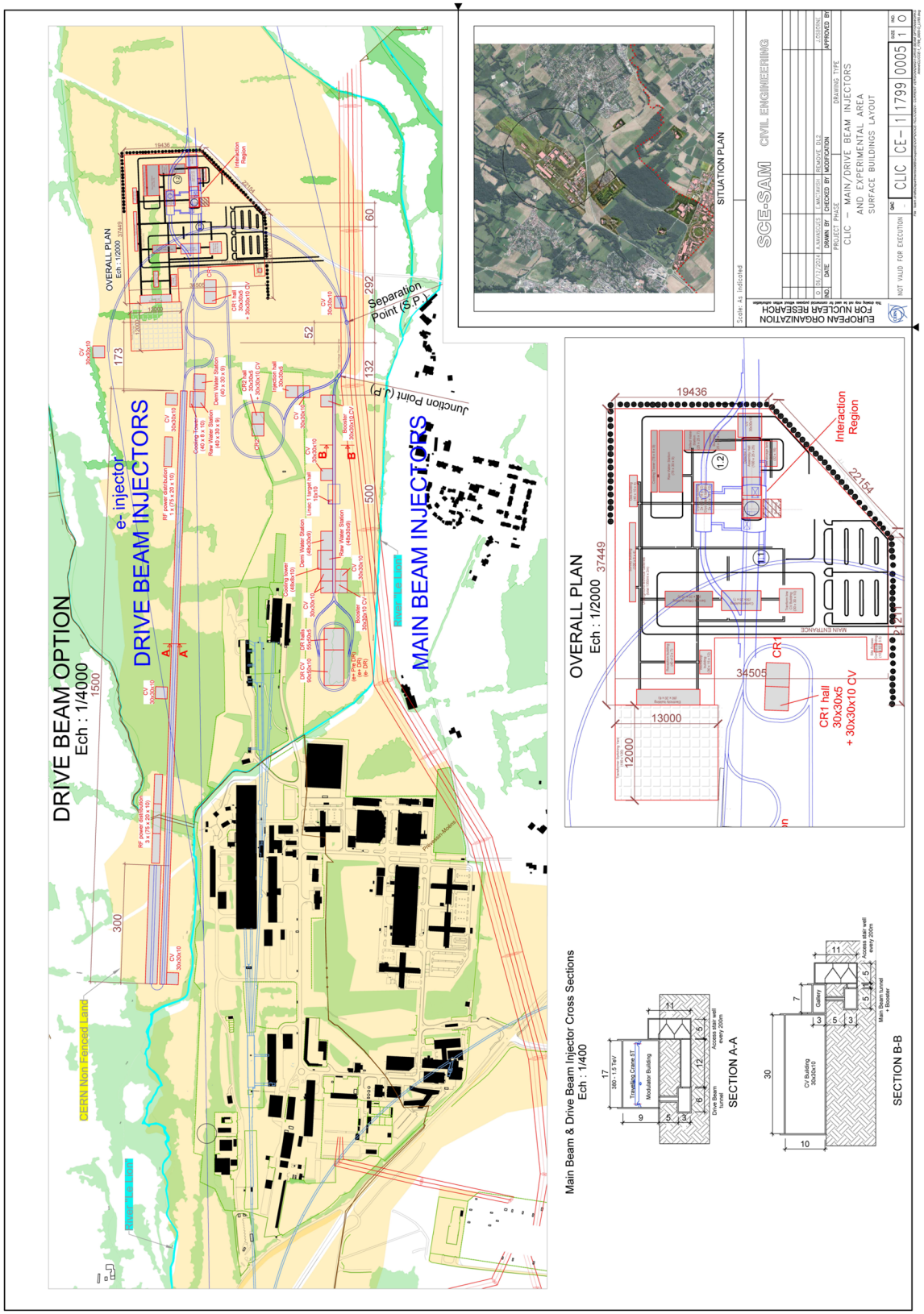

Fig. 73 Schematic layout of the Injector Complex and Surface Experimental Site

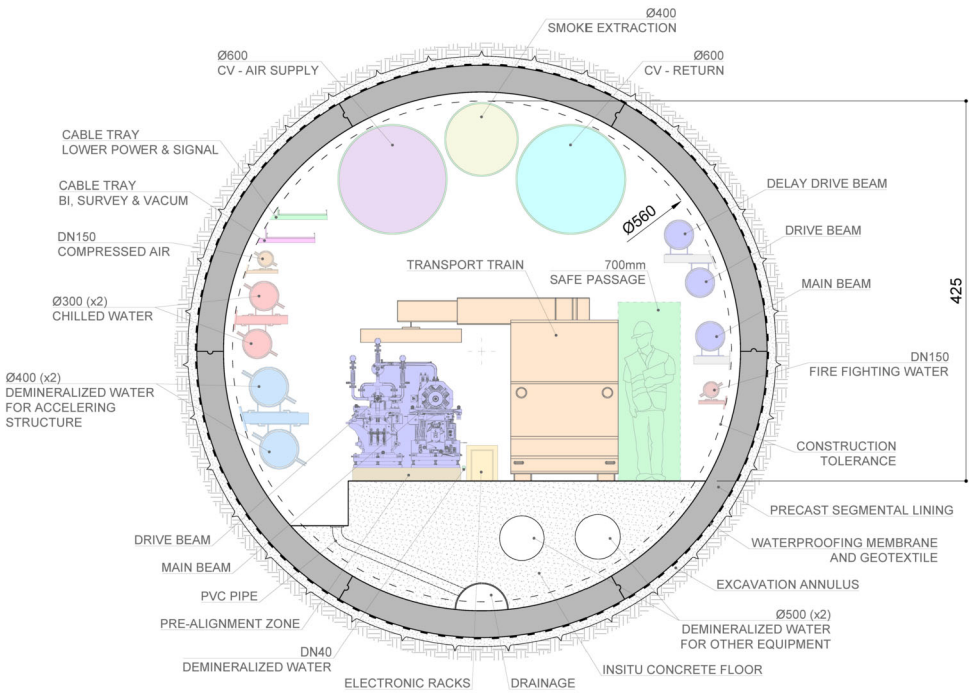

Fig. 74 Cross section of the underground tunnel

to the independence of the 2 sides of the IR, two experimental and two service shafts are required to install the detectors and provide access to either side of the IR.

5.1.6 Cost consideration

The overall cost has been minimised for the 380 GeV machine. The cost estimates are based on those used for other ongoing CERN projects and the full cost analysis includes all aspects of construction, including, but not limited to, labour costs, material costs and consumables as well as design, consultancy, and site investigation works.

The further design optimisation of the Drive Beam Injector Complex provides a significant decrease in costs. The most significant decrease being due to the inclusion of the Booster into the Main Beam Injectors. Alongside this, the relocation of the Main beam Injectors to the east side of the Prévessin site and the stacking of the damping rings reduces transfer tunnel lengths.

As a result of the dual interaction point update, the BDS tunnel costs have increased. 2 km of tunnel widening either side of the interaction region induces a major cost. The existing detector hall suitably houses both detectors and thus doesn't induce any additional costs. Despite the cost reduction as a result of the Injector Complex optimisation, the overall civil engineering cost increases predominantly, due to the major tunnel widening works.

The decision to use the alternate IR design, despite the removal of the tunnel widening sections, would slightly increase the cost due to the extra shafts, caverns and surface structures.

5.2 Electrical network

The design of the CLIC electrical network is driven by three main factors:

- the estimated electrical power requirements (Fig. 91);
- the location and type of equipment to be supplied and;
- the expected level of electrical network availability and operability.

The electrical network is composed of a transmission and a distribution level. The transmission level transmits power from the European Grid to the CLIC sites and between the eleven CLIC surface locations and finally to the underground infrastructure. This network typically operates at high voltage levels from 400 kV down to 63 kV. The distribution level distributes the power from the transmission level to the end users at low and medium voltage levels in the range of 400 V and 36 kV.

5.2.1 Source of electrical energy

The electrical power for the 380 GeV machine is supplied from the European Grid. There are two 400 kV sources and one 230 kV source located within close proximity to the proposed CLIC location (Fig. 78). At the time of

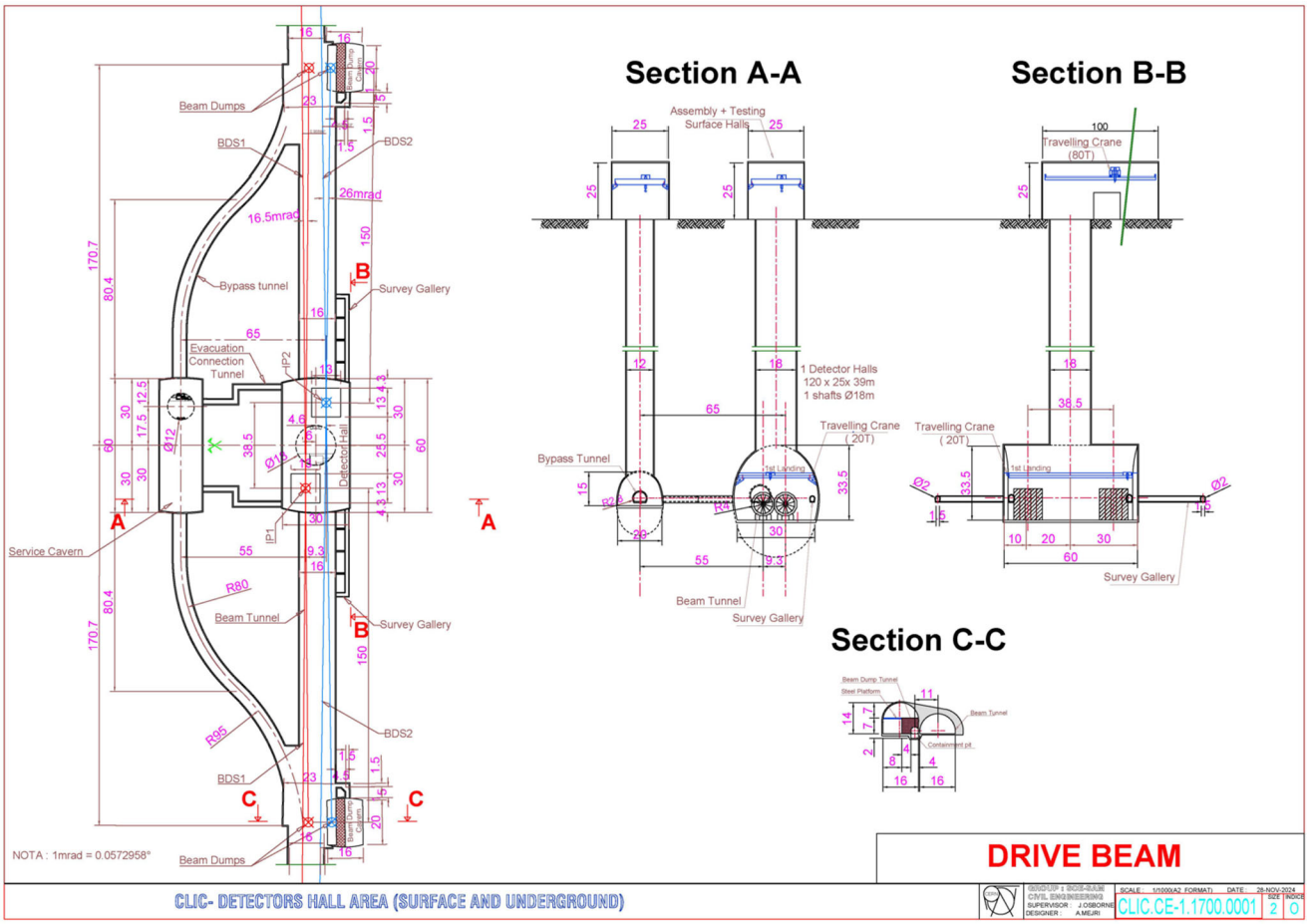

Fig. 75 Layout of the CLIC Interaction Region

the CDR, RTE (Reseau Transport Electricité) confirmed that on the time horizon of 2035, each of the French supplies is capable of providing 200 MW of power in addition to their present load; nevertheless, no further checks have been performed with RTE in the following years. The long-term availability of power from the Swiss supply is unknown. Assuming that 200 MW of power is available from each of the three sources, the necessary power supply for all CLIC configurations is currently available. For all CLIC configurations, roughly 70% of the total power required is for the injection infrastructure located on the main campus (point 1 in Fig. 78). The proposed transmission and distribution network considers the upgrade of the European Grid to make available the total CLIC power requirements at point 1.

5.2.2 Transmission network

The transmission network configuration for 380 GeV is identical for both the Drive Beam and Klystron options. The network will expand progressively for the 1.5 TeV stage. The proposed voltage levels and network are optimised to allow the use of the existing electrical infrastructure when expanding to the higher CLIC energy stages.

5.2.3 Transmission network for the 380 GeV stage

The transmission network scheme for the 380 GeV stage (Fig. 79) includes a primary transformer substation at point 1. From the 400 kV European Grid, a 400/132 kV step-down transformer substation supplies a transmission network that connects to points 2 and 3 through a 132 kV transmission line. From the 132 kV substations at points, 1, 2 and 3 the required 132/36 kV step-down transformer substations will supply the distribution network. The design includes redundant bus bars at 400 kV and 132 kV levels, and redundant power transformers in order to provide the required level of availability, operability and maintainability.

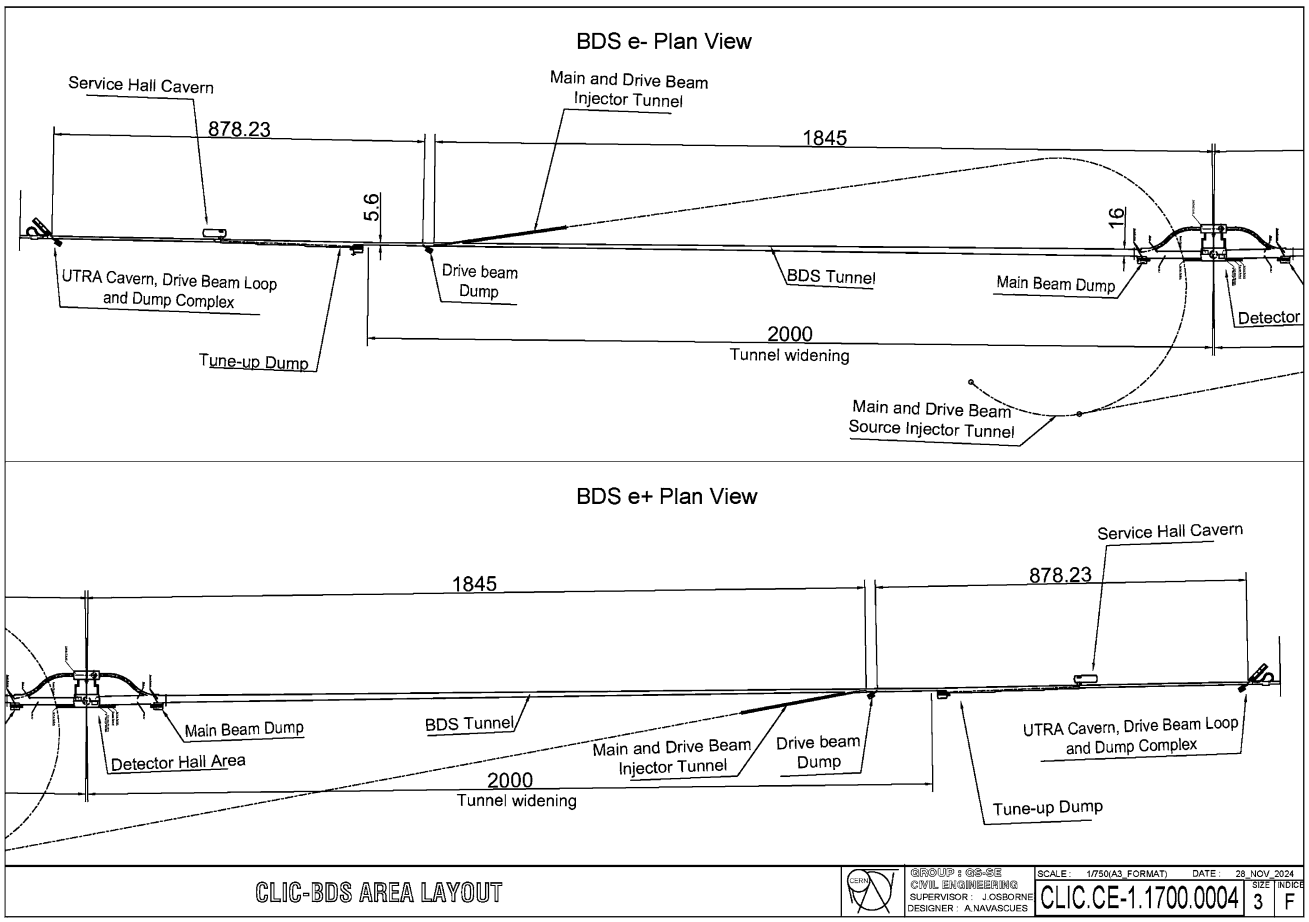

Fig. 76 CLIC 380 GeV BDS Layout

5.2.4 Transmission network for the 1.5 TeV stage

The upgrade of the transmission network from the 380 GeV stage to the 1.5 TeV stage includes the extension of the transmission network to the adjacent points 4, 5, 6 and 7 (Fig. 80). On each of these four points, a 132/36 kV step-down transformer substation is constructed and interconnected to the existing substations at points 2 and 3 through new 132 kV transmission line segments. The ampacity of the existing transmission line segments between points 1, 2 and 3 is increased by adding a second line in parallel to the existing ones. At point 1 the existing 400/132 kV and 132/36 kV step-down transformer substations are extended to provide the necessary power requirements for the supply of the Drive-Beam infrastructure.

5.2.5 Distribution network topology

The distribution network connects the transmission network to equipment and systems installed on the surface and underground. During nominal operation, the transmission network supplies the distribution network. Alternative sources of supply are required in order to achieve the required level of network availability and to cope with degraded scenarios such as general or local power supply disruption. Therefore, the distribution network includes a second source of supply, rated between 2 and 10 MVA, fed from a regional grid node, a third source of supply rated from 1 to 5 MVA of local diesel power stations and a fourth source of supply which provides uninterruptable power. Figure 81 shows the single line diagram of the distribution network of an individual CLIC surface point including the alternative power sources.

The distribution network consists of a primary surface indoor substation composed of several bus bars. The incoming feeders are the two redundant 135/36 kV transformers on the transmission network, that is, the second supply from a regional source and the third supply from a local diesel power station. The outgoing feeders supply the secondary substations. These are located on either the surface or underground, near the load. The operating voltage of the distribution network is typically 36 kV for the power distribution over distances greater than 750 m.

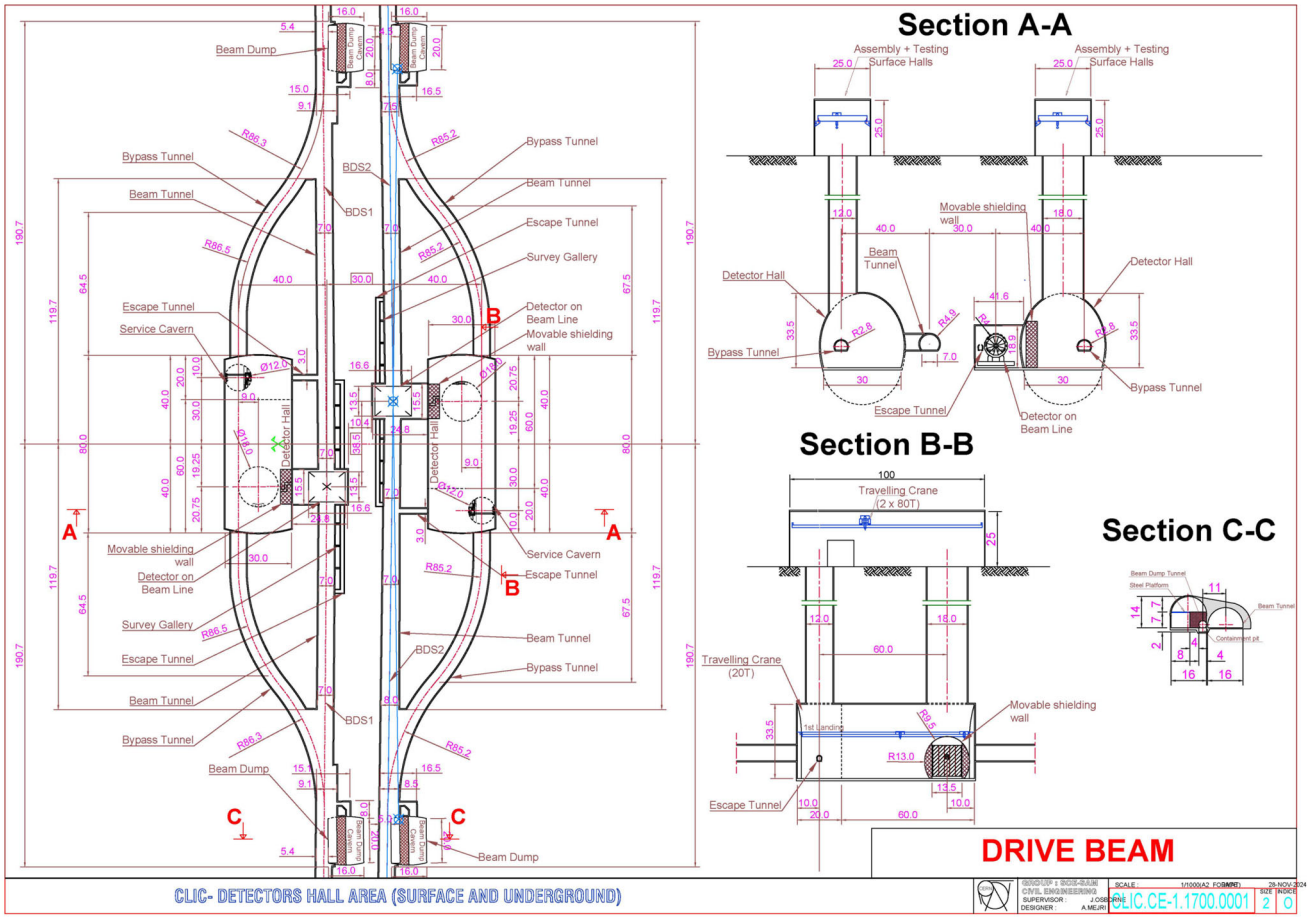

Fig. 77 Alternate layout of the CLIC Interaction Region

Fig. 78 Location of existing power sources near CERN

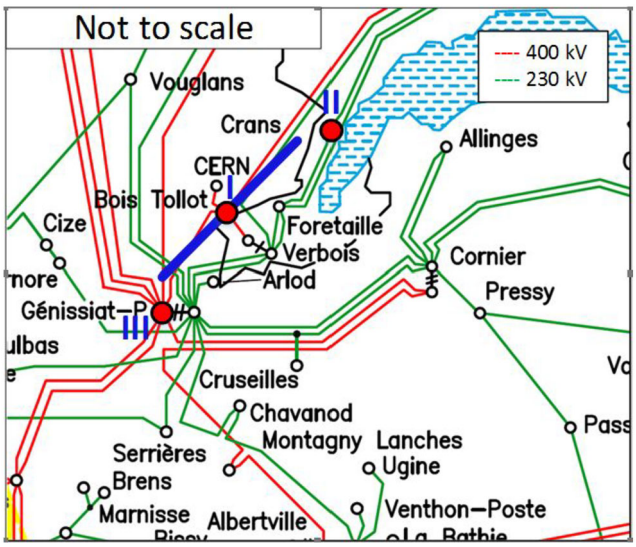

Voltage step-down transformers feed end users from the secondary substations over a maximum cable length of 750 m. End users are supplied from the secondary substations at voltage levels between 400 V for wall plug equipment and 3.3 kV for high power motors for cooling, ventilation and cryogenic systems.

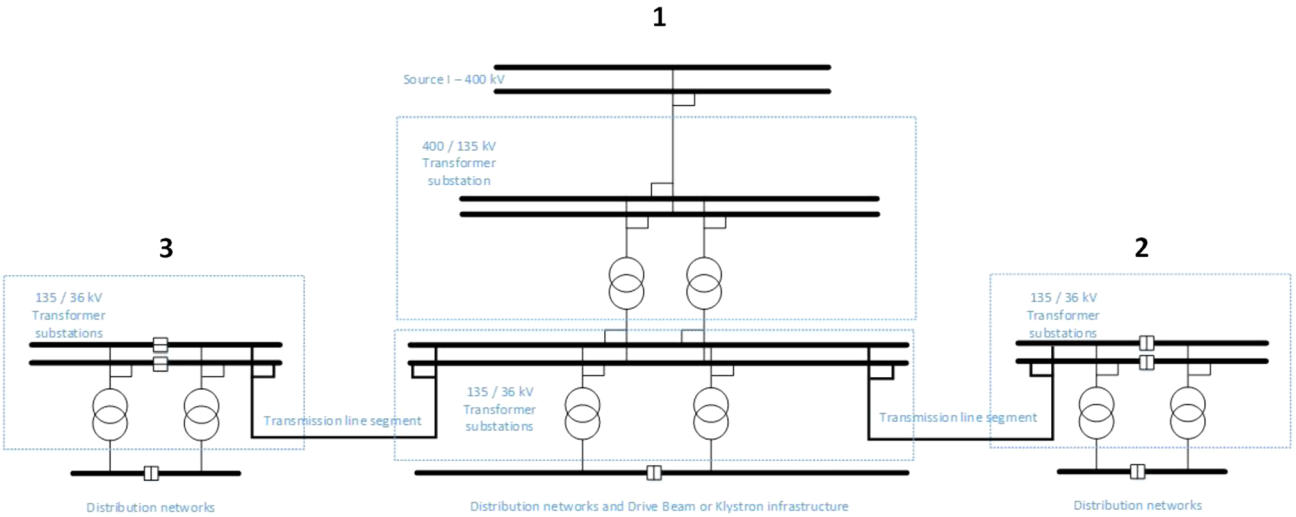

Fig. 79 Transmission network scheme for 380 GeV Drive Beam and Klystron configurations

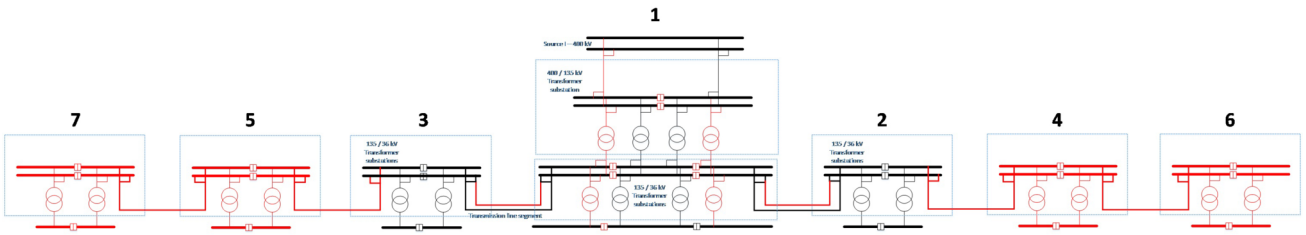

Fig. 80 Transmission network baseline for 1.5 TeV. The extension from the 380 GeV stage to the 1.5 TeV stage is shown in red

Table 41 Load classes and main characteristics

Load class	Loads type (non-exhaustive list)	Power unavailability duration in case of degraded scenario
Machine	Power converters, cooling and ventilation motors, radio frequency	Until return of main supply
General Services	Lighting, pumps, vacuum, wall plugs	Until return of main or secondary supply
Secured	**Personnel safety:** Lighting, pumps, wall plugs, elevators	10 – 30 seconds
Uninterruptable	**Personnel safety:** evacuation and anti-panic lighting, fire-fighting system, oxygen deficiency, evacuation **Machine safety:** sensitive processing and monitoring, beam loss, beam monitoring, machine protection	Interruptions not allowed, continuous service mandatory

5.2.6 Emergency power

The emergency power concept is based on the requirement to keep essential parts of the accelerator infrastructure operational if the normal power source fails. Particular emphasis is put on loads related to personnel and machine safety during degraded situations. The various load classes and types can be characterized as shown in Table 41. The main ranking parameters are the acceptable duration of the power interruption and whether the load is part of a personnel or accelerator safety system.

Machine loads are energised from the transmission network through the distribution network and do not have a second source of supply. The general services loads typically accept power cuts between several minutes and several hours, sufficiently long to commute to the second source or to wait until the main source is restored. In contrast, a more robust supply is required for secured loads, they include personnel and machine safety equipment or systems

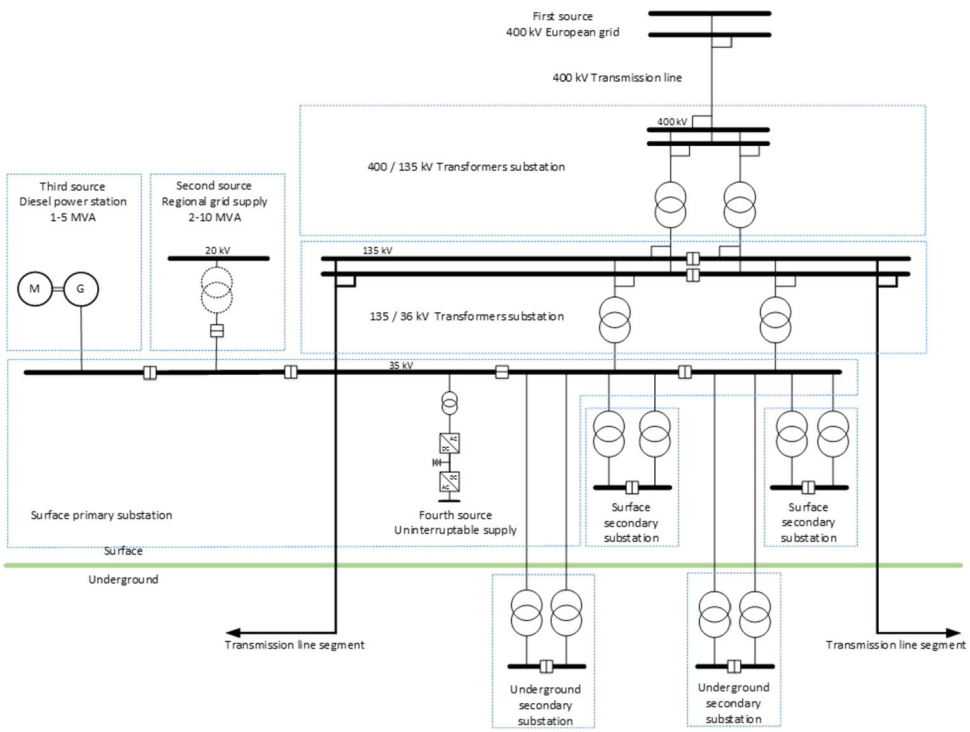

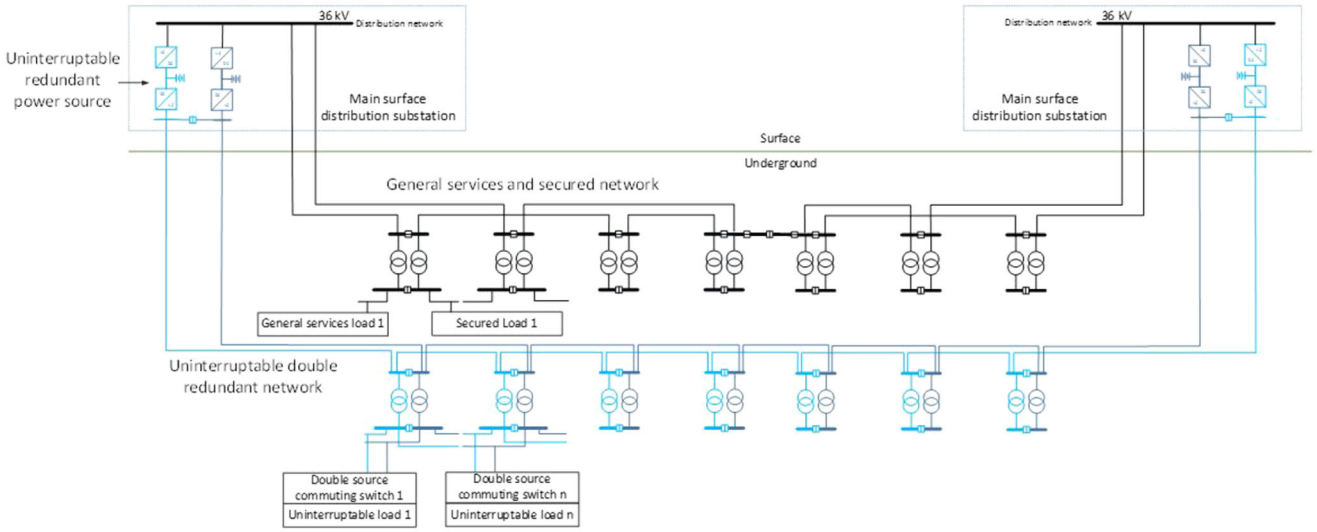

Fig. 81 Diagram of the distribution network of one CLIC point including the alternative power sources

Fig. 82 Functional scheme of the general services loads network and the double redundant uninterruptable loads network

that can sustain short power cuts up to a duration of 30 s. This is provided using three sources of supply. In a degraded situation, the first level backup is provided by the diesel power station, which typically starts up within 10 s. If the diesel power station is unavailable, the second level back-up supply comes from the regional grid. Finally, the most robust supply is provided to uninterruptable loads, which include personnel and machine safety equipment or systems that require continuous and stable power supply. A specific distribution scheme is used, the uninterruptable network scheme, which is composed of two redundant uninterruptable power supply (UPS) systems supplied from the distribution network in the two adjacent points. Downstream of the redundant UPS systems, a double redundant network delivers two independent sources, each coming from an adjacent point to the end-user plug. Each piece of end-user equipment has two entries and will manage the double source of supply. To meet safety and access requirements, UPS and batteries are located outside the tunnel and above ground. Figure 82 represents the functional scheme of the general services network and the double redundant uninterruptable loads network.

5.3 Cooling and ventilation

5.3.1 Introduction

This section is composed of two parts, the first detailing the piped utilities and the second outlining the ventilation systems for the CLIC complex. Throughout this chapter we introduce cooling equipment that has been selected according to the currently available heat loads. No safety margin has been applied to account for uncertainties, possible upgrades, or extensions.

This document reflects the current study for which most of the details are given for the 380 GeV scenario. Several uncertainties are yet to be clarified and some technical solutions will be revised as the project progresses through the technical design stage; however, the main architecture of the infrastructure is defined and will not change.

5.3.2 Piped utilities

Introduction The piping systems are mainly dedicated to the cooling of the accelerator equipment and the related infrastructure such as power converters, electronic racks, cables, etc. In addition, specific systems are foreseen to cover other general needs such as fire extinguishing plants, drainage and sump installations (for both surface and underground areas) and compressed air. The main systems presented within this section are:

1. Industrial and demineralized water: for the cooling of accelerator equipment and infrastructure;
2. chilled water: for ventilation plants;
3. drinking water: for sanitary purposes and make up of industrial water circuits as well as production of demineralized water;
4. industrial water for firefighting systems;
5. waste water: reject and clear water from underground and surface premises;
6. compressed air.

Water cooling circuits The two main typologies of water cooling circuits are defined according to their working temperatures: circuits cooled by cooling towers and working at temperatures higher than 27 °C and circuits using chillers to produce water at 6 °C.

The cooling plants have been divided into four independent sectors considering the working parameters, thermal loads and operability constraints. The sectors are as follows:

1. Drive-Beam Injector complex
2. Main-Linac tunnel
3. Experimental complex
4. Main-Beam Injector complex

The cooling towers for sectors 1, 3 and 4 are centralised at a single location set to minimise the distances to the different premises requiring cooling. For sector 2, a set of cooling towers are located at the surface "odd" shaft sites and will serve the two adjacent sectors via secondary circuits. For the 380 GeV machine, sector 2 will be exclusively served by the cooling towers placed centrally, close to the interaction point on the Prévessin site.

Where possible, the cooling plants will be located on the surface for accessibility and to facilitate operation and maintenance related activities.

In order to ensure the smooth running and operation of these systems and considering the accessibility conditions mentioned above, the redundancy has been set to N+1 for electromechanical systems. It is not necessary to ensure the same level of redundancy for the electrical cubicles and the control cubicles. In addition, a secured power supply for the cooling plants is not planned: in case of power failure, all accelerator related equipment will stop and therefore, will not require cooling.

Primary circuits The primary industrial water circuits, cooled by open wet cooling towers, are configured in closed loops to minimise the water consumption. These circuits will be used to cool demineralised secondary circuits, refrigerate chillers and direct expansion units.

Considering a tolerance of 0.5 °C, the design parameters are the following:

1. Cooling tower inlet: 33 °C
2. Cooling tower outlet: 25 °C

Primary circuits will use raw industrial water and the make-up is made with drinking water; a continuous water treatment against legionellae, scaling and proliferation of algae is foreseen.

Primary circuits are located at the surface. The only exceptions are the circuits connected to the underground caverns, where the distribution systems serving the equipment are installed. For most cases, this distribution system constitutes the secondary circuits.

Table 42 Primary circuit specifications, Two-Beam Machine

Sector	Structure	Cooling Power MW	Flow Rate m^3/h
1	Drive Beam Injector U	3.1	335
	Drive Beam Injector S	14.8	1595
	Frequency Multiplication Circuit a)	3.2	350
	Frequency Multiplication Circuit b), CR1 S, CR2 S and Transfer Line - CR2 to J.P.	16.8	1820
	Chillers Refrigeration - Drive Beam Injector S/U, Frequency Multiplication Circuit 1, RF Distribution Circuit 1,2 and 3	9.9	1070
	Chillers Refrigeration - CR1 S, CR2 S, Frequency Multiplication Circuit 2, 3, 4 and Transfer Line - CR2 to J.P.	1.8	200
2/3	Accelerator - LINAC	18.8	2030
	Main Tunnel (other equipment)	33.4	3600
	Injection Hall and Transfer Lines - e^+/e^-, Loop, J.P to S.P (P&ID Circuit B)	5.9	640
	Detectors S	0.9	100
	Detectors U	2.0	230
	Chillers Refrigeration - Buildings IP	1.7	190
	Chillers Refrigeration - Main tunnel	5.3	580
	Chillers Refrigeration - Detectors Hall S/U, Injection Hall, Transfer Lines - Loop and J.P. to S.P. (P&ID Circuit A)	2.2	240
	Main Tunnel Purge	1.2	130
4	Main Beam Injector U	3.9	420
	Main Beam Injector S	4.9	530
	Booster S/U, Damping Ring e^- S/U, and Transfer Line - Booster to J.P.	11.2	1210
	Pre Damping Ring S/U, Damping Ring e+ S/U	8.3	900
	Chillers Refrigeration - Main Beam Injector S/U, Compton Ring S, Traget Hall S	2.4	260
	Chillers Refrigeration - Pre Damping Ring S/U, Damping Rings e^+, e^- S/U, Booster S/U and Transfer Line - Booster to J.P.	4.4	480
	Total Cooling	156	

Secondary circuits Considering a tolerance of 0,5 °C, the working parameters are:

1. Supply from the station: 27 °C
2. Heat exchanger inlet: 35 °C

Secondary circuits will generally use demineralised water with a maximum conductivity of 0.5 μS/cm in a closed loop.

The demineralized water will partially be produced in a new central station for the entire complex. However, given the long distances between the central area and the equipment, it will not be possible to have an automatic refill pipework without degrading the quality of the water. Therefore, the refill can also be made by transporting the required volume of water in tanks.

Tables 42 and 43, outline the main cooling circuits, the associated cooling powers and flow rates for each sector.

Chilled water circuits Chilled water is used in the cooling batteries of air-handling units to cool the air; the working temperatures are:

1. Outlet from the station: 6 °C if dehumidification is required, if not: 12 °C
2. Return to the station: 12 °C if dehumidification is required, if not: 18 °C

Chilled water production plants are as close as possible to the air-handling units to which they are connected. Smaller stations, that are closer to the equipment, are preferred over one single central station.

Table 43 Secondary circuit specifications, Two-Beam Machine

Secondary Circuits, Demineralized Water			
Sector	Structure	Cooling Power MW	Flow Rate m^3/h
1	Drive Beam Injector U	3.1	335
	Drive Beam Injector S	14.8	1595
	Frequency Multiplication Circuit a)	3.2	350
	Frequency Multiplication Circuit b), CR1 S, CR2 S and Transfer Line - CR2 to J.P.	16.8	1820
2/3	Accelerator - LINAC	18.8	2030
	Main Tunnel (other equipment)	33.4	3600
	Injection Hall and Transfer Lines - e^+/e^-, Loop, J.P to S.P	5.9	640
	Detectors S	0.9	100
	Detectors U	2.0	230
4	Main Beam Injector U	3.9	420
	Main Beam Injector S	4.9	530
	Pre Damping Ring S/U, Damping Ring e^+ S/U	8.3	900
	Booster S/U, Damping Ring e^- S/U, and Transfer Line - Booster to J.P.	11.2	1210
	Total Cooling	127	

Most of the chillers will be water-cooled. Air-cooled chillers will only be employed if there are no cooling towers in the vicinity.

Air-handling units are located at the surface and in the caverns; therefore, there are chilled water circuits located in the main tunnels. The possibility of having direct expansion units instead of installing air-handling units is to be studied in the future.

The redundancy level follows the same principle as the primary circuits.

The chilled water circuit specifications are provided in Table 44.

See Fig. 83 for the process and instrumentation diagrams (P&ID) concerning the cooling plants for sectors 2 and 3.

Drinking water Drinking water is used for sanitary purposes and as make-up water for the cooling towers. At the central part of the accelerator and the injector complex it will be supplied via an extension of the existing drinking water network at CERN, the local public network will supply all the other surface sites.

Firefighting water network A firefighting water network will be implemented in all underground and surface areas: fire hydrants are foreseen at external areas, while flexible hoses are foreseen inside all premises.

These networks are to be connected to existing firefighting lines that are close to each surface point. For the injector complex they are connected to CERN's existing line.

Reject water Two separate networks, one for clear and one for sewage water will be installed in all underground and surface areas; these networks will then be connected to the corresponding existing systems at each area or surface Point.

At the release point in the surface, the pH and temperature of the rejected water will be monitored and corresponding alarms installed; if the quality of the water does not comply with the required level, retention basins or other measures will be taken to improve the quality before discharge.

Compressed air Compressed air production stations are foreseen on the surface, to serve both surface and underground areas. Their number and location will depend on future needs; it is likely that it will be necessary to install a station for the central area and another one for each surface point. An N+1 redundancy is foreseen for the air compressors of each station.

Table 44 Chilled water circuits specifications, Two-Beam Machine

Secondary Circuits, Demineralized Water			
Sector	Structure	Cooling Power	Flow Rate
		MW	m3/h
1	Drive Beam Circuit 1	2.0	340
	Drive Beam Circuit 2	1.4	250
	Drive Beam Circuit 3	1.4	250
	Drive Beam Injector S and Frequency Multiplication Circuit 1	1.5	260
	CR2 S, Frequency Multiplication Circuit 4 and Transfer Line - CR2 to J.P.	0.8	150
	RF Power Distribution Circuit 1	0.5	80
	RF Power Distribution Circuit 2	0.5	80
	RF Power Distribution Circuit 3	0.5	80
	CR1 S and Frequency Multiplication Circuits 2,3	0.6	100
2/3	Injection Hall, Transfer Line - Loop Circuit 1, J.P. to S.P. and e+	0.7	120
	Transfer Line - Loop Circuit 2 and e-	0.3	60
	Detectors Hall U and Detectors Hall S	0.7	120
	Main Tunnel	4.1	710
	Buildings IP	1.3	240
	Main Tunnel Purge	0.9	160
4	Main Beam S/U Circuit 1	0.8	150
	Main Beam S/U Circuit 2	0.4	80
	Main Beam S/U Circuit 3	0.4	80
	Booster S/U and Transfer Line - Booster to J.P.	0.9	170
	Damping Rings S/U and Pre Damping Rings S/U	2.4	420
	Buildings Shaft 2	0.3	50
	Buildings Shaft 3	0.3	50
	Compton Ring S, Traget Hall S	0.2	30
	Total Cooling	23	

5.3.3 Heating, ventilation and air conditioning

Introduction The heating, ventilation and air conditioning plants are designed to:

1. Supply fresh air for personnel,
2. Filter the supply and exhaust air,
3. Sustain a given temperature and/or humidity in each area,
4. Extract smoke and gas if necessary,
5. Purge the tunnels if necessary.

Indoor conditions Additional requirements for the temperature stability along the accelerator tunnel, operational, energetic and economical aspects have been taken into account. However, a detailed study considering all these points is still required.

The defined design ambient temperatures are:

1. Main-Linac tunnel, BDS, detector hall, caverns, dumps and turnarounds: 28 °C
2. Injectors, Booster, Damping rings, Transfer lines: 22 °C
3. Surface Buildings: 18 °C during winter, 25 °C during summer

The dew point is kept below 12 °C within the underground areas, no other regulation for the humidity is foreseen.

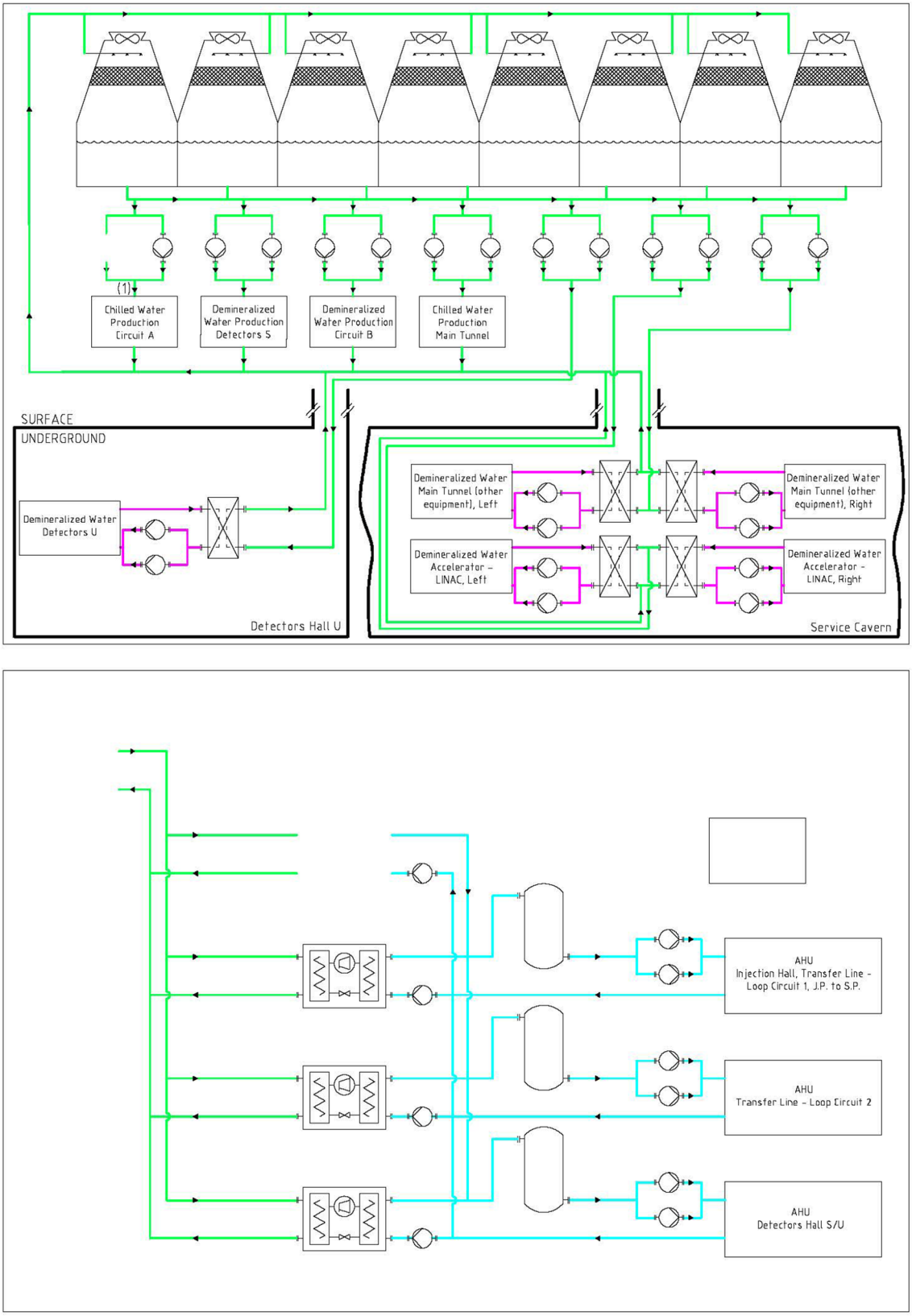

Fig. 83 Simplified P&ID concerning the cooling plants for sector 2 and 3

Table 45 Operational modes

Mode	Conditions
Run	No access, machines running, maximum air recycling
Purge	Before access where it is necessary, accelerator stopped, only fresh air
Shutdown	Open access, accelerator stopped, fresh air supply for people

Fig. 84 Drive-Beam option, HVAC schematic

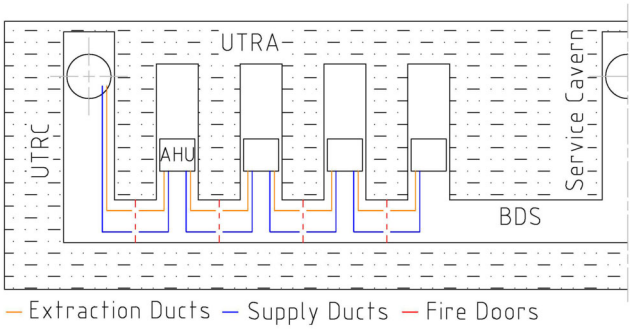

Table 46 Ventilation infrastructure for the accelerator gallery, Two-Beam Machine

Structure	Air-Handling Units			
	N°	N°	Cooling Power	Flow Rate
		—	kW	m^3/h
Accelerator Gallery - LINAC side	1	6	190	100540
		4	100	50270

The general outdoor conditions for the Geneva region, used to specify the air handling equipment, are 32 °C dry bulb and 40% for RH during summer and −12 °C and 90% during winter. Free cooling and air recycling principles will be adopted whenever possible.

Underground areas All underground areas are ventilated by air handling units located at the surface or in the caverns; a redundancy level of N+1 is foreseen, where required, to allow constant operation of the accelerator in case of a breakdown.

Smoke extraction shall be ensured by extraction units that are not equipped with filters to avoid clogging.

Operational modes A number of different modes are foreseen depending on the operating conditions. The fans have variable speed drives in order to adjust to the different operating conditions (Table 45).

Accelerating gallery Two different ventilation systems are foreseen for the main tunnel according to the operational mode of the accelerator:

- Shutdown and Purge mode: longitudinal ventilation is ensured by air handling units at the surface;
- Run mode: local cooling is ensured by units sited in the caverns, fresh air intake is not required.

During Shutdown and Purge mode, air handling units will supply air at a certain surface point and a second unit will extract the air at the adjacent surface point. For higher energy stages (1.5 TeV and 3 TeV) air is then recycled from the extraction unit to the supply unit of the adjacent point.

Additionally, it may be necessary to heat the air. For this propose, a heating coil is included in the air handling units.

In Run Mode, air is treated by air handling units located inside the UTRAs and UTRCs; each of these units are connected to ducts (supply and return) see Fig. 84. These units will be sized to absorb the heat loads in the tunnel. Presently, these units are not redundant due to space issues.

The supply and return grills at each of the ducts are longitudinally offset to ensure a better air distribution throughout the tunnel and to avoid bypass.

Table 46 shows the main parameters of the ventilation systems for the Two-Beam machine during run mode.

Other underground areas The remaining underground areas will use different ventilation schemes depending on heat loads, geometry and operational requirements.

The BDS is conditioned by air handling units placed at the surface, the detector hall and the experimental caverns will be ventilated by units located on the surface, while the beam dump caverns and UTRAs are ventilated by units installed within each structure. Ducts will provide proper air diffusion at these locations.

The Drive-Beam turnarounds are spatially close to the UTRAs and UTRCs. Hence, ducts will extend from an AHU, in the caverns, to the turnarounds. Due to space constraints there will be no redundancy for the AHUs serving the Drive-Beam turnarounds.

A longitudinal duct-free HVAC system is foreseen for the shallow underground tunnels: injectors, damping and combiner rings and transfer lines. The air-handling units are placed at the surface, close to the shafts, and supply the required ventilation.

The operational parameters for the underground areas are listed in Table 47, for the particular case of run mode.

Surface buildings The surface buildings will be ventilated by dedicated air handling units where heat loads or the size of the building requires it, several units shall be installed in the same building with each unit ventilating a specific area. Smoke extraction shall be ensured by dedicated smoke extractors located on the roof.

The operational parameters for the ventilation of the surface buildings are listed in Table 48 for the run mode.

A simplified P&ID concerning the ventilation of the service cavern and adjacent areas is shown in Fig. 85

Safety Smoke extraction systems are present in all the facilities presenting a risk related to fire loads or, where it is necessary to ensure the safety of personnel. In the event of a fire, the Fire Service will be able to switch off or manually reconfigure the ventilation system.

The concrete module for the lift and staircase in the shafts giving access to UTRCs will be kept over-pressured with respect to the surrounding underground areas thus allowing its use as a safe area in case of emergencies.

A pressure cascade is foreseen to prevent the migration of activated air from areas of high levels to areas with low levels of activation.

5.4 Transport and installation

5.4.1 Overview

The transport and installation activities for the CLIC construction start from the unloading of components when they arrive at the CERN site.

The most notable issue for transport and handling is the installation of the underground equipment. This section will focus on the significant changes to the Two-Beam module design and briefly discussing the CDR proposals. It is necessary to consider all the items that are to be transported and not only those that challenge the space constraints within the tunnel.

5.4.2 Equipment to be transported

Below is a list of the key equipment that will need to be installed in the underground structures:

1. RF modules
2. Magnets
3. Vacuum pipes
4. Beam dumps
5. Cooling and ventilation equipment
6. Electrical cables and cable trays
7. Racks

Transport and handling solutions for all standard equipment are the same as the ones defined in detail in the CDR, it is therefore foreseen to use industrial off-the-shelf handling equipment. The most significant challenge for transport and handling for the 380 GeV stage is the installation of the largest pieces of equipment, including, but not limited to, accelerating structures, klystron modules and magnets.

The transport and installation operations include:

1. Unloading and transportation within and between surface buildings for the purposes of assembly, testing and storage.
2. Transportation to the shaft access sites where items will, either, be installed in surface buildings or lowered to underground areas.
3. Transportation and installation throughout the tunnels and underground structures.

Table 47 Ventilation infrastructure for the underground facilities, excluding the accelerator gallery and redundant units, for Two-Beam machine

Sector	Structure Name	Air-Handling Units			Extraction Units	
		N	Cool. Power kW	Heat. Power kW	N	Flow Rate m3/h
1	Drive Beam Injector U	1	700	900	3	90740
		2	160	90		
	Frequ. Multip. U	1	200	70	1	96720
		1	90	40	1	48360
		1	70	30	1	36270
	Transfer Line - CR2 to J.P.	1	250	240	1	60450
		1	160	170	1	67170
2/3	Transfer Line - J.P. to S.P.	1	230	40	1	134330
	Transfer Line - Loop	2	120	40	2	68660
	Transfer Line - e^+	1	130	120	0	0
	Transfer Line - e^-	1	190	180	0	0
	Detectors Hall U	1	350	460	1	64180
	Main Beam Dumps	2	40	0		
	Drive Beam Dumps	8	10	0		
	Drive Beam Turnaround	8	20	0		
	UTRA	8	110	0		
	UTRC	2	110	0	2	56700
	Caverns 1.3 and 1.4	2	110	0		
	Survey Cavern 2.1 and 3.1	2	0	0		
	Additional Caverns 2.2 and 3.2	2	170	0		
	Service Cavern	2	110	0	2	56700
	BDS	4	130	0		
	Main Beam Turnaround e^+/e^- and Tunnel BC2 e^+/e^-	2	40	0		
	BC2 Caverns	2	30	0		
	Tunnel Purge	2	470	470	2	60570
	Lift Pressurized Area	3	0	0		
4	Main Beam Injector U	1	530	690	3	68790
		2	120	40		
	Booster U	2	110	20	3	60070
	Transfer Line - Booster to J.P.	1	160	80	1	67170
	Pre Damping Ring U	1	840	70	1	159190
	Damping Rings e+ U	1	610	450	1	203960
	Damping Rings e- U	1	350	80	1	203960

5.4.3 Surface

The capacities of the overhead travelling cranes are listed in Table 49.

5.4.4 Shafts

In the 380 GeV option three shafts provide underground access for the transportation of equipment. Considering the distances between the shafts (approximately 5 km) it was decided that two 3 tonne lifts per shaft will be used,

Table 48 Ventilation infrastructure for the surface buildings excluding redundant units, for Two-Beam machine

Sector	Structure Name	Air-Handling Units		
		N	Cooling Power kW	Heating Power kW
	Drive Beam Injector S	40	130	110
1	RF Power Distribution	3	450	450
	CR1 S and CR2 S	8	110	10
	Detectors Hall S	1	340	220
	IP - Electricity	1	240	240
	IP - Reception	1	40	40
	IP - Workshop	1	70	70
	IP - Service Office	1	180	180
2/3	IP - Control	1	100	100
	IP - Cryo	4	140	140
	IP - Survey	1	120	120
	IP - Gaz	1	60	60
	IP - Site Access Control	1	10	10
	Injection Hall	2	110	20
	Main Beam Injector S	9	100	20
	Compton Ring	1	140	140
4	Target Halls (LINACs 1 and 2)	2	20	20
	Booster S	6	100	10
	Damping Rings e^+/e^- S and Pre Damping Ring S	6	110	20
	Building Shaft 2 + 3 - Electricity	2	30	30
	Building Shaft 2 + 3 - Workshop	2	70	70
	Building Shaft 2 + 3 - Survey	2	10	10
	Building Shaft 2 + 3 - Access Control	2	10	10
	Building Shaft 2 + 3 - Shaft Access	2	160	160

as well as a handling opening (Fig. 87). This will significantly increase the rate of equipment transfer and provide a much-needed redundancy in case of failure or emergencies.

5.4.5 Underground

The main challenges for transport and handling throughout the main tunnel and ancillary structures are described. As the Drive Beam option has undergone only minor civil engineering upgrades, the most notable change between the 3 TeV and 380 GeV study is the number of modules to be transported in the tunnel presented in Table 50.

A conceptual design produced for the CDR [55] of a combined trailer-crane vehicle unit was elaborated for the transport and installation of modules and magnets to achieve the highest rates of installation compatible with space, precision, interconnection and fragility constraints. In view of the narrow transport passage and the distances to travel, the trailer-crane transport vehicles will be equipped with an automated guidance system. Each vehicle will be able to simultaneously transport two modules for logistics reasons.

UTRCs are designed so that modules and other equipment can be taken from the lift and positioned close to the transport and installation vehicle loading area, the loading of equipment is achieved by the vehicles' own lifting equipment or by the 10 tonne travelling crane installed in the UTRC. During the module installation phase it is planned to use the whole UTRC gallery floor for transport activities.

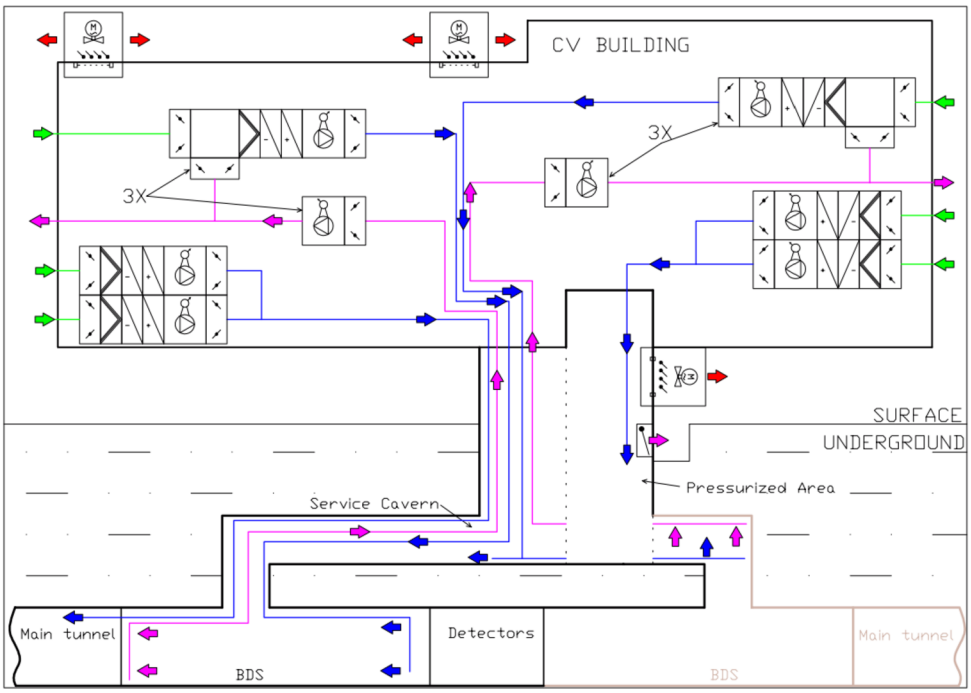

Fig. 85 Simplified P&ID concerning the ventilation of the service cavern and adjacent areas

Table 49 List of crane capacities

Building Type	Crane load capacity (tonnes)
Detector Assembly	2 × 80t + strand jacks (CMS approach)
Cooling Tower and Pump Station	3.2
Cooling and Ventilation	20
Cryogenic Warm compressor	20
Cryogenic Surface Cold Box	20
Workshop	10
Central Area Machine Cooling Towers	5
Shaft Access	20
Drive-Beam Injectors	5 × 5 (for 380 GeV)

5.4.6 Cost considerations

The greatest change in cost estimate for 380 GeV in comparison with 1.5 TeV comes from the reduction of the cost of operation (generally manpower), lifts and cranes (number of shafts) which is directly related to the length of the tunnel. As the installation rate is the same, based on the installation schedule, the number of special underground vehicles and expenses related to them will stay the same.

5.5 Safety systems during operations

The scale and complexity of a major scientific facility such as CLIC requires detailed consideration of the impacts that this could have on the health and safety of workers, visitors and those in the local community, as well as on the sustainability of the local environment. Through identification of the hazards at the earliest possible stage the risks can be mitigated by implementing appropriate control measures throughout the design process. Hazard controls can be implemented using standard best practices, or if necessary by performance based design (empirical methods or simulations, evaluated against key Health, Safety and Environment performance criteria). A hazard register has been drawn up to categorise such hazards, and identify the measures needed to assure both personal and process safety; this register will be kept live throughout the lifecycle of the project, to encompass changes and add detail as it develops. No substantial additional hazards have been identified for the expansion to the 1.5 TeV stage, with the same hazards as those for the 380 GeV Drive Beam option expected to apply.

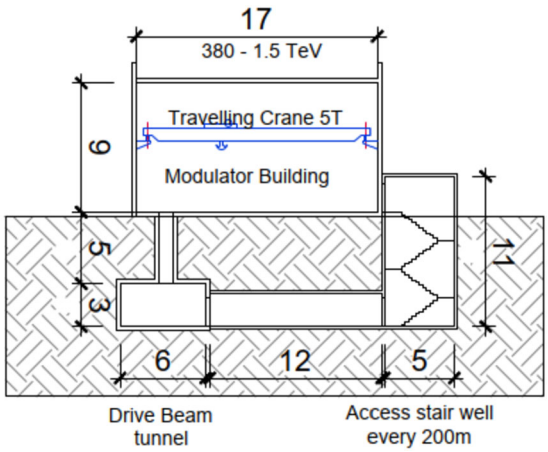

Fig. 86 Cross section of the Drive-Beam Injectors building

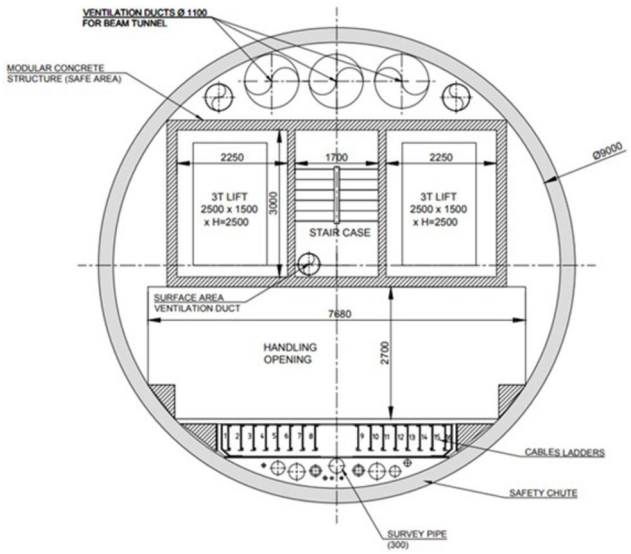

Fig. 87 Cross-section of the access shaft

Table 50 Modules for the 380 GeV stage, Two Beam machine

Type of equipment	Number
Modules	2,976
DB quadrupoles	5,952
MB Short quadrupoles	712
MB Long quadrupoles	436
Total	**10,076**

5.5.1 Mechanical hazards

No significant mechanical hazards have been identified beyond those expected for a comparable scientific or industrial installation. Lifting and handling of large pieces of equipment must be considered, as well as the number of motorised vehicles throughout the site, both during technical stops and operation. The limited number of cryogenic components (i.e. the superconducting wiggler magnets and other superconducting components) may introduce oxygen deficiency hazards, and a further risk assessment is to be made as part of detailed design to determine the need for additional mitigation or compensatory measures. There will also be a danger of hot or cold surfaces due to thermal inertia; the magnets and klystron HV tanks will be water cooled, and should therefore maintain a safe surface temperature. All of these hazards can be mitigated through compliance with the applicable CERN Safety Rules and use of European harmonised standards for design and fabrication.

5.5.2 Chemical hazards

The klystrons for the Drive-Beam option will be located within the surface building, with each modulator assembly being immersed in 1500 litres of oil, with the potential to use a lower flashpoint oil. The mitigation strategies will consist of a retention basin for each HV tank, with sufficient capacity for the entire quantity of oil stored in the tank. Coupled with this, an oil level detector shall be used to indicate any drop in level. As a further measure, consideration shall be given to the potential leak path should oil be spilled outside of the retention basins.

Another chemical hazard to be considered is that of lead used in shielding, most particularly around the klystrons for the shielding of X-rays. If embedded within the klystrons, care and appropriate personal protective equipment (PPE) will be required when handling the lead plates. However, if separate plates or blocks are used care must be taken so that the necessary procedures are followed for purchasing, shipping, storing and handling of the blocks to limit the dangers of lead poisoning or exposure to activated materials.

5.5.3 Fire safety

The CDR [55] set out the fire strategy for the Drive Beam option to include the following measures:

- Limiting the probability of onset of fire, with fire compartments every 439 m in the main accelerator tunnels,
- Early fire detection and intervention,
- Safe evacuation of personnel,
- Limiting the propagation of fire and smoke along the facility, including hot smoke extraction in the main accelerator tunnels.

These remain valid for the current design.

5.5.4 Environmental hazards

The environmental considerations are considerable, across a wide variety of environmental domains. A dedicated Whole Life Cycle Assessment (WLCA) has been performed to evaluate the carbon footprint for the CLIC realization and operation, with its impact on the environment. A separate paragraph is summarizing the most relevant outcomes of the study. Besides this, important considerations identified include:

- The volume of soil that will need to be excavated (and relocated) for the tunnels and shafts; the presence of natural hydrocarbons in the soil will also need to be taken into account,
- The use of surface cooling towers will require a study into the likely environmental impact and strategies (such as the disposal of rejected water),
- The effect of the construction on the water table, natural aquifers, and natural protected areas,
- The effect of the extremely large electrical infrastructure that will need to be installed, including many kilometres of electrical transmission cabling,
- Potential leakage of oil, and the dangers of this entering the surrounding environment or water sources,
- Identification and monitoring of ionising radiation effects on the surrounding environment,
- Greenhouse gas emissions from electrical, HVAC or detection equipment,
- Noise emissions of mobile or fixed sources,
- Electricity consumption.

A strategy for addressing these issues will be split across the project lifecycle phases. Initially, as part of early detailed design, the project will review and determine any potential additional environmental and socio-economic implications of those surface sites on the affected French and Swiss territories, and thus define any required additional mitigation measures that will be needed. All measures shall be planned and taken to reduce the environmental impact.

Once the general layout and site master plans are determined and following the indications of the WLCA, the project shall make an independent Environmental Impact Assessment (EIA) to provide assurance that all necessary measures to limit the impact of the project on the environment to an appropriate level have been taken. This assessment shall be based on the requirements of the applicable Host State legislation, i.e. *Ordonnance relative à l'étude de l'impact sur l'environnement (OEIE) and the Code de l'environnement, Livre I, Titre II, Chapitre II de la Partie Législative et Réglementaire.*

Electrical hazards The electrical hazards present for this project are considered standard for such an installation, but are nevertheless significant in their scale. Inside the tunnels there will be a number of high voltage systems, including the klystrons, modulators and magnets. The HV oil tank will be in place to insulate the klystrons and modulators, with pulse quality monitoring to identify any breakdown in the oil. NF C 18-510 compliant covers, and

restriction of access to those with the appropriate electrical training, shall also be in place. An effective strategy for the earthing system will also be required for areas of high voltage and power.

The supply infrastructure potentially represents a large number of hazards, from those frequently found at CERN, such as uninterruptable power supplies, transformers and power converters, through to some more novel challenges, such as the dangers of having high voltage and current supply cables close to workers during installation and maintenance, and the need to have protected control systems across adjacent fire compartments. The CERN Electrical Safety Rules shall be followed throughout the design process; where exceptions are required, this shall be subject to an appropriate level of risk assessment to evaluate the residual risk, and determine the mitigation strategies required.

Biological hazards The primary biological safety consideration identified for the project is the danger of Legionella in the cooling water circuits, and most particularly in the cooling towers. This hazard can be mitigated by following the regulations and standards for limiting the risk of Legionella bacteria and its dispersion in the atmosphere, and practices already in place for CERN's existing installations.

Non-ionising radiation hazards One significant hazard in this domain will be the Q-Switched, polarised laser, operating at a mean power per pulse of 1.5 kW, which will be used in the e^- production target. This will likely be a Class 4 laser, and the safety system will therefore need to meet the appropriate IEC required control measures; its operation in the 780-880 nm wavelength range indicates a particular danger to eyesight, which shall be compensated for accordingly and the appropriate interlock systems installed.

RF will also be a significant hazard throughout the accelerator. RF components purchased from industry are required to be CE marked and to comply with the EU emission norms for industrial environments. RF equipment built or installed at CERN shall be "leak-tight", and tested against EU industrial norms for RF emissions in situ. In case of an RF-related accident (for example the breaking of a waveguide), the mismatch in reflected power shall be detected, and trigger a cut in the electrical supply.

One comparatively novel hazard for CLIC is the potential presence of high flux density permanent, or hybrid magnets in the main accelerator. The extent of stray magnetic fields is not fully determined at this stage, but having permanent strong magnetic fields would mean that access to affected areas must be denied to those with pacemakers, and similar measures to those implemented in equivalent existing areas at CERN must apply, such as the requirement for non-magnetic tools.

Workplace hazards Many standard industrial hazards will need to be considered for those working in the CLIC tunnels and surface complexes. These include noise, lighting, air quality, and working in confined spaces, which can be satisfied by following existing CERN Safety practices and the Host States' regulations for workplaces.

The machine heat loads and the current design for the cooling and ventilation in the Main-Beam tunnel predict an ambient temperature of 30-40 °C during beam operation, when there is no access. The ambient temperature will therefore be important for access and work during both the short technical stops during the runs and the longer annual technical stops. With acceptable cooling periods during short shutdowns still to be decided, an initial guideline of 28 °C is recommended for manual work within the tunnels (across the full range of relative humidity values) during extended access periods. At higher temperatures, where manual work is required, care must be taken to monitor the condition of workers, ensuring reduced working time and increased rest and hydration in proportion to any increased heat stress.

Structural safety All infrastructure shall be designed in accordance with the applicable Eurocodes to withstand the expected loads during construction and operation, but shall also consider accidental actions, such as seismic activity, fire, release of cryogens and the effect of radiation on the concrete matrix of the tunnels.

Access safety and control systems The CLIC access system is based on several protection layers comprising site access, building access and personnel protection with dedicated access points to regulate the personnel access to the supervised and controlled machine areas. Each access point has one or more personnel access booths and an optional material booth. This ensures identification and biometric authentication thus regulating access at the highest safety level required according to the operation modes which are managed remotely by the CCC. In the machine tunnel, the safety is ensured by access or beam "Important Element for Safety (EIS)". The access system controls a number of independent beam zones divided into access sectors equipped with various safety elements. These access sectors are important for patrolling the machine and to minimise radiation exposure. Three access modes are foreseen; general, restricted with a safety token, and equipment test, these are automatically managed by the Personnel Protection System (PPS) or controlled by a human operator, locally or remotely from the CCC.

Each beam zone has its own independent access conditions, the absence of beam in each beam zone is guaranteed by at least two beam safety elements, with at least one passive element and one active element. These safety

measures are activated and interlocked by the access system, and, the access status can make a zone unsafe for operation with beam, or forbid access to the Machine if the status of a safety element is unsafe.

For this study, we have considered three protection layers: site, building and PPS for each of the five Main-Beam areas of the CLIC infrastructure.

1. Injector Linacs;
2. Sub-surface accelerator complex;
3. Transfer tunnels;
4. Main-Beam tunnel;
5. Experimental area.

The access conditions for CLIC require further studies once the accessibility requirements of each machine segment have been defined. Each of the four shafts are equipped with access points, at the surface and underground, to regulate access from the shaft caverns to the main tunnel and experimental area. There are also several other access points required to regulate access to each sector of the Machine.

5.6 Radiation protection

For the mitigation of risks associated with ionising radiation, the existing CERN radiation protection rules and procedures are used. Risks resulting from ionising radiation must be analysed from a very early design phase onwards and mitigation approaches must be developed. Design constraints will ensure that the doses received by personnel working on the sites, as well as the public, will remain below regulatory limits under all operation conditions. A reliable and continuously operating radiation monitoring system will therefore be an important part of the system implementing risk control measures.

Radiation protection is concerned with two aspects: protection of personnel operating and maintaining the installations and the potential radiological environmental impact. The potential radiological hazards to personnel working on the site are classified by the following sources, particle beam operation, activated solids, liquids and gases and parasitic X-ray emitters.

5.6.1 Particle beam operation

Radiation hazards will arise from the operation of the electron and positron beams. The direct exposure to stray radiation is prevented by installing the high energy accelerator parts in a deep underground tunnel, which is inaccessible during beam operation. The central injector complex, where beams operate at lower energies, is closer to the surface and covered by about 5 m of shielding. Access shafts and ducts to the tunnels are located and designed to effectively reduce the transmission of ionising radiation to acceptable levels in all accessible areas.

The radiation protection aspects remain unchanged with respect to the points addressed in the CDR [55]. For both the Drive and Main Beams, an upper beam loss limit of 10^{-3} was determined. Monte Carlo simulations demonstrated that even with this pessimistic beam loss scenario, residual dose rates in the range of 10-100μ Sv/h in the accelerator tunnel will allow hands-on maintenance after reasonable cool-down times.

5.6.2 Activated solids, liquids and gases

The residual dose rate levels from activation in the Main and Drive-Beam tunnels are of lesser concern [55]. The average dose rate levels will be relatively low in the μSv/h range or below, and compatible with standard intervention procedures. Special attention needs to be paid to particular beam line elements and areas where beam losses will be concentrated.

The activation of the positron production target and its surroundings must be studied in detail. The design will need to take into account the potentially high activation of the target and the need for specific shielding and target handling.

Further radiation protection studies are required on:

- Activation in the various bending structures,
- The Main-Beam collimation systems,
- The Drive-Beam PET structures.

Activation of beam line elements and the resulting needs for material optimisation and specific handling procedures may be a technical and engineering challenge, but, are considered to be feasible considering the existing experience in the design of targets and collimators at CERN.

The beam dumps for the Drive and Main Beams require a careful technical design to contain and handle the activated water. More detailed studies on the activation of the post-collision absorbers, intermediate and final

dumps and their respective shielding are required. Initial studies of the Main-Beam dump indicate a considerable activity inventory of several tens of TBq of Tritium after several years of operation [108], which nevertheless can be technically handled.

The activation of water in the closed water cooling circuits needs to be evaluated in more detail. However, given the low residual dose rates from the limited beam losses in the Main-Beam tunnel, water activation in these circuits is not expected to be a major concern.

Air activation needs to be studied as it may be the major contributor to the radiological environmental impact. A good design approach will foresee recycling modes for the ventilation systems during beam operation which will effectively reduce the release of short-lived isotopes. Before access is granted, the tunnel air will need to be purged after a short waiting time to avoid undue exposure of personnel during the interventions.

5.6.3 Parasitic X-ray emitters

Klystrons are strong parasitic X-ray emitters. The design of these devices must include shielding against the generated X-rays so that they can be installed in areas accessible during their operation. Standard prescriptive regulations are an effective control measure for this specific hazard.

6 Schedule, cost estimate, and power consumption

6.1 Construction and operation schedules

The construction schedules presented in this section are based on the same methodologies as those used for the CLIC CDR [1]. Following input from equipment experts and the CERN civil engineering and infrastructure groups, small adjustments were made to the construction and installation rates used for the schedule estimates. Details about the various parameters used can be found in [5]. The installation is followed by hardware commissioning, final alignment and commissioning with beam.

6.1.1 380 GeV schedule

The technically limited schedule for the first stage of CLIC stage at 380 GeV is shown in Fig. 88. It comprises the following time-periods:

- Slightly more than five years for the excavation and tunnel lining, the installation of the tunnel infrastructures, and the accelerator equipment transport and installation.
- Eight months for the system commissioning, followed by two months for final alignment.
- One year for the accelerator commissioning with beam.

In parallel, time and resources are allocated for the construction of the drive-beam surface building, the combiner rings, damping rings, main-beam building and experimental areas, and their corresponding system installation and commissioning, as shown in Fig. 88.

6.1.2 Schedules for the stages at higher energies and the complete project

The 380 GeV collider is designed to be extended to higher energies. Most of the construction and installation work can be carried out in parallel with the data-taking at 380 GeV. However, it is estimated that a stop of two years in accelerator operation is needed between two energy stages. This time is needed to make the connection between the existing machine and its extensions, to reconfigure the modules used at the existing stage for their use at the next stage, to modify the beam-delivery system, to commission the new equipment and to commission the entire new accelerator complex with beam.

As the construction and installation of the 1.5 TeV extension cover a period of 4.5 years, the decision about the next higher energy stage needs to be taken after ∼4-5 years of data taking at the existing stage, based on physics results available at that time. The corresponding schedule scenario is shown in Fig. 89 for the drive-beam based scenario. A more detailed breakdown of the full technical project schedule can be found in [5].

In a schedule driven by technology and construction, the CLIC project would cover 29 years as shown in Fig. 89 [5], counted from the start of construction. This schedule has a technically limited seven years of construction and commissioning phase, which we increase to ten years to provide some contingency in the overall schedule presented in Table 55. The suggested 22 years of CLIC data-taking include an interval of two years between the stages.

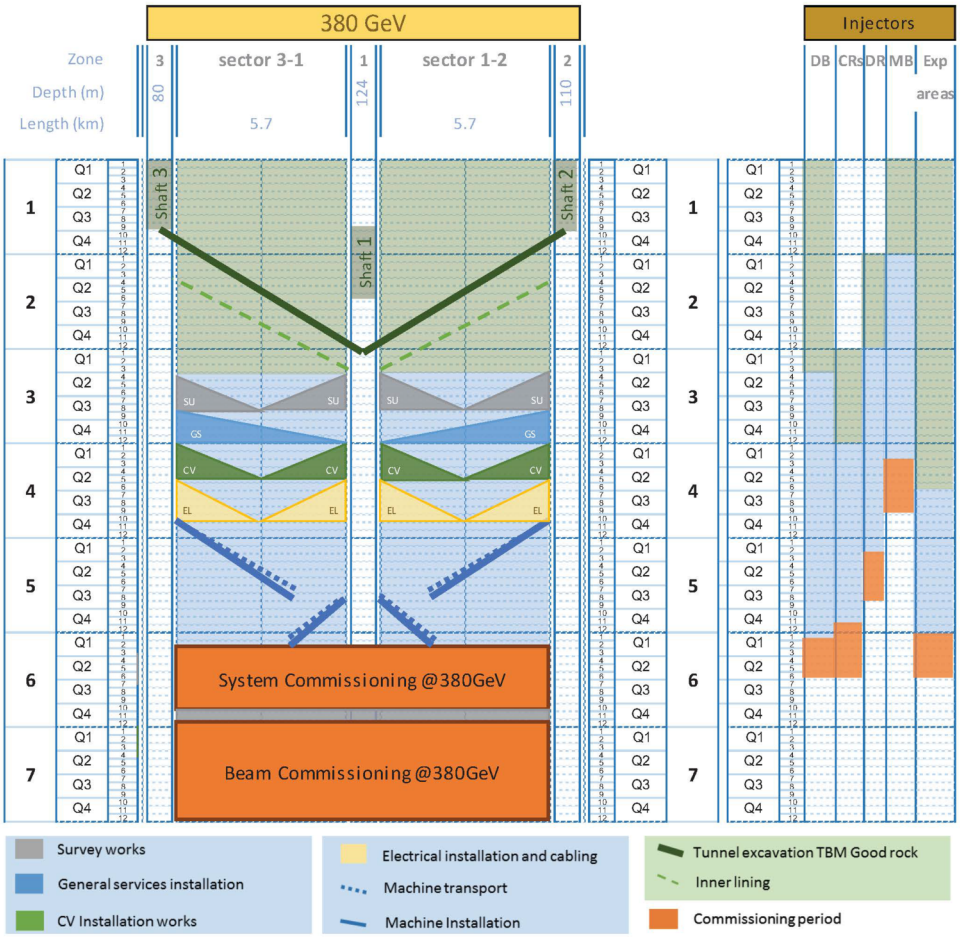

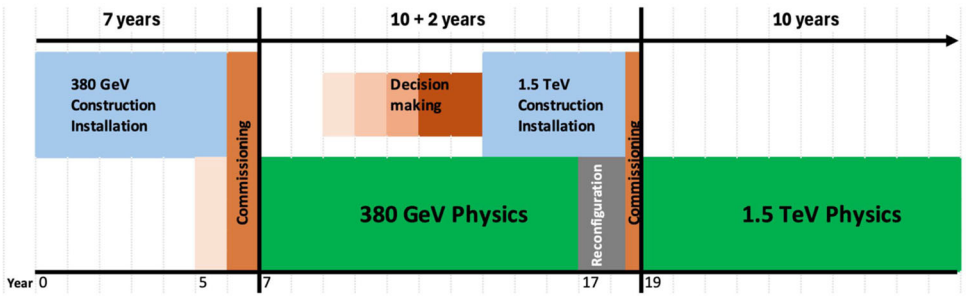

Fig. 88 The technically limited construction and commissioning schedule for the 380 GeV drive-beam based CLIC facility. The vertical axis represents time in years. The abbreviations are introduced in Fig. 1

Fig. 89 Technology and construction-driven CLIC schedule, showing the construction and commissioning period and two stages for data taking. In the CLIC implementation planning the construction phase is increased to ten years to provide some contingency in the overall schedule presented in Table 55. The time needed for reconfiguration (connection, hardware commissioning) between the stages is also indicated and will be further refined based on the experience gained during the initial stage installation and operation phases. The energy of the high-energy stage can be decided upon, and most of the tunnel can be dug and equipped, while running the first energy stage

6.1.3 Concluding remarks on the construction schedule

The schedule for construction, installation and hardware commissioning shows that the initial 380 GeV stage of CLIC can be completed in ten years from construction launch.

The most critical CLIC technology-specific items driving the schedule are the main-beam module production and installation, as well as the RF units. The other schedule drivers, such as the tunnelling, the buildings, and the infrastructures are more common, similar to other projects at CERN and elsewhere.

6.2 Cost estimate

For the cost estimate of CLIC the methodology used is the same as for previous CLIC cost estimates and the estimates of other projects, such as the LHC experiments and the Reference Design Report and Technical Design Report of the International Linear Collider (ILC) [300, 301]. Previous CLIC cost estimates were reported in the CLIC CDR [2] for two different implementation options at 500 GeV. The methodology and results were reviewed by an international panel at that time.

An initial cost estimate for the first stage at 380 GeV was presented together with the introduction of the corresponding CLIC energy staging scenario in [4]. Since then, many CLIC optimisation studies were undertaken with a particular focus on cost reduction, for the 2018 Project Implementation Plan [5]. The resulting cost estimates, as well as the methodologies and assumptions used were presented in November 2018 to a cost review panel composed of international experts. After recommendations on minor issues by the review panel, the estimates were updated accordingly.

For the 2024 value estimate, again a bottom-up approach is used, following the work breakdown structure of the project, starting from unit costs and quantities for components, and then moving up to technical systems, subdomains and domains. This allows accounting for all aspects of the production process and the application of learning curves for large series. For some parts (e.g. standard systems), cost scaling from similar items is used, implying that detailed knowledge on the work breakdown is not required, but rather estimators characterising the component. When possible bench-marking has been made with other project studies at CERN, in many cases costed by the same equipment groups.

The resulting estimated cost of the 380 GeV stage is presented, together with an estimate for upgrading to higher energies.

6.2.1 Scope and method

CLIC is assumed to be a CERN-hosted project, constructed and operated within a collaborative framework with participation and contributions from many international partners. Contributions from the partners are likely to take different forms (e.g. in kind, in cash, in personnel, from different countries, in different currencies or accounting systems). Therefore a "value and explicit labour" methodology is applied. The value of a component or system is defined as the lowest reasonable estimate of the price of goods and services procured from industry on the world market in adequate quality and quantity and satisfying the specifications. Value is expressed in a given currency at a given time. Explicit labour is defined as the personnel provided for project construction by the central laboratory and the collaborating institutes, expressed in Full Time Equivalent (FTE) years. It does not include personnel in the industrial manufacturing premises, as this is included in the value estimate of the corresponding manufactured components. The personnel in industrial service contracts that are part of the accelerator construction, outside CERN or at CERN, are also accounted for in the value estimate of the corresponding items.

The basic value estimate concerns the construction of the 380 GeV CLIC stage on a site close to CERN, where the 380 GeV stage of CLIC constitutes a project in itself. As a consequence, large-series effects expected on unit costs – learning curves and quantity rebates – remain limited to the quantities required for the completion of the 380 GeV stage. The corresponding incremental value for upgrading to higher energies is given.

The value estimates given cover the project construction phase, from approval to start of commissioning with beam. They include all the domains of the CLIC complex from injectors to beam dumps, together with the corresponding civil engineering and infrastructures. Items such as specific tooling required for the production of the components, reception tests and pre-conditioning of the components, and commissioning (without beam) of the technical systems, are included. On the other hand, items such as R&D, prototyping and pre-industrialisation costs, acquisition of land and underground rights-of-way, computing, and general laboratory infrastructures and services (e.g. offices, administration, purchasing and human resources management) are excluded. Spare parts are accounted for in the operations budget. The value estimate of procured items excludes VAT, duties and similar charges, taking into account the fiscal exemptions granted to CERN as an Intergovernmental Organisation.

As mentioned the CLIC cost estimate and the adopted methodology were already reviewed a first time in 2012, at the time of the CDR, by a panel of international experts chaired by Lyn Evans, and later in 2018, in preparation of the PIP, by a smaller panel of external reviewers, who focused their attention on the 380 GeV stage. The method followed for the 2024 cost update is based on the analysis of the work breakdown structure similarly as in 2018. The approach consisted primarily in the identification of major cost drivers and areas of the machine where significant changes in the design were produced or where a more accurate costing could be obtained with respect to the previous exercise.

The motivation for a deeper cost update for some cost elements and the methodology followed are summarized in the following list:

- **Main Beam production**: a new design was produced for the Main Beam injectors and the Damping Rings. An important reduction of the energy consumption is now realized in the injectors, with new and optimized accelerating structures. The cost review could benefit from the accurate study produced by PSI for the proposal of the injector complex for the FCC and the cost values that were entered here have been provided by industrial suppliers. The re-design of the CLIC Damping Rings was suggested by the considerable progress observed in recent years with the lattice design of light sources, with the additional motivation of introducing a superconducting RF system to drastically reduce the thermal losses. In this case the cost of the RF system could benefit from the analysis work produced by the CERN RF Group that was also used for the FCC costing while the cost of magnets was built on the figures developed in 2018 [279] and escalated to 2024 following the increase of the Swiss price index for import and industrial production equal to 5% [302].
- **Drive Beam production**: also in the case of the Drive Beam injector, the possibility to reduce the overall energy consumption together with the availability of more powerful klystrons led to the design of a more efficient accelerating structure with respect to 2018, which allowed for a reduction in the number of RF systems. The cost of klystrons and modulators was increased by 20% to take the cost associated to the power increase into account. The costs of these items use a common methodology for CERN studies and projects. The cost of accelerating structures was increased by 10% to account for the length increase.
- **Two-Beam accelerator**: in 2018 the analysis of cost was based on the CDR estimate produced in 2012, with the cost for the production of the RF structures for the main beam accelerator (SAS) and those for the RF power transfer (PETS) that was updated to the most recent experience with the fabrication of prototype structures. Mild learning curves were applied to the small series cost and the average resulting cost was benchmarked to values that resulted from the study that had been performed for the CDR in collaboration with industry [303]. Initial values for 2024 were obtained from reviewed 2018 estimates that were escalated to the 2024 cost index, following the increase of the Swiss price index for import and industrial production equal to 5% [302]. In this report, very conservative learning curves were adopted for accelerating cavities and PETS, with a learning factor at 0.94.

  The cost of power converters and cabling for the Main Beam and Drive Beam quads was also updated and documented [304].
- **Beam Delivery System(s)** (BDS): The complete reorganization of the interaction region, to make space for two experiments that may take data at the same time, has produced two new beam delivery systems that maintain the magnet design adopted in 2018, for which a fabrication cost was provided at the time. As for all magnets, which are all of the warm kind, their cost was calculated on the basis of a rather detailed design that produced realistic cost figures. The 2018 cost for magnets has been escalated to 2024.
- **Beam Instrumentation**: the value of the different beam instrumentation devices was re-evaluated, by considering recent information from industry and direct experience with recent purchase orders in the frame of the HL-LHC and LHC Injectors Upgrade (LIU). The requirements for signal transmission were included whenever they were not already present. The complete need of instrumentation was reviewed across the whole complex and aligned to the criteria expressed for other CERN projects.
- **Civil Engineering**: due to the general reorganization of the CLIC complex layout, an updated design for the Civil Engineering realizations was produced. The cost estimate has been built from scratch by following the methods that were already in place at the time of the Project Implementation Plan, in 2018, and by sharing the approach and the assumptions adopted for the LCF@CERN and also to FCC when possible.
- **Electrical and Cooling and Ventilation Systems**: Both systems have been impacted by the new high efficiency injector complex on the one side and by the increased duty cycle at 380 GeV for the two detector operation on the other side. A review of the 2018 design and costing was necessary, based on the existing architecture. The new cost estimate benefits from the data collection of recent estimates performed for other projects and from revisited quantities.

The uncertainty objective for the final estimate is ±25%. To this aim, uncertainties on individual items are grouped in two categories. The first one, *technical uncertainty*, relates to technological maturity and likelihood of evolution in design or configuration. The second category, *commercial uncertainty*, relates to uncertainty in commercial procurement. Based on a statistical analysis of LHC procurements this uncertainty is estimated as $50\%/n$, where n is the number of expected valid bids for each component [305].

The CLIC value estimates are expressed in Swiss franc (CHF) of December 2024, with a EURO/CHF exchange rate of 0.94.

6.2.2 Value estimates and cost drivers

The breakdown of the resulting cost estimate up to the sub-domain level is presented in Table 51 for the 100 Hz, double BDS-version of the 380 GeV stage of the accelerator complex. Figure 90 illustrates the sharing of cost between different parts of the accelerator complex. The injectors for the main-beam and drive-beam production

Table 51 Cost breakdown for the 380 GeV stage of the CLIC accelerator

Domain	Sub-Domain	Cost [MCHF]
Main-Beam Production	Injectors	168
	Damping Rings	386
	Beam Transport	492
Drive-Beam Production	Injectors	560
	Frequency Multiplication and Beam Transport	500
Main Linac Modules	Main Linac Modules	2133
	Post decelerators	46
Beam Delivery and Post Collision Lines	Beam Delivery Systems	172
	Final focus, Exp. Area	20
	Post-collision lines/dumps	100
Civil Engineering	Surface installations	367
	Underground structures	936
Infrastructure and Services	Electrical distribution	265
	Survey and Alignment	204
	Cooling and ventilation	562
	Transport / installation	62
Machine Control, Protection and Safety systems	Safety systems	76
	Machine Control Infrastructure	153
	Machine Protection	15
	Access Safety & Control System	24
Total (rounded)		7240

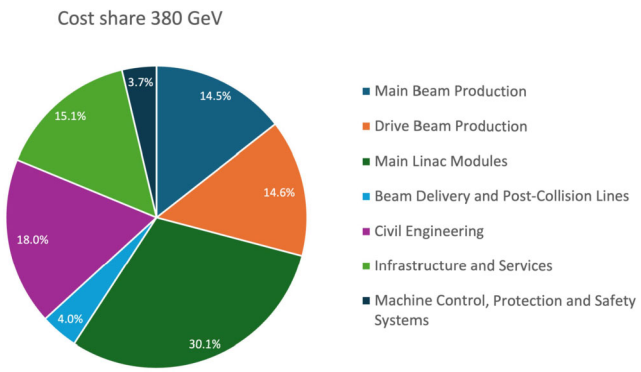

Fig. 90 Cost breakdown for the 100 Hz 380 GeV stage of the CLIC accelerator, with a dual beam-delivery system and two interaction regions. The total cost is 7240 MCHF

are among the most expensive parts of the project, together with the main linac, and the civil engineering and services. A very preliminary estimate of costs, based on scaling from other CERN projects and studies and referring to the treatment of excavated materials, would add 1.0-1.5% to the total cost.

Combining the estimated technical uncertainties yields a total (1σ) error of 1561 MCHF for the drive-beam based facility. In addition, the commercial uncertainties, defined above, need to be included. They amount to 910 MCHF. The total uncertainty is obtained by adding technical and commercial uncertainties in quadrature. Finally, for the estimated error band around the cost estimate, the resulting total uncertainty is used on the positive side, while only the technical uncertainty is used on the negative side [2]. The cost estimate for the first stage of CLIC including a 1σ overall uncertainty is therefore:

$$\text{CLIC 380 GeV, 100 Hz, two interaction regions:} \quad 7240^{+1807}_{-1561}\ \text{MCHF}.$$

The 250 GeV configuration will cost around 10% less than the 380 GeV complex, by making the assumption that it would adopt the same civil engineering and technical infrastructure as the 380 GeV stage. The only difference between the two energy stages would be that fewer RF modules would be installed in the Main Linac tunnel for the 250 GeV stage and a reduction of the drive beam energy would be possible.

The increase of cost to go from 380 GeV to 550 GeV is 30%, since it would require an extension of the Main Linac tunnel and additional modules.

The cost composition and values of the 1.5 TeV configuration has also been estimated in some detail. The energy upgrade from 380 GeV to 1.5 TeV has an estimated cost of ∼7.1 billion CHF, including the upgrade of the drive-beam RF power needed for the 1.5 TeV stage.

The CLIC technical cost drivers have been identified, together with potential cost mitigation alternatives. These will be addressed in the next phase of the CLIC project as discussed in Sect. 7. In general, further cost reduction studies will require close collaboration with industry. Beyond technical developments, optimal purchase models need to be defined, optimising the allocation of risks and production responsibilities between industry, CERN and collaboration partners in each case. In particular, the module production and RF units are important cost drivers where further industrial studies and validation will be important.

6.2.3 Labour estimates

A first estimate of the explicit labour needed for construction of the CLIC accelerator complex was obtained for the CLIC CDR in 2013 [2] by assuming a fixed ratio between personnel and material expenditure for projects of similar nature and size. Scaling with respect to the LHC - a CERN-hosted collider project of similar size to CLIC - provides a good estimator. Data from the LHC indicate that some 7000 FTE-years were needed for construction, for a material cost of 3690 MCHF (December 2010), corresponding to about 1.9 FTE-year/MCHF. About 40% of this labour was scientific and engineering personnel, and the remaining 60% worked on technical and project execution tasks. In the ILC TDR in 2013 a bottom up estimate made for ILC yielded 1.8 FTE-year/MCHF. In terms of complexity, the different CLIC sub-systems resemble the LHC and ILC cases. Although the RF technology differs between ILC and CLIC, the main elements of the accelerator complex are similar in the two projects.

The Snowmass 2021 Collider Implementation Task Force [306] built further on this methodology, considered estimates from several other projects, and proposed a more general formula:

$$Explicit\ Labour = 15.7 \cdot (Value)^{0.75}, \tag{4}$$

with Explicit Labour in FTE-years and Value in MCHF of 2010. Civil Engineering Costs are not included in the Value. Applying the formula above yields approximately 10500 FTEy of explicit labour. An important part of these could be covered outside CERN, for in-kind deliverables.

6.2.4 Operation costs; replacements, energy and personnel

A preliminary estimate of the CLIC accelerator operation cost, with focus on the most relevant elements, is presented here. The material cost for operation is approximated by classifying construction items into:

- Fixed accelerator installations, taken to be the total costs for modules, magnets, etc
- “Consumables”, taken to be the costs for RF power equipment, magnet power supplies, etc
- Technical infrastructure, taken to be the costs for infrastructure such as cooling and ventilation, electric power infrastructure, installation equipment, etc

and assuming a replacement and maintenance cost per year of 1% / 3% / 5%, respectively, of the corresponding capital expense.

An important ingredient of the operation cost is the CLIC power consumption and the corresponding energy cost. With an energy consumption at 0.82 TWh for 380 GeV and a price of 80 CHF / MWh the energy costs will be 66 MCHF annually, increasing to 112 MCHF at 1.5 TeV for 1.40 TWh. The expected energy consumption of the 380 GeV CLIC accelerator, operating at nominal luminosity, corresponds to 2/3 of CERN’s total energy consumption today.

Concerning personnel needed for the operation of CLIC, one can assume efforts that are similar to large accelerator facilities operating today. Much experience was gained with operating Free Electron Laser linacs and light-sources with similar technologies. The maintenance programme for equipment in the klystron galleries is demanding, but is not expected to impact strongly on the overall personnel required for operation. The RF systems, injectors and drivebeam, are above ground concentrated in a small area at the CERN Prévessin site. The ILC project has made a detailed estimate of the personnel needed to operate ILC, yielding 640 FTE for 250 GeV and 850 FTE for 500 GeV. Such numbers are also in line with LHC experience, assuming personnel costs to be similar

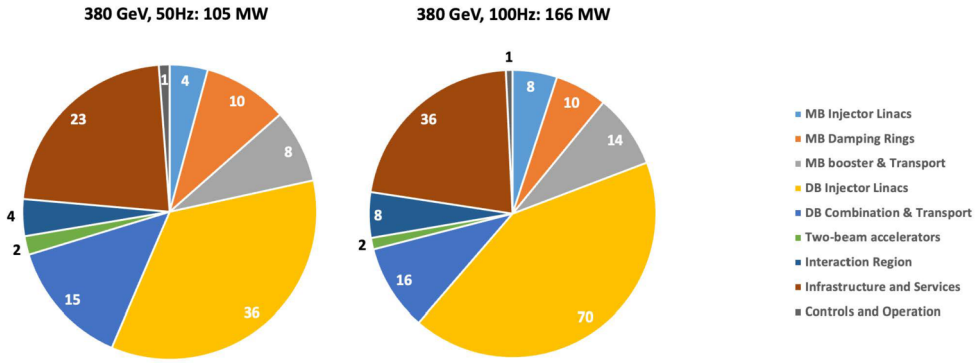

Fig. 91 Breakdown of power consumption between different domains of the CLIC accelerator in MW, at a centre-of-mass energy of 380 GeV. For the 100 Hz baseline machine, with two interaction regions, the contributions add up to a total of 166 MW. For the 50 Hz machine, with one interaction region, the contributions add up to 105 MW

Fig. 92 Breakdown of power consumption at a centre-of-mass energy of 1.5 TeV. For the 50 Hz machine, with one interaction region, the contributions add up to 287 MW

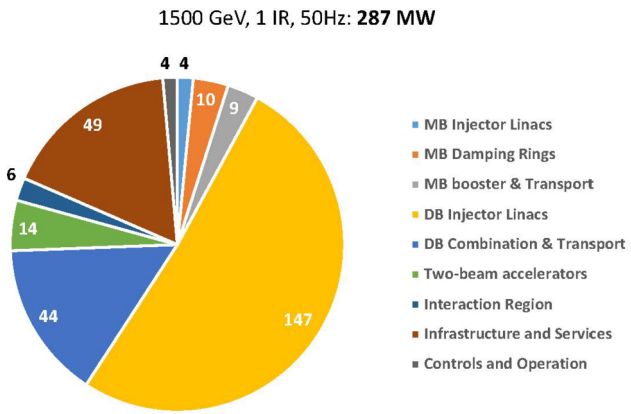

to hardware maintenance costs, and estimating an average cost of 210k per FTEy. In the framework of CERN, these numbers would distribute across scientific/engineering/technical staff, technical service contracts, fellows and administrative staff. The level of CLIC annual operational personnel support required is thus expected to be around 650 FTEy for CLIC 380 GeV.

Given the considerations listed above, one can conclude that operating CLIC is well within the resources deployed for operation at CERN today. Operating CLIC concurrently with other programmes at CERN is also technically possible. This includes LHC, as both accelerator complexes are independent. Building CLIC is not destructive with respect to the existing CERN accelerator complex. Electrical grid connections are also independent. However, important limitations would arise from availability of resources, in particular personnel, maintenance costs and overall energy consumption.

6.3 Power and energy consumption

The nominal power consumption at the 380 GeV stage has been estimated based on the detailed CLIC work breakdown structure. This yields, for the 100 Hz baseline option at 380 GeV with two interaction regions, a total of 166 MW for all accelerator systems and services, taking into account network losses for transformation and distribution on site. For the 50 Hz reduced power machine, assuming one interaction region, the total is 105 MW. The breakdown per domain in the CLIC complex (including experimental area and detector [307]) and per technical system is shown in Fig. 91. The equivalent analysis at 1.5 TeV yields 287 MW running at 50 Hz. Most of the power is used in the drive-beam and main-beam injector complexes, comparatively little in the main linacs. Among the technical systems, the RF represents the major consumer.

These numbers are significantly reduced over the last five years [5] due to the optimisation of the injectors for 380 GeV, introducing optimised accelerating structures for this energy stage, significantly improving the RF efficiency for all systems, and consistently using the expected operational values instead of the full equipment capacity in the estimates. Notably, re-design (2020-2021) of the damping ring RF systems, and the introduction of higher efficiency L-band klystrons (discussed in Sect. 4.4.2), have brought significant reductions.

The reductions have also been applied to the 1.5 TeV stage, see Fig. 92, operating at 50 Hz.

Table 52 Estimated power consumption of CLIC at the two centre-of-mass energy stages and for different operation modes

Collision energy [GeV]	Running [MW]	Short [MW]	Off [MW]
380 50 Hz	105	17	10
380 100 Hz	166	17	10
1500 50 Hz	287	33	13

Fig. 93 Operation schedule in a "normal" year (days/year)

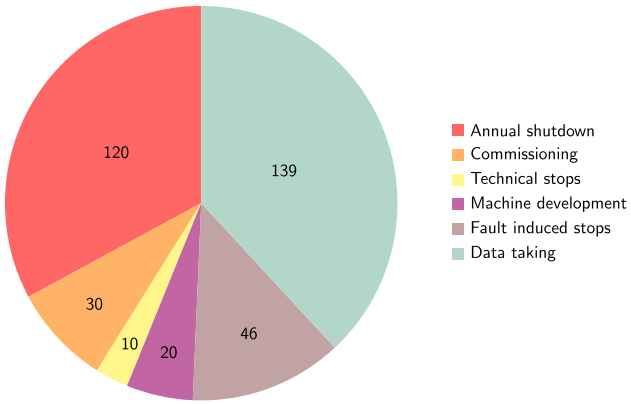

Table 53 Estimated annual energy consumption of CLIC, for 380 GeV and 1.5 TeV, when the machine is running at full luminosity, using the running scenario shown in Fig. 93

Collision energy [GeV]	Annual Energy Consumption [TWh]
380 50 Hz	0.54
380 100 Hz	0.82
1500 50 Hz	1.40

The first years at each stage the energy consumption will be less due to ramp up of the luminosity as described above.

Table 52 shows the nominal power consumption in three different operation modes of CLIC, including the "running" mode at the different energy stages, as well as the residual values for two operational modes corresponding to short ("short") and long ("off") beam interruptions. Intermediate power consumption modes exist, for example when a part of the complex is being tested, or during transitional states as waiting for beam with RF on. The contribution of these transitional states to the annual energy consumption is dealt with by averaging between "running" and "short" for certain periods, as described below.

6.3.1 Energy consumption

Estimating the yearly energy consumption from the power numbers requires an operational scenario, which is detailed in [18] and depicted in Fig. 93. In any "normal" year, i.e. once CLIC has been fully commissioned, the scenario assumes 120 days of annual shutdown, 30 days for beam-commissioning, and 30 days of scheduled maintenance, including machine development and technical stops (typically 1 day per week, or 2 days every second week). This leaves 185 days of operation for physics, for which 75% availability is assumed, i.e. 46 days of fault-induced stops. This results in 139 days, or 1.2×10^7 seconds, per year for physics data taking.

In terms of energy consumption the accelerator is assumed to be "off" for 120 days and "running" for 139 days. The power consumption during the remaining time, covering commissioning, technical stops, machine development and fault-induced stops is taken into account by estimating a 50/50 split between "running" and "short".

The resulting electrical energy consumption is shown in Table 53. For comparison, CERN's current energy consumption is approximately 1.2 TWh per year, of which the accelerator complex uses around 90%.

In addition, one has to take reduced operation into account in the first years at each energy stage to allow systematic tuning up of all parts of the accelerator complex. A luminosity ramp-up of three years (10%, 30%, 60%) in the first stage and two years (25%, 75%) in subsequent CLIC stages is considered. For the energy consumption estimate we change the corresponding reduction in "running" time to a 50/50 mixture of the two states mentioned above, resulting in a corresponding energy consumption ramp-up.

6.3.2 Summary of power reduction studies

Since the CDR [1] in 2012 the CLIC collaboration has systematically explored power reduction and technical system optimisation across the complex. The main contributors to the reduced estimate were:

- The accelerating structures were optimised for 380 GeV and corresponding luminosity, impacting among others on RF power needs and the machine length. The optimisation was done for cost but it was also shown that cost and power are strongly correlated.
- High efficiency klystron studies have reached a maturity such that 82% efficiency can be taken as the baseline for the drive-beam L-band klystrons.
- Redesigning the RF system of the damping rings, reducing the influence of transient loading effects, which earlier was dealt with by using a very high peak power. This in turn led to excessive power use.
- The injector systems and drive-beam facility were optimised to the 380 GeV parameters taking into account R&D on various technical systems, for example reducing the number of drive-beam klystrons to around 60% of earlier designs.
- Permanent magnets can partly replace electromagnets. Such a reduction is however not included in the estimates above.
- Nominal settings of RF systems, magnets and cooling have consistently been used, analysing the power consumption when running at full luminosity. This replaces earlier estimates which, in some cases, were based on maximum equipment capacity.

6.3.3 Adaptive energy-price optimisation

CLIC is a normal-conducting accelerator running at room temperature. Turning it on/off or into intermediate power states can, with appropriate thermo-mechanical considerations, be done relatively quickly. This means that CLIC could possibly be operated as a “Peak Shaving Facility” for the electrical network, matching not only seasonal, but also daily fluctuations of the demand. This particular feature constitutes a strong asset towards optimal energy management, a necessary approach in view of the large values of power consumption of the CLIC complex during nominal operation, in particular for the higher-energy stages. Furthermore, given the societal move towards renewable energies and the increased focus on energy recovery measures for any future facility, studies were launched addressing the following three issues: energy management and costs, operating with a large part of the power from renewable sources, and possible energy recovery measures. All of these issues require much more work in the next phase of the project, but a brief summary of the results obtained in initial case-studies [308] based on CLIC 380 GeV specifications is provided in the following three paragraphs.

Cost reductions have been studied by optimising the CLIC running schedule, at a daily, weekly and yearly level. With the flexibility of the accelerator to go from one mode to another quickly it is possible to avoid the high-cost periods. In order to minimize energy costs, optimization of operational strategies for the accelerator to achieve a fixed integrated luminosity per year have been investigated. For these investigations, the operation states of CLIC were described by a finite state machine (FSM). The general approach was to develop an operation strategy by dynamically shifting the operation states with high power demand to time slots with low energy prices. Three different operating strategies were developed, which generate optimized operating schedules for CLIC. Daily and Weekly Scheduling optimize the distribution of the various operation states of CLIC over the respective period using fixed state sequences with variable durations. Dynamic Scheduling distributes all operating states over the whole year without using predefined sequences, which leads to a high flexibility. The investigations are mainly based on the energy price curve for 2020 from the European energy spot market (EPEX SPOT) and a forecast for 2030 covering much more renewable energies. In addition, numerous boundary conditions and the requirement to reach a fixed integrated luminosity were considered. Figure 94 shows the main investigation results for the study. The best-/worst-case analysis provides the theoretical range of energy operation costs. The central value of the range should be considered to be a best estimate. Best-/worst-case restricted can be reached by avoiding the cold months with high energy prices and results already in a reduction of almost two thirds of the total energy cost savings. Furthermore, more than one third of the savings is attained by using optimized operational strategies. The simulation results for three different schedulers show similar cost distributions. Regarding the price curve of 2020, the minimal attainable total energy costs are 31 million EUR for Daily/Weekly Scheduling and 32 million EUR for Dynamic Scheduling. For the forecast of 2030, the lowest reachable energy price is even lower due to the higher fluctuation of the energy price. The actual running scenario, as well as prices and flexibility obtainable in future energy contract for CERN are very uncertain for the time period in question, but the possibility to adjust the running scenario and hence power consumption of CLIC to take advantage of low cost periods also outside the winter shut-downs seems worth pursuing.

Given the flexibility on running and power consumption, it is also interesting to consider how effectively the accelerator can be powered by renewable energies. First of all, it is likely that the overall energy landscape in

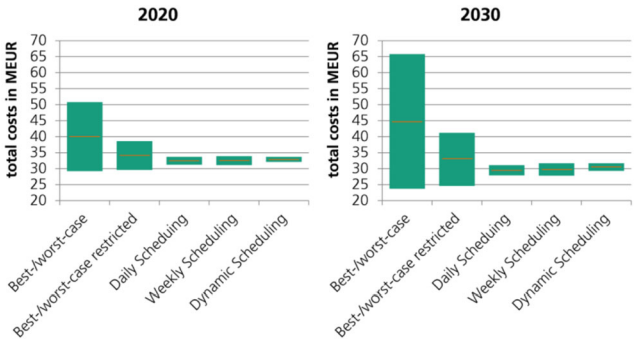

Fig. 94 Relative energy cost by no scheduling, avoiding the winter months (restricted), daily, weekly and dynamic scheduling. As explained in the text the central values of the ranges shown should be considered the best estimates. The absolute cost scale will depend on prices, contracts and detailed assumption about running times, but the relative cost differences indicate that significant cost-reductions could be achieved by optimising the running schedule of CLIC to avoid high energy cost periods, also outside the winter shut-down periods. (image credit: Fraunhofer)

Europe will shift over the next decades towards renewables, secondly the investment costs of such power sources are decreasing so one can consider moving investments in energy production into the construction costs, hence lowering the operation costs. By installing a portfolio of different renewable generators (different technologies, like wind and photovoltaic (PV), or different types of installations, like photovoltaic modules orientated into different directions) it becomes possible to partly level out the individual fluctuations of single generators in the aggregated generation curve. Combining the flexibility of the CLIC accelerator with this generation curve can increase the level of self-sufficiency. While it is possible to fully supply the annual electricity demand of CLIC by installing local wind and PV generators (this could be e.g. achieved by 330 MW-peak PV and 220 MW-peak wind generators, at a cost of slightly more than 10% of the CLIC 380 GeV cost), self-sufficiency during all times cannot be reached and only 54% of the time CLIC could run independently from public electricity supply with the portfolio simulated. About 1/3 of the generated PV and wind energy will be available to export to the public grid even after adjusting the load schedule of CLIC. Because of the correlation between electricity price and (national) generation from wind and PV, own local generators can generally not step in during times of high energy prize. Large storage systems are still too expensive to shift power accordingly. Installing such large renewable power plants is a process of some years, so energy would not be available on short term. Besides the direct investment in the generation technology, many aspects of standards, regulations, land-use, landscape-protection etc. would have to be considered. One alternative to own renewable power plants could be the participation in projects of other investors to build large renewable power plants. Yet financial advantages from local own consumption (like lower grid fees) would get lost in that case. The conclusion is that on a medium to long-term time scale local renewable generation could cover a fraction of the total load, but self-sufficiency of CLIC based on local renewables is not a realistic scenario.

Waste heat recovery also constitutes an interesting option in view of the large power rejected into water from CLIC. However, the use of waste heat to generate electricity is technically difficult due to the low temperature of the waste heat. The heat would have to be raised to a significantly higher level and more electricity would be consumed than can be generated again in the later process. A reasonable option is to use the waste heat to provide space heating. Also for this option, the temperature must be raised via a heat pump and thus additional electricity must be used. Another possibility would be the research of further innovative concepts for the use of waste heat with very low temperature (for example very low temperature ORCs, thermoelectric generators or the storage of heat in zeolites). The fact that the maximum energy need locally is during the winter, when it is favourable for energy cost reasons to not run the accelerator, also makes is more difficult today to envisage efficient large-scale energy recovery strategies.

6.4 Life cycle assessment studies for CLIC

The challenge of establishing a sustainable future accelerator facility demands more than “just” reducing operational power and energy consumption, and adapting to low-carbon power sources. It requires a direct quantification of the ecological footprint from start to end, from the emission of greenhouse gases during construction or operation, to the use of “problematic or rare” materials or energy consuming production processes.

A complete Life Cycle Assessment (LCA) emerges as a much more comprehensive approach, including a much-extended timeline and metric for assessing impacts. A Life Cycle Assessment is a structured, comprehensive and internationally standardised method to quantify all relevant emissions and resources consumed and the related environmental and health impacts and resource depletion issues that are associated with any goods or services.

Table 54 Data on GWP for the CLIC project

CLIC	Stage 1	Stage 2	Reduce by 2040-50
CoM energy [GeV]	380	1500	
Luminosity/IP [10^{34} cm^{-2}s^{-1}]	2.3	3.7	
Number of IPs	2	1	
Operation time for physics/yr [10^7 s/yr]	1.2		
Integrated luminosity/yr [1/fb/yr]	540	444	
Host countries	France and Switzerland		
GHG emissions from construction, stage A1-A3			
Subsurface structures [kt CO2 eq.]	286	199	40-50%
Surface sites constructions [kt CO2 eq.]	118	0	40-50%
Accelerator (coll.) [kt CO2 eq.]	60	∼125	25%
Accelerator (drivebeam and inj.) [kt CO2 eq.]	80	∼10	25%
Services [kt CO2 eq.]	19	∼20	25%
Two detectors [kt CO2 eq.]	94	upgrades	25%
Total [kt CO2 eq.]			
Collider tunnel length [km]	11.5	29.1	
Collider tunnel diameter [m]	5.6		
Collider tunnel GWP/m [t CO2 eq/m]	8.1		
Concrete GWP [kg CO2 eq./kg]	0.16		
Accelerator GWP/m [t CO2 eq./m]	Not estimated		
GHG emissions from operation			
Maximum power in operation [MW]	166	287	
Average power in operation [MW]			
Electricity consumption / yr [TWh/yr]	0.82	1.40	
Years of operation	10	10	
Carbon intensity of electricity [g CO2 eq./kWh]	16		Estimate for 2050
Average Scope 2 emissions / yr [kt CO2 eq.]	13	22	Estimate for 2050

These numbers are based on the reports mentioned above and will be further developed. Stage 2 is the delta for the upgrade based on the increase needed of the relevant components. All numbers are today's values, except the carbon intensity of electricity for operation. The last column indicates reduction potentials.

LCAs bring into focus the impact of the construction, primarily from embedded carbon in materials, the upgrades and the decommissioning, and includes many more parameters than CO_2 emission, such as water consumption, radioactive materials and more. The summary below has nevertheless been limited to Global Warming Potential (GWP) measured as kg CO_2 eq. emissions.

The ILC and CLIC projects have commissioned two lifecycle assessment (LCA) studies with ARUP, a consultancy company [309, 310]. In 2023 a comprehensive LCA was made for ILC in Japan and CLIC at CERN, commissioned by the CERN SCE department. The study focused on the civil engineering aspects, i.e. of the construction of tunnels, caverns and shafts. A second study was made 2024-2025 addressing the accelerator components, infrastructure and also providing complementary information to the civil engineering study performed in 2023. These lifecycle assessments form the basis for the Green House Gas (GHG) emission numbers summarised below, and also in Table 54:

- "Cradle to gate analysis" (LCA A1 to A5 modules) focussing on GHG emissions and therefore expressed in g CO_2 eq. (or multiples of) for:
  - civil engineering;
  - hardware components and infrastructure for the accelerator complex;
  - detectors.

- The Global Warming Potential (GWP) emission due to the generation of the electricity required for the operation of the accelerator complex (main collider and injectors).

Although the above list is not exhaustive, it provides an indicative assessment of the relative impact of construction and operation of the accelerator. In 54 several parameters are still being estimated but some conclusions can be made:

- For CLIC the embodied carbon in materials used for civil engineering and accelerator components is significantly larger (by a factor 3-4) than the emissions due to 10 years of operation. This factor will become smaller when the reductions possible for 2040 for the embodied carbon have been analysed and validated in more detail.
- The surface installations, drive-beam & main-beam injectors and buildings for these, plus buildings at the integration points of the two experiments and near shafts, contribute a factor two-three more than the initial 11.5 km main tunnel. This also means that layout changes and optimisation of cut-and-cover installations and related building can provide important additional improvements for CLIC.
- While reduction of the impact of the civil engineering – close to a factor two – seems within reach on the timescale of 2040, the reductions due to decarbonising of the society/industry/materials as a whole on this timescale are difficult to estimate for the accelerator, detector and infrastructure components.
- First estimates of the impact of two detectors, even with supports and all their services not included, indicate that they contribute at a level approaching the civil engineering impact of 10 km of tunnel.

7 CLIC objectives for the next period

This section covers the design and technology work for the next period, including R&D, the environmental studies and civil engineering preparatory work. A budget estimate and a personnel estimate are also presented.

7.1 CLIC project development timeline

The implementation schedule with emphasis on the next period is summarised in Table 55.

7.2 Technology readiness

As described with examples in Sect. 4 and Appendix A most of the central elements of CLIC have been developed into prototypes - in some cases several generations of them, and tested in laboratories, beam-tests facilities, or operational machines. Overall design and performance studies have also been implemented and verified, including beam-based steering and tuning procedures.

The challenges of the X-band technology and two beam acceleration scheme are discussed in other sections of this report, including the test and beam-facilities used to verify their performances, among others the CTF3 facility. The nanobeam challenge encompasses several technologies and systems, from damping rings to the interaction point, from alignment and stability to instrumentation and beamdynamics. CLIC has systematically addressed all the issues and components of relevance and the status is similar for the various parts in terms of design, prototyping and beam tests. System level tests have also been implemented as described in Sect. 2.1.5. In many cases, for example for the damping ring systems, synchrotron sources or free electron laser linacs provide very important additional confidence and test-grounds for the performances needed.

The key components of CLIC are therefore mainly at Technology Readiness Level (TRL) 6 (“A representative model or prototype system/subsystem is tested in a relevant environment - in our case typically a beamline or test facility, representing a major step up in a technology’s demonstrated readiness”) or 7 (“Prototype as part of an operational system, representing a major step up from TRL 6, requiring the demonstration of an actual system prototype in an operational environment, in our case as part of an accelerator”). A summary of the TRLs and some key improvements foreseen over the next phase are shown in Table 56.

Many components of CLIC require little further R&D, but require developments and further work to optimize and validate large scale industrial processes and samples, typically addressed in the pre-series phase. This is discussed in the following Sect. 7.3.

7.3 Main points to address in the preparation phases

The project implementation for CLIC foresees two preparation phases prior to a construction start, see Table 55. In order to analyse the priorities for the preparation phases, the following project risks and mitigations have been considered:

Table 55 Timeline of essential development and construction steps of the CLIC project

CLIC	Years
Conceptual Design Study	2004 – 2012
Project Implementation Plan and Readiness Report	2013 – 2025
Project Preparation Phase 1	2026 – 2028
Definition of the placement scenario	
Design optimisation and finalization	
Main technologies R&D conclusions	
Technical Design Report – two IPs at CERN	
Project Preparation Phase 2	T_0 – $(T_0 + 5)$
Site investigation and preparation	
Implementation studies with the Host states	
Environmental evaluation & Project authorisation processes	
Industrialization of key components	
Engineering design completion	
Construction Phase (from ground breaking)	T_1 – $(T_1 + 10)$
Civil engineering	
Construction of components	
Installation and hardware commissioning	
Beam commissioning and physics operation start	$T_1 + 11$

T0 is determined by a process in 2028-29 to validate the progress and promise of the project for a further development towards implementation. T1 following Preparation Phase 2 will be determined by the processes needed, by the CERN Council and with host-states, for project approval and to start construction. The construction phase is extended by three years with respect to the technically-limited schedules to allow a transfer time into construction, and to avoid the resource conflict between HL LHC operation and initiating beam commissioning for a next collider.

Table 56 Technology readiness and R&D for the CLIC accelerator

Component/Sub-system	TRL	Goals, risks being addressed
X-band technology	6	Larger systems and industrial readiness, cost and yields
HOM detuning/damp	6	Robustness in system tests, luminosity
Positron source	5	Benchmarking, positron yield verification
Two-beam acceleration	7	DB design and component developments, RF power
Initial emitt. and preservation	6	Design, luminosity margins
IP spot size/stability	5	Beamtests, stability and robustness

- Performance: The dominant performance risk is related to the luminosity. The luminosity performance relies on technical performance and reliability as well as design robustness and system redundancy. Risk mitigation implies further studies at design and technical level, including on variation of parameters such as temperatures, mechanical instabilities and vibrations, magnetic fields, etc. Performance validations in normal-conducting Free Electron Laser (FEL) Linacs and other compact linac systems will provide powerful demonstrations and new benchmarks for reliability, technical parameters, simulation and modelling tools.
- Technical systems: The main technical risks are related to RF sources, the X-band components, and overall system integration for the main linac. Reliable, efficient and cost-effective klystrons, modulators and X-band structures are components which are crucial for the machine. Additional thermo-mechanical engineering studies of the main linac tunnel, integrating all components, are important in order to further improve the understanding of the mechanical and thermal stability needed for CLIC. Further development (beyond what has been achieved with CTF3) of the high-power drive beam would be most desirable.
- Implementation: Principal risks are associated with the industrial production of large numbers of modules (cost, performance, yields) and the civil engineering. Work during the preparation phases includes qualifying

Table 57 Main CLIC accelerator objectives and activities in the next phase

Activities	Purpose
Design and parameters	
Beam dynamics studies, parameter optimisation, cost, power, system verifications in linacs and low emittance rings	Luminosity performance and reduction of risk, cost and power
Main linac modules	
Construction of ~ 5 prototype modules in qualified industries, optimised design of the modules with their supporting infrastructure in the main linac tunnel	Final technical design, qualification of industrial partners, production models, performance verification
Accelerating structures	
Production of ~ 50 accelerating structures, including structures for the modules above	Industrialisation, manufacturing and cost optimisation, conditioning studies in test-stands
Operating X-band test-stands, high efficiency RF studies	
Operation of X-band RF test-stands at CERN and in collaborating institutes for structure and component optimisation, further development of cost-optimised high efficiency klystrons.	Building experience and capacity for X-band components and structure testing, validation and optimisation of these components, cost reduction and increased industrial availability of high efficiency RF units
Other technical components	
Magnets, instrumentation, alignment, stability, vacuum	Luminosity performance, costs and power, industrialisation
Drive beam and main beam injector studies, incl. L&S band RF sources	
Drive-beam detailed design and component prototypes for drivebeam and main beam injectors.	Verification of the most critical parts of the drive-beam and injectors, among them further development of industrial capabilities for high efficiency L-band klystrons
Civil Engineering, siting, infrastructure	
Detailed site specific technical designs, site preparation, environmental impact study and corresponding procedures in preparation for construction	Preparation for civil engineering works, obtaining all needed permits, preparation of technical documentation, tenders and commercial documents

companies for industrial production and optimising the work distribution and component integration. The module installation and conditioning procedures need to be refined and further verified. Cost control is crucial and is an integral part of these studies. This requires work on optimising the risk sharing models between industry, CERN and collaborative partners for the most critical and costly components. Detailed site-specific design work related to civil engineering and infrastructure needs to be performed, including environmental studies and host-countries.

7.4 Summary of the R&D and study plans for the preparation phases

To address the issues described above the forthcoming preparation phases will comprise further design, technical and industrial developments, with a focus on cost, power and risk reduction.

The key elements of the CLIC accelerator activities during the Preparation Phases 1 and 2 in the timeline (Table 55) are summarised in Table 57. The programme covers the R&D on the critical technologies affecting the main parameters of the accelerators and technical infrastructure and/or having an impact on civil engineering, procurement of components requiring large scale production, acceptance tests and validation or production with long lead times.

Civil engineering and infrastructure preparation will become increasingly detailed during the preparation phase. The first step is final placement of the collider complex and its infrastructure after assessment of their territorial compatibility, both for its initial phase and potential upgrades. This step is particularly urgent to establish that a linear collider such as CLIC can be constructed at CERN as outlined in this report. This will be followed by optimisation of the placement scenario with the relevant regional and local stakeholders as a part of wider implementation studies with the Host Regions/States. An environmental impact study and corresponding public inquiry will be needed as a prerequisite to authorisations for construction.

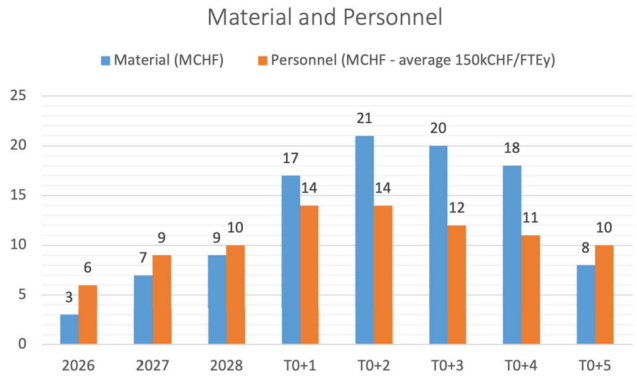

Fig. 95 Resource timeline for accelerator R&D in the next phases (Phase 1 and 2 in the timeline) addressing the studies described in Table 57. The use of construction resources after a potential approval is not included

A Technical Design Report (TDR) is foreseen outlining the detailed design, technical specifications and solutions for the accelerator, and an implementation of the dual BDS and two interaction regions at CERN. The TDR will present the critical technologies of the project and the R&D result.

The resources for such a programme are summarised in Fig. 95, showing that the initial part of the programme (Phase 1 in the time-line) requires limited resources while the larger industrial prototyping and pre-series efforts occur later (Phase 2), combined with construction preparation. Around 1/3 of these resources could be available outside CERN.

In parallel, civil engineering preparation to be able to place time-critical contracts to start the construction, including continued environmental studies, will require significant resources during the second parts of Phase 2, typically 5% of the civil engineering budget.

7.5 Technology demonstrators and collaboration

The design studies and technical work for CLIC are broadly shared among the CLIC collaboration partners.

The potential for collaborative projects is increasing with the current expansion in the field of Free Electron Laser (FEL) linacs and next-generation light sources. In particular, the increasing use of X-band technology, either as the main RF technology or for parts of the accelerators (deflectors, linearisers), is of high relevance for the next phase of CLIC.

Construction, upgrades and operation of FEL linacs and conventional light sources, several of which are located at laboratories of CLIC collaboration partners, provide many opportunities for common design and component developments, and for acquiring crucial system test experience. Furthermore, the fact that there are significant resources invested in such accelerators world-wide, provides excellent opportunities for building up industrial capabilities and networks.

X-band RF systems and structure manufacturing used to be exclusively available in the US and Japan. However, today there are around fifteen institutes capable of developing and testing X-band structures with their industry partners. All are working together on optimising the technology. The increasing number of qualified companies for accelerating structure manufacturing, together with the growing industrial availability of RF systems, make it easier for new groups to engage in these technologies. As a consequence, several smaller accelerators using X-band technology are in a proposal or technical preparation phase. In this context it is important to mention the SPARC 1 GeV X-band linac at INFN [311] and the CompactLight [312] FEL study. The CompactLight design study was co-financed by the European Commission. It involved 24 partners preparing technical designs for compact FELs based on X-band linacs at energies ranging from 6 GeV down to small room-size systems for X-ray production through Inverse Compton Scattering (e.g. SmartLight [313]), and served as a catalyst for the spread of the technology.

The growing use of CLIC technology allows for implementing several of the CLIC project activities described in Table 57 in the form of collaborative projects together with the project and technology partners mentioned above. Nevertheless, the principal ingredient to a successful preparation phase for CLIC, and the ability to team up with such partner projects, is funding for the next phase that allows the programme above to initiate.

8 Summary

This document presents a summary of research and development efforts on the Compact Linear Collider (CLIC), with a focus on recent studies and advancements related to the CLIC accelerator complex. Important technical progress related to X-band technology and klystron designs has been achieved. Integrated beam simulations have concluded on a 50% increase in luminosity at 380 GeV, with respect to previous evaluations. A significant power

reduction has been achieved, enabling a factor of two increased bunch-train repetition rate of 100 Hz with a power consumption of 166 MW at 380 GeV. Compared to the 2018 values, this represents a total factor of three increase in luminosity for the initial stage.

An interaction region with two beam delivery systems hosting two detectors has been designed, where luminosity can be delivered to each detector. CLIC provides ±80% longitudinal electron polarisation and proposes a sharing between the two polarisation states at each energy stage for optimal physics reach [19]. The layout of the Injector and Experimental complexes, located at the CERN Prévessin site, has been optimised to be completely located on CERN territory. The cost for the initial 11.4 km 380 GeV stage has been estimated at around 7.2 BCHF (2024).

A higher-energy stage, still using the initial single drive-beam complex, can be optimized for any energy up to approximately 2 TeV. Parameters are worked out in detail for a 1.5 TeV stage, with a site length of 29 km. Parameters for 550 GeV operating at 100 Hz are also provided, requiring less than 4 km extra tunneling at an additional cost around 30% higher than the 380 GeV cost. The precise energy of the high-energy stage can be decided upon, and most of the tunnel can be dug and equipped, while running the initial energy stage.

Beam experiments and hardware tests described in this report demonstrate that the CLIC performance goals can be met. For instance, accelerating gradients of up to 145 MV/m are reached with the two-beam concept at CTF3, and breakdown rates of the accelerating structures well below the limit of 3×10^7 m^{-1} are achieved at X-band test platforms. High luminosities can be achieved by using nanometre beam sizes. This requires low-emittance beams as well as novel alignment and stabilisation techniques. The performances needed for the CLIC damping rings are achieved by modern synchrotron light sources; special alignment procedures for the main linac are now available; sub-nanometre stabilisation of the final focus quadrupoles is demonstrated.

The preparation phases for CLIC will comprise further design, technical, and industrial developments, with a focus on cost, power, and risk reduction. The programme covers R&D on the critical technologies affecting the main parameters of the accelerators and technical infrastructure and/or having an impact on civil engineering, optimization of components requiring large scale production, preparation of infrastructure, and of productions with long lead times. Furthermore, civil engineering and infrastructure preparation will become progressively more detailed, in parallel with environmental impact studies and construction authorisation processes.

The CLIC physics programme spans over 20-25 years. This report provides details of an updated staging scenario. Taking the 380 GeV and 1.5 TeV stages as an example, CLIC proposes a scenario with a running period of 10 years each. The initial stage at a centre-of-mass energy of $\sqrt{s} = 380$ GeV, motivated by an optimal combination of Higgs and top-quark measurements, delivers an integrated luminosity of 4.3 ab^{-1}. A subsequent stage would increase the energy up to 1.5 TeV with an integrated luminosity of 4.0 ab^{-1}.

CLIC offers the unique combination of high collision energies and the clean environment of e^+e^- collisions. This enables the guaranteed physics programme of SM parameter measurements with unprecedented precision, ranging from the top-quark mass and other top-quark properties to the Higgs couplings, including the Higgs self-coupling. In addition, CLIC offers a rich potential for extensive exploration of the terascale in the form of direct and indirect searches of BSM effects. Direct searches are often possible up to the kinematic limit for particles with electroweak-sized coupling strength and detectable decay products. Beyond the kinematic reach, new physics effects might be found through effects of their mixing with known particles.

In summary, CLIC represents a compelling opportunity for the post-LHC era.

Appendix A System tests and performance demonstrations

A.1 Introduction

CLIC requires excellent beam quality to achieve its luminosity goal. The assumed performances are based on extensive theoretical studies and experimental results. Development of components and their testing and a number of different beam facilities were instrumental for this. Foremost, the SLC [36] has demonstrated the feasibility of the concept. Many lessons have been learned there and have been integrated into the design of CLIC. Light sources and FELs have advanced the design of low emittance rings and linacs, respectively. The experience gained in b-factories has also been important, and the construction and operation of test facilities specifically dedicated to linear colliders, such as CTF3 and ATF2, has been fundamental.

The SLC reached more than half of the luminosity goal. Its failure to reach two design parameters were the main cause; The repetition rate was 120 Hz, instead of 180 Hz and the bunch charge reached $3–4 \times 10^{10}$ particles instead of 7.2×10^{10} [37]. For otherwise unchanged parameters this would have led to a luminosity reduction by more than a factor of six. However the SLC achieved better than planned beta-functions and emittances at the collision point, mainly in the vertical plane, which allowed it to recover more of the luminosity goal.

In the SLC two main limitations existed for the bunch charge and have been addressed in CLIC, the beam stability in the damping rings and in the Main Linac:

- The SLC damping ring showed a sawtooth instability at a bunch charge of 3×10^{10}, which made the extracted beam at this charge useless. Later upgrades of the damping ring design to lower its impedance managed to reduce the instability but the bunch charge remained below 4.5×10^{10} [37]. This effect is theoretically understood and the CLIC damping ring design takes it into account and profits from the enormous progress that has been made in the field of low emittance rings also thanks to the development of light sources and the b-factories.
- Wakefield effects in the main linac of the SLC amplified incoming beam jitter if the charge reached about 3×10^{10}. CLIC avoids such amplification by the use of strong focusing and a choice of bunch charge and length that is consistent with stable beam transport in the presence of the wakefields. This design choice is one of the main ingredients of the CLIC parameter optimisation and includes some margin.

While the SLC failed to reach the full bunch charge it provided important physics results. It also successfully demonstrated a number of important key concepts and managed to address critical performance limitations. In particular:

- The strong beam-beam forces in CLIC lead to shrinking beam sizes during the collision and an increase in luminosity. This effect has been experimentally observed at the SLC, in which a luminosity enhancement by a factor two has been gained. The experiment agrees very well with the simulations [38].
- CLIC aims at 80% electron polarisation at the IP. The SLC demonstrated a value of 78%. This gives confidence that the CLIC goal can be met with the new, improved photo cathodes.
- In CLIC, stable beam transport in the main linac requires BNS damping. This concept has been successfully tested in routine operation at the SLC.
- Beam jitter is a key issue in CLIC. At the SLC during operation more than 50 feedback loops were developed in iterations and successfully implemented to stabilise the beam. In CLIC similar feedback systems are integrated from the beginning and profit from the SLC experience. Feedback systems were also a key ingredient in the successful operation of the CLIC Test facility CTF3, where further experience has been gained.
- Machine-induced background in the detector can limit the physics reach. In the SLC beam tails in the collimation system produced muons that perturbed the experiment. Muon spoilers resolved the problem and space for them is integrated in the CLIC design.

The CLIC parameters are more ambitious than the ones of SLC but also the understanding of the relevant physics and the technologies have improved significantly. Important examples are:

- As discussed above, the SLC charge limitation is understood and avoided in the CLIC design.
- The novel Drive-Beam scheme and the Drive-Beam quality have been demonstrated in CTF3, as well as its use to produce high-power RF pulses and the Two-Beam acceleration concept.
- Modern light sources achieve CLIC-level, nano-metre normalised emittances in the vertical plane in routine operation. In the vertical plane they are three orders of magnitude below the SLC level.
- CLIC parameters require strong focusing at the IP. This focusing has been demonstrated at two test facilities, i.e. FFTB at SLAC and ATF2 at KEK. The achieved vertical beam sizes were close to the target, see Sect. A.4. Also the super B-factory at KEK aims at beta functions that are slightly larger but this in a circular collider where the beam repeatedly passes through the system.
- The use of dispersion-free steering to maintain small emittances in a linac has successfully been tested in FACET, a test facility that used a part of the old SLC linac.
- Better understanding of the technical limitations and the improved CLIC structure design allow to reach higher gradients than the SLC. High gradient accelerating structures are in routine operation today and prove high gradient and reliability.
- The novel precision pre-alignment system of CLIC and sophisticated beam-based alignment and tuning ensure the preservation of the beam quality during transport. The alignment system is based on a concept developed for the LHC interaction regions with improved performance and prototypes have been built. The beam-based alignment has been simulated and has been experimentally verified.
- Quadrupole jitter has been an important source of beam jitter in the SLC. For CLIC this has been addressed by designing the magnet supports to avoid resonances at low frequencies and by developing an active stabilisation system for the magnets, which demonstrated a reduction of the jitter to the sub-nm regime.
- CLIC requires excellent relative timing at the femtosecond level over the collider complex. Modern FELs have developed the relevant technology.
- The impact of time varying magnetic fields has been explored and the necessary mitigation methods have been developed, see Sect. A.8.

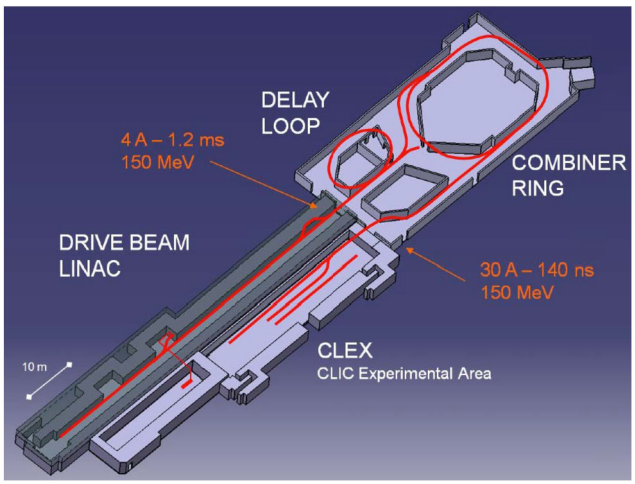

Fig. 96 Schematic CTF3 layout

- High availability is key to achieve the luminosity goal. The very reliable routine operation of light sources, FELs, the b-factories and the LHC provide key concepts to address this issue.

In conclusion, the CLIC parameters are ambitious but are supported by experience in existing facilities. This permits a confidence that the goals can be met. In the following these performance benchmarks are presented in more detail.

A.2 Drive Beam generation, power production and Two-Beam acceleration in the CLIC Test Facility CTF3

The aim of the CLIC Test Facility CTF3 (see Fig. 96), built at CERN by the CLIC International Collaboration, was to prove the main feasibility issues of the Two-Beam acceleration technology [29]. CTF3 consisted of a 150 MeV electron linac followed by a 42 m long Delay Loop (DL) and a 84 m Combiner Ring (CR). The beam current from the linac was first doubled in the loop and then multiplied by a further factor of four in the ring, by interleaving bunches in transverse RF deflectors. The beam was then sent into the CLIC experimental area (CLEX) where it was decelerated to extract from it RF power at 12 GHz. Such power was used to accelerate a probe beam, delivered by a 200 MeV injector (Concept d'Accèlèrateur Linéaire pour Faisceaux d'Electrons Sondes, CALIFES) located in the same area.

The main issues explored in CTF3 can be divided in two main areas [55]:

1. Drive-Beam generation: efficient generation of a high-current electron beam with the proper time structure to generate 12 GHz RF power. In order to achieve this, CLIC relies on a novel technique: fully-loaded acceleration in normal conducting travelling wave structures followed by beam current and bunch frequency multiplication in a series of delay lines and rings by injection with RF deflectors. CTF3 used such method to produce a 28 A electron beam with 12 GHz bunch repetition frequency. The Drive Beam was then sent to the experimental area, CLEX.
2. RF power production and Two-Beam acceleration: in CLIC the needed 12 GHz RF power is obtained by decelerating the high current Drive Beam in special resonant structures called PETS (Power Extraction and Transfer Structures). The power is then transferred to high gradient accelerating structures, operated at about 100 MV/m. In the CTF3 experimental area (CLEX), the Drive Beam is decelerated in a string of PETS in the Test Beam Line, (TBL). The Drive Beam can alternatively be sent to another beam line (Two Beam Test Stand, TBTS, renamed later to Test Beam Module, TBM) where one or more PETS powered one or more structures, further accelerating a 200 MeV electron beam provided by CALIFES.

CTF3 was installed and commissioned in stages starting from 2003. The beam commissioning of the DL was completed in 2006. The CR and the connecting transfer line were installed and put into operation in 2007, while the transfer line to CLEX was installed in 2008. In 2009 this last beam line and the CLEX beam lines, including the CALIFES injector, were commissioned. During the autumn of 2009, recombination with the DL and CR together was achieved, yielding up to 28 A of beam current. In 2010 the nominal power production from the PETS was obtained, and the first Two-Beam test was performed, reaching a measured gradient of 100 MV/m. In 2011 a gradient of 145 MV/m was reached and the PETS On-off mechanism was successfully tested. At the end of 2014 the TBTS was replaced by the Two-Beam Module, TBM, a 2 m long fully representative unit of the CLIC Main

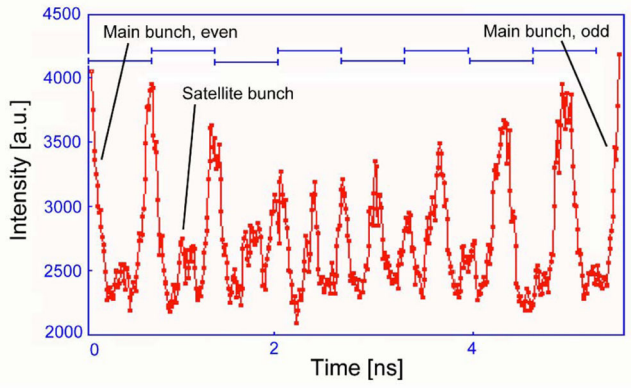

Fig. 97 Fast bunch phase switch, measured by a streak camera. At the top the 1.5 GHz periods are shown

Linac. In 2015 the Drive Beam was decelerated by 50% of its initial energy in the TBL. Drive Beam stability and the overall performances of the facility were continually improved after the initial commissioning, until the final run in 2016.

A.2.1 Drive Beam generation: injector – Beam current and time structure

The CTF3 Drive-Beam Injector consisted of a high current thermionic gun, three 1.5 GHz sub-harmonic bunchers (SHBs) and a 3 GHz system composed of a pre-buncher and a buncher [314]. The SHBs gave the first energy-time modulation to the beam and performed the phase coding by means of fast 180° RF phase switches. The 6-cell travelling wave (TW) SHBs had a nominal power of 40 kW. Downstream, a 3 GHz single-cell pre-buncher and a TW buncher were installed to create the final bucket structure and accelerate the beam up to 6 MeV/c. The 2 cm long pre-buncher nominal power was 100 kW, while the half-meter long buncher was fed a maximum power of 40 MW. Exhaustive simulations were performed using PARMELA to guide the optimization of the transverse emittance, the bunch length and the satellite population. The magnetic field distribution was optimized to keep the emittance at the exit of the injector below 50 µm, as confirmed by measurements [315]. A bunch length of 1 mm was measured with a streak camera at the end of the linac [168]. Some particles form unwanted satellites in between the 1.5 GHz main bunches; the measured fraction of the satellites is about 8%, compared to the design figure of 7%. Figure 97, a projection of a streak camera image, shows the bunch population vs. time during the 180° phase switch. As can be seen from the figure, the measured switch time is less than 6 ns (eight 1.5 GHz periods), well below the 10 ns target [316].

A.2.2 Drive Beam generation: linac — full beam-loading acceleration

Overall efficiency is paramount for linear colliders, and a very efficient RF energy transfer to the Drive Beam, obtained by means of full beam-loading operation, is one of the key ingredients in CLIC. The high pulse current in both CLIC and CTF3 (about 4 A in both cases), accelerated in short travelling-wave RF structures with relatively low gradient, results in an extremely high transfer efficiency. No RF power is transmitted to the load when the beam is present and the resistive losses in the cavity walls are minimal, such that an overall efficiency of about 98% is calculated in the CLIC case. However, an energy transient is present at the beginning of the pulse, and the first bunches may have twice the energy of the steady-state part; this mode of operation also strongly couples beam current fluctuations to the beam energy.

The 3 GHz TW accelerating structures designed and built for CTF3 [317] work in the $2\pi/3$ mode, have a length of 1.22 m and operate at a loaded gradient (nominal current) of 6.5 MV/m. The large average current also implies that transverse higher order modes (HOMs) must be damped in order to prevent beam instability and control emittance growth. A Slotted Iris - Constant Aperture structure (SICA), in which irises are radially slotted to guide dipole and quadrupole modes into SiC loads, was designed for the purpose. The selection of the damped modes is obtained through their field distribution, strongly damping the HOMs (Q typically below 20), while monopole modes are not influenced. In addition HOM detuning along the structure (by nose cones of variable geometry) is used; this improves their suppression and modulates the group velocity to control the gradient profile. The aperture is therefore kept constant along the structure, reducing short range wakefields. The RF is supplied by klystrons with power ranging from 35 MW to 45 MW, compressed by a factor two to provide 1.3 µs pulses with over 30 MW at each structure input. The pulse compression system uses a programmed phase ramp to provide a constant RF power.

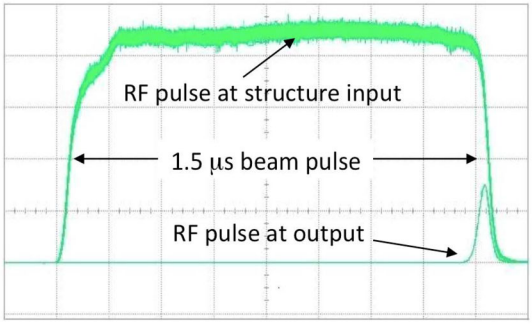

Fig. 98 RF power measured at the accelerating structure input and output with beam

Beam commissioning started in June 2003. The design beam current and pulse length were rapidly reached. The beam was remarkably stable and no sign of beam break-up was observed at high current, thus proving for the first time operation under full beam loading [318]. The measured normalized emittance at the end of the CTF3 linac was routinely about $\epsilon_{x,y} \simeq 50$ µm, confirming negligible wakefield effects as predicted by simulations. The energy spread of the initial beam transient ($\simeq 100$ ns) could also be reduced to a few percent by partial RF filling of the structures at beam injection. The observation of the RF signals at the structure output couplers was particularly useful, allowing to easily adjust the beam-to-RF phase by maximizing the beam loading. The acceleration efficiency was demonstrated in a dedicated experiment [319].

After careful calibration of beam current and RF power measurements, the beam energy gain was calculated and compared to spectrometer measurements. Figure 98 shows an example of the RF pulse measured at the structure input and output, showing that the RF power is almost fully absorbed by the beam. The measurements were in excellent agreement with the theoretical energy gain. Including the resistive losses, the obtained RF-to-beam transfer efficiency was 95.3%. CTF3 was routinely operated over several years with fully loaded structures, successfully proving the stable, highly efficient acceleration of the Drive Beam.

A.2.3 Drive Beam generation: delay loop and CR – bunch combination

Beam recombination in CTF3 is done in two stages. First, using the Delay Loop (DL), a 1120 ns long bunch train with a current of 4 A is converted into 4 pulses of 140 ns and 7.5 A (not counting the charge contained in satellite bunches). Later, the pulses are interleaved in the Combiner Ring (CR) to produce a single 140 ns long pulse with a maximum current of about 30 A. The first RF deflector, operating at 1.5 GHz, sends odd and even phase-coded sub-pulses either straight to the CR or into the DL, whose length is equal to the sub-pulse length. The sub-pulses circulating in the DL come back in the deflector at half a wavelength distance, and their orbits are merged with the following ones to obtain 140 ns long pulses with twice the initial current and twice the bunch repetition frequency. The pulses are combined again in the CR. A pair of RF deflectors is employed to create a time-dependent closed bump at injection, used to interleave bunches.

The combination process must preserve transverse and longitudinal beam emittances: isochronous lattices, smooth linear optics, low impedance vacuum chambers and diagnostics, HOM free RF active elements are all needed to accomplish this task. A short bunch length is fundamental for efficient RF power production in the PETS. Bunch length preservation requires the use of isochronous optics (which implies $R_{56} = 0$) in the DL, the CR and the transfer line connecting them. The isochronicity requirement is $|R_{56}| \leq \pm 1$ cm. The DL and CR are based on the use of three-dipole isochronous cells with three independent quadrupole families, whose tunability range fits well the requirements. Sextupoles can be used to control the second-order matrix term T_{566}. Bunch length control to down to less than 1 mm R.M.S. was shown after the linac. In CLEX a bunch length of 2 mm R.M.S. was estimated from RF power production and confirmed by direct streak camera measurements. Such length is consistent with required isochronicity conditions and entirely sufficient for CTF3 operation, avoiding also coherent synchrotron radiation, which would affect shorter bunches. Damping and detuning is used in the RF deflectors of the ring in order to minimize wakefields in the vertical plane [320]. The lowest order horizontal dipole mode is the operational one and cannot be damped or detuned. However, the fill-time of the travelling wave deflectors is short enough to avoid turn-by-turn direct build-up. In order to avoid any residual amplification of the orbit errors by wakefields, the fractional tune of the CR is set to be about 0.6 in both planes. Also, the β-function in the deflectors is kept small to minimize amplification. The ring length must be $(N \pm 1/N_f)\lambda_{RF}$, where N is an integer number, N_f the combination factor (here 4), and λ_{RF} is the RF wavelength. The fractional part λ_{RF}/N_f can be determined precisely from a Fourier transform of the dedicated beam phase monitor signal, and when needed the ring length can be adjusted using a wiggler.

In the last experimental runs, a large fraction of beam time was dedicated to improvements of the Drive Beam performance, especially control of emittance growth, availability and stability. Apart from enabling a better exploitation of the beam by the users, this was an integral part of the CTF3 experimental program, aimed at demonstrating a beam quality close to the one required for CLIC. Emittance preservation requires good control of the optics, a very good closure of the DL and CR orbits, proper matching from the linac and control of spurious dispersion. The CTF3 Drive Beam has a R.M.S. energy spread of about 0.6%, and the isochronous optics in DL, CR and transfer lines are strongly focusing. This leads to a large non-linear dispersion, which is the main source of emittance growth. The main contribution was coming from the DL, whose optics is constrained by building space limitations. A new more forgiving DL optics was developed and deployed, and tools to precisely measure Twiss parameters and dispersion in the different beam lines were put in place. Dispersion Free Steering and Dispersion Target Steering procedures were implemented and applied. While the beam combined in the CR met the CLIC emittance requirements (<150 µm) in both planes, the minimum horizontal emittance for the factor 8 recombined Drive Beam was about 250 µm (100 µm in vertical). Besides demonstrating the feasibility of the CLIC bunch combination principle, CTF3 has allowed the development of an optimized setting-up procedure of such a process, validating the special diagnostics needed [168, 321].

A.2.4 Drive Beam generation: beam stability issues and phase feed-forward

In CLIC, the Two-Beam Acceleration scheme puts tight constraints on the Drive-Beam current, energy and phase stability. In particular, both bunch charge and phase jitter contribute quadratically to the luminosity loss [322]; a maximum variation of $0.75*10^{-3}$ for the Drive-Beam current and about 2° at 12 GHz for the Drive-Beam bunch phase after combination are allowed, for a maximum of 1% to the luminosity loss per parameter and assuming a feed-forward system – discussed later – capable of reducing the phase jitter to 0.2° at 12 GHz. During the first years of operation CTF3 suffered from relatively large beam jitters and drifts; dedicated studies discovered most of the sources, which were either removed or corrected by feedback systems. Dedicated tests aimed at demonstrating performances close to the CLIC requirements (including a feed-forward experiment, see later for a full description) were added to the CTF3 experimental program in its final years. The CLIC tolerances on the Drive-Beam Linac RF, for instance, were verified for the CTF3 klystrons, measuring the short-term RF stability over 500 consecutive RF pulses ($\simeq$ 10 min). The mean pulse-to-pulse phase jitter measured with respect to an external reference was 0.035° (3 GHz) and the relative pulse-to-pulse amplitude jitter has been 0.21%, to be compared with the CLIC requirements of 0.05° R.M.S. phase jitter and 0.2% R.M.S. amplitude jitter [323]. The pulse-to-pulse current variations in the CTF3 linac were measured using inductive beam position monitors. The initial stability ($\Delta I/I = 2 \times 10^{-3}$) was improved by better stabilizing the gun heater power supply and by a feedback, to obtain $\Delta I/I = 0.54 \times 10^{-3}$ [323], better than the required current stability for CLIC of $\Delta I/I = 0.75 \times 10^{-3}$. After further improvements, in 2016 the R.M.S. current jitter at the end of the Drive-Beam Linac was routinely better than 2×10^{-4}, corresponding to the electronic noise floor of the BPMs (the observed jitter is the same with and without beam). Such performance is currently achieved for long periods, even tens of hours [324]. The stability of the combined beam current in CLEX, at the end of the experimental lines, was also largely improved and 3×10^{-3} R.M.S. was measured for periods longer than 5 hours [31].

In CLIC a Drive-Beam phase feed-forward system is required to achieve a timing stability of 50 fs R.M.S., or equivalently a phase stability (jitter) of 0.2 degrees at 12 GHz. This system poses a significant challenge in terms of bandwidth, resolution and latency and therefore a prototype of the system was designed, installed and tested in CTF3. After one year of experience a phase jitter of 0.28 ± 0.02 was demonstrated, very close to the CLIC specifications [325]. With additional fine-tuning in 2016, the final year of operation at CTF3, it was possible to further reduce the achieved phase jitter to below the CLIC requirement of 0.2° and to keep it at such level on timescales of about 10 minutes [326].

A.2.5 Two-Beam Acceleration: power generation, PETS on-off and deceleration

In CTF3, PETS prototypes were tested with beam in TBL and in TBTS (and later TBM). The prototypes tested in both lines were very similar, differing mainly in length and some construction detail. In both cases the nominal CLIC parameters for power and pulse length were reached and exceeded. In particular during the 2010 run, RF power levels of about 300 MW were reached at the nominal pulse length of 240 ns, well above the nominal value for CLIC, 135 MW [327]. Another milestone was the validation of the PETS On-Off concept. The PETS On-Off mechanism is required in CLIC in order to be able to switch on and off individual PETS whenever localized

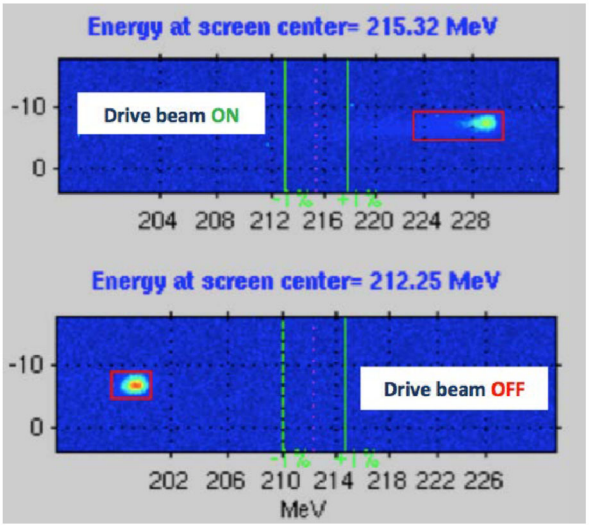

Fig. 99 Probe Beam observed in the TBTS spectrometer screen with the 12 GHz RF power from the Drive Beam on (top) and off (bottom). The energy gain is about 32 MeV, corresponding to a gradient of 145 MV/m

breakdowns threaten the normal machine operation. The system should also provide a gradual ramp-up of the generated power in order to reprocess either the main accelerating structure and/or the PETS itself. A prototype of the CLIC PETS On-Off mechanism, a compact external extension to PETS, consisting of two high power variable RF reflectors, was developed, manufactured and extensively tested with beam in the TBTS. The switching off of the PETS power production has been demonstrated with different beam and RF settings, up to 16 A and 200 MW [328]. The model describing the RF behaviour agreed with the measurements under all conditions. When the PETS is switched off, the accelerating structure sees less than 1% of the extracted power, basically making breakdown events impossible. The likelihood of a breakdown in PETS is also reduced by a factor $10^2 - 10^3$ due to the power attenuation to $\sim 25\%$ of the nominal value.

The stability of the Drive Beam during deceleration was studied in the Test Beam Line (TBL), consisting of a FODO lattice with 14 consecutive PETS installed in the drift spaces. High precision BPMs and quadrupole active movers are used for precise beam alignment. In the TBL a 25 A Drive Beam was decelerated from it initial energy, 135 MeV, down to a minimum of 67 MeV, reaching the 50% deceleration milestone which was one of the initial goals of CTF3. On average the produced power was 90 MW per PETS. The total peak RF power produced in less than 20 m deceleration line reached 1.3 GW. The beam energy loss and its energy spread was measured in a time-resolved spectrometer, and agreed very well with simulations. The dynamics of the Drive Beam while undergoing deceleration was studied in detail, and both transverse and longitudinal parameters were in agreement with the simulations [329].

A.2.6 Two-Beam Acceleration: two-beam test stand and Two-Beam module

The key purpose of CTF3 was to demonstrate the CLIC Two-Beam Acceleration scheme, including efficient power transfer to high-gradient structures and acceleration of a Probe Beam. The Probe Beam was provided by the 24 m long injector linac, CALIFES [330], located in CLEX and delivering single bunches or bunch trains at 1.5 GHz bunch repetition rate and energies up to 200 MeV. The beam was generated and accelerated to ~ 5 MeV/c in a photo-injector and further accelerated in three 3 GHz accelerating structures recuperated from the LEP Injector Linac (LIL). The accelerating structures and the photo-injector were powered by a single 3 GHz klystron delivering 4 MW RF pulses during 5.5 µs to an RF pulse compressor. CALIFES was usually operated with bunch charges of ~ 0.1 nC and a normalized R.M.S. emittance of 10 µm.

The Probe-Beam energy was measured in a spectrometer as a function of the Probe Beam 3 GHz RF phase, phase-locked to the laser pulse timing. A phase scan was then used to adjust the relative timing between Probe and Drive Beam for maximum acceleration. The nominal CLIC accelerating gradient of 100 MV/m corresponds to an energy gain of $\Delta E = 21$ MeV. Energy gains of up to $\Delta E = 32$ MeV were achieved with relatively low breakdown rates (a few 10^{-3}), while higher gradients, up to 165 MV/m were achieved with higher rates [327]. Figure 99 shows an example of $\Delta E = 32$ MeV Probe-Beam Acceleration measured on the spectrometer screen, corresponding to an accelerating gradient of 145 MV/m.

The effect of breakdown kicks on the Probe Beam was also extensively studied [331]. At the end of 2014 the TBTS was replaced by the Two-Beam Module, TBM, a 2 m long fully representative unit of the CLIC Main Linac, including an active alignment system (Fig. 100). The nominal CLIC gradient/pulse length was again established,

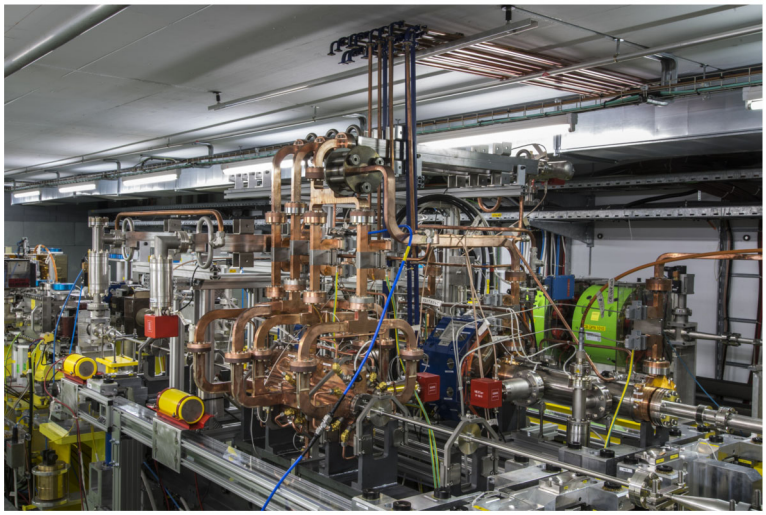

Fig. 100 The Two-Beam Module, TBM, a 2 m long fully representative unit of the CLIC main linac, installed in the CLEX area of CTF3

and extensive tests of the module functionality, including precision and reliability studies of the active alignment system, and measurements of transverse wakefield effects were carried out. The experimental results were consistent with specifications and simulations.

A.2.7 Conclusions on CTF3

The CLIC Test Facility CTF3 provided a rich experimental programme, addressing various aspects of the accelerator technology needed for CLIC and solving the vast majority of issues related to Drive-Beam generation, power production and Two-Beam Acceleration. In particular, high-gradient acceleration beyond 10 MV/m using X-band room temperature is now well established, as well as the production and use of a high-current Drive Beam as an efficient and reliable source of X-band RF power in the range of hundreds of MWs. CTF3 successfully completed its experimental program in December 2016 as planned, and stopped operation.

A.3 Drive-Beam injector performance

A.3.1 Drive-Beam electron source

The CLIC Drive-Beam electron source has been designed taking into account the results from CTF3. The source is a scaled version of the CTF3 gun originally developed and contributed by SLAC and LAL. The current of 4.2 A is very similar to the one used in CTF3 but the pulse duration is 140 s and therefore 100 times longer than in CTF3, thus covering the main difference in performances with respect to the CTF3 gun. The second very challenging specification is the required beam stability over such a long pulse. The charge needs to be stable to 0.1% both along the pulse and from pulse to pulse. An electron gun based on a commercial thermionic cathode with a voltage of 140 kV has been developed and a prototype was built [332]. The cathode has a grid which allows beam current regulations. A test stand has been built at CERN to demonstrate the performance of the Drive-Beam electron source. The experimental setup can be seen in Fig. 101. The source produced pulses of 140 s duration with a current of 4.2 A. The stability of the beam has been measured and a shot to shot reproducibility of 0.2% has been achieved already. The emittance of the beam has been estimated to be below 10 mm mrad by comparison with PIC simulations. Since the stored energy needed to use a DC high voltage with a 10^{-4} stability is quite substantial, a pulsed high-voltage modulator based on a Marx-topology has been developed in collaboration with CEA [333]. The modulator demonstrated a stability of 0.1%. Therefore the concept for the critical Drive-Beam electron source as described in the CDR can be considered as validated.

A.3.2 Sub-harmonic bunching system

In addition to the source, another critical item of the Drive-Beam Injector, the sub-harmonic buncher, has been investigated experimentally. The Drive-Beam Injector uses three sub-harmonic bunchers at 499.75 MHz to pre-

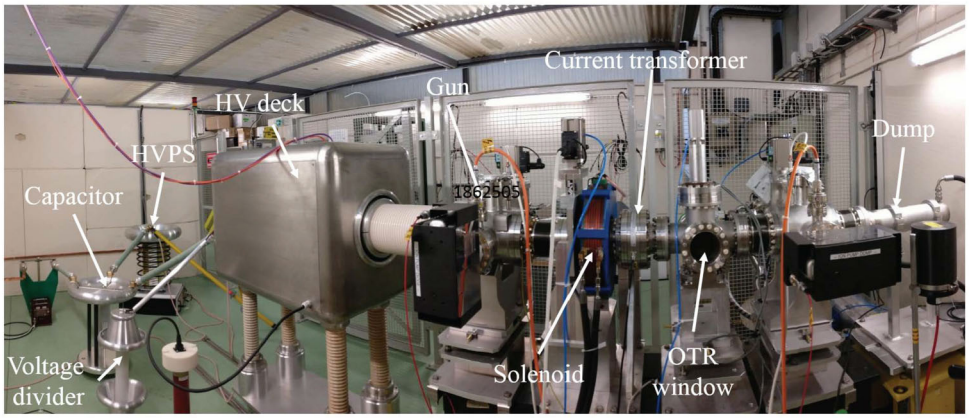

Fig. 101 Drive-Beam Electron Source test stand at CERN. The cathode is installed within a ceramic insulator while the anode is on ground potential. All drive electronics for the cathode is installed on a high voltage deck at a potential of 140 kV. The beam can be diagnosed to measure its current, shape and emittance

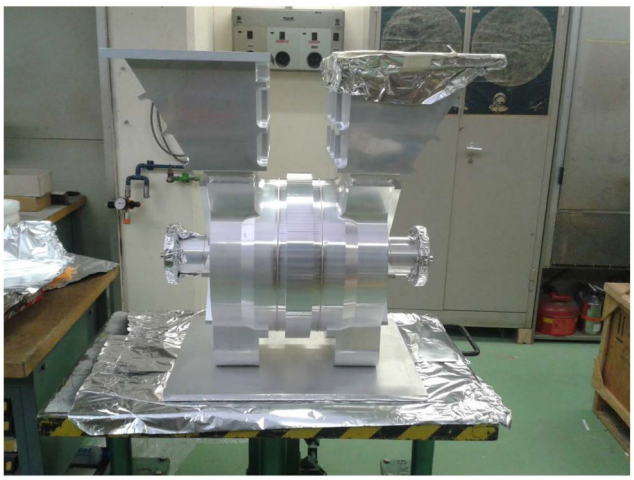

Fig. 102 Prototype of a 500 MHz sub-harmonic buncher for the CLIC Drive-Beam Injector. The cavity was made of aluminium

bunch the beam out of the DC source and switch the phase of the bunches by 180 deg every 240 ns to enable the beam for later recombination. The buncher and its RF power supply need therefore to have a bandwidth of about 10%. In order to ease the requirements for the RF power source a buncher was developed which minimizes the power needs. The solution found is a two cell, backward-wave, travelling-wave structure. The detailed design of the buncher cavities can be found in [112]. A prototype is shown in Fig. 102. The innovative prototype was built out of aluminium because of weight and cost considerations. The cells were joined by electron beam welding. In parallel a solid state amplifier with an output power of 20 kW was developed by RRCAT in India as a prototype for the necessary RF source. The amplifier architecture could be scaled up the 100 kW needed for the third buncher in the CLIC injector scheme. The amplifier and the buncher were tested together at full output power, pulse length and duty factor successfully fulfilling as well the stability requirements.

A.4 BDS beam dynamics, experimental studies in ATF2 and FFTB

A.4.1 Achievements and plans

The Final Focus Systems (FFS) envisaged for future linear colliders are regarded as major challenges requiring experimental demonstrations. Table 58 shows the main FFS parameters of the different experimental projects [42–45, 91, 334, 335].

The first FFS experiment was FFTB [42], which used a traditional chromaticity correction scheme. The achieved vertical beam size was more than 50% larger than the design. It was suspected that this deviation was due to orbit jitter.

ATF2 was conceived to demonstrate the compact chromaticity correction scheme presented in [93] and it operates with extended goals to demonstrate CLIC chromaticity levels. It has occassionally reached 41 nm vertical beam size, just 10% above design, but using relaxed optics with ten times larger β_x^*. According to simulations the need to enlarge β_x^* may come from poor orbit control or magnetic aberrations [336].

Table 58 FFS parameters for CLIC and related experimental projects [42–45, 91, 334, 335]

		CLIC	FFTB	ATF2			SKEKB
		3 TeV		Nom.	UL β^*	Long L^*	Low β^*
L^*	[m]	6	0.4	1	1	2	0.9
β_y^*	[mm]	0.12	0.1	0.1	0.025	0.1	0.09
$\xi_y \approx L^*/\beta_y^*$	[10^3]	50	4	10	40	20	10
ϵ_y	[pm]	0.003	22	12	12	12	13
σ_y design	[nm]	1	52	37	23	37	34
σ_y measured	[nm]	-	70±6	41±2	-	-	-

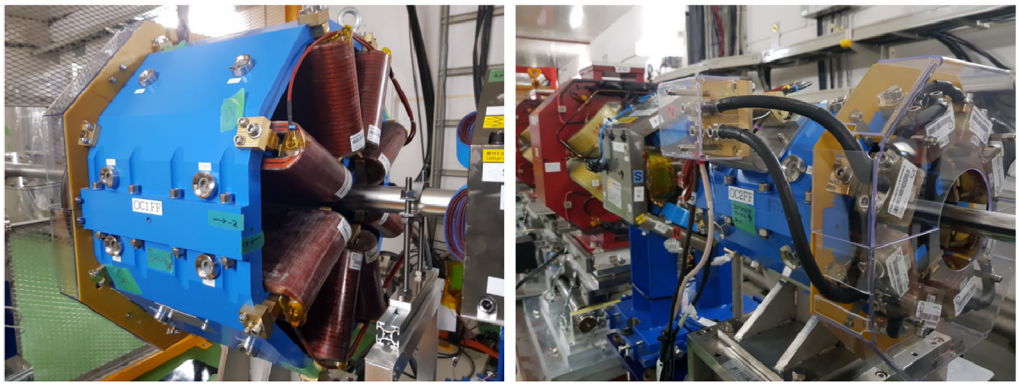

Fig. 103 Octupole magnets OCT1 (left) and OCT2 (right) installed at ATF2 beamline

The ATF2 Ultra-low β^* proposal aims at reducing beam size below 30 nm achieving similar chromaticity levels as the CLIC FFS. Two octupoles manufactured by CERN have been installed in order to cancel high order aberrations. Fig. 103 shows the octupole magnets installed in the beamline. Another option to increase the ATF2 chromaticity without reducing the IP beam size is to increase L^*. This modification could be considered once ATF2 has reached its main goals. Actually further R&D proposals exist related to CLIC as the study of crystal focusing [337].

SuperKEKB is an e^+e^- circular collider aiming at reaching 60 nm beam size at the IP with a traditional chromaticity correction system. An alternative FFS design using the traditional chromaticity correction was proposed for CLIC [338]. A pushed optics version of SuperKEKB FFS has been presented in [45] to approach its chromaticity levels to CLIC and an IP beam size of about 40 nm. An experimental program to test CLIC FFS in SuperKEKB is being considered.

A.4.2 Ultra-low β^* with octupoles in ATF2

Reducing the β functions at IP to such small values reported in Table 58 imposes tight constraints on the machine imperfections. A clear example was the field quality of the quadrupole magnets installed in 2009 in the ATF2 beamline. Some of the measured [339] multipolar components present in the Final Doublet magnets exceed the tolerances of both the ATF2 Nominal and Ultra-low β^* lattices, as shown in [44, 340, 341]. The Ultra-low β^* is the most severe case, as expected. Possible solutions can be found by decreasing the horizontal β function along the beamline so that the impact of the multipolar components is reduced accordingly. However, this option deviates from the beam size aspect ratio required to test the FFS of the future linear colliders. A pair of octupole magnets would be required to effectively test the pushed optics at ATF2 without altering the β^*, as shown in [342]. Additionally it was found that the effect of the fringe fields of the FD quadrupoles would also preclude to reach a $\sigma_y^* \leq 30$ nm. Nevertheless, this detrimental effect could also be compensated thanks to the octupole magnets, as shown in [343]. Finally the pair of octupole magnets would provide additional knobs to carry out the tuning of ATF2 under machine imperfections, as considered in [344]. Therefore, a pair of octupole magnets were fabricated [345] at CERN following the specifications given in [346] and installed in ATF2 by 2016. Presently the octupole magnets are in operation and provide additional tuning knobs for the ATF2 ultra-low β^* tuning [347]. The latest works on ATF2 ultra-low β^* tuning can be found in [348, 349].

A.4.3 Ground motion in ATF2

Ground motion (GM) is not a limiting factor in the ATF2 performance. We use ATF2 as a test bed for CLIC GM concepts. 14 Güralp 6T seismometers have been installed at ATF2. They have been used to measure GM and magnet vibrations regularly and to identify their main sources [242]. Recently, these seismometers, in combination with a transverse kicker, have been used to demonstrate for the first time an orbit feed-forward system based on quadrupole motion measurements [350]. About 80% of the quadrupole-induced jitter was successfully cancelled with the transverse kicker. Future studies will aim to use more than one kicker to increase the efficiency of the feed-forward further.

A.4.4 Wakefields

The ATF2 IP vertical beam size was observed to increase with bunch intensity by about a factor 2 in [43, 44, 336]. This could be partially explained by the combination of wakefields and a large orbit jitter of 0.4 σ_y. Many wakefield sources were removed from the beamline, including cavity BPMs and a reduction of the beam size growth with intensity was observed. However, $\sigma_y = 41$ nm has not been reached again in ATF2, and the intensity dependence has not been evaluated in the same conditions.

An attempt to study this intensity-dependent effect has been made using the beam orbit [351, 352]. However, 36 of the 46 BPMs in the machine (striplines and cavity BPMs) do not provide the required precision for such studies. A Wakefield Free Steering (WFS) correction scheme was tested on the machine in February 2018 with promising results [352, 353]. The method consists of correcting the orbit difference due to the charge-related effects using the ATF2 steering magnets. Further work will be done to improve the technique. WFS could be considered an integral part of the tuning procedure.

A.5 Low emittance preservation (FACET / elettra)

The proposed high luminosity of CLIC (and ILC) requires normalised vertical emittances of a few tens of nanometers at the interaction point to reach the target luminosity. Because of these ultra-low emittances, preserving the emittance throughout the entire accelerator from the damping rings to the interaction point has been regarded as a potential feasibility issue for the whole project. The primary sources of emittance growths are misalignments of the accelerator components, which cause transverse deflections, introduce dispersions and might create short and long wakefields in the accelerator structures. The long train of bunches might suffer from long-range wakefields, which induce beam breakup and cause beam losses. Spurious dispersion in the quadrupoles causes emittance dilution, which scales as the squared of the absolute misalignment of the beam BPMs, and the emittance dilution due to single-bunch transverse wakefields, which scales as the square of the accelerator structure offset [354]. Other sources of the emittance growth include bending magnets where consistent emission of synchrotron radiation occurs, geometric and chromatic aberrations in nonlinear magnets, correlated energy spread due to longitudinal short-range wakefield effects in the accelerator structures, etc.

Most of these effects are excited by transverse installation misalignments of the elements, and therefore, a tight pre-alignment of the components is required; in the case of the CLIC Main Linacs, this means one order of magnitude better than the available off-the-shelf solutions. The CLIC-motivated, EU-funded PACMAN project [201] was launched to address this issue and, within its duration, successfully reached the required precision and accuracy. Yet, excellent pre-alignment is insufficient to preserve the ultra-low emittances, and dedicated beam-based techniques must be put in place to mitigate the impact of the imperfections further. In CLIC, this problem is even magnified by the sheer number of accelerator components: the Main Linacs of CLIC, at 380 GeV centre-of-mass energy, are about 3 km long and contain about 600 quadrupoles and as many BPMs (which, anyway, is just less than half the total number of components traversed by the electrons and by the positrons along their way from the damping rings through the interaction point). Such a large number of components adds at least two complications: (1) it increases the number of potential sources of emittance growth, and (2) it makes local correction techniques impractical and excessively time-consuming. Instead, in order to align such linacs robustly and more practically, global correction algorithms need to be used. Such algorithms have been studied and modelled intensively during the last decades [355–357]. In conjunction with even more sophisticated algorithms, a global dispersion-free correction has been proposed and foreseen as an integral part of the linac tuning procedures for CLIC and ILC.

Another significant effect that might harm the beam is the long-range wakefields in the accelerator structures. In this case, each bunch can affect later bunches within the same train and induce beam breakup. Analytic evaluations of the tolerance of the beam to such long-range wakefield kicks lead to key design choices for the CLIC main accelerating structure, which, in fact, features both waveguide damping and cell-to-cell detuning to provide strong broadband suppression of the long-range wakefields (see [358] and CLIC CDR [55]). Our tests at FACET aimed at a direct measurement of the long-range wakefield kicks *with beam*, ultimately validating this design.

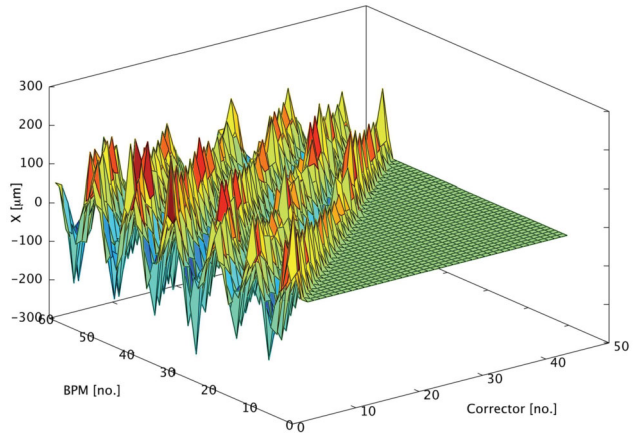

Fig. 104 The orbit response matrix, R, as measured by estimating the orbit difference from systematic alternating-sign correctors kicks and applying the system identification algorithm

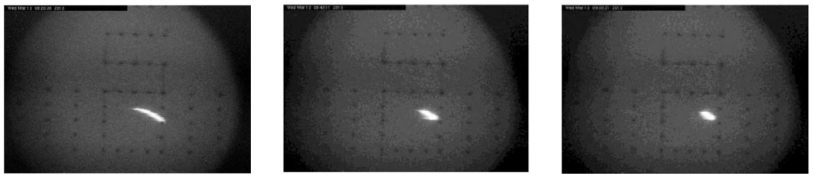

iteration 0 iteration 1 iteration 3

Fig. 105 Phosphorous beam profile monitor measurements at the end of the FACET linac, before the dispersion correction, after one iteration step, and after three iteration steps. Iteration zero is before the correction

To assess the criticality of the issues mentioned above, a programme of experimental verifications was launched, making use of the FACET linac at the SLAC National Accelerator Laboratory [48] and of the linac of FERMI@Elettra free-electron laser in Trieste, Italy [49]. The goals of this measurement campaign were twofold: (1) demonstrate the effectiveness of global beam-based alignment algorithms, (2) measure the long-range wakefields in the CLIC structure and validate the design. Both goals have been successfully achieved.

A.5.1 Beam-based alignment

Experience at FACET The latest incarnation of the SLC linac, i.e. the FACET test facility at SLAC, was the ideal testbed for our linear collider beam-based techniques. The FACET facility used the first 2 km of the Stanford Linear Collider, accelerating electrons (and positrons) from 1 GeV to 20 GeV beam energy, with several tens of correctors and BPMs. Here, we report on the experimental proof-of-principle of emittance reduction techniques in a long line by applying dispersion-free correction with automatic "system identification" algorithms. The test was structured in two phases; first, we deployed an automatic procedure to perform a system identification aimed at computing the response matrices from measurements, and then we made use of such response matrices to perform tests of dispersion-free steering (DFS) correction. We verified the combined effect of the system identification and dispersion-free correction by preparing extensive PLACET [359] simulations of a model of the FACET linac before the measurement. Furthermore, PLACET was used in flight-simulator mode to develop and fine-tune all the scripts for the online operation. Detailed explanations of the procedure are presented in [46].

The response of each BPMs to beam corrector excitations was measured using state-of-the-art system identification procedures [360] both for the nominal and dispersive test beams, required for the dispersion correction. The response matrices were obtained by operating the linac in nominal conditions for the orbit correction and changing the phase of a single klystron in the upstream section of interest from 0 to 90 degrees for the test beam. The selection of klystron and phase change was based on simulated evaluations. Figure 104 shows the measured orbit response matrix.

Figure 105 shows one of the best results of the experiment, which demonstrated how the algorithm successfully corrected dispersion and, in so doing, helped to recover the transverse emittances. The horizontal dispersion was robustly corrected by a factor 3 and the vertical by a factor 4. It should be noted that during the correction, the absolute orbit diverges from its initial course, as the dispersion is reduced. This is to be expected.

Experience at FERMI@Elettra Spurred on by the success of the tests of beam-based alignment performed at FACET, we had the chance to test our beam-based alignment algorithms at other machines. The linac of the free-

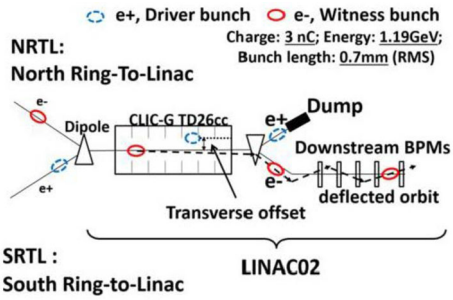

Fig. 106 Layout of the wakefields measurement experiment

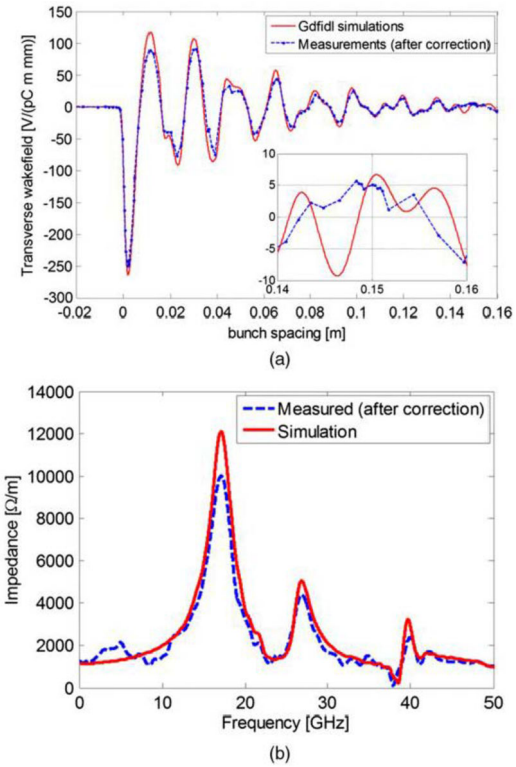

Fig. 107 (a) Wakefield plots compared with numerical simulations. (b) Spectrum of measured data versus numerical simulation

electron laser FERMI@Elettra at Sincrotrone Trieste, Italy, was probably the ideal one for us, given the presence of an X-band accelerator structure, used as RF lineariser, and of several C-band structures featuring strong transverse wakefields [49]. At FERMI@Elettra we took the chance to test a variant of dispersion-free steering, called wakefield-free steering (WFS), where the effect of the wakefields on the orbit is removed by means of dipole corrector magnets, rather than the dispersion. The results of this experiment have been published in [47].

A.5.2 Long-range wakefields

The design of the CLIC main accelerator structure, heavily damping the high-order modes, was validated at FACET. This demonstration aimed to validate that the beam dynamics requirements are met and to prove that the computer-simulated transverse wakefields are accurate [361]. This latter condition was essential since the design may evolve in the future. The experimental demands were significant since the suppression must be measured at bunch distances from the peak of the transverse wakefield to the end of the CLIC bunch train, which spans more than four orders of magnitude, namely from 1 mm to 50 m and over approximately three orders of magnitude of wakefield level. These requirements could only be met at the FACET facility at SLAC. The peculiarity of this facility, which is unique and essential for this type of measurement, is that it could simultaneously deliver positron and electron bunches. This allowed us to excite wakes with a positron bunch and then measure the transverse kick directly on the following electron bunches at a variable distance. The experiment setup and the main results are shown in Fig. 106 and 107. The agreement between simulation and measurement is strikingly good. A detailed explanation of the experiment was presented in [362].

Table 59 Operating parameters for the structures of the two energy stages

Structure	G [MV/m]	P [MW]	τ [ns]	BDR [10^{-7}/pulse]
380 GeV	72	60	244	3
3 TeV	100	61	244	3

G is the beam-loaded accelerating gradient, P is the input power for the beam-loaded accelerating gradient, τ is the total RF pulse length, and BDR is the breakdown rate in units of breakdowns per pulse.

A.5.3 Summary

The campaign of experiments at FACET and FERMI@Elettra proved extremely fruitful:

1. It demonstrated the effectiveness and the portability of global system identification and beam-based algorithms
2. It validated the design of the CLIC accelerator structure with respect to the heavy damping of high-order modes
3. It validated the numerical wakefields calculation by 3-D electromagnetic codes, and increased our trust in these codes.

A.6 Performance of high-gradient accelerating structures

Accelerating gradient is one of the most influential parameters in determining the performance and cost of CLIC. The two fundamental phenomena limiting gradient in a normal conducting accelerating structure are breakdown, also known as vacuum arcing and pulsed surface heating. A multi-decade effort by the CLIC collaboration has been made to understand these phenomena and demonstrate in test devices and prototype accelerating structures that the design gradient for CLIC can be met. In addition, supporting gradient results have been achieved in relevant RF systems of linacs dedicated to other applications. This section gives an overview of the theoretical background and critical issues for high-gradient accelerating structure testing and feasibility demonstration. A near-comprehensive table of prototype testing results is also presented.

There are two types of accelerating structures for CLIC; one optimized for the 380 GeV energy stage, also used for the 550 GeV energy stage, and the other initially designed for the 3 TeV energy stage and now foreseen for part of the 1.5 TeV energy stage. The structures are described in Sect. 4.5.3, and the corresponding key operating parameters are summarized here in Table 59.

For a given fabrication technology, the field holding capability, and consequently the achievable accelerating gradient of a specific structure design, depends on its geometry. Quantitative models based on the power flow of this geometrical dependence are described in [363, 364]. More generally, the fundamental breakdown processes are described in a comprehensive review [365]. The strongest geometric dependence of the accelerating gradient is on the structure aperture, with a smaller aperture giving a higher and a larger aperture giving a lower gradient. Through overall facility optimization, the 380 GeV structure has a larger aperture than the 3 TeV structure, as listed in Table 4.5.3, with a correspondingly lower accelerating gradient as listed in Table 59. Both structure types have been tested and operated in the CLIC structure development program. Historically, 3 TeV structure tests were carried out first due to the earlier emphasis on demonstrating the feasibility of the 3 TeV CLIC design. The focus of the tests shifted to the 380 GeV structure as the energy staging of the CLIC project was elaborated. In addition, the 3 TeV structure was developed in two basic iterations.

Testing for structures has been carried out first without higher-order-mode damping waveguides (so-called undamped structures), then in structures with higher-order-mode damping waveguides and finally including the damping waveguide terminating loads. So far, the last has been carried out in a limited way for the 3 TeV structure, and the first was skipped for 380 GeV structures. The logic for this sequence is that the basic level field holding capability of the design is determined by the iris aperture, and undamped structures are the simplest and least expensive to fabricate. Hence, undamped structures were tested first. Damping features have a predicted reduction in performance, essentially through lowering the shunt impedance, but also possibly by unexpected phenomena, for example, due to side effects caused by the increased mechanical complexity of including the damping waveguides. Thus, testing of damped structures is an important second step. The third, and final step, is to include the waveguide terminating loads. These loads are placed far from the high field regions of the cavity, so are expected not to affect the achievable accelerating gradient. However, the loads require adaptation and further complexity of the mechanical design of the accelerating structures, so the absence of any side effects must be demonstrated. Additional design details, such as the type of input and output power couplers, have evolved during the testing program.

In addition to RF design, fabrication technology can have a strong influence on achievable gradients. A common feature of all the test and prototype structures described below is that for the individual cells, the final machining

step is made with single-point diamond turning and milling in the case of structures with higher-order-mode damping waveguides. The initial and majority of structures were joined by diffusion bonding at 1040 °C. Later test structures were joined using silver brazing at 850 °C. The brazed structures performed as well as the bonded ones.

Another issue to introduce before continuing to the performance results, is that the accelerating gradient specification is accompanied by pulse length specification as well as a breakdown rate requirement. The relation amongst these parameters is discussed extensively in Refs. [363, 364] and is described by the relation $BDR\alpha E^{30}\tau^5$. BDR is the breakdown rate, the average number of breakdowns divided by the number of pulses in a measurement window, E is the field level and τ is the pulse length. As a practical matter, experiments are inevitably carried out at different combinations of these parameters, but results can be compared to each other by scaling using the dependency presented above. This is particularly the case for the breakdown rate. The breakdown rate per meter requirement for CLIC is quite low, $O(10^{-7})$ for 3 TeV, in order to limit the loss of luminosity due to breakdown. The CLIC main linacs are quite long and a breakdown anywhere will cause loss of luminosity on that pulse. A practical consequence is that it has often been necessary to operate structures at a breakdown rate higher than the CLIC specification due to limited testing time.

High-gradient test results, organized by structure type, are presented are summarized in Table 60. More information about the test of these structures, analysis of high-field behavior more generally and the performance of related structures can be found in the non-exhaustive list of references [366–378].

The tests of undamped 3-TeV structures show that gradients well over 110 MV/m are feasible. Adding damping features results in the roughly 10% reduction in gradient expected from changes in RF parameters. The damped structure gradient is somewhat below specification when the 15 MV/m beam loading is considered. For this reason, a 10% reduction of high-field limits was taken when designing the 380-GeV structures. The first 380-GeV structures, which directly include higher-order-mode damping features, currently under test are already fulfilling specifications.

All the results presented above were taken during tests where no beam was present. To achieve high RF-to-beam efficiency in CLIC, beam loading is very high, resulting in the difference of 20 MV/m between loaded and unloaded gradient described above for the 380 GeV structure. Beam loading in travelling wave structures is not spatially uniform but results in field levels that are reduced in the downstream part of the structures, although fields are unchanged at the upstream end of the structure. In order to obtain a conservative feasibility demonstration, the tests have targeted the input power which would give the design gradient with beam loading. A dedicated test of the effect of beam loading on breakdown rate is described in [379].

A.7 Damping rings

The main challenge of the Damping Rings (DRs) is the generation of ultra-low emittances in all planes in order to achieve the high brightness beams required for the linear collider luminosity production. In Fig. 108 [380], the transverse geometrical emittances of low emittance rings in operation (red) and design are presented. In recent years, it is apparent that, in particular, the new generation light sources are approaching and even superseding the horizontal emittance target of the CLIC DRs, whereas the vertical emittance has been reached in operating storage rings. What differentiates the CLIC DRs compared to other low emittance rings, is the necessity to reach these emittances simultaneously, and having a low longitudinal emittance, translated to bunch lengths, of below 2 mm.

This high beam brightness drives the design choices of the DRs. The approach is to design a compact ring, attaining a sufficiently low emittance taking into consideration collective effects, such as Intra-Beam Scattering (IBS), e-cloud or even space-charge, which dominate the emittance evolution along the 20 ms cycle. In this respect, all the design parameters including optics were carefully chosen and optimised in order to mitigate the impact of collective effects [57, 58]. In particular, an effort was made to reduce the effect of IBS on the "zero-current" emittance. A further improvement can be made by replacing the arc bending magnets with ones including a variation in the longitudinal plane and considering wigglers with even higher field in the straight sections.

The natural lattice choice for the arc optics are the Theoretical Minimum Emittance (TME) cells [59], which can provide very small emittances, as well as high compactness. The horizontal emittance can be further reduced below the TME limit by considering dipole magnets with longitudinal variable bending field [65, 66, 381–384]. Based on an analytical evaluation [67] and magnet design considerations [68], an optimised trapezium bending radius profile is employed, i.e. with parabolic field evolution in the edges and constant in the centre.

A.7.1 Optimization of the arc TME cell

In the considered arc cell, the dipole length is $L = 0.58$ m and the maximum dipole field is 2.3 T. When the uniform dipoles of the current design are replaced by variable bends, the resulted emittance is lower than the required one.

Table 60 High-gradient testing results for CLIC-type structures

Energy Stage	Structure Type	Gradient [MV/m]	Pulse Length [ns]	BDR [10^{-7}/pulse]
3 TeV	T18	90	230	13
	T18	110	230	770
	T18	102	252	8
	T18	105	230	16
	TD18	87	252	20
	TD18	85	230	24
	T24	120	252	15
	T24	85	230	20
	T24	80	200	50
	T24	110	252	13
	TD24	105	252	60
	TD24	100	250	3
	TD24	100	252	12
	TD26	100	250	69
	TD24open	97	200	50
	TD24	103	525	3.7
	TD24	104	252	8.3
	TD26	113	200	80
	TD26	110	100	120
	TD24SiC	94	100	10^3
	T24	121	200	750
	T24	113	200	180
	TD24SiC	105	50	50
	TD24	95	150	70
	TD24	98	100	200
	TD24	97	200	150
	TD24	100	60	250
380 GeV	*TD31	75	60	10
	*TD31	84	212	179
	*TD31	84	100	179

'T' denotes undamped structures and 'TD' damped structures. An asterisk before the structure type indicates the test is underway at the time of writing. The results are presented in approximately chronological order.

In this case, the subtraction of some TME cells from the existing arc is possible. Actually, the number of dipoles (i.e. total number of TME cells) can be reduced to such an extent that the required emittance is still achieved, thereby resulting in a shorter ring.

As soon as the characteristics of the dipole are fixed, the drift space lengths are chosen [67]. Afterwards, it is necessary to find the phase advances that guarantee low chromaticities and small quadrupole strengths. Keeping in mind that a modified TME cell with a combined function dipole, i.e. having a small defocusing gradient, has a positive impact on the IBS effect [385] assists in choosing the proper phase advances. The parametrization with the emittance showed that the quadrupole strengths for which $f_1 < 0$ and $f_2 > 0$, can only be found for $\mu_x < 0.5 \cdot 2\pi$. Another reason that renders larger phase advances inappropriate is that they result in huge anharmonicities. A good compromise for the horizontal phase advance is to be around $0.43 \cdot 2\pi$ and for the vertical phase advances to be always below $0.5 \cdot 2\pi$. After a detailed scanning of the cell characteristics, the horizontal and vertical phases advances of the TME cell are respectively chosen to be around $0.44 \cdot 2\pi$ and $0.1 \cdot 2\pi$, corresponding to an emittance reduction factor that is $\epsilon_r = 6.5$. Taking into account the fact that for the designed variable bend it is $F_{TME} = 7.1$, emittances smaller than the ones of the current design with the uniform dipoles, are reached. In this respect, it

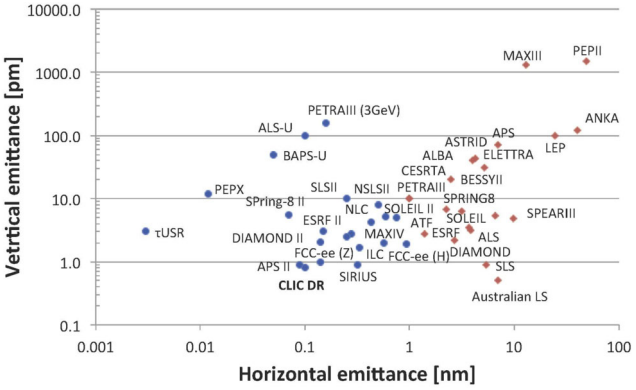

Fig. 108 Horizontal versus vertical geometrical emittance of low emittance rings in operation (red) and design (blue)

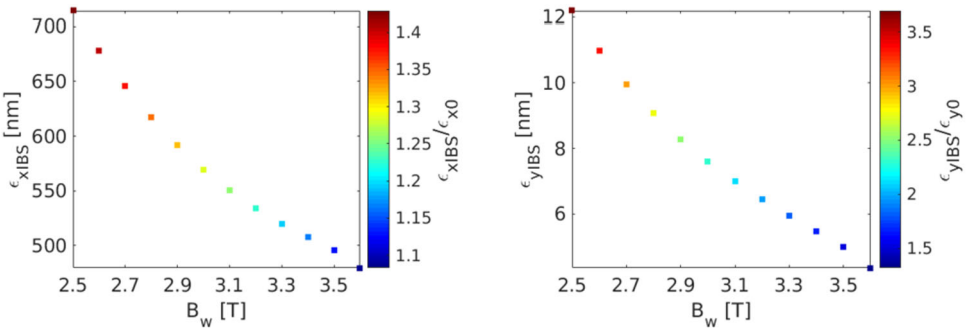

Fig. 109 The dependence of the steady state emittances (ϵ_{xIBS} and ϵ_{yIBS}) and their ratio with the corresponding equilibrium emittances (ϵ_{x0} and ϵ_{y0}) on the wiggler peak field B_w, for the trapezium dipole profile

was possible to reduce the number of dipoles down to $N_d = 90$ for the case of the designed trapezium profile with 2.3 T maximum field.

A.7.2 Optimization of the FODO cell

The damping wigglers are necessary for achieving low emittances within a fast damping time. Each FODO structure of the straight section accommodates two wigglers. The use of super-conducting technology is mandatory in order to have a high wiggler field and a relatively short period for obtaining low emittances and fast damping time. The super-conducting magnet wigglers used in the current design have a $B_w = 2.5$ T peak field and $\lambda_w = 5$ cm period [71]. A prototype wiggler with these characteristics was build by BINP and installed and tested in the ANKA storage ring, in particular for the cooling principle [70].

It was further shown that by targeting higher wiggler fields not only the emittance but also the IBS effect can be reduced [58, 283]. Taking into account the optimization of the arc cells and the fact that the emittance with IBS is significantly lowered after increasing the wiggler's peak field, the FODO cells per straight section can be reduced from 13 down to 10. The plots in Fig. 109 show the MADX results of the parametrization of the steady state transverse emittances including the IBS effect with the wiggler peak field B_w, starting from the 2.5 T, i.e. the field of the existing wiggler design, for the 10 FODO cells. Clearly, the wiggler field increase corresponds to a significant reduction of the IBS effect, through the minimisation of the damping time. Regarding the fact that the required output emittance is 500 nm-rad, a new working point for the damping wigglers that complies with the technological restrictions is proposed to be at 3.5 T and with a 49 mm period length. This design necessitates a different wire technology, using Nb_3Sn material [283].

A.7.3 Optical functions and new design parameters

The final lattice, with a smaller number of dipoles and wigglers than the ones of the existing design, is the one designed for the re-baselining exercise. In Fig. 110 (left), the matched optics, i.e. horizontal dispersion, horizontal and vertical beta functions, are plotted for one arc TME cell. On the top part of the figure, a schematic layout of the cell is presented, showing the two doublets of quadrupoles and the sextupoles that are placed between the two mirror symmetric defocusing quadrupoles and between the dipole and the focusing quadrupoles. In Fig. 110 (right), the matched optics of the dispersion suppressor-beta matching section followed by the wiggler FODO cell, are presented.

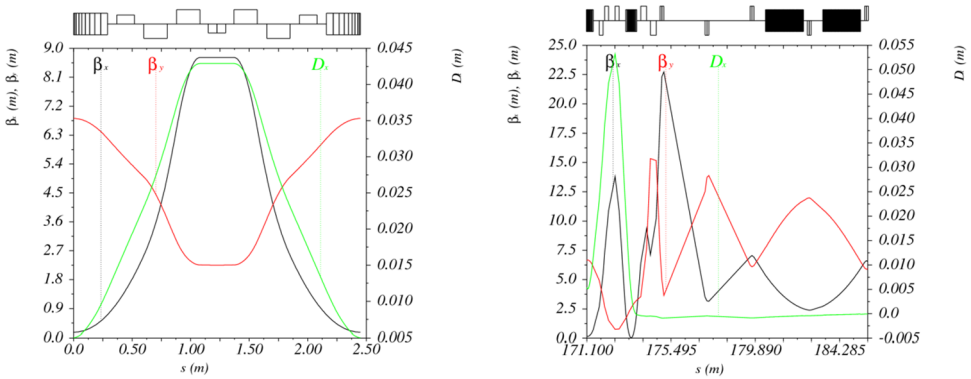

Fig. 110 Optical functions of the TME cell (left) and of the dispersion suppressor-beta matching section followed by the FODO cell (right), when using in the arcs the trapezium dipole profiles

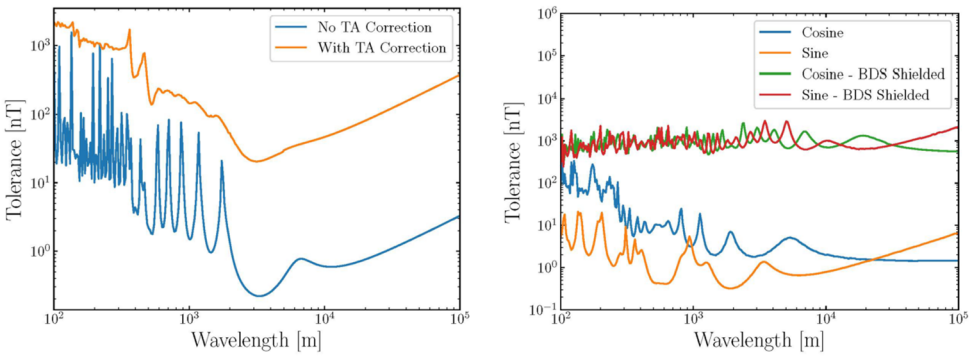

Fig. 111 Stray field tolerances for the 380 GeV CLIC design [388]. Simulations were performed with the particle tracking code PLACET [389]. The tolerance was calculated as the stray field amplitude that corresponds to a 1.2 nm emittance growth (equivalent to a 2% luminosity loss)

The parameters of the original design and the alternative one are displayed in Table 61. Note that for the nominal bunch charge, all emittance targets are reached, including IBS, as calculated by the Bjorken-Mtingwa formalism through MADX. Due to the larger bunch population of $N_b = 5.7 \times 10^9$ for the case of low energy CLIC and $V_{RF} = 6.5$ MV [7], the final emittances are increased up to 536 nm and 6.5 nm in the horizontal and the vertical plane, respectively. One of the main advantages of the alternative design is that the damping ring becomes around 20% shorter. In addition, the damping times are significantly reduced and this is quite beneficial for all collective effects, including IBS.

A.8 Impact of stray magnetic fields

Another source of luminosity loss which has been investigated is the effect of external dynamic magnetic fields (stray fields).

A.8.1 Tolerances

Simulations of sinusoidally varying stray fields experienced directly by the beam have shown nT tolerances to remain within a 2% luminosity loss budget [82, 386–388]. Shown in Fig. 111 is the tolerance for the long transfer line in the RTML, with and without a correction in the TA - discussed in Sect. A.8.3. The tight tolerance arises from the relatively weak focusing and long drifts in the transfer line. A minimum tolerance of approximately 0.1 nT corresponds to the stray field wavelength approaching the betatron wavelength of the lattice.

Shown in Fig. 111 is the tolerance for a stray field in the ML and BDS, along with the effect of shielding the BDS - discussed in Sect. A.8.3. Two types of stray fields have been considered, those which are symmetric about the IP (Cosine) and those which are anti-symmetric about the IP (Sine). Sine-like stray fields introduce an offset at the IP, which is not present for cosine-like stray fields, generally leading to tighter tolerances. The sensitivities in the tolerance for the ML and BDS come almost exclusively from the BDS, particularly in cases where the stray field wavelength resonates with the betatron motion at locations in the BDS where the beta function is large, such as the collimation section and bends before the final focus. The minimum tolerance observed is approximately 0.1 nT for sine-like stray fields and a tolerance of approximately 1 nT emerges for coherent (long wavelength, cosine-like) stray fields.

Table 61 Design parameters for the original and the improved designs of the CLIC DRs, for the case of $f_{RF} = 2$ GHz and $N_b = 5.7 \times 10^9$

Parameters, Symbol [Unit]	Uniform	Trapezium
Energy, E [GeV]	2.86	
Bunch population, N_b [10^9]	5.7	
Circumference, C [m]	427.5	359.4
Basic cell type in the arc/LSS	TME/FODO	
Number of arc cells/wigglers, N_d/N_w	100/52	90/40
RF Voltage, V_{RF} [MV]	4.50	6.50
RF Stationary phase [^{o}]	62.3	63.0
Harmonic number, h	2850	2398
Momentum compaction, α_c [10^{-4}]	1.3	1.2
Damping times, (τ_x, τ_y, τ_l) [ms]	(1.98, 2.05, 1.04)	(1.15, 1.18, 0.60)
Energy loss/turn, U [MeV]	4.0	5.8
Quadrupole gradient strengths, (k_1, k_2) [T/m]	(−26, 53)	(−29, 56)
Phase advances per arc cell, (μ_x, μ_y) [360^o]	0.408/0.050	0.442/0.100
Horizontal and vertical tune, (Q_x, Q_y)	(48.35, 10.40)	(45.61, 13.55)
Horizontal and vertical chromaticity, (ξ_x, ξ_y)	(−113, −82)	(−169, −51)
Dipole length, L_d [m]	0.58	
Dipole field, (B_{min}, B_{max}) [T]	(0.97, 0.97)	(0.69, 2.32)
Lengths and bending radii ratio, (λ, ρ)	(1, 1)	(0.04, 0.29)
Emittance reduction factor, F_{TME}	1	7.1
Normalized gradient in dipole [m^{-2} or T/m]	−1.1 or −10.5	
Wiggler peak field, B_w [T]	2.5	3.5
Wiggler length, L_w [m]	2	
Wiggler period, λ_w [cm]	5.0	4.9
	without IBS	
Normalized horiz. emittance, $\gamma\epsilon_x$ [nm-rad]	312.2	438.46
Normalized vert. emittance, $\gamma\epsilon_y$ [nm-rad]	3.3	3.3
Energy spread (R.M.S.), σ_δ [%]	0.11	0.13
Bunch length (R.M.S.), σ_s [mm]	1.4	1.3
Longitudinal emittance, ϵ_l [keVm]	4.4	4.6
	with IBS	
Normalized horiz. emittance, $\gamma\epsilon_x$ [nm-rad]	478.9	535.9
Normalized vert. emittance, $\gamma\epsilon_y$ [nm-rad]	5.0	6.5
Energy spread (rms), σ_δ [%]	0.11	0.13
Bunch length (rms), σ_s [mm]	1.5	1.3
Longitudinal emittance, ϵ_l [keVm]	4.7	4.8
IBS factors hor./ver./long.	1.53/1.52/1.08	1.22/1.96/1.05

A.8.2 Sources and measurements

Sources of stray fields can be classified as man-made or natural. Natural sources of dynamic stray fields typically have a coherence length of 100 km or longer. The frequencies of most of the natural sources are below 1 Hz. Such stray fields can be effectively mitigated with beam-based feedback systems. A review of natural sources above 1 Hz [390] concludes that they occur infrequently (less than once a month) or typically have pT amplitudes and are therefore within the tolerances. Natural sources should not pose a serious problem for CLIC.

Man-made sources can either be an environmental source, which is a piece of equipment that produces a stray field, but is not an element of CLIC, or a technical source, which is an element of CLIC. Examples of environmental

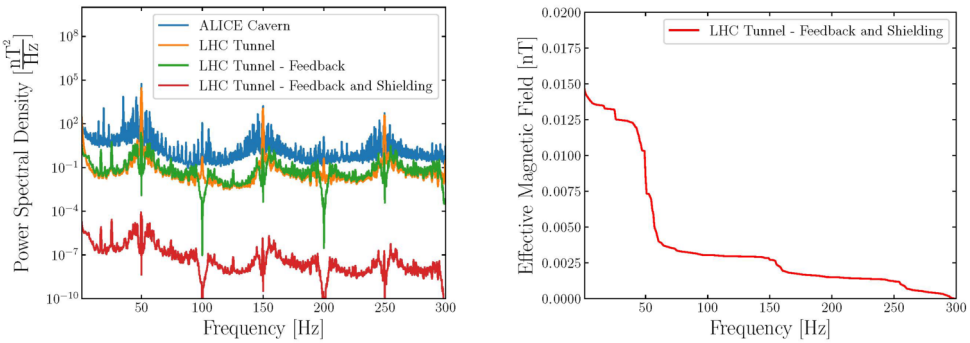

Fig. 112 On the left is the average total power spectral density of the background magnetic field measured at 8 different locations in the LHC tunnel and ALICE detector cavern along with the effective reduction in power due to the currently designed beam-based feedback system and a 1 mm mu-metal coating (with a relative magnetic permeability of 10,000) around a beam pipe of radius 1 cm. On the right is the square root of the integrated power spectral density, representing the magnetic field in the LHC tunnel after mitigation

sources are the electrical grid and railways. Other running accelerators can also act as an environmental source, particularly on the CERN site where there are several other running experiments.

Technical sources, such as RF systems, vacuum pumps and power cables, pose the greatest risk. These are capable of producing stray fields across a wide frequency range. A campaign to measure the power spectra of stray fields with an emphasis on technical sources has been carried out.

To characterise a background magnetic field, the power spectrum in the LHC tunnel and ALICE detector cavern was measured. This is shown in Fig. 112 along the effect of different mitigation techniques - discussed in Sect. A.8.3. Although this measurement doesn't replicate the exact magnetic environment of CLIC, it does represent the magnetic field that can be expected underground and in the presence of technical equipment and environmental sources. There is a significantly larger magnetic field in the ALICE detector cavern, highlighting that the detector can act as a technical source.

A.8.3 Mitigation

The sensitivity to stray fields arises in the RTML transfer line and BDS. The ML was the most robust section with respect to stray fields, with tolerances on the order of μT. There will also be an additional benefit in the ML of magnetic shielding provided by the copper walls that form each cavity, suggesting that an effective mitigation strategy can be obtained by targeting just the RTML transfer line and BDS. Two mitigation techniques are anticipated: a beam-based feedback system that will act across the entire accelerator, and a metallic coating of the beam pipe for magnetic shielding. The coating will only be applied to particular sections. Calculations of tolerances with different mitigation techniques are presented in [388].

A beam-based feedback system is modelled as an effective reduction in the power spectrum of the magnetic field. This is a simplification as the beam-based feedback does not act directly on the magnetic field, but its effect is equivalently modelled as a suppressed power spectrum. The effective reduction in power that the currently designed feedback system would provide on the magnetic field in the LHC tunnel is shown in Fig. 112. The largest contributions to the magnetic field are the harmonics of 50 Hz coming from the electrical grid. The feedback system mostly cures these harmonics, however there is some amplification of the frequencies in between due to the feedback system.

The effectiveness of a metallic coating with a material of high magnetic permeability, such as mu-metal, is under investigation. The effect of a 1 mm mu-metal coating on the magnetic field in LHC tunnel, shown in Fig. 112, is to reduce the effective magnetic field experienced by the beam to within the 0.1 nT tolerance of CLIC. This technique is well suited for long drifts and would be an effective strategy for mitigation in the RTML transfer line. It is expected that a stray field would not be able to penetrate through a magnet to influence the beam, therefore shielding the drifts only would suffice. Figure 112 shows the effectiveness of the mu-metal shield increases with frequency, which means frequencies above 300 Hz will be suppressed heavily.

The RTML transfer line will be parallel to the ML and the Drive-Beam Decelerators. Because of this, the optics of the RTML transfer line has been designed to reduce any effect stray fields associated with the decelerators could have. By ensuring a 90° phase advance between decelerators, any periodic perturbation from the decelerators would cancel. A feedforward trajectory correction could also be applied in the RTML TA. Figure 111 shows the tolerance can be increased by roughly two orders of magnitude with a feedforward correction.

A mu-metal shield can also be applied to sections of the BDS. As shown in Fig. 111, the tolerance can be increased by two orders of magnitude by surrounding the BDS with a perfect shield. It may not be necessary to shield the entire BDS, an order of magnitude increase in the tolerance can be obtained by shielding just the bends in the BDS [388].

The exact design of the mitigation has to be optimised taking into account the detailed technical design of components, and a measurement campaign to characterise a realistic power spectrum of magnetic fields for CLIC would likely be needed during the construcion phase. However, from the preliminary studies carried out, it is expected that a combination of beam-based feedback and magnetic shielding will be able to effectively mitigate the effects of stray fields.

Appendix B High-gradient and X-band applications

B.1 Introduction

The CLIC linear collider project has developed a significant body of high-performance linac technology, in particular in X-band and high-gradient RF accelerating systems. Although developed for the project, CLIC has made a significant effort to encourage the transfer of this technology to other applications. The main objective for the transfer effort has been to leverage the direct development investment in CLIC by the much greater resources available cumulatively in small and medium-scale projects. In addition, the near and medium-term timescales of such projects provide a steadier and larger market for commercial suppliers of components and processes needed for the high-gradient accelerator technology. This helps build the commercial base for an eventual linear collider in a more substantial way than direct development resources would alone.

This transfer of high-gradient and high-frequency technology has been quite successful and the technology is now being applied to a wide range of applications outside of high-energy physics. The transfer has been carried out through various means. These include federating a community by initiating and organizing the International Workshop on Breakdown Physics and High-Gradient Technology and hosting of engineers and scientists from other projects at CERN. Technology transfer has also been encouraged by sharing designs of components and systems through open hardware licenses. This successful technology transfer shows how developments driven by fundamental science can spread to applied science and direct societal applications.

There are three main areas to which the technology has spread. The first is to high-gradient test stands. A number of such test stands have been built where prototypes for future projects are validated. In some of these test stands studies are carried out on the fundamental processes of high fields like breakdown, field emission and pulse surface heating. The prototype testing and fundamental studies carried out in the CLIC test stands provide reference testing protocols, measurement and data analysis techniques so that results from different devices at different laboratories can be compared and benchmarked against know performance standards.

The second area of technology transfer is to the development of beam manipulation devices which need either high-gradients and/or high operating frequency. Such devices include energy spread linearizers, deflecting cavities for longitudinal bunch profile measurement and energy spread compressors. They are used in high-performance linear accelerators such as free electron lasers. In addition to the devices themselves, the rf powering stations closely resemble those of the CLIC test stands.

The third area where CLIC-heritage technology is used is in high-gradient linacs. Facilities that benifit from high-gradient include free electron lasers, inverse Compton scattering sources, light source injectors, test-beam facilities and medical linacs. The gradients for these facilities range from 30 MV/m to up to 70 MV/m. The high gradient technology is in some cases included in the initial design but in others is used to provide an energy upgrade to a facility. The latter is often the case where an energy upgrade must fit within the space of the original linac.

A special edition of the European Journal of Physics entitled X-Band and High-Gradient Technology covering some of these projects is under preparation [391].

B.2 Lists of facilities and devices

Non-comprehensive lists of facilities and devices which use CLIC-developed, or CLIC-related technology are shown in Tables 62–65. Table 62 lists high-power test stands, Table 63 lists X-band and high-gradient beam manipulation components, Table 64 lists high-performance linacs and Table 65 lists beam test stands.

Table 62 Test stands

Facility name	Host laboratory	Target project or application	Technical characteristics	Status
XBox - 1, 2, 3	CERN	CLIC, broad support to multiple projects, high-gradient studies	X-band - 50 MW, 50 MW, both 50 Hz, 2 × 6 MW, 400 Hz. XBox-1 connected to CLEAR	operational
CTF	Sincrotrone Trieste	FERMI energy upgrade	S-band - 45 MW, 50 Hz	operational
VBox	IFIC, University of Valencia	High gradient development	S-band - 2 × 7.5 MW, 400 Hz	operational
TEX	INFN Frascati	EuPRAXIA, CLIC, high gradient development	X-band - 50 MW, 50 Hz	operational
TEX upgrade	INFN Frascati	EuPRAXIA, CLIC, high gradient development	X-band 20 MW HE, C-Band 20 MW	procurement
Muon collider RF test stand	INFN-LASA Milano	Muon collider, HG in magnetic field, cryogenic	S-band	proposal
Muon collider RF test stand	tbd	Muon collider, HG in magnetic field, cryogenic	tbd	forming proposal
NEXTEF2	KEK	High gradient development	X-band - 50 MW, 60 Hz	operational
TPOT-X	Tsinghua University	High gradient development	X-band - 50 MW, 60 Hz	operational
XLab	Melbourne University	High gradient development	X-band - 2 × 6 MW, 400 Hz	operational
NLCTA-XTA, Klystron lab	SLAC	High gradient development	X-band - 2x50 MW, 2 × 50 MW, 60 Hz	operational
CERF-NM	Los Alamos	High gradient development	C-band, 50 MW, 100 Hz	operational
AWA	Argonne	Photoinjector, High gradient development	C-band to THz, 500 MW beam-driven	operational
SBox	CERN	Photoinjector, medical, high-gradient development	S-band - 45 MW, 50 Hz	operational
CARIE	Los Alamos	Photoinjector	C-band, 50 MW, 100 Hz	construction
Photoinjector test stand	PSI	Photoinjector	C-band - 45 MW	construction
MOTHRA/-SAMURI	UCLA	Photoinjector, high gradient development	C-band - 1-2 MW, cryogenic	operational
Advanced Accelerator Techniques Test-stand	NSRL, University of Science and Technology of China	Photoinjector, high gradient development	C-band - 50 MW	design study, prototype development
C-band test stand at SXFEL	SARI, Shanghai	Photoinjector, High gradient development, cryogenic	C-band - 45 MW	operational
C-band test stand at Radiabeam	Radiabeam	Product development	C-band	operational
C-band cryogenic	IHEP, Dongguan	CEPC injector development	C-band cryogenic	comissioning
Pulsed DC	CERN	CLIC, LINAC4 RFQ, fundamental high-gradient	pulsed dc	operational
Pulsed DC	Uppsala University	Cryogenic, fundamental high-gradient	cryogenic pulsed dc	operational
Pulsed DC	INFN-LASA	Muon collider	pulsed dc in external magnetic field	operational

Table 63 Accelerator components

Facility	Host laboratory	System type	Technical characteristics	Status	Comments
FERMI	Sincrotrone Trieste	Linearizer	X-Band, 50 MW	operational	
SwissFEL	PSI	Linearizer	X-Band, 50 MW	operational	
SXFEL	SARI, Shanghai	Linearizer	X-Band, 50 MW	operational	
LCWS	SLAC	Linearizer	X-Band, 50 MW	operational	
CLARA	Daresbury	Linearizer	X-band, 6 MW	commissioning	
FLASHForward, FLASH2	DESY	Deflector	1 PolariX, 6 MW	operational	switchable between facilities
ARES	DESY	Deflector	2 PolariX	operational	
SXFEL	SARI	Deflector	5 MW	construction	
SHINE	SARI	Deflector	6 × 16 MW	construction	
AWA	Argonne	Deflector	10 MW	operational	
S3FEL	IASF, Shenzhen	Deflector	5 S-band and 6 X-band	planned	
LUX		Energy compressor	S-band	proposal	First implementation in S-band

Table 64 High performance linacs

Facility name	Host laboratory	Application	Technical characteristics	Status
SACLA	RIKEN	XFEL	C-band, 8 GeV, 66+5 units, 30 MV/m (check)	operational
NewSUBARU	RIKEN	storage ring injector (check)	C-band, 4 units	operational
SwissFEL	PSI	XFEL	C-band, 5.8 GeV, ? units, 28 MV/m	operational
FERMI Energy upgrade	Trieste	XFEL	10 S-band modules (in upgrade)	CDR completed
FEBE (CLARA phase 2)	Daresbury	User facility, XFEL	250 MeV	operation, upgrade underway
ARES	DESY	User facility, short bunch capability	20-160 MeV, S-band with 2 PolariX	operational
SXFEL	SARI	Soft XRay FEL	C-band, 1.5 GeV, 10 units, 37 MV/m	operational
Smart*Light	Technical University Eindhoven	ICS	X-band, 6 MW, 14 MeV	comissioning
CXLS	University of Arizona	ICS/XFEL	X-band (9.3 GHz), 35 MeV	comissioning
CXFEL	University of Arizona	ICS/XFEL	60 MeV, 1 kHz	funded
Thompson source (check)	Tsinghua University	ICS	S-band with X-band energy upgrade, 50 MW	operational
VIGAS	Tsinghua University	ICS	50 and 7.5 MW S, 3 × 50 MW X-band	construction
EuPRAXIA	INFN Frascati	Drive beam for plasma accelerator, XFEL	3 S-band, X-band 8 × 25 MW, 400 Hz	prototyping and procurement
FERMI Energy upgrade	Sincrotrone Trieste	XFEL +500 MeV energy upgrade	S-band, 10 modules	approved and prototyping

Table 64 (*Continued*)

Facility name	Host laboratory	Application	Technical characteristics	Status
AWAKE	CERN	Proton-driven plasma acceleration	18.5 MeV (second line 150 MeV)	operational (second line under procurement)
DEFT	CHUV/CERN/TH-ERYQ	VHEE FLASH (medical)	X-band, 100-200 MeV	prototyping and procurement
SAFEST	Sapienza	VHEE FLASH (medical)	60-130 MeV, C-band	prototyping first phase
?	Marie Curie/THALES	VHEE FLASH (medical)	C-band	design study
CompactLight	EU design study	XFEL	X-band, 68 units 5.6 GeV 100 Hz, 1.95 GeV 1 kHz	CDR completed
VULCAN	DAES	Pulsed Neutron source	40-50 MeV	design study
eSPS	CERN	HEP, dark photon search	3.5 GeV	CDR completed
CLIC	CERN, international collaboration	HEP, linear collider	380 GeV, X-band	design study, prototype development
Muon collider	CERN, international collaboration	HEP, lepton collider	High-gradient in high magnetic field	design study
C^3	SLAC	HEP, linear collider	C-band, cryogenic NC	design study
AWA	Argonne	Compact XFEL, Linear collider	11.7 and 26 GHz	development
Hefei Advanced Light Facility (HALF)	NSRL, University of Science and Technology of China	Linear injector for synchrotron radiation storage ring	S-band, 20 modules (40 3-meter S-band structures)	Fully funded, under construction
HG booster linac for LANSCE	Los Alamos	HG upgrade of proton accelerator	S or C-band	study
UCXFEL	UCLA	XFEL	C-band, cryogenic NC	study
HEPS injector	HEPS Beijing, IHEP	light source injector	500 MeV S-band	construction
CEPC injector	IHEP	collider injector	30 GeV S-band	design

Table 65 Beam test stands

Facility Name	Host Laboratory	Technical Characteristics	Status	Comments
CLEAR	CERN	Up to 220 MeV, 50 MW (connected to XBox-1)	Operational	X-band system on hold
SPARC_LAB	INFN Frascati	Plasma and XFEL studies	2 S-band, 1 C-band, 150 MeV	operational
NLCTA/XTA	SLAC	2×50 MW	Operational	
AWA (Advanced Wakefield Accelerator)	Argonne	8-65 MeV (L-band), 2 MeV L-band, 3-10 MeV (X-band)	Operational	
CYBORG	UCLA	cryogenic	construction	

Appendix C Klystron-based alternative design

C.1 Introduction

An alternative design for the 380 GeV stage of CLIC is based on the use of X-band klystrons to produce the RF power for the Main Linac. On the one hand, this solution increases the cost of the Main Linac because the

Table 66 Key parameters of the CLIC accelerating structures

Parameter	Symbol	Unit	Klystron	Drive Beam
Frequency	f	GHz	12	12
Acceleration gradient	G	MV/m	75	72
RF phase advance per cell	$\Delta\phi$	°	120	120
Number of cells	N_c		28	33
First iris radius / RF wavelength	a_1/λ		0.145	0.1625
Last iris radius / RF wavelength	a_2/λ		0.09	0.104
First iris thickness / cell length	d_1/L_c		0.25	0.303
Last iris thickness / cell length	d_2/L_c		0.134	0.172
Number of particles per bunch	N	10^9	3.87	5.2
Number of bunches per train	n_b		485	352
Pulse length	τ_{RF}	ns	325	244
Peak input power into the structure	P_{in}	MW	42.5	59.5

klystrons and modulators are more expensive than the Drive-Beam Decelerator and also because a larger tunnel is needed to house the additional equipment. On the other hand, it avoids the substantial cost of the construction of the Drive-Beam Complex and makes the linac more modular. One can therefore expect a competitive cost at low energies while the Drive Beam solution leads to lower cost at high energies. The upgrade of the complex is cheaper with a Drive Beam-based design, since the additional cost to upgrade the Drive-Beam Complex to feed a longer linac is relatively modest. However, an important advantage of the Klystron-based design is that the Main Linac modules can easily be fully tested for performance when they are received. In contrast, the Drive Beam option requires the construction of a substantial complex that can produce a 100 A Drive Beam before modules can be fully tested. The Klystron-based option could therefore be implemented more rapidly than the Drive Beam-based solution.

The Klystron-based option has not been updated for this Readiness Report, and the parameters are therefore the same as in the 2018 Project Implementation Plan [5].

C.2 Design choice

The Klystron-based alternative design is based on a study [4] that used the same optimisation tools as for the Drive Beam-based option. The required changes were made in the algorithms and a cost model included for the klystrons and modulators. Based on the conclusions of the study a tentative structure and parameter set have been chosen for this design. The optimum structure differs from the Drive Beam-based design, the parameters are given in Table 66. If one were to use the same structure as for the Drive Beam-based design, the expected cost would be about 330 MCHF higher.

The basic unit of the Main Linac consists of a pair of X-band klystrons, a pulse-compressor, an RF distribution system and a number of accelerating structures, see Fig. 116. The klystrons produce an RF pulse, which is then compressed in time to match the required RF pulse length. This compression increases the power of the RF pulse and hence the number of accelerating structures that can be powered per pair of klystrons. However, a significant amount of power is lost in the compressors. This limits the useful klystron pulse length. The final RF pulse is then split to feed a number of accelerating structures. For each design of the accelerating structure, the RF input power and pulse length were used to determine the pulse compressor parameters.

As can be seen in Table 67, the beam emittance, energy spread and charge of the Klystron-based design are very similar to the 3 TeV parameters, while the bunch is somewhat longer. The vertical emittance is also the same as for the Drive Beam-based design, while the horizontal emittance is smaller and proportional to the bunch charge. The number of bunches per train is significantly higher in order to produce the required luminosity.

The evolution of the vertical emittance along the collider is similar to the Drive Beam-based design, while the horizontal emittance corresponds to the 3 TeV design. The horizontal and vertical emittances remain below 500 nm and 5 nm at extraction from the Damping Ring, below 600 nm and 10 nm at injection into the Main Linac and below 630 nm and 20 nm at the end of the Main Linac.

Table 67 Key beam parameters at the collision point

Particles per bunch	3.87×10^9	bunches per pulse	485
bunch spacing	15 cm	bunch length	60 µm
final r.m.s. energy spread	0.35%		
horizontal/vertical beam size	119 nm/2.9 nm		

Table 68 The main parameters of the different lattice sectors

Sector Number	1	2	3	4	5
Number of quadrupoles	148	138	76	100	126
Quadrupole length [m]	0.4	0.4	0.4	0.65	0.65
Quadrupole spacing [m]	2.613	4.62	6.63	6.88	8.89

C.3 Design implications

For the Klystron-based alternative the Main Linac has been redesigned to evaluate the cost and verify the beam dynamics. No design optimisation has been performed for the other systems. We expect this to have a minor impact on cost and system performance as detailed below.

The Klystron-based injector RF design has to differ from the Drive Beam-based case, in order to accommodate the longer bunch train. However, the total charge per pulse is the same in both cases. Hence, to first order the same amount of installed RF is required. However, the choice of accelerating structure and pulse compressor in the injection system would be slightly different to obtain optimum efficiency.

The single bunch parameters at the entrance of the linac are very similar to the Drive Beam-based design. The main difference is the lower bunch charge, which helps the emittance preservation, and the smaller horizontal emittance, which needs to be achieved. Both parameters are very similar to the 3 TeV design and can thus be achieved with the corresponding design. The bunch length at the start of the Main Linac and afterwards is larger in the Klystron-based design, which requires less compression in the RTML and eases the system requirements.

The BDS has to provide the same beta-functions in the Drive Beam and klystron-based designs. Hence the Drive Beam-based design fully achieves the required performance for both options.

C.4 Main linac layout and optics

The Main Linac consists of a sequence of accelerating modules interleaved with modules that support quadrupoles detailed in Table 68. The accelerating modules are 2.01 m long and support eight structures. Two different types of quadrupole modules exist, with a length of 0.6 m and 0.85 m. Each of them supports a BPM and a quadrupole with a length of either 0.4 m or 0.65 m, respectively.

C.4.1 Accelerator physics issues

The beam dynamics of the Klystron-based design do not differ from the Drive Beam-based design. The increase of the wakefields due to the smaller accelerating structure aperture is, by design, compensated by the reduced bunch charge and length. The expected emittance growth is shown in Table 69 and the probability distribution in Fig. 113 [87].

C.4.2 Components

The total number of components is listed in Table 70. The alignment tolerances are the same as for the Drive Beam-based design.

C.5 Main Linac RF unit

Figure 114 shows the top view of one RF unit installed in the klystron and Main-Linac tunnels, with the detailed view of the distribution network from the pulse compression onwards. A solid-state modulator delivering 400 kV and 2 × 190 A drives two 53 MW X-band klystrons (see Sect. 4.4). The RF power from the two klystrons is recombined and sent to the Main-Linac tunnel beyond the shielding wall, which has been dimensioned to allow access to the klystron gallery under certain conditions during operation. After having been processed by an 8-cavity

Table 69 Key alignment specifications for the Main-Linac components and the resulting emittance growth

Imperfection	With respect to	Value	$\Delta\epsilon_y$ [nm]		
			1-2-1	DFS	RF
Girder end point	Wire reference	12 µm	11.37	11.31	0.07
Girder end point	Articulation point	5 µm	1.45	1.45	0.02
Quadrupole roll	Longitudinal axis	100 µrad	0.04	0.04	0.04
BPM offset	Wire reference	14 µm	154.54	14.01	0.10
Cavity offset	Girder axis	14 µm	5.51	5.50	0.04
Cavity tilt	Girder axis	141 µrad	0.10	0.47	0.25
BPM resolution		0.1 µm	0.01	1.03	0.02
Wake monitor	Structure centre	3.5 µm	0.01	0.01	0.40
All			176.68	32.72	0.84

The values after simple steering (1-2-1), Dispersion Free Steering (DFS) and realignment of the accelerating structures using the wakefield monitors (RF) are shown.

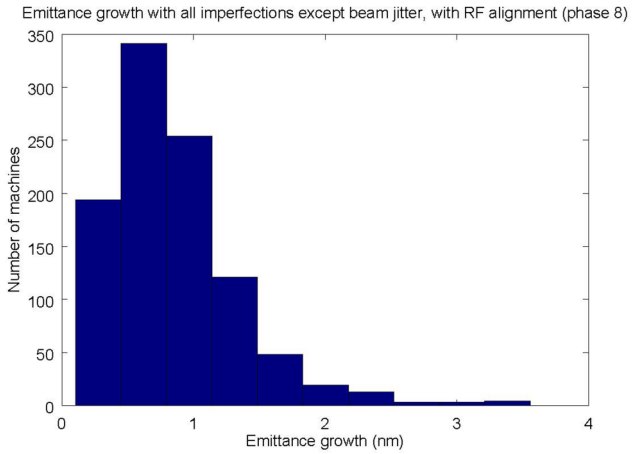

Fig. 113 Probability distribution of the emittance growth for static imperfections for a Main Linac average RF phase of 12°

Table 70 Key components for each Main Linac

Quadrupoles T0	1456
Quadrupoles T1	362
Quadrupoles T2	226
BPMs	588
Accelerating structures	11648

linearisation system, the RF signal is split in two and delivered to two pulse compression devices, one on each half of the module (Sect. C.7). The compressed RF pulse is then distributed through two hybrid splitters in cascade to four of the accelerating cavities by a double-height waveguide system, so to minimise RF losses and the risk of breakdown.

The numbers in the drawing assume a klystron efficiency of 70%, which is the minimum goal for the development of high efficiency klystrons [392]; any additional gain in klystron efficiency could then be reflected in a reduction of the HV level of the modulator pulse and in an increase of the operational margins, with benefits for cost and reliability. This scheme also can foresee a pulse compression factor of 3.5, obtained by means of two separate compression cavities of the BOC type, one for each side of the RF module; a well known compression scheme already used in S-band and C-band RF systems. The RF pulse, compressed in time, reaches 170 MW at the entrance of the first hybrid splitter and 40.6 MW are delivered to each of the four accelerating structures connected to each BOC pulse compressor. Some of the fundamental RF devices that have been specifically developed to be integrated into

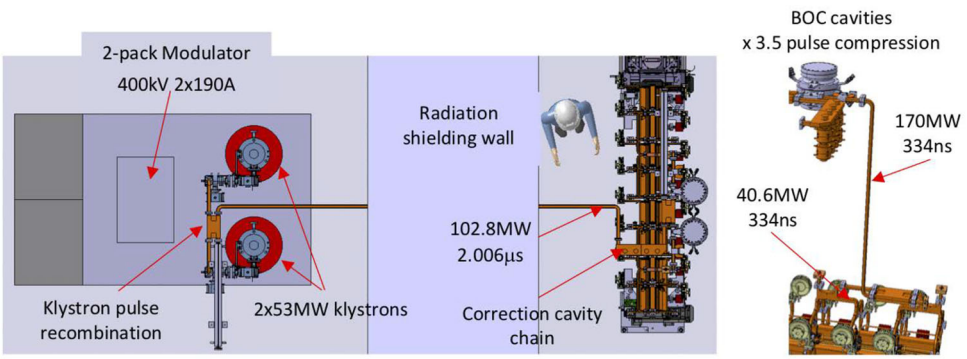

Fig. 114 The RF unit: top view of one RF unit in the klystron and Main-Linac tunnels (left) and detailed view of the distribution network (right)

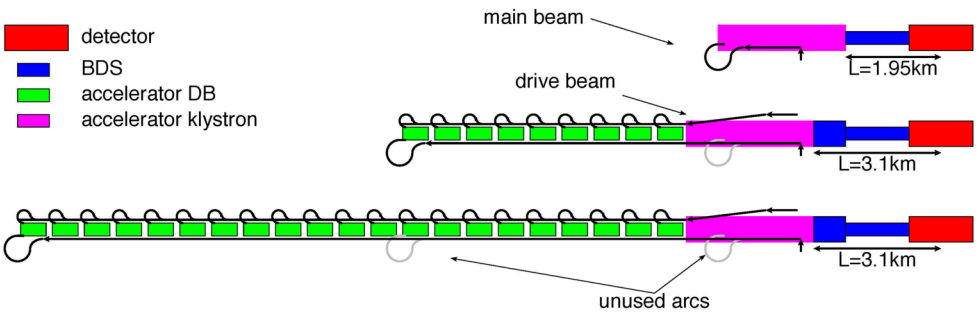

Fig. 115 The concept of the CLIC energy staging with a klystron-based first energy stage

the RF power delivery system include the correction cavity chain, for the linearisation of the compressed pulse [393], compact spiral loads and high-power hybrid splitters.

The klystron feeding would give an advantage in terms of flexibility for operation, by providing the possibility to independently set the amplitude and phase of the accelerating field for each module; this flexibility would not only be restricted to the 380 GeV stage, but could be extended to the higher energy stages by maintaining the klystron-powered section in front of the BDS, making the control of the colliding beam energy spread more straightforward.

C.5.1 Upgrade from the klystron-based option

The upgrade from a klystron-based first stage to higher energies is also possible by reusing the klystron-driven accelerating structures and the klystrons and by adding new drive-beam powered structures. In the klystron-based first energy stage, the single bunch parameters are the same as for the high energy stages, only the bunch charge will be slightly reduced at higher energies. Shorter bunch trains need to be accelerated at higher energies, which does not add any difficulty.

An important difference with respect to the drive-beam powered first energy stage is the placement of modules. In order to provide the space for klystrons and modulators, the klystron-powered main linac tunnel has to be larger in radius than the tunnel housing the beam-driven acceleration. Therefore it appears best to extend the main linac for 1200 m with a large tunnel and then continue with a smaller tunnel. All drive-beam powered modules are then placed in the smaller tunnel. The klystron-powered structures remain in the large tunnel. They need to be moved longitudinally slightly in order to adjust the lattice for the high energy, which requires longer quadrupoles with a wider spacing. The last 1200 m of the linac is moved to the beginning of the large tunnel to provide the space for the high energy beam delivery system, see Fig. 115.

The impact of the energy upgrade on the main-beam injectors and damping rings is quite small. The bunch charge at 3 TeV is smaller than at 380 GeV; the difference is at the 4%-level, significantly smaller than for the upgrade of the drive-beam based machine. At higher energy, the number of bunches per beam pulse is also smaller, which is straightforward to accommodate. The beam delivery system for klystron- and drive-beam based design are the same; hence the upgrade path is also the same.

C.6 Technology: the Klystron modules

C.6.1 The Klystron-based module

If a Klystron-based design is adopted for the 380 GeV stage, the acceleration of the two colliding beams, from the injection energy of 9 GeV to 190 GeV, is provided by a sequence of 1,456 modules for each linac, each module

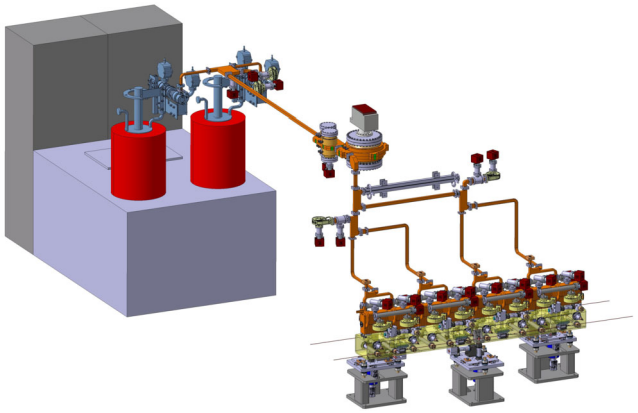

Fig. 116 The klystron-based module with pulse compression and linearisation system

Table 71 Summary of beam and RF structure characteristics in the klystron-based accelerator

Beam Parameters	Value
Particles / bunch [$\times 10^9$]	3.87
Bunches / train	485
Train length [ns]	242
Bunch separation [ns]	0.5
RF Structure Characteristics	**Value**
Cells / structure	28
Structures / module	8
Accelerating gradient [MV/m]	75
Structure input power [MW]	40.6
Module input power [MW]	340
RF Frequency [GHz]	12

being fed by a dedicated RF power station. The modules are assembled in a FODO lattice with quadrupoles of two different lengths, 0.4 m and 0.65 m, following the beam energy increase along the length of the accelerator. A total of 724 short quadrupoles and 452 long quadrupoles are required for the two linacs.

In the Klystron-based design, a single type of module is considered; the module includes a common support for eight RF accelerating structures, which are coupled two-by-two to form SAS. The total number of SAS required for the two linacs is 11,648. The quadrupoles in the focusing channel are mechanically independent of the module itself, being equipped with a dedicated support that, in addition, integrates a stabilisation system capable of assuring the compensation of ground vibrations. Since those vibrations can strongly affect the beam luminosity at the IP, the stabilisation system must guarantee a quadrupole stability of the order of 1 nm.

An image of the Klystron-based module is shown in Fig. 116; most RF components used for this module have been built and are being tested in the X-band test facilities under nominal power conditions.

The accelerating structures are 0.23 m long and require a peak RF power 40.6 MW in the pulse length of 334 ns (see Sect. 4.5). The choice of the module length is defined by the RF power available from a modulator station and how that power can be distributed to the accelerating structures. A two-pack modulator equipped with two 53 MW klystrons can feed one module made of eight accelerating structures. If the design accelerating gradient of 75 MV/m is reached in the RF structures, the average energy gain per module is about 135 MeV. The module length is 2.01 m. The powering system efficiency, from plug to RF delivered to the accelerating structures, is 22.2%.

In a machine where the main source of power consumption is the RF losses in the copper walls of the accelerating structures, the quest for efficiency represents a crucial task in the design exercise. This starts from the design of the RF structure cells, which has increased the RF efficiency to 38.2%. The same attention has been given to the design of the RF network. This has led to the adoption of double-height waveguides, which are effective in reducing the attenuation by 40% and electric and magnetic fields by 30% with respect to standard-height waveguides. Table 71 gives a summary of the beam characteristics and the RF structures for the klystron-based Main Linac.

Due to the intrinsic inefficiency of the pulse compression process the power dissipation in the Main-Linac tunnel is increased in the klystron-based module configuration, with respect to the DB accelerator, and is summarised in Table 72.

Table 72 Power dissipation in the klystron-based module under loaded conditions

Module Component	Number	Item Dissipation [W]	Total Dissipation [W]
SAS	4	1,100	4,400
SAS RF Loads	16	178	2,842
Waveguides	1	1,034	1,034
Total per module			8,276

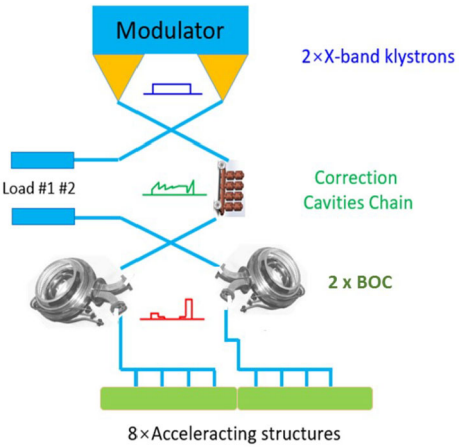

Fig. 117 The layout of RF unit of the klystron-based CLIC Main Linac

For the Klystron-based configuration, a technical complication and an important contribution to the total cost of the accelerator arises from the need to have a parallel gallery to the Main-Linac tunnel hosting the klystrons and modulators. An extensive study compared the two configurations and the technical details of this study can be found in Sect. C.10.

C.7 Technology: pulse compression system

The layout of an RF unit of the klystron-based Main Linac is shown in Fig. 117. The two X-band klystrons, mounted on a single HV modulator, produce long RF pulses. These pulses are combined on the 3 dB hybrid into a single pulse with doubled RF power. The combined RF power is conveyed via waveguide to the Correction Cavities Chain (CCC). The CCC pre-modulates the shape of RF pulse and then splits it in two with each sharing half the power. These pulses feed the two BOC-type RF pulse compressors [394]. Each BOC shortens the pulse and amplifies the peak RF power. This arrangement is chosen in order to reduce the maximal peak power that has to be transported in a single waveguide system. Finally, these pulses are split and distributed to the eight accelerating structures.

The combination of the BOC single cavity pulse compressor and CCC allows one to generate efficiently the RF pulses with a flat top [395]. This system is very compact compared to the SLED II, as it does not require the long delay lines for the RF pulse-forming network. The use of the CCC with its limited number of elements, however, provides the pulses with a small residual modulation on the flat top (see Fig. 118, left). To mitigate this effect, and to enable the required initial ramping of the RF pulse for the beam loading compensation, special RF phase modulation is applied to the klystron pair (see Fig. 118, right).

The power gain in such a system depends on the frequency, on the quality factor of the BOC storage cavity, on the duration of the output pulse and on the compression factor – the ratio between input and output pulse lengths. In Fig. 119 (left), the power gain curve simulated for the system with $Q_{BOC} = 2.0\ x\ 10^5$ and $Q_{CCC} = 4.5\ x\ 10^4$ for 334 ns compressed pulses as a function of the compression factor is shown. For four accelerating structure per klystron and 40.6 MW per structure, anticipating 90% efficiency of the waveguide RF transmission circuit, this curve can be translated into one which connects the required peak power and pulse length of the individual klystron (Fig. 119 right and Table 73.). Following these simulations, the most comfortable parameters for the high-power klystrons are 51.4 MW peak RF power and 2 µs pulse length.

The X-band version of BOC RF pulse compressor, together with new bowl-type correction cavity prototypes were developed and built at CERN [396, 397], (see Fig. 120). The X-band BOC will be tested at high RF power in 2025. As a proof-of-concept, at PSI a 5.7 GHz version of such a system has already been built and tested in operation at high RF power [378]. An X-band CCC unit based on the coupled spherical cavity pair, has been built at Tsinghua University in China. It was successfully tested at high RF power at CERN [398].

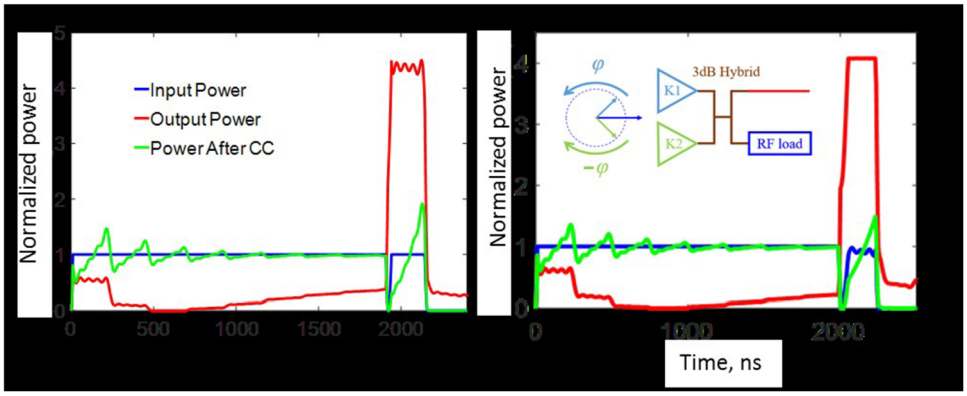

Fig. 118 The RF pulse envelopes in a system without (left) and with (right) special RF phase modulation of the klystron pair

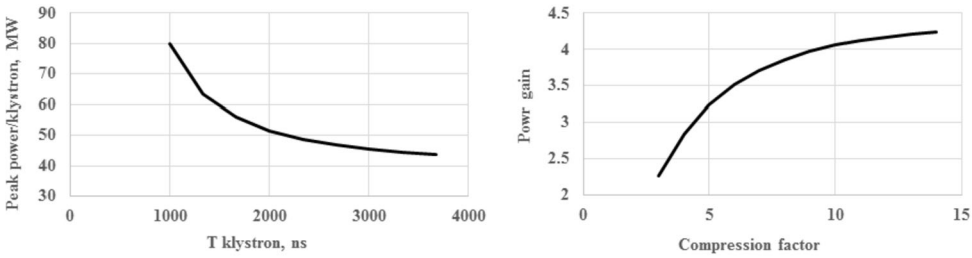

Fig. 119 Power gain vs. compression factor (left) and klystron power / pulse length curve (right)

Table 73 The klystron peak power and pulse length adopted for the CLIC accelerator unit

Pulse (ns)	1,002	1,336	1,670	2,004	2,338	2,672	3,006
Power (MW)	79.8	63.5	55.9	51.4	48.6	46.7	45.5

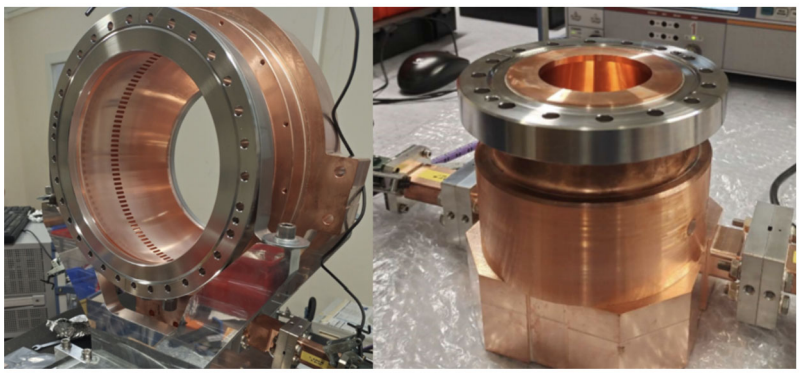

Fig. 120 X-band BOC (shown left) and bowl-type correction cavity (shown right) prototypes fabricated at CERN

C.8 Technology: klystrons and modulators

C.8.1 RF power source for 380 GeV Klystron option

The klystron-driven 380 GeV option will require a high-efficiency RF power source comprising 5,800 klystrons and 2,900 pulsed modulators. Each klystron will provide a peak RF power of 53 MW at a frequency of 11.9942 GHz with a pulse width of 2 µs and a pulse repetition rate of 50 Hz. The klystrons will be combined in pairs to increase the peak power available to the pulse compression system, feeding eight structures in the Main-Beam Linac and allowing control of the amplitude and phase stability. With such a large number of RF units required, efficiency is imperative in the design of both the klystron and modulator.

An RF unit consists of the following components, which all contribute to the overall operational performance and cost:

1. Modulator
2. Klystron (+ Klystron Heater Power Supply)

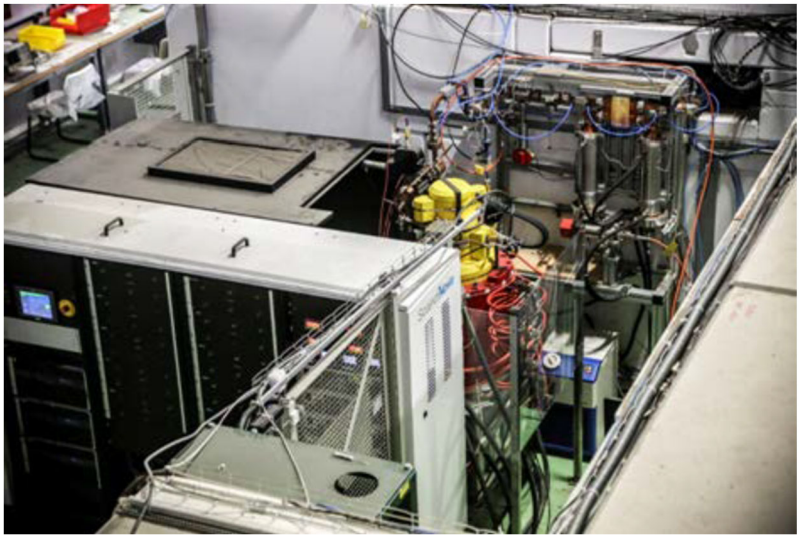

Fig. 121 High-Gradient Test Stand facility at CERN, showing modulator, klystron and pulse compressor

3. Solenoid Magnet (+ Solenoid Power Supplies)
4. Low-Level RF (LLRF) (+ Klystron pre amp driver)

At present, the high-gradient test stands at CERN [399, 400] are operating on a 24/7 basis showing that the peak power and reliability requirements are achievable using technology already available from industry. This includes a commercially available modulator and a high-power X-band klystron, based on the original SLAC XL4 concept [401]. Figure 121 shows a picture of a high-power X-band RF source at CERN.

C.8.2 X-band Klystrons

With recent developments on higher efficiency klystrons [402], a study is ongoing to improve the existing design of the klystron to achieve an efficiency of 70% while maintaining the required peak power. This will have a significant impact on reducing the average power required and the physical size of the modulators needed to fit in the tunnel.

The operational parameters for the existing klystron modulator and the future high-efficiency, dual klystron modulator option are shown in Table 74.

C.8.3 X-band modulators

State of the art modulators using solid-state switching technology have shown that the pulse-to-pulse stability and pulse flatness requirements for CLIC are already achievable today. The high voltage pulse in the modulator is generated by charging and discharging many capacitors in parallel using solid-state switches, reducing the DC voltage requirements on the primary side of the pulse step-up transformer to less than 1.4 kV. This results in a significant reduction in the volume and footprint of the modulator compared to the traditional 50 kV line-type modulators, easing the constraints for installation in the tunnel. Figure 122 shows a simplified functionality diagram of the modulator and klystron system.

Using a pulse transformer implies rising and falling edges on the voltage pulses that are normally not usable for the RF pulse thus reducing the efficiency of the electrical energy available to 77%. A study is ongoing to see if the efficiency increases by applying RF during the rise time of the voltage pulse, to fill the pulse compressor cavities.

C.9 Technology: survey and alignment

C.9.1 The Support Pre-alignment Network (SPN)

Figure 123 shows the support pre-alignment Network proposed for the klystron option.

C.10 Civil engineering

The following sections contain information on Civil Engineering and Infrastructure specific to the Klystron option.

Table 74 Parameters for dual X-band klystron modulator

Main Parameters	Existing klystron modulator	Future high-efficiency, dual klystron modulator
RF Peak Power	50 MW	2 × 53 MW
RF Average Power	3.75 kW	2 × 5.3 kW
Pulse Length	1.5 μS	2 μS
Pulse Repetition Rate	50 Hz	50 Hz
Klystron Efficiency	44%	70%
Perveance	1.15 μperv	0.75 μperv
Modulator Voltage	420 kV	400 kV
Peak Pulse Current	2 × 310 A	2 × 190 A
Modulator Average Power	24.597 kW	21.85 kW
Klystron Solenoid Average Power (Super Conducting Solenoid Average power)	20 kW	20 kW (1.6 kW)
Klystron Heater Power	1 kW	1 kW
Average Power Consumption (5,800 klystrons, 2900 modulators)	193.131 MW	185.169.4 MW (78.469 MW) SC Solenoids
Flat-Top Stability (FTS)	+/− 0.25%	+/− 0.25%
Pulse to pulse repeatability (PPR)	0.01%	0.01%
Rise and fall times (t_{rise}, t_{fall})	<1 µs	<1.2 µs

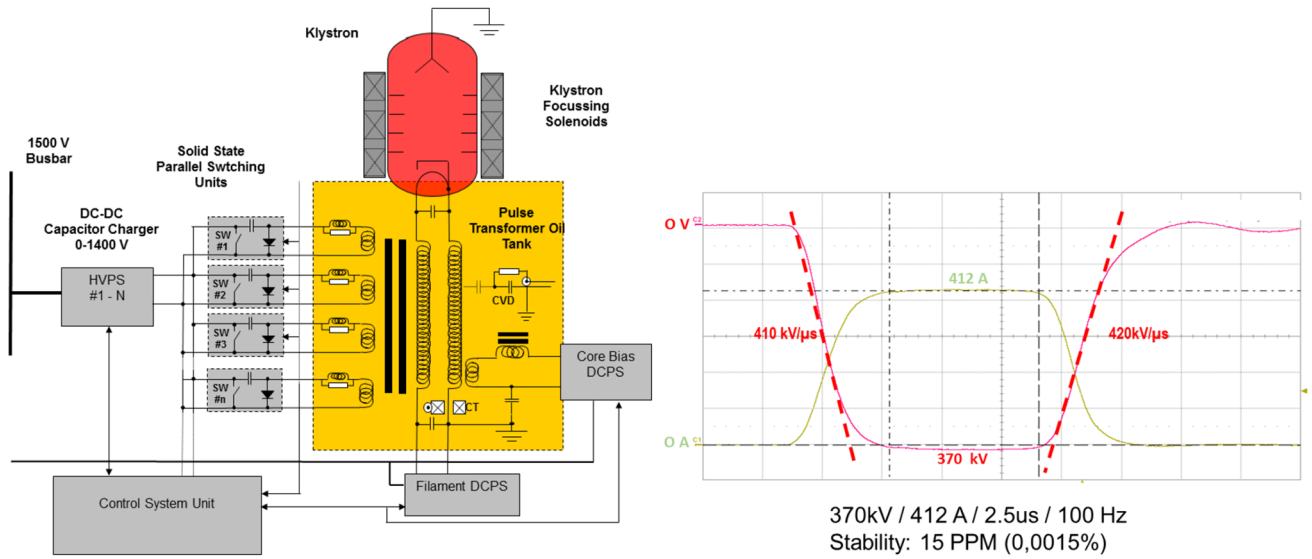

Fig. 122 Left: Schematic of solid-state modulator and klystron; Right: Typical voltage and current waveforms achieved in state-of-the-art modulators

Fig. 123 Pre-alignment network sensors configuration for 380 GeV Klystrons option

Injector complex No Drive-Beam Injector is required for the Klystron-based option which simplifies the complex significantly and reduces cost. The Main-Beam Injector complex is similar to the Drive-Beam based design (Fig. 124).

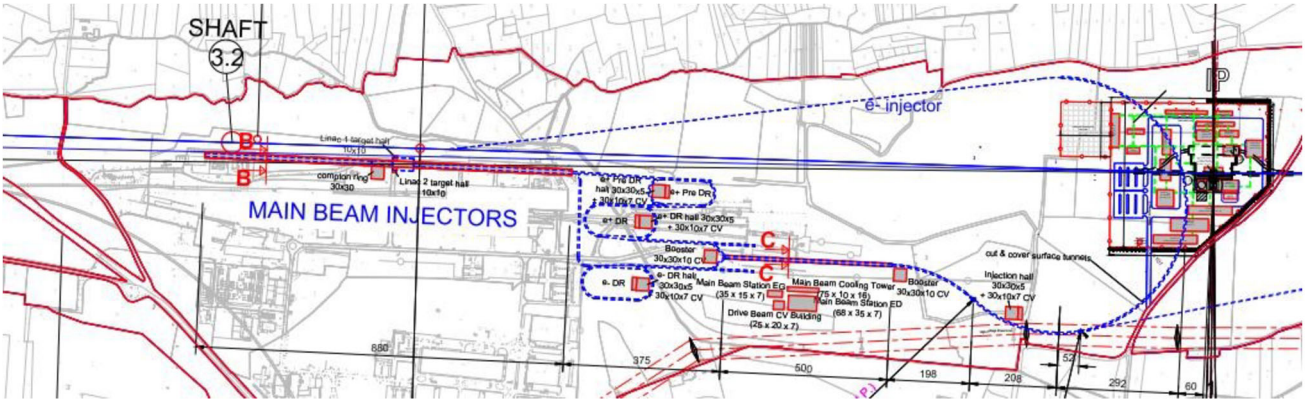

Fig. 124 Schematic layout of the Klystron option injection complex

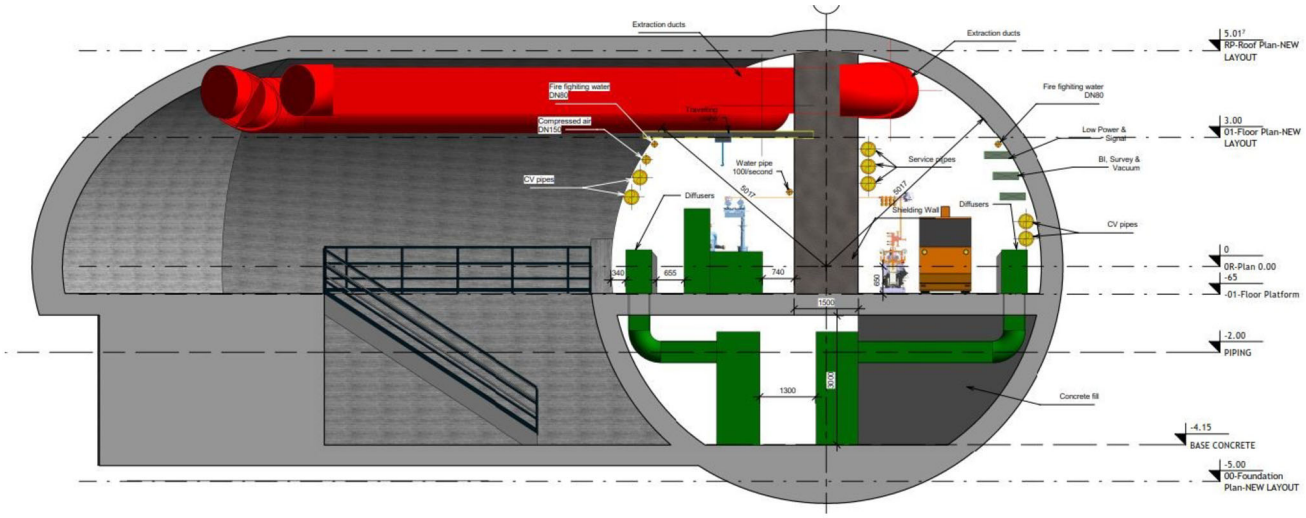

Fig. 125 Main Linac cross section for the klystron option

Main tunnel layout and cross section The length of the Main-Linac tunnel is similar to the Drive-Beam option, however, it does not contain the turn-arounds for the Drive Beam. A larger 10 m internal diameter tunnel is required to house both the accelerating structures and the klystron modules, separated by a 1.5 m thick shielding wall, which are connected by waveguides (Fig. 125). In order to minimise the impact of vibrations on the accelerating modules, a services compartment will be located below the less sensitive klystron modules. At each UTRC along the tunnel length the 1.5 m thick shielding wall will contain a contractible section that can be slid out during long shutdowns to allow vehicle access between the two tunnel compartments.

The air supply ducts and refrigeration units will be located within this service compartment, which is accessible from the UTRC and UTRA caverns. Access will be provided to these compartments at intervals of 880 m via the UTRAs and UTRCs for general maintenance of services. Provisions are required to allow diffusers to be located every 20 m on both sides of the tunnel. A typical cross-section of the klystron Main-Linac tunnel with access to a UTRA is shown in Fig. 125. *Smoke extraction duct and sprinkler integration still required.*

BDS and interaction region This region is basically the same for both the Drive Beam and Klystron options. However, for efficiency, the cross-section of the BDS tunnel for the klystron design will have a larger internal diameter of 10 m. This allows the use of the same TBMs for the Main Linacs and the BDS.

Construction and installation methods It is envisaged that the construction method for the Klystron option will be the same as that used for the Main-Linac tunnel, however, once the excavation and tunnel lining is complete the installation of the smaller civil engineering works will differ. As seen in Fig. 125 the klystron option will require a larger concrete invert with a service compartment cast in. The concrete invert will be separated into

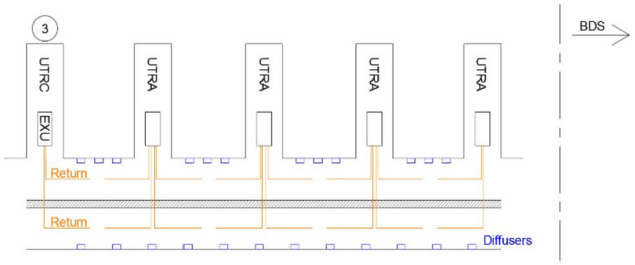

Fig. 126 Klystron machine, HVAC schematic

two sections with a compressive filler between each. The construction of the shielding wall will be staggered with the construction of the concrete invert to allow time for the concrete to cure. This will then be followed by the installation of any internal structural steelwork required for the cooling and ventilation services.

C.10.1 Cost consideration

The major differences between the Klystron-based option in comparison to the Drive Beam option are; larger cost for the Main-Linac tunnel for the former due to the increased tunnel diameter and a lower cost for the Injector Complex due to the removal of Drive-Beam Injector infrastructure.

C.11 Cooling and ventilation

Tables 77 to 82 are the Klystron-option versions of the tables presented in Sect. 5. Note that there is no drive beam generation complex for the klystron option, therefore there is no "Sector 1" in the tables.

Tables 77 and 78, outline the main cooling circuits, the associated cooling powers and flow rates for each sector.

The chilled water circuit specifications are provided in Table 79.

Table 80 shows the main parameters of the ventilation systems for klystron machine during run mode.

The operational parameters for the underground areas are listed in Table 81, for the particular case of run mode.

The operational parameters for the ventilation of the surface buildings are listed in Table 82 for the run mode.

C.11.1 Heating, ventilation and air conditioning

Accelerator gallery The ventilation concepts for the klystron and the Two-Beam machines are similar: different systems cover the operational modes as mentioned above.

During shutdown, air-handling units (AHUs) placed at the surface force a push and pull arrangement, similarly to the system described for the Two-Beam machine. The local air handling units are not running.

During run mode, air is treated by a number of AHUs cooled by chilled water and located in the service compartment below the tunnel floor. These units are connected to diffusers located at the tunnel invert level in the klystron and accelerator tunnels. Extraction units (EXU) located in the UTRAs and shaft surface buildings drive the air from the tunnel to the service compartment, where it is discharged. A schematic is presented in Fig. 126. Presently, the units in the UTRAs are not redundant due to space issues.

C.12 Transport and installation

It is anticipated that transport operations for the installation of equipment in the klystron option will be considered on two fronts; the klystron module installation and the accelerating structure installation as shown in Fig. 125 on the left and right sides of the tunnel cross section respectively.

C.12.1 Surface

The most notable change for the klystron design is the removal of the Drive-Beam Injection complex. This will considerably reduce the number of cranes required and the number of items to be transported on the surface. The removal of the Drive-Beam building seen in Fig. 86 will lead to the removal of the Drive-Beam Injection overhead cranes identified in Table 49.

C.12.2 Underground

The number of modules to be transported in the tunnel presented in Table 75.

Table 75 Modules for the 380 GeV stage, Klystron machine

Type of equipment	Number
Modules	2,912
DB quadrupoles	-
MB Short quadrupoles	724
MB Long quadrupoles	452
Total	**4,088**

C.12.3 Cost considerations

The major difference between the two-beam and the klystron 380 GeV options is the requirement for klystrons and modulators within the main tunnel. A smaller diameter tunnel is required for the Drive Beam option with a large amount of machine modules to be transported and installed, and, the requirement for a surface Drive Beam Injector complex with a 2 km long building. Whereas, for the Klystron solution we are considering the Main Linac as two separate tunnels (no access from one side to another) with smaller machine equipment but equally challenging Klystron modules in the other part.

Main Beam side The dimensions and weight of the modules and magnets that need to be transported requires the development of special equipment similar to that identified in the Drive Beam option. Specialized equipment will allow one to achieve the highest rate of installation compatible with the constraints identified in the CDR [55]. These operations will not significantly differ from that of the Drive Beam option, it is foreseen that the transport vehicles will be equipped with an automated guidance system. A clear interconnection plane between the modules is necessary to allow each module to be lowered into position without interfering with adjacent modules, supports are installed before installation of the modules.

Klystron modules: maintenance and installation Two options were considered for the maintenance of the klystron modules, the first option requires a continuous monorail to be installed above the solenoids. To allow extraction of the solenoids, hoists are foreseen. It is essential that there is adequate clearance above the solenoids to extract them from the modulator tanks, therefore, the tunnel diameter and cross-section have been designed accordingly, see Fig. 125. As the solenoids are expected to be extracted relatively frequently, in comparison to the other klystron components, it is recommended to have a fixed maintenance solution installed within the tunnel.

On the other hand, as the monorail requires fixing before installation of the equipment can begin, the mounting accuracy of the solenoids would need to be defined beforehand. Therefore, the solenoid design must be adapted to include lifting points located directly below the hoists. The fact that the continuous rail is located throughout the entirety of the 380 GeV tunnel means that obtaining the desired accuracy will be a significant challenge. Further integration studies will be required if this installation scenario for the Klystron option is selected.

The preferred solution is the use of traditional transport means such as forklifts (jib instead of fork) or pallet trucks. Although this method of transportation is more flexible, it is currently limited by space constraints. For both of these maintenance approaches there is a requirement to ensure the necessary space needed for operation is available. It is essential that adequate space be provided to allow the transportation of the solenoids subsequent to extracting them with hoists, forklifts or other equipment.

More information and details of the transport systems will be provided after a detailed design of the tunnel services mounted on the ceiling has been done. Also clarification of the modulator tank and solenoid design as well as the necessity for the electrical racks is required.

C.13 Safety systems during operations

It is to be noted that, while many of the hazards identified are common to both the Drive Beam and Klystron options for the 380 GeV stage, there are some significant differences, and the klystron-option specific issues have been highlighted below for the relevant domains.

C.13.1 Chemical hazards

The most significant hazard identified for the klystron option is the large quantity of oil in the HV tanks for the klystron and modulator assemblies. There will be 800-1000 litres of oil in each of the 2912 modulator assemblies. This is currently expected to be a highly refined mineral oil, capable of withstanding the high voltages. The mitigation strategies are as described for the two-beam option in Sect. 5.

Table 76 The 2018 PIP [5] cost breakdown for the 380 GeV stage of the CLIC accelerator, for the klystron option

Domain	Sub-Domain	Cost [MCHF]
Main-Beam Production	Injectors	175
	Damping Rings	309
	Beam Transport	409
Main Linac Modules	Main Linac Modules	895
Main Linac RF	Main Linac Xband RF	2788
Beam Delivery and Post Collision Lines	Beam Delivery Systems	52
	Final focus, Exp. Area	22
	Post-collision lines/dumps	47
Civil Engineering	Civil Engineering	1479
Infrastructure and Services	Electrical distribution	243
	Survey and Alignment	147
	Cooling and ventilation	410
	Transport / installation	36
Machine Control, Protection and Safety systems	Safety systems	114
	Machine Control Infrastructure	131
	Machine Protection	8
	Access Safety & Control System	23
Total (rounded)		**7290**

C.13.2 Fire safety

The strategy for the klystron option has to be adjusted due to the requirement for large quantities of flammable electrical insulating oil within the tunnels, as this represents an additional and very significant fire load. The longitudinal fire compartment spacing will be the same as for the Drive Beam option, however the cross section will additionally be divided into three separate compartments, corresponding to the Klystron side, the Accelerating Structure side and the Service Compartment below. Sprinklers will be required in the Klystron side of the tunnels, covering the Klystrons, modulators and the oil retention basins. Fire detection will also be required in each the separate compartments of the tunnel, and hot smoke extraction will at minimum be required in the Klystron and Accelerating Structure compartments.

C.14 Radiation protection

C.14.1 Parasitic X-ray emitters

The klystron option introduces a klystron gallery running parallel and close to the Main-Beam tunnel. The gallery will be closed during beam operation, but will remain accessible during certain operational conditions without beam. While the distances between klystrons and RF cavities are kept short, minimum shielding is required for radiation protection when the RF cavities in the Main-Beam tunnel are powered. The maximum dose rate in the gallery, will be compliant with a Supervised Radiation Area, therefore the radiation levels must not exceed 3μ Sv/h.

The driving parameter for the shielding dimension is the expected dark current generated by the electric field in the accelerating structures and the level and spectrum of the produced X-rays. This source term cannot be easily determined and requires a study of the operational conditions taking into account the experiences gained during the development and testing of the prototype RF structures.

The input parameters for a first radiation transport study were based on data from CLIC-type RF structures operated at the X-band facilities at CERN, where average dark currents of about 10 nA per structure were measured. The dark current was scaled to a full module, consisting of 8 structures, and a scaled energy spectrum was used from tracking studies for a single structure.

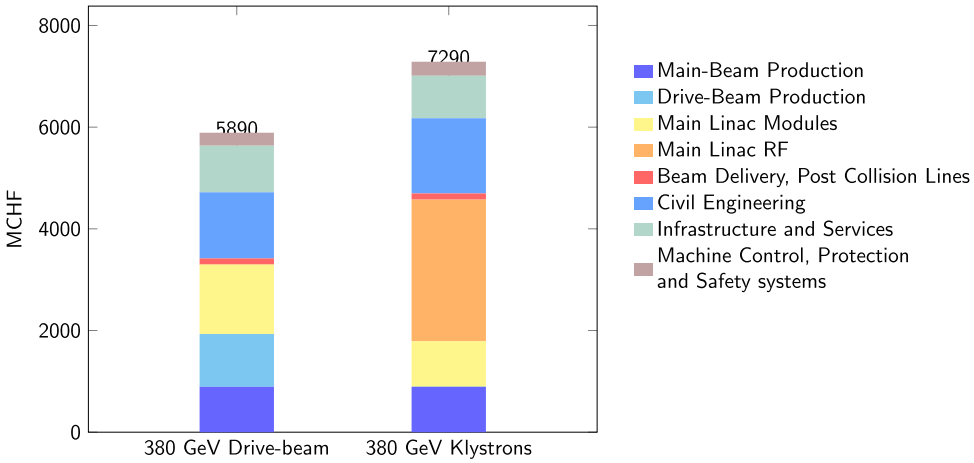

Fig. 127 The 2018 PIP [5] cost breakdown for the 380 GeV stage of the CLIC accelerator, for the drive-beam baseline option and for the klystron option

Table 77 Primary circuit specifications, Klystron Machine

Sector	Structure	Cooling Power MW	Flow Rate m^3/h
2/3	Accelerator - Klystron	25	2670
	Accelerator - LINAC	27	2930
	Main Tunnel (other equipment)	24	2610
	Injection Hall and Transfer Lines - e^+/e^-, Loop, J.P to S.P (P&ID Circuit B)	5.9	640
	Detectors S	0.9	100
	Detectors U	2.0	230
	Chillers Refrigeration - Buildings IP	1.7	190
	Chillers Refrigeration - Main tunnel	7.0	750
	Chillers Refrigeration - Detectors Hall S/U, Injection Hall, Transfer Lines - Loop and J.P. to S.P. (P&ID Circuit A)	2.2	240
	Main Tunnel Purge	3.6	390
4	Main Beam Injector U	3.9	420
	Main Beam Injector S	5.1	560
	Booster S/U, Damping Ring e^- S/U, and Transfer Line - Booster to J.P.	11.2	1210
	Pre Damping Ring S/U, Damping Ring e+ S/U	8.3	900
	Chillers Refrigeration - Main Beam Injector S/U, Compton Ring S, Traget Hall S	2.4	260
	Chillers Refrigeration - Pre Damping Ring S/U, Damping Rings e^+, e^- S/U, Booster S/U and Transfer Line - Booster to J.P.	4.4	480
	Total Cooling	135	

Dephased RF conditioning of modules will be implemented to prevent the capture and subsequent acceleration of the dark current in adjacent modules. With this restriction, a 1.5 m thick shielding wall is compatible with the targeted maximum dose rate level. Specific shielding arrangements still need to be made at the locations where ventilation ducts have to cross the shielding wall. Further safety margins could be obtained by optimising the concrete composition of the shielding wall or the use of local shielding at the loss points.

Further studies and optimisation during the technical design phase must be foreseen, using refined input parameters.

Table 78 Secondary circuit specifications, Klystron Machine

Secondary Circuits, Demineralized Water			
Sector	Structure	Cooling Power	Flow Rate
		MW	m^3/h
2/3	Accelerator - Klystron	24.8	2670
	Accelerator - LINAC	27.1	2930
	Main Tunnel (other equipment)	24.1	2610
	Injection Hall and Transfer Lines - e^+/e^-, Loop, J.P to S.P	5.9	640
	Detectors S	0.9	100
	Detectors U	2.0	230
4	Main Beam Injector U	3.9	420
	Main Beam Injector S	5.1	560
	Pre Damping Ring S/U, Damping Ring e^+ S/U	8.3	900
	Booster S/U, Damping Ring e^- S/U, and Transfer Line - Booster to J.P.	11.2	1210
	Total Cooling	113	

Table 79 Chilled water circuits specifications, Klystron Machine

Secondary Circuits, Demineralized Water			
Sector	Structure	Cooling Power	Flow Rate
		MW	m^3/h
2/3	Injection Hall, Transfer Line - Loop Circuit 1, J.P. to S.P. and e+	0.7	120
	Transfer Line - Loop Circuit 2 and e−	0.3	60
	Detectors Hall U and Detectors Hall S	0.7	120
	Main Tunnel	5.4	930
	Buildings IP	1.3	240
	Main Tunnel Purge	2.7	160
4	Main Beam S/U Circuit 1	0.8	150
	Main Beam S/U Circuit 2	0.4	80
	Main Beam S/U Circuit 3	0.4	80
	Booster S/U and Transfer Line - Booster to J.P.	0.9	170
	Damping Rings S/U and Pre Damping Rings S/U	2.4	420
	Buildings Shaft 2	0.3	50
	Buildings Shaft 3	0.3	50
	Compton Ring S, Traget Hall S	0.2	30
	Total Cooling	17	

C.15 Construction and operation schedules

For the klystron option the RF power is provided by X-band klystrons and modulators, installed underground all along the main linac. The total time for installation is slightly different from the drive-beam case. The surface buildings and installations are reduced to those exclusively needed for the main beam and experimental area, reducing the surface construction activities correspondingly. On the other hand, the installation time in the main tunnel is longer, due to the RF units and the additional infrastructures required. Even though it is possible to work in parallel in the main linac tunnel and in the klystron gallery, the overall transport, installation and handling logistics are more time consuming. The time needed for construction, installation and commissioning is eight years, compared to seven years for the drive-beam option at the same CLIC energy of 380 GeV.

Table 80 Ventilation infrastructure for the accelerator gallery, Klystron Machine

Structure		Air-Handling Units		
	N°	N°	Cooling Power	Flow Rate
		—	kW	m^3/h
Accelerator Gallery - LINAC side	1	8	200	104550
Accelerator Gallery - Klystron side	1	16	90	45780

Table 81 Ventilation infrastructure for the underground facilities, excluding the accelerator gallery and redundant units for Klystron machine

Sector	Structure Name	Air-Handling Units			Extraction Units	
		N	Cool. Power	Heat. Power	N	Flow Rate
			kW	kW		m^3/h
	Transfer Line - J.P. to S.P.	1	230	40	1	134330
	Transfer Line - Loop	2	120	40	2	68660
	Transfer Line - e^+	1	130	120	0	0
	Transfer Line - e^-	1	190	180	0	0
	Detectors Hall U	1	350	460	1	64180
	Main Beam Dumps	2	40	0		
	Drive Beam Dumps					
	Drive Beam Turnaround					
	UTRA	8	110	0		
2/3	UTRC	2	110	0	2	56700
	Caverns 1.3 and 1.4		2	110	0	
	Survey Cavern 2.1 and 3.1	2	0	0		
	Additional Caverns 2.2 and 3.2	2	170	0		
	Service Cavern	2	110	0	2	56700
	BDS	4	130	0		
	Main Beam Turnaround e^+/e^- and Tunnel BC2 e^+/e^-	2	40	0		
	BC2 Caverns	2	30	0		
	Tunnel Purge	4	690	970	5	97240
	Lift Pressurized Area	3	0	0		
	Main Beam Injector U	1	530	690	3	68790
		2	120	40		0
	Booster U	2	110	20	3	60070
4	Transfer Line - Booster to J.P.	1	160	80	1	67170
	Pre Damping Ring U	1	840	70	1	159190
	Damping Rings e+ U	1	610	450	1	203960
	Damping Rings e− U	1	350	80	1	203960

C.16 Power and energy consumption

The power and energy comsumption for the klystron based option has not been updated since the 2018 Project Implementation Plan [5], in which the power and energy comsumption of both the 380 GeV drive-beam option and the 380 GeV klystron option are compared, and found to be very similar.

Table 82 Ventilation infrastructure for the surface buildings excluding redundant units, for Klystron machine

Sector	Structure Name	Air-Handling Units		
		N	Cooling Power	Heating Power
			kW	kW
	Detectors Hall S	1	340	220
	IP - Electricity	1	240	240
	IP - Reception	1	40	40
	IP - Workshop	1	70	70
	IP - Service Office	1	180	180
2/3	IP - Control	1	100	100
	IP - Cryo	4	140	140
	IP - Survey	1	120	120
	IP - Gaz	1	60	60
	IP - Site Access Control	1	10	10
	Injection Hall	2	110	20
	Main Beam Injector S	9	100	20
	Compton Ring	1	140	140
4	Target Halls (LINACs 1 and 2)	2	20	20
	Booster S	6	100	10
	Damping Rings e+/e− S and Pre Damping Ring S	3	110	20
	Building Shaft 2 + 3 - Electricity	2	30	30
	Building Shaft 2 + 3 - Workshop	2	70	70
	Building Shaft 2 + 3 - Survey	2	10	10
	Building Shaft 2 + 3 - Access Control	2	10	10
	Building Shaft 2 + 3 - Shaft Access	2	160	160

C.17 Cost estimate

The cost estimate for the klystron based option has not been updated since the 2018 Project Implementation Plan [5], where the 2018 cost of both the drive-beam option and the klystron option are compared. The cost estimate given in this appendix can therefore not be compared directly to the updated cost for the drive-beam option in Sect. 6.2.

The 2018 cost estimate for the first stage of CLIC including a 1σ overall uncertainty, for both the drive-beam based and the klystron based, is:

$$\text{2018 CLIC 380 GeV drive-beam based:} \quad 5890^{+1470}_{-1270}\ \text{MCHF}.$$

$$\text{2018 CLIC 380 GeV klystron based:} \quad 7290^{+1800}_{-1540}\ \text{MCHF}.$$

Refer to Sect. 6.2 for explanations of the uncertainly.

The breakdown of the cost estimate up to the sub-domain level is presented in Table 76 for the 380 GeV stage of the accelerator complex. Figure 127 illustrates the sharing of cost between different parts of the accelerator complex.

The difference between the drive-beam and klystron-based estimates is mainly due to the current cost estimates for the X-band klystrons and corresponding modulators. The increased diameter of the main linac tunnel, required to host the RF gallery in the klystron-based option, also contributes to the cost-difference. By reducing the X-band RF costs by 50% in the klystron option, the overall cost of the two options becomes similar. To achieve such a reduction would require a dedicated development programme together with industry for X-band klystrons and associated modulators. There is still room for possible gains through optimising the accelerating structure parameters, klystron design and luminosity performance. The cost of the klystron-based option is more affected by the luminosity specification than the drive-beam option.

In the case of expanding from a klystron-based initial stage, the energy upgrade from 380 GeV to the 1.5 TeV stage is expected to be 25% more expensive than for the drive-beam option.

For a klystron-based implementation, the study of further cost reductions of the RF system is of crucial importance.

Funding information Open access funding provided by CERN (European Organization for Nuclear Research).

Data availability The CLIC project adheres to the CERN Open Access policy. To facilitate a wide use of the project results, most of the CLIC publications and data are generally "open data", and any interested parties are encouraged to contact the project team to discuss their ideas.

References

1. M. Aicheler, P. Burrows, M. Draper, T. Garvey, P. Lebrun, K. Peach, N. Phinney, H. Schmickler, D. Schulte, N. Toge, A multi-TeV linear collider based on CLIC technology: CLIC conceptual design report. Technical Report CERN-2012-007, CERN (2012). https://doi.org/10.5170/CERN-2012-007
2. P. Lebrun, L. Linssen, A. Lucaci-Timoce, D. Schulte, F. Simon, S. Steinar, N. Toge, H. Weerts, J. Wells, CLIC conceptual design report: the CLIC programme: towards a staged e^+e^- linear collider exploring the terascale. Technical Report CERN-2012-005, CERN (2012). https://doi.org/10.5170/CERN-2012-005
3. L. Linssen, A. Miyamoto, M. Stanitzki, H. Weerts, CLIC Conceptual Design Report: Physics and Detectors at CLIC. Technical Report CERN-2012-003, CERN (2012). https://doi.org/10.5170/CERN-2012-003
4. P.N. Burrows, P. Lebrun, L. Linssen, D. Schulte, E. Sicking, S. Stapnes, M.A. Thomson, Updated baseline for a staged Compact Linear Collider. Technical Report CERN-2016-004, CERN (2016). https://doi.org/10.5170/CERN-2016-004
5. M. Aicheler, et al., The Compact Linear Collider (CLIC) – Project Implementation Plan. Technical Report CERN-2018-010-M, CERN, December 2018 (2018). https://doi.org/10.23731/CYRM-2018-004
6. P.N. Burrows, et al., The Compact Linear e^+e^- Collider (CLIC) - 2018 summary report. CERN Yellow Rep. Monogr. **1802**, 1–98 (2018). https://doi.org/10.23731/CYRM-2018-002. arXiv:1812.06018 [physics.acc-ph]
7. M. Boland, Updated baseline for a staged Compact Linear Collider. Technical Report CERN-2016-004, CERN, Geneva, August 2016 (2016). https://doi.org/10.5170/CERN-2016-004
8. H. Abramowicz, et al., Higgs physics at the CLIC electron-position linear collider. Eur. Phys. J. C **77**(7), 475 (2017). https://doi.org/10.1140/epjc/s10052-017-4968-5
9. H. Abramowicz, et al. Top-Quark Physics at the CLIC Electron-Positron Linear Collider. Technical report, CERN (2018)
10. P. Roloff, U. Schnoor, R. Simoniello, B. Xu, Double Higgs boson production and Higgs self-coupling extraction at CLIC. Eur. Phys. J. C **80**(11), 1010 (2020). https://doi.org/10.1140/epjc/s10052-020-08567-7. arXiv:1901.05897 [hep-ex]
11. The CLIC Potential for New Physics. https://arxiv.org/abs/1812.02093
12. P. Roloff, R. Franceschini, U. Schnoor, A. Wulzer, The Compact Linear e^+e^- Collider (CLIC): Physics Potential. https://cds.cern.ch/record/2652257
13. A. Robson, P. Roloff, J. Blas, CLIC Higgs Prospects with 100 Hz Operation. http://cds.cern.ch/record/2927905
14. D. Arominski, et al., A detector for CLIC: main parameters and performance. Technical Report CLICdp-Note-2018-005, CERN (2018). http://cds.cern.ch/record/2649437
15. Detector Technologies for CLIC. Technical Report CERN-2019-001, May 2019 (2019). https://doi.org/10.23731/CYRM-2019-001
16. D. Dannheim, L. Linssen, A. Sailer, Progress on Detector R&D for CLIC 2019-2025. https://cds.cern.ch/record/2927639
17. V. Cilento, R. Tomás, B. Cure, A. Faus-Golfe, B. Dalena, Y. Levinsen, Dual beam delivery system serving two interaction regions for the Compact Linear Collider. Phys. Rev. Accel. Beams **24**, 071001 (2021). https://doi.org/10.1103/PhysRevAccelBeams.24.071001
18. F. Bordry, et al., Machine Parameters and Projected Luminosity Performance of Proposed Future Colliders. At CERN. Technical report, CERN (2018)
19. P.G. Roloff, A. Robson, Updated CLIC Luminosity Staging Baseline and Higgs Coupling Prospects. https://cds.cern.ch/record/2645352
20. C. Gohil, P.N. Burrows, N. Blaskovic Kraljevic, A. Latina, J. Ögren, D. Schulte, Luminosity performance of the Compact Linear Collider at 380 GeV with static and dynamic imperfections. Phys. Rev. Accel. Beams **23**, 101001 (2020). https://doi.org/10.1103/PhysRevAccelBeams.23.101001

21. Y. Han, A. Latina, L. Ma, D. Schulte, Beam-Based Alignment for the Rebaselining of CLIC RTML (CERN-ACC-2017-195), 099–4 (2017)
22. Y. Zhao, A. Latina, Optimization of the compact linear collider rings-to-main-linac at 380 GeV. Phys. Rev. Accel. Beams **28**, 021003 (2025). https://doi.org/10.1103/PhysRevAccelBeams.28.021003
23. N. Blaskovic Kraljevic, D. Schulte, Beam-based beamline element alignment for the main linac of the 380 GeV stage of CLIC. Technical Report CLIC-Note-1140, CERN (2018). https://edms.cern.ch/document/2053412/
24. J. Ogren, Tuning of the CLIC 380 GeV Final-Focus System with Static Imperfections. Technical Report CLIC-Note-1141, CERN (2018). https://edms.cern.ch/document/2053415/
25. V.M. Juravlev, W. Coosemans, G. Ramseier, A. Seryi, A.I. Sleptsov, I.H. Wilson, Investigations of power and spatial correlation characteristics of seismic vibrations in the cern lep tunnel for linear collider studies. Technical Report CERN-SL-93-53. CLIC-Note-217, CERN, Geneva, December 1993 (1993). https://cds.cern.ch/record/258752
26. B. Bolzon, Étude des vibrations et de la stabilisation à l'échelle sous-nanométrique des doublets finaux d'un collisionneur linéaire. PhD thesis, Université de Savoie, France (2007). http://cds.cern.ch/record/1100434. LAPP-T-2007-05
27. C. Gohil, P.N. Burrows, D. Schulte, Integrated Simulation of Dynamic Effects for the 380 GeV. CLIC Design. Technical Report CLIC-Note-1138, CERN (2018). https://edms.cern.ch/document/2053401/
28. B. Heilig, C. Beggan, J. Lichtenberger, Natural sources of geomagnetic field variations. Technical Report CERN-ACC-2018-0033, CLIC-Note-1083, CERN, Geneva, October 2018 (2018). http://cds.cern.ch/record/2643499
29. G. Geschonke, A. Ghigo, Ctf3 design report. Technical Report CERN-PS-2002-008-RF, CTF-3-NOTE-2002-047, LNF-2002-008-IR, CERN (2002). https://cds.cern.ch/record/559331
30. D. Schulte, R. Tomas, Dynamic effects in the new CLIC main linac, in *Proceedings of PAC 2009*, Vancouver, BC, Canada (2009), pp. 3811–3813. http://accelconf.web.cern.ch/accelconf/PAC2009/papers/th6pfp046.pdf
31. L. Malina, Recent improvements in drive beam stability in CTF3, in *Proc. of International Particle Accelerator Conference (IPAC'16)*, Busan, Korea, May 8-13 (2016), pp. 2673–2676. https://doi.org/10.18429/JACoW-IPAC2016-WEPOR007
32. J. Roberts, P. Skowronski, P.N. Burrows, G.B. Christian, R. Corsini, A. Ghigo, F. Marcellini, C. Perry, Stabilization of the arrival time of a relativistic electron beam to the 50 fs level. Phys. Rev. Accel. Beams **21**(1), 011001 (2018). https://doi.org/10.1103/PhysRevAccelBeams.21.011001
33. R. Corsini, in *Final Results from the CLIC Test Facility (CTF3)* (2017), pp. 1–6. https://doi.org/10.18429/JACoW-IPAC2017-TUZB1
34. CLEAR Official Website. http://clear.web.cern.ch/
35. R. Corsini, et al., Status of the CLEAR user facility at CERN and its experiments, in *Proceedings of LINAC2022* (2022), p. 05. https://doi.org/10.18429/JACoW-LINAC2022-THPOPA05. https://cds.cern.ch/record/2844844
36. SLC Design Handbook. Stanford Linear Collider: Design Report. SLAC, Stanford, CA (1984). http://cds.cern.ch/record/105035
37. N. Phinney, SLC final performance and lessons. eConf **C00082**, 102 (2000). arXiv:physics/0010008 [physics.acc-ph]
38. R.W. Assmann, et al., *Accelerator Physics Highlights in the 1997 / 98 SLC Run*. Conf. Proc. C9803233, vol. 474 (1998)
39. M. Aiba, M. Boege, N. Milas, A. Streun, Ultra low vertical emittance at SLS through systematic and random optimization. Nucl. Instrum. Methods A **694**, 133–139 (2012). https://doi.org/10.1016/j.nima.2012.08.012
40. R. Dowd, Y.-R. Tan, K. Wootton, Vertical emittance at the quantum limit, in *Proceedings of IPAC 2014*, Dresden, Germany (2014), p. 035. https://doi.org/10.18429/JACoW-IPAC2014-TUPRO035
41. K.P. Wootton, M.J. Boland, R.P. Rassool, Measurement of ultralow vertical emittance using a calibrated vertical undulator. Phys. Rev. Spec. Top., Accel. Beams **17**, 112802 (2014). https://doi.org/10.1103/PhysRevSTAB.17.112802
42. V. Balakin, V.A. Alexandrov, A. Mikhailichenko, K. Floettmann, F. Peters, G.-A. Voss, V. Bharadwaj, M. Halling, J.A. Holt, J. Buon, J. Jeanjean, F. LeDiberder, V. Lepeltier, P. Puzo, G. Heimlinger, R. Settles, U. Stierlin, H. Hayano, N. Ishihara, H. Nakayama, K. Oide, T. Shintake, Y. Takeuchi, N. Yamamoto, F. Bulos, D. Burke, R. Field, S. Hartman, R. Helm, J. Irwin, R. Iverson, S. Rokni, G. Roy, W. Spence, P. Tenenbaum, S.R. Wagner, D. Walz, S. Williams, Focusing of submicron beams for TeV-scale e^+e^- linear colliders. Phys. Rev. Lett. **74**, 2479–2482 (1995). https://doi.org/10.1103/physrevlett.74.2479.
43. S. Kuroda, ATF2 for final focus test beam for future linear colliders. Nucl. Part. Phys. Proc. **273–275**, 225–230 (2016). https://doi.org/10.1016/j.nuclphysbps.2015.09.030
44. T. Okugi, Achievement of small beam size at ATF2 beamline, in *Proc. LINAC 2016* (2016). https://doi.org/10.18429/JACoW-LINAC2016-MO3A02
45. P.C.V. Thrane, Probing LINEAR Collider Final Focus Systems in SuperKEKB. Technical Report CERN-ACC-2017-0052. CLIC-Note-1077, CERN, Geneva, June 2017 (2017). https://cds.cern.ch/record/2276026
46. A. Latina, J. Pfingstner, D. Schulte, E. Adli, F.J. Decker, N. Lipkowitz, Experimental demonstration of a global dispersion-free steering correction at the new linac test facility at SLAC. Phys. Rev. Accel. Beams **17** (2014). https://doi.org/10.1103/physrevstab.17.042803
47. A. Latina, D. Pellegrini, J. Pfingstner, D. Schulte, E. Adli, Toolbox for applying beam-based alignment to linacs, in *Proceedings of LINAC 2014*, Geneva, Switzerland (2014). https://cds.cern.ch/record/2062614
48. FACET User Facility. http://portal.slac.stanford.edu/sites/ard_public/facet/Pages/default.aspx
49. FERMI (Free Electron laser Radiation for Multidisciplinary Investigations). https://www.elettra.trieste.it/lightsources/fermi.html

50. H. Zha, A. Latina, A. Grudiev, G. De Michele, A. Solodko, W. Wuensch, D. Schulte, E. Adli, N. Lipkowitz, G.S. Yocky, Beam-based measurements of long-range transverse wakefields in the compact linear collider main-linac accelerating structure. Phys. Rev. Accel. Beams **19**, 011001 (2016). https://doi.org/10.1103/PhysRevAccelBeams.19.011001
51. C. Gohil, A. Latina, D. Schulte, S. Stapnes High-Luminosity CLIC Studies. Technical report, CERN, Geneva, August 2020 (2020). https://cds.cern.ch/record/2687090
52. F. Zhou, A. Brachmann, T. Maruyama, J.C. Sheppard, Polarized photocathode R&D for future linear colliders. AIP Conf. Proc. **1149**(1), 992–996 (2009). https://doi.org/10.1063/1.3215803. SLAC-PUB-13514
53. Y. Zhao, S. Doebert, A. Latina, Performance optimization of the CLIC positron source. Phys. Rev. Accel. Beams **28**, 011002 (2025). https://doi.org/10.1103/PhysRevAccelBeams.28.011002
54. Y. Zhao, S. Doebert, A. Latina, Performance Optimization of the CLIC Positron Source. Technical report, CERN, Geneva (2024). https://cds.cern.ch/record/2916863
55. M. Aicheler, P. Burrows, M. Draper, T. Garvey, P. Lebrun, K. Peach, N. Phinney, H. Schmickler, D. Schulte, N. Toge, A multi-TeV linear collider based on CLIC technology: CLIC conceptual design report. Technical Report CERN-2012-007. SLAC-R-985. KEK-Report-2012-1. PSI-12-01. JAI-2012-001, CERN, Geneva (2012). https://doi.org/10.5170/CERN-2012-007
56. A. Kurtulus, S. Doebert, A. Grudiev, A. Latina, Y. Zhao, RF Design and Optimization of Linacs for the CLIC Main Beam Injector Complex. Technical Report CERN-ACC-2025-0004 ; CLIC-Note-1201, CERN, Geneva (2025). https://cds.cern.ch/record/2944951
57. Y. Papaphilippou, et al., Conceptual design of the CLIC damping rings, in *Proceedings of IPAC 2012*, New Orleans (2012), pp. 1368–1370. http://accelconf.web.cern.ch/AccelConf/IPAC2012/papers/TUPPC086.PDF
58. F. Antoniou, Optics design of intrabeam scattering dominated damping rings. Nat. Tech. U. Athens (2012). PhD thesis, Presented 08 Jan 2013. https://cds.cern.ch/record/1666863
59. F. Antoniou, Y. Papaphilippou, Analytical considerations for linear and nonlinear optimization of the theoretical minimum emittance cells: application to the compact linear collider predamping rings. Phys. Rev. Spec. Top., Accel. Beams **17**, 064002 (2014). https://doi.org/10.1103/physrevstab.17.064002
60. S. Papadopoulou, F. Antoniou, Y. Papaphilippou, Emittance reduction with variable bending magnet strengths: analytical optics considerations and application to the compact linear collider damping ring design. Phys. Rev. Accel. Beams **22**, 091601 (2019). https://doi.org/10.1103/PhysRevAccelBeams.22.091601
61. M. Zampetakis, F. Antoniou, F. Asvesta, H. Bartosik, Y. Papaphilippou, Interplay of space charge, intrabeam scattering, and synchrotron radiation in the compact linear collider damping rings. Phys. Rev. Accel. Beams **27**, 064403 (2024). https://doi.org/10.1103/PhysRevAccelBeams.27.064403
62. A. Grudiev, Conceptual design of the CLIC damping ring RF system, in *Proc. of IPAC 2012*, New Orleans, Louisiana, USA (2012), pp. 1870–1872. http://accelconf.web.cern.ch/AccelConf/IPAC2012/papers/TUPPR026.PDF
63. A. Grudiev, T. Mastoridis, Novel cavity with ultra-low R/Q for CLIC damping ring RF system. Technical report, CERN, Geneva (2021). https://cds.cern.ch/record/2792558
64. T. Mastoridis, B. Miller, A. Grudiev, Low level radio frequency studies for the compact linear collider damping rings. Nucl. Instrum. Methods Phys. Res., Sect. A **985**, 164659 (2021). https://doi.org/10.1016/j.nima.2020.164659
65. Y. Papaphilippou, P. Elleaume, Analytical considerations for reducing the effective emittance with variable dipole field strengths. Conf. Proc. **C0505161**, 2086 (2005)
66. Y. Papaphilippou, P. Elleaume, L. Farvacque, A. Ropert, Lattice upgrade options for the esrf storage ring. Conf. Proc. **C0505161**, 2047 (2005)
67. S. Papadopoulou, Y. Papaphilippou, F. Antoniou, Emittance reduction with variable bending magnet strengths: Analytical optics considerations. Phys. Rev. Spec. Top., Accel. Beams (2018). Submitted
68. M.A.D. Martinez, F. Toral, H. Ghasem, P.S. Papadopoulou, Y. Papaphilippou, Longitudinally variable field dipole design using permanent magnets for CLIC damping rings. IEEE Trans. Appl. Supercond. **28**(3), 1–4 (2018). https://doi.org/10.1109/TASC.2018.2795551
69. L.G. Fajardo, F. Antoniou, A. Bernhard, P. Ferracin, J. Mazet, S. Papadopoulou, Y. Papaphilippou, J.C. Perez, D. Schoerling, Design of Nb3Sn wiggler magnets for the Compact Linear Collider and manufacturing of a five-coil prototype. IEEE Trans. Appl. Supercond. **26**(4), 1–6 (2016). https://doi.org/10.1109/TASC.2016.2517938
70. A. Bernhard, et al., A clic damping wiggler prototype at ANKA: commissioning and preparations for a beam dynamics experimental program, in *Proceedings, 7th International Particle Accelerator Conference (IPAC 2016)*, Busan, Korea, May 8-13 (2016), p. 002. https://doi.org/10.18429/JACoW-IPAC2016-WEPMW002
71. D. Schoerling, F. Antoniou, A. Bernhard, A. Bragin, M. Karppinen, R. Maccaferri, N. Mezentsev, Y. Papaphilippou, P. Peiffer, R. Rossmanith, G. Rumolo, S. Russenschuck, P. Vobly, K. Zolotarev, Design and system integration of the superconducting wiggler magnets for the Compact Linear Collider damping rings. Phys. Rev. Spec. Top., Accel. Beams **15**, 042401 (2012). https://doi.org/10.1103/PhysRevSTAB.15.042401
72. A. Bernhard, A. Bragin, S. Casalbuoni, P. Ferracin, L. Garcia Fajardo, S. Gerstl, J. Gethmann, A. Grau, E. Huttel, S. Khrushchev, N. Mezentsev, A.-S. Müller, Y. Papaphilippou, D. Jauregui, H. Schmickler, D. Schoerling, V. Shkaruba, N. Smale, V. Tsukanov, P. Zisopoulos, K. Zolotarev, A CLIC Damping Wiggler Prototype at ANKA: Commissioning and Preparations for a Beam Dynamics Experimental Program (CERN-ACC-2016-222, CLIC-Note-1095), 002 (2016)
73. C. Belver-Aguilar, Development of stripline kickers for low emittance rings: Application to the beam extraction kicker for CLIC damping rings. Phdthesis (April 2015) (2015). Presented 22 Oct 2015. https://cds.cern.ch/record/2062835

74. M. Pont, et al., The stripline kicker prototype for the CLIC damping rings at ALBA: installation, commissioning and beam characterisation, in *Proc. 9th International Particle Accelerator Conference (IPAC'18)*, Vancouver, BC, Canada, April 29-May 4, 2018 (2018), pp. 4062–4065. https://doi.org/10.18429/JACoW-IPAC2018-THPMF013
75. J. Holma, M. Barnes, A. Ferrero Colomo, Demonstration of feasibility of the CLIC damping ring extraction kicker modulators, in *Proceedings of IPAC 2018*, Vancouver, BC, Canada (2018), p. 077. https://doi.org/10.18429/JACoW-IPAC2018-WEPMF077
76. J. Holma, M. Barnes, M. Carlà, N. Catalán Lasheras, U. Iriso, Z. Martí, Y. Papaphilippou, F. Pérez, M. Pont, Beam-based measurements on two ±12.5 kV inductive adders, together with striplines, for CLIC damping ring extraction kickers, in *10th International Particle Accelerator Conference* (2019), p. 071. https://doi.org/10.18429/JACoW-IPAC2019-THPRB071. https://accelconf.web.cern.ch/ipac2019/papers/thprb071.pdf
77. M. Pont, et al., The stripline kicker prototype for the CLIC damping rings at ALBA: installation, commissioning and beam characterisation, in *Proceedings of IPAC 2018*, Vancouver, BC, Canada (2018), p. 013. https://doi.org/10.18429/JACoW-IPAC2018-THPMF013
78. A. Poyet, M. Domínguez, R. Geometrante, E. Karantzoulis, Y. Papaphilippou, F. Toral, Emittance reduction with the variable dipole for the ELETTRA 2.0 ring, in *JACoW* IPAC2022, 2586–2589 (2022). https://doi.org/10.18429/JACoW-IPAC2022-THPOPT013
79. A. Latina, N. Solyak, D. Schulte, A spin rotator for the compact linear collider, in *Proc. 1st Int. Particle Accelerator Conf.*, 23-28 May 2010, Kyoto, Japan (2010), pp. 4608–4610. http://accelconf.web.cern.ch/accelconf/IPAC10/papers/thpe040.pdf
80. Y. Han, A. Latina, L. Ma, D. Schulte, Beam-based alignment for the rebaselining of CLIC RTML, in *Proceedings, 8th International Particle Accelerator Conference (IPAC 2017)*, Copenhagen, Denmark, May 14–19, 2017 (2017), p. 099. https://doi.org/10.18429/JACoW-IPAC2017-TUPIK099
81. T. Lienart, Study of Pre-Alignment tolerances in the RTML. Technical Report CERN-OPEN-2012-014. CLIC-Note-943, CERN, Geneva, May 2012 (2012). http://cds.cern.ch/record/1452626
82. C.G. Gohil, P. Burrows, M.C.L. Buzio, E. Marín, D. Schulte, Measurements and impact of stray fields on the 380 GeV design of CLIC, in *Proc. 9th International Particle Accelerator Conference (IPAC'18)*, Vancouver, BC, Canada, April 29-May 4, 2018 (2018), pp. 3072–3075. https://doi.org/10.18429/JACoW-IPAC2018-THPAF047
83. C. Belver-Aguilar, A. Faus-Golfe, F. Toral, M.J. Barnes, Stripline design for the extraction kicker of Compact Linear Collider damping rings. Phys. Rev. Spec. Top., Accel. Beams **17**, 071003 (2014). https://doi.org/10.1103/PhysRevSTAB.17.071003
84. R. Apsimon, A. Latina, D. Schulte, J. Uythoven, Feed forward orbit correction in the CLIC ring to main linac transfer lines, in *Proceedings of IPAC 2014* (2014). https://doi.org/10.18429/JACoW-IPAC2014-MOPRO029
85. A. Latina, P. Eliasson, D. Schulte, Implications of a curved tunnel for the main linac of CLIC, in *Proc. 10th European Particle Accelerator Conf.*, 26–30 June 2006, Edinburgh, Scotland, UK (2006), pp. 864–866. http://accelconf.web.cern.ch/accelconf/e06/PAPERS/MOPLS130.PDF
86. D. Schulte, Beam-based alignment in the new CLIC main linac, in *Proc. 23rd IEEE Particle Accelerator Conf.*, 4-8 May 2009, Vancouver, British Columbia, Canada (2009), pp. 3808–3810. http://accelconf.web.cern.ch/accelconf/PAC2009/papers/th6pfp045.pdf
87. N. Blaskovic Kraljevic, D. Schulte, Beam-based beamline element alignment for the Main Linac of the 380 GeV stage of CLIC. Technical Report CERN-ACC-2018-0053. CLIC-Note-1140, CERN, Geneva, November 2018 (2018). https://cds.cern.ch/record/2649489
88. A. Pastushenko, D. Schulte, Emittance tuning bumps for the main linac of CLIC 380 GeV, in *JACoW* IPAC2023, 087 (2023). https://doi.org/10.18429/JACoW-IPAC2023-THPL087
89. L. Mether, Update on FASTION code development, and new results, in CLIC Beam Physics Meeting, 31 March 2016, CERN (2016). https://indico.cern.ch/event/514861/
90. CLICdp-collaboration: the post-CDR CLIC detector model. Technical Report CLICdp-Note-2017-001, CERN (2017). https://cds.cern.ch/record/2254048
91. F. Plassard, A. Latina, E. Marin, R. Tomas, P. Bambade, Quadrupole-free detector optics design for the Compact Linear Collider final focus system at 3 TeV. Phys. Rev. Accel. Beams **21** (2018). https://doi.org/10.1103/PhysRevAccelBeams.21.011002
92. P. Lebrun, L. Linssen, A. Lucaci-Timoce, D. Schulte, F. Simon, S. Stapnes, N. Toge, H. Weerts, J. Wells, The CLIC programme: towards a staged e^+e^- linear collider exploring the terascale: CLIC conceptual design report. Technical Report arXiv:1209.2543. CERN-2012-005. ANL-HEP-TR-12-51. KEK-Report-2012-2. MPP-2012-115, CERN, Geneva (2012). https://doi.org/10.5170/CERN-2012-005
93. P. Raimondi, A. Seryi, Novel final focus design for future linear colliders. Phys. Rev. Lett. **86**, 3779–3782 (2001). https://doi.org/10.1103/physrevlett.86.3779
94. R. Tomás, Nonlinear optimization of beam lines. Phys. Rev. Spec. Top., Accel. Beams **9**, 081001 (2006). https://doi.org/10.1103/PhysRevSTAB.9.081001
95. B. Dalena, J. Barranco, A. Latina, E. Marin, J. Pfingstner, D. Schulte, J. Snuverink, R. Tomas, G. Zamudio, Beam delivery system tuning and luminosity monitoring in the Compact Linear Collider. Phys. Rev. Spec. Top., Accel. Beams (2012). https://doi.org/10.1103/PhysRevSTAB.15.051006
96. E. Marin, A. Latina, R. Tomas, D. Schulte, Final focus system tuning studies towards Compact Linear Collider feasibility. Phys. Rev. Accel. Beams (2018). https://doi.org/10.1103/PhysRevAccelBeams.21.011003

97. Y. Nosochkov, P. Raimondi, T. Raubenheimer, A. Seryi, Tuning knobs for the NLC final focus, in *Particle Accelerator. Proceedings, 8th European Conference, EPAC 2002*, Paris, France, June 3-7, 2002 (2002), pp. 476–478. http://accelconf.web.cern.ch/AccelConf/e02/PAPERS/MOPRI047.pdf
98. J. Ögren, A. Latina, R. Tomás, D. Schulte, Tuning of the CLIC 380 GeV Final-Focus System with Static Imperfections. Technical report, CERN, Geneva, November 2018 (2018). http://cds.cern.ch/record/2651111
99. J. Ögren, A. Latina, R. Tomás, D. Schulte, Tuning the Compact Linear Collider 380 GeV final-focus system using realistic beam-beam signals. Phys. Rev. Accel. Beams **23**, 051002 (2020). https://doi.org/10.1103/PhysRevAccelBeams.23.051002
100. N. Alipour Tehrani, et al., CLICdet: the post-CDR CLIC detector model. https://cds.cern.ch/record/2254048
101. A. Ferrari, V. Ziemann, R.B. Appleby, M.D. Salt, Conceptual design of a beam line for post-collision extraction and diagnostics at the multi-TeV compact linear collider. Phys. Rev. Spec. Top., Accel. Beams **12**, 021001 (2009). https://doi.org/10.1103/PhysRevSTAB.12.021001
102. D. Angal-Kalinin, R. Appleby, J. Jones, A. Scarfe, S. Tygier, ATF2 tests and CLIC ir study. Technical Report EuCARD-REP-2013-021 (2013). http://cds.cern.ch/record/1710304
103. E. Gschwendtner, CLIC Post-Collision Line and Dump (2010). https://indico.cern.ch/event/110479/contributions/43439/
104. A. Vorozhtsov, Preliminary design of CLIC Main Beam normal conducting magnets required for the Post-Collision Line (2010)
105. L.J. Nevay, S.T. Boogert, J. Snuverink, A. Abramov, L.C. Deacon, H. Garcia-Morales, H. Lefebvre, S.M. Gibson, R. Kwee-Hinzmann, W. Shields, S.D. Walker, BDSIM: an accelerator tracking code with particle–matter interactions. Comput. Phys. Commun. **252**, 107200 (2020). https://doi.org/10.1016/j.cpc.2020.107200
106. S.T. Boogert, A. Abramov, A. Butcher, S.D. Walker, L.J. Nevay. pyg4ometry. https://bitbucket.org/jairhul/pyg4ometry
107. D. Arominski, CLIC Beam-beam Interactions. https://doi.org/10.5281/zenodo.1467017
108. A. Mereghetti, C. Maglioni, V. Vlachoudis, Fluka and thermo-mechanical studies for the CLIC main dump. Technical Report CERN-OPEN-2011-030. CLIC-Note-876, CERN, Geneva, March 2011 (2011). http://cdsweb.cern.ch/record/1355402/files/CERN-OPEN-2011-030.pdf
109. J. Cai, I. Syratchev, Modeling and technical design study of two-stage multibeam klystron for CLIC. IEEE Trans. Electron Devices **67**(8), 3362–3368 (2020). https://doi.org/10.1109/TED.2020.3000191
110. M. Dayyani Kelisani, S. Doebert, M. Aslaninejad, Low emittance design of the electron gun and the focusing channel of the Compact Linear Collider drive beam. Phys. Rev. Accel. Beams **20**, 043403 (2017). https://doi.org/10.1103/PhysRevAccelBeams.20.043403
111. S.S. Hajari, H. Shaker, S. Doebert, Beam dynamics design of the Compact Linear Collider drive beam injector. Nucl. Instrum. Methods Phys. Res., Sect. A, Accel. Spectrom. Detect. Assoc. Equip. **799**, 172–186 (2015). https://doi.org/10.1016/j.nima.2015.07.043
112. S.H. Shaker, S. Döbert, R. Leuxe, S. Sanaye Hajari, L. Dassa, Sub-harmonic buncher design for the CLIC drive beam injector, in *Proceedings, 4th International Particle Accelerator Conference (IPAC 2013)*, Shanghai, China, May 12-17, 2013 (2013). http://JACoW.org/IPAC2013/papers/tupme052.pdf
113. H. Shaker, RF Design of the TW Buncher for the CLIC Drive Beam Injector (2nd report). Technical Report CERN-ACC-2016-0113. CLIC-Note-1068, CERN, Geneva, June 2016 (2016). https://cds.cern.ch/record/2217866
114. A. Aksoy, CLIC drive beam linac optimization, in *CLIC Workshop 2018*, CERN, Geneva, 22-26 January 2018 (2018). https://indico.cern.ch/event/656356/contributions/2832818/
115. A. Aksoy, D. Schulte, O. Yavas, Beam dynamics simulation for the Compact Linear Collider drive-beam accelerator. Phys. Rev. Spec. Top., Accel. Beams **14**, 084402 (2011). https://doi.org/10.1103/PhysRevSTAB.14.084402
116. C. Biscari, D. Alesini, A. Ghigo, F. Marcellini, J.B. Jeanneret, CLIC drive beam frequency multiplication system design, in *Proc. 23rd IEEE Particle Accelerator Conf.*, Vancouver, British Columbia, Canada, 4-8 May 2009 (2009), pp. 2673–2675. http://accelconf.web.cern.ch/accelconf/PAC2009/papers/we6pfp076.pdf
117. R. Costa, Simulation and optimisation of CLIC's recombination complex. Phdthesis (2018). . Aveiro University. Presented 01 Feb 2018. https://cds.cern.ch/record/2309454
118. R. Costa, Phd thesis in preparation. PhD thesis, Uppsala University, Sweden (2024)
119. A. Vorozhtsov, Preliminary design of CLIC drive beam magnets required for the, in *Delay Line, Combiner Rings, Turn-Around, Transport to Tunnel, Long Transfer Line and Injector Linac* (2010)
120. D. Pellegrini, PLACET2: a novel code for beam dynamics in recirculating machines. Technical Report CERN-ACC-2015-322, CERN. https://cds.cern.ch/record/2141792
121. E. Adli, A study of the beam physics in the CLIC drive beam decelerator. PhD thesis, University of Oslo (2009). http://cdsweb.cern.ch/record/1239173/files/CERN-THESIS-2010-024.pdf
122. J. Esberg, A. Latina, R. Apsimon, D. Schulte, Effect of CSR shielding in the compact linear collider, in *Proceedings of IPAC2014* (2014), p. 4. https://cds.cern.ch/record/1742292
123. E. Marin, Update on the CLIC drive beam lattice optimization studies, in *CLIC Workshop 2016*, CERN, Geneva, 18-22 January 2016 (2016)
124. R. Costa, Performance optimisation of the CLIC drive beam recombination complex, in *Asian Linear Collider Workshop* (2018). https://agenda.linearcollider.org/event/7826/
125. D. Gamba, Online optimisation of the CLIC Drive-Beam bunch train recombination at CTF3. PhD thesis, Oxford University (2016). https://cds.cern.ch/record/2230011

126. I. Syratchev, E. Adli, D. Schulte, M. Taborelli, High RF power production for CLIC, in *Proc. 22nd Particle Accelerator Conf.*, Albuquerque, New Mexico, USA, 25-29 June 2007 (2007), pp. 2194–2196. http://accelconf.web.cern.ch/accelconf/p07/PAPERS/WEPMN071.PDF
127. J.B. Jeanneret, Dumping the decelerated beams of CLIC. Technical Report CERN-OPEN-2011-039. CLIC-Note-887, CERN, Geneva (2011). http://cdsweb.cern.ch/record/1376685/files/CERN-OPEN-2011-039.pdf
128. F. Zhou, A. Brachman, J. Sheppard, Preliminary design of a bunching system for the CLIC polarized electron source. Technical Report CERN-OPEN-2010-025. CLIC-Note-813, CERN, Geneva (2009). http://cdsweb.cern.ch/record/1308186/files/CERN-OPEN-2010-025.pdf
129. Y. Han, C. Bayar, S. Döbert, A. Latina, L. Ma, D. Schulte, Update of the CLIC positron source, in *Proc. 9th International Particle Accelerator Conference (IPAC'18)*, Vancouver, BC, Canada, April 29-May 4, 2018 (2018), pp. 236–239. https://doi.org/10.18429/JACoW-IPAC2018-MOPMF055
130. H. Bajas, S. Doebert, A. Latina, Y. Zhao, Flux concentrator optimization for future positron sources. IEEE Trans. Appl. Supercond. **32**(6), 1–5 (2022). https://doi.org/10.1109/TASC.2022.3160405
131. C. Bayar, A.K. Ciftci, S. Doebert, A. Latina, Design and optimisation of the positron production chain for CLIC from the target to the damping ring. Nucl. Instrum. Methods Phys. Res., Sect. A, Accel. Spectrom. Detect. Assoc. Equip. **869**, 56–62 (2017). https://doi.org/10.1016/j.nima.2017.07.010
132. A. Vamvakas, Results from the two-beam module experimental program. Technical Report EDMS 2054219, CERN, Geneva (2018). https://edms.cern.ch/document/2054219/1
133. M. Capstick, State of the clic module design and development q4 2024. Technical report, CERN (2024). https://edms.cern.ch/document/3229217/1
134. G.L. D'Alessandro, Development of X-Band high-power RF load for CLIC applications using additive manufacturing techniques. Mathesis, Salento University (2015). Presented 30 October 2015 https://cds.cern.ch/record/2139981
135. D. Aguglia, C. Martins, M. Cerqueira Bastos, D. Nisbetl, D. Siemaszko, E. Sklavounou, P. Viarouge, Klystron modulator technology challenges for the Compact Linear Collider (CLIC), pp. 1413–1421 (2011). https://doi.org/10.1109/PPC.2011.6191626
136. M. Jankovic, A. Watson, J. Clare, P. Wheeler, D. Aguglia, Grid interface challenges and candidate solutions for the compact linear collider's (CLIC) klystron modulators, in *Proceedings, 40th IEEE International Conference on Plasma Science (ICOPS 2013)*, San Francisco, California, June 16-21, 2013 (2013). https://doi.org/10.1109/PLASMA.2013.6635182
137. M. Jankovic, A. Watson, J. Clare, P. Wheeler, D. Aguglia, Optimal power system and grid interface design considerations for the CLIC klystron modulators, in *Proceedings, 2014 IEEE International Power Modulator and High Voltage Conference (2014 IPMHVC)*, Santa Fe, New Mexico, June 1-5, 2016 (2014), pp. 83–88. https://doi.org/10.1109/IPMHVC.2014.7287213
138. F.C. Magallanes, D. Aguglia, P. Viarouge, J. Cros, Novel active bouncer topology for klystron modulators based on pulsed transformers, in *Proc. 17th European Power Electronics Conference (EPE'15-ECCE Europe)*, Geneva, Switzerland (2015). https://doi.org/10.1109/EPE.2015.7311698
139. S. Candolfi, P. Viarouge, D. Aguglia, J. Cros, Hybrid design optimization of high voltage pulse transformers for klystron modulators. IEEE Trans. Dielectr. Electr. Insul. **22**, 3617–3624 (2014). https://doi.org/10.1109/TDEI.2015.005047
140. S. Blume, J. Biela, Optimal transformer design for ultraprecise solid state modulators. IEEE Trans. Plasma Sci. **41**, 2691–2700 (2013). https://doi.org/10.1109/TPS.2013.2280429
141. S. Blume, A. Jehle, Y. Schmid, J. Biela, Control of an active bouncer for an ultra precise 140 US solid state modulator system, in *Proc. 17th European Power Electronics Conference (EPE'15-ECCE Europe)*, Geneva, Switzerland (2015). https://doi.org/10.1109/EPE.2015.7311737
142. F.C. Magallanes, Integrated design of high performances pulsed power converters – application to klystron modulators for the Compact Linear Collider. PhD thesis, Laval University, Canada (2018)
143. A.D. Gobbo, D. Aguglia, Global design analysis for highly repeatable solid-state klystron modulators, in *IEEE International Power Modulator and High Voltage Conference (IPMHVC)* (2014). https://doi.org/10.1109/IPMHVC.2014.7287235
144. C. Baccigalupi, High-repeatable data acquisition systems for pulsed power converters in particle accelerator structures. phdthesis. Universita' Della Calabria (2015). Presented 11 Feb 2016. http://cds.cern.ch/record/2231052
145. C. Gough, Jitter measurement to 10ppm level for pulsed RF power amplifiers 3-12 GHz, in *Proc. of the International Particle Accelerator Conference IPAC'17*, Copenhagen, Denmark (2017). https://doi.org/10.18429/JACoW-IPAC2017-THPIK096
146. G. D'Auria, The X-band system for the FERMI@ELETTRA FEL project, in *Proc. of the International Particle Accelerator Conference IPAC'10*, Kyoto, Japan (2010). http://accelconf.web.cern.ch/AccelConf/IPAC10/papers/tupe015.pdf
147. X. Huang, A. Grudiev, Z. Zhao, W. Fang, CLIC380: RF design and parameters of 2017 re-baselined 380 GeV CLIC linac accelerating structure. Nucl. Instrum. Methods A **916**, 230–237 (2019). https://doi.org/10.1016/j.nima.2018.11.104
148. J. Liu, A. Grudiev, RF design of accelerating structure for the main linac of the klystron-based first stage of CLIC at 380 GeV. Technical report, CERN, Geneva (2018). https://cds.cern.ch/record/2643505
149. H. Zha, A. Grudiev, Design and optimization of compact linear collider main linac accelerating structure. Phys. Rev. Accel. Beams **19**, 111003 (2016). https://doi.org/10.1103/PhysRevAccelBeams.19.111003

150. S. Walstong, S. Boogert, C. Chungg, P. Fitsosg, J. Frischi, et al., Performance of a high resolution cavity beam position monitor system. Nucl. Instr. Methods A **578**, 1–22 (2007). https://doi.org/10.1016/j.nima.2007.04.162
151. F.J. Cullinan, S.T. Boogert, W. Farabolini, T. Lefevre, A. Lunin, A. Lyapin, L. Soby, J. Towler, M. Wendt, Long bunch trains measured using a prototype cavity beam position monitor for the Compact Linear Collider. Phys. Rev. Spec. Top., Accel. Beams **18** (2015). https://doi.org/10.1103/physrevstab.18.112802
152. J. Maxson, D. Cesar, G. Calmasini, A. Ody, P. Musumeci, D. Alesini, Direct measurement of sub-10 fs relativistic electron beams with ultralow emittance. Phys. Rev. Lett. **118**(15), 154802 (2017). https://doi.org/10.1103/PhysRevLett.118.154802 [physics.acc-ph]
153. G. Berden, S. Jamison, A. MacLeod, W. Gillespie, B. Redlich, A. Meer, Electro-optic technique with improved time resolution for real-time, nondestructive, single-shot measurements of femtosecond electron bunch profiles. Phys. Rev. Lett. **93**, 114802 (2004). https://doi.org/10.1103/PhysRevLett.93.114802
154. G. Berden, W.A. Gillespie, S.P. Jamison, E.-A. Knabbe, A.M. MacLeod, A.F.G. Meer, P.J. Phillips, H. Schlarb, B. Schmidt, P. Schmuser, B. Steffen, Benchmarking of electro-optic monitors for femtosecond electron bunches. Phys. Rev. Lett. **99** (2007). https://doi.org/10.1103/physrevlett.99.164801
155. E. Roussel, et al., Phase diversity electro-optic sampling: a new approach to single-shot terahertz waveform recording. Light: Sci. Appl. **11**(14) (2022). https://doi.org/10.1038/s41377-021-00696-2
156. A. Hofmann, *The Physics of Synchrotron Radiation* (Cambridge University Press, UK, 2004). https://doi.org/10.1017/CBO9780511534973
157. S. Takano, M. Masaki, H. Ohkuma, X-ray imaging of a small electron beam in a low-emittance synchrotron light source. Nucl. Instr. Methods A **556**, 357–370 (2006). https://doi.org/10.1016/j.nima.2005.08.108
158. A. Andersson, O. Chubar, M. Rohrer, V. Schlott, A. Streun, Electron beam profile measurements with visible and X-ray synchrotron radiation at the Swiss light source, in *Proceedings of the European Particle Accelerator Conference*, Edinburgh, Scotland (2006), p. 090. https://cds.cern.ch/record/1078665
159. M. Siano, B. Paroli, M.A.C. Potenza, U. Iriso, A.A. Nosych, L. Torino, S. Mazzoni, G. Trad, A.N. Goldblatt, Characterizing temporal coherence of visible synchrotron radiation with heterodyne near field speckles. Phys. Rev. Accel. Beams **20** (2017). https://doi.org/10.1103/physrevaccelbeams.20.110702
160. M. Siano, B. Paroli, M.A.C. Potenza, L. Teruzzi, U. Iriso, A.A. Nosych, E. Solano, L. Torino, D. Butti, A. Goetz, T. Lefevre, S. Mazzoni, G. Trad, Two-dimensional electron beam size measurements with x-ray heterodyne near field speckles. Phys. Rev. Accel. Beams **25**(5), 052801 (2022). https://doi.org/10.1103/PhysRevAccelBeams.25.052801
161. S.T. Boogert, G.A. Blair, G. Boorman, A. Bosco, L.C. Deacon, P. Karataev, et al., Micron-scale laser-wire scanner for the KEK Accelerator Test Facility extraction line. Phys. Rev. Spec. Top., Accel. Beams **13**, 122801 (2010). https://doi.org/10.1103/PhysRevSTAB.13.122801
162. P. Karataev, A. Aryshev, S. Boogert, D. Howell, N. Terunuma, J. Urakawa, First observation of the point spread function of optical transition radiation. Phys. Rev. Lett. **107** (2011). https://doi.org/10.1103/physrevlett.107.174801
163. B. Bolzon, A. Aryshev, T. Aumeyr, S. Boogert, P. Karataev, K.O. Kruchinin, T. Lefevre, S. Mazzoni, L. Nevay, M. Shevelev, N. Terunuma, J. Urakawa, C.P. Welsch, Very high resolution optical transition radiation imaging system: Comparison between simulation and experiment. Phys. Rev. Spec. Top., Accel. Beams **18** (2015). https://doi.org/10.1103/physrevstab.18.082803
164. R. Kieffer, M. Bergamaschi, E. Bravin, W. Farabolini, P. Karataev, T. Lefevre, S. Mazzoni, Experimental observation of shadowing in optical transition radiation. Phys. Rev. Lett. **120** (2018). https://doi.org/10.1103/physrevlett.120.094802
165. C.P. Welsch, H.-H. Braun, E. Bravin, R. Corsini, S. Doebert, T. Lefevre, F. Tecker, B. Pand Buonomo, O. Coiro, A. Ghigo, B. Preger, Longitudinal beam profile measurements at CTF3 using a streak camera. J. Instrum. **1**, 09002 (2006). https://doi.org/10.1088/1748-0221/1/09/P09002
166. M. Micheler, R. Ainsworth, G.A. Blair, G. Boorman, R. Corsini, P. Karataev, T. Lefevre, K. Lekomtsev, Longitudinal beam profile monitor at CTF3 based on coherent diffraction radiation. J. Phys. Conf. Ser. **236**, 012021 (2010). https://doi.org/10.1088/1742-6596/236/1/012021
167. K. Lekomtsev, G. Boorman, R. Corsini, P. Karataev, T. Lefevre, Investigation of coherent diffraction radiation from a dual target system at CTF3. J. Polit. **357**, 012021 (2012). https://doi.org/10.1088/1742-6596/357/1/012021
168. A.E. Dabrowski, S. Bettoni, E. Bravin, R. Corsini, S. Doebert, T. Lefevre, A. Rabiller, L. Soby, P.K. Skowronski, F. Tecker, D. Egger, C.P. Welsch, A. Ferrari, Measuring the bunch frequency multiplication at CTF3, in *Proc. 1st Int. Particle Accelerator Conf.*, Kyoto, Japan, 23-28 May 2010 (2010), pp. 1107–1109. http://accelconf.web.cern.ch/accelconf/IPAC10/papers/mope058.pdf
169. C. Welsch, E. Bravin, T. Lefevre, Optimization of OTR screen surface materials and OTR screen geometry at CTF3. Rev. Adv. Mater. Sci. **16**, 73–79 (2007)
170. C.P. Welsch, E. Bravin, B. Burel, T. Lefevre, T. Chapman, M.J. Pilon, Alternative techniques for beam halo measurements. Meas. Sci. Technol. **17**, 2035–2040 (2006). https://doi.org/10.1088/0957-0233/17/7/050
171. M. Olvegard, E. Adli, H.H. Braun, E. Bravin, N. Chritin, R. Corsini, A.E. Dabrowski, S. Doebert, C. Dutriat, D. Egger, T. Lefevre, O. Mete, P.K. Skowronski, F. Tecker, High intensity profile monitor for time resolved spectrometry at the CLIC Test Facility 3. Nucl. Instrum. Methods Phys. Res., Sect. A, Accel. Spectrom. Detect. Assoc. Equip. **683**, 29–39 (2012). https://doi.org/10.1016/j.nima.2012.04.065
172. A. Jeff, E.B. Holzer, T. Lefèvre, V. Tzoganis, C.P. Welsch, H. Zhang, A quantum gas jet for non-invasive beam profile measurement, in *Proc. IBIC*, Monterey, USA (2014). http://jacow.org/IBIC2014/papers/tuczb3.pdf

173. A. Jeff, E.B. Holzer, T. Lefèvre, V. Tzoganis, C.P. Welsch, A gas-jet profile monitor for the CLIC drive beam, in *Proc. IBIC*, Oxford, UK (2013), p. 4. https://cds.cern.ch/record/1637775
174. V. Tzoganis, H.D. Zhang, A. Jeff, C.P. Welsch, Design and first operation of a supersonic gas jet based beam profile monitor. Phys. Rev. Accel. Beams **20**, 062801 (2017). https://doi.org/10.1103/PhysRevAccelBeams.20.062801
175. A. Salehilashkajani, H.D. Zhang, M. Ady, N. Chritin, P. Forck, J. Glutting, O.R. Jones, R. Kersevan, N. Kumar, T. Lefevre, T. Marriott-Dodington, S. Mazzoni, I. Papazoglou, A. Rossi, G. Schneider, O. Sedlacek, S. Udrea, R. Veness, C.P. Welsch, A gas curtain beam profile monitor using beam induced fluorescence for high intensity charged particle beams. Appl. Phys. Lett. **120**(17), 174101 (2022). https://doi.org/10.1063/5.0085491
176. M. Gasior, An inductive pick-up for beam position and current measurements, in *Proc. 6th European Workshop on Beam Diagnostics and Instrumentation for Particle Accelerators*, Mainz, Germany, 5-7 May 2003 (2003), pp. 53–55. http://accelconf.web.cern.ch/accelconf/d03/papers/CT01.pdf
177. M. Krupa, M. Gasior, The wall current transformer – a new sensor for precise bunch-by-bunch intensity measurements in the LHC, in *Proceedings of the International Beam Instrumentation Conference*, Barcelona, Spain (2016), p. 568. https://doi.org/10.18429/JACoW-IBIC2016-WEAL02
178. T. Aumeyr, M.G. Billing, L.M. Bobb, B. Bolzon, E. Bravin, P. Karataev, K. Kruchinin, T. Lefevre, S. Mazzoni, Advanced simulations of optical transition and diffraction radiation. Phys. Rev. Accel. Beams **18** (2015). https://doi.org/10.1103/physrevstab.18.042801
179. P. Karataev, S. Araki, R. Hamatsu, H. Hayano, T. Muto, G. Naumenko, A. Potylitsyn, J. Urakawa, Beam-size measurement with optical diffraction radiation at KEK Accelerator Test Facility. Phys. Rev. Lett. **93**, 244802 (2004). https://doi.org/10.1103/PhysRevLett.93.244802
180. L. Bobb, R. Kieffer, T. Lefevre, S. Mazzoni, T. Aumeyr, P. Karataev, M. Billing, J. Conway, J. Shanks, Feasibility of diffraction radiation for noninvasive beam diagnostics as characterized in a storage ring. Phys. Rev. Accel. Beams **21** (2018). https://doi.org/10.1103/physrevaccelbeams.21.032801
181. M. Bergamaschi, A. Aryshev, P. Karataev, R. Kieffer, T. Lefevre, S. Mazzoni, N. Terunuma, R. Yang, Noninvasive micrometer-scale particle-beam size measurement using optical diffraction radiation in the ultraviolet wavelength range. Phys. Rev. Appl. **13**(1), 014041 (2020). https://doi.org/10.1103/PhysRevApplied.13.014041
182. R. Kieffer, L. Bartnik, M. Bergamaschi, V.V. Bleko, M. Billing, L. Bobb, J. Conway, M. Forster, P. Karataev, A.S. Konkov, R.O. Jones, T. Lefevre, J.S. Markova, S. Mazzoni, Y. Padilla Fuentes, A.P. Potylitsyn, J. Shanks, S. Wang, Direct observation of incoherent Cherenkov diffraction radiation in the visible range. Phys. Rev. Lett. **121**, 054802 (2018). https://doi.org/10.1103/PhysRevLett.121.054802
183. E.B. Holzer, B. Dehning, E. Effinger, J. Emery, G. Ferioli, J.L. Gonzalez, E. Gschwendtner, G. Guaglio, M. Hodgson, et al., Beam Loss Monitoring System for the LHC. Technical Report CERN-AB-2006-009, CERN (2005). http://cds.cern.ch/record/930275/files/ab-2006-009.pdf
184. M. Kastriotou, S. Döbert, W. Farabolini, E.B. Holzer, E. Nebot Del Busto, F. Tecker, C. Welsch, A versatile beam loss monitoring system for CLIC, in *Proceedings of the 7th International Particle Accelerator Conference (IPAC 2016)*, Busan, Korea, May 8-13, 2016 (2016), p. 024. https://doi.org/10.18429/JACoW-IPAC2016-MOPMR024
185. E. Nebot Del Busto, M. Boland, S. Döbert, F. Domingues Sousa, E. Effinger, W. Farabolini, E.B. Holzer, M. Kastriotou, R. Rassool, W. Viganò, C. Welsch, Position resolution of optical fibre-based beam loss monitors using long electron pulses, in *Proceedings of the 4th International Beam Instrumentation Conference*, Melbourne, Australia (2015), p. 5. https://doi.org/10.18429/JACoW-IBIC2015-WEBLA03
186. M. Kastriotou, S. Döbert, F. Domingues Sousa, E. Effinger, W. Farabolini, E.B. Holzer, E. Nebot Del Busto, W. Viganò, C. Welsch, BLM crosstalk studies on the CLIC two-beam module, in *Proceedings, 4th International Beam Instrumentation Conference, IBIC2015*, Melbourne, Australia (2015), p. 3. https://doi.org/10.18429/JACoW-IBIC2015-MOPB045
187. C. Garion, Simulations and Vacuum Tests of a CLIC Accelerating Structure (2011). (CERN-ATS-2011-268, CLIC-Note-924)
188. L. Lain Amador, Production of ultra-high-vacuum chambers with integrated getter thin-film coatings by electroforming. PhD thesis, U. Bourgogne Franche-Comte (2019). https://doi.org/10.17181/CERN.A2EJ.YIS2. Presented 03 May 2019. https://cds.cern.ch/record/2693564
189. L.L. Amadora, P. Chiggiato, L.M.A. Ferreira, V. Nistor, A.T.P. Fontenla, M. Taborelli, W. Vollenberg, M.-L. Doche, J.-Y. Hihn, Development of copper electroformed vacuum chambers with integrated non-evaporable getter thin film coatings. J. Vac. Sci. Technol. A **36**, 021601 (2017). https://doi.org/10.1116/1.4999539
190. L.L. Amador, J. Rolet, M.-L. Doche, P. Massuti-Ballester, M.-P. Gigandet, V. Moutarlier, M. Taborelli, L.M.A. Ferreira, P. Chiggiato, J.-Y. Hihn, The effect of pulsed current and organic additives on hydrogen incorporation in electroformed copper used in ultrahigh vacuum applications. J. Electrochem. Soc. **166**(10), 366 (2019). https://doi.org/10.1149/2.1211908jes
191. L.L. Amador, P. Chiggiato, L.M.A. Ferreira, E. Garcia-Tabares, T. Koettig, M.S. Meyer, A.T. Perez-Fontenla, K. Puthran, G. Rosaz, M. Taborelli, Electrodeposition of copper applied to the manufacture of seamless superconducting RF cavities. Phys. Rev. Accel. Beams **24**(8), 082002 (2021). https://doi.org/10.1103/PhysRevAccelBeams.24.082002
192. L. Lain Amador, P. Chiggiato, L.M.A. Ferreira, V. Nistor, A.T. Perez Fontenla, M. Taborelli, W. Vollenberg, M.-L. Doche, J.-Y. Hihn, Development of copper electroformed vacuum chambers with integrated non-evaporable getter thin film coatings. J. Vac. Sci. Technol. A **36**(2), 021601 (2018). https://doi.org/10.1116/1.4999539
193. C. Garion, A. Lacroix, H. Rambeau, Development of a new RF finger concept for vacuum beam line interconnections, in *Proceedings, 3rd International Particle Accelerator Conference (IPAC 2012)*, New Orleans, Louisiana, USA (2012). https://cds.cern.ch/record/1470597

194. J. Perez-Espinos, C. Garion, Analysis and testing of a new RF bridge concept as an alternative to conventional sliding RF fingers in LHC, in *Proceedings, 7th International Particle Accelerator Conference (IPAC 2016)*, Busan, Korea, May 8-13, 2016 (2016). http://cds.cern.ch/record/2207465
195. F. Niccoli, V. Giovinco, C. Garion, C. Maletta, P. Chiggiato, NiTi shape memory alloy pipe couplers for ultra-high vacuum systems: development and implementation. Smart Mater. Struct. **31**(6), 065014 (2022). https://doi.org/10.1088/1361-665x/ac6999
196. F. Niccoli, V. Giovinco, C. Garion, C. Maletta, P. Chiggiato, A simplified analytical model to simulate martensite reorientation and plasticity in shape memory alloy ring couplers. J. Intell. Mater. Syst. Struct., 1045389–2110572 (2021). https://doi.org/10.1177/1045389x211057215
197. F. Niccoli, C. Garion, C. Maletta, C. Cangialosi, A. Infantino, S. Danzeca, P. Chiggiato, Particle radiation effects on shape memory alloy couplers for ultra-high vacuum sealing: a preliminary study. Smart Mater. Struct. **28**(8), 085023 (2019). https://doi.org/10.1088/1361-665x/ab0caa
198. H.M. Durand, Micrometric propagation of error using overlapping stretched wires for the CLIC pre-alignment, in *Proceedings, 8th International Particle Accelerator Conference (IPAC 2017)*, Copenhagen, Denmark (2017). https://doi.org/10.18429/JACoW-IPAC2017-TUPIK098
199. H. Mainaud Durand, J.-C. Gayde, J. Jaros, V. Rude, M. Sosin, A. Zemanek, The new CLIC Main Linac installation and alignment strategy, in *Proceedings, 9th International Particle Accelerator Conference (IPAC 2018)*, Vancouver, BC Canada (2018), p. 066. https://doi.org/10.18429/JACoW-IPAC2018-WEPAF066
200. D. Caiazza, N. Catalan Lasheras, H. Mainaud Durand, M. Modena, C. Sanz, D. Tshilumba, V. Vlachakis, M. Wendt, S. Zorzetti, New solution for the high accuracy alignment of accelerator components. Phys. Rev. Accel. Beams **20**, 083501 (2017). https://doi.org/10.1103/PhysRevAccelBeams.20.083501
201. PACMAN Particle Accelerator Components' Metrology and Alignment to the Nanometre Scale. Last accessed 14 December 2018. https://web.archive.org/web/*/https://pacman.web.cern.ch
202. H.M. Durand, J. Jaros, J. Kemppinen, M. Sosin, V. Rude, A. Zemanek, CLIC pre-alignment strategy: final proposal and associated results, in *IWAA 2018*, Fermilab, Chicago, USA (2018). https://indico.fnal.gov/event/16262/session/6/contribution/21/material/paper/0.pdf
203. M. Sosin, Issues and feasibility demonstration of CLIC supporting system chain active pre-alignment using a multi-module test setup (mock-up) (2016). CERN-ACC-Note-2016-0063
204. J. Kemppinen, H. Mainaud Durand, Z.S. Kostka, Cam mover alignment system positioning with the wire positioning with the wire position sensor feedback for CLIC (2016). (CERN-ACC-2016-0339. CLIC-Note-1072)
205. Z. Kostka, Control of Main Beam quadrupole magnets active pre-alignment based on cam movers. Master's thesis, AGH University of Science and Technology, Krakow, Poland (2017)
206. S. Redaelli, Stabilization of nanometre-size Particle Beams in the Final Focus System of the Compact Linear Collider (CLIC). Technical Report CERN-AB-2004-026 (ABP). CLIC-Note-595, Université de Lausanne, Lausanne, Switzerland (2003). http://cdsweb.cern.ch/record/740518/files/ab-2004-026.pdf
207. S. Janssens, Stabilisation and precision pointing quadrupole magnets in the Compact Linear Collider (CLIC). Phdthesis (Jan 2015). Presented 14 Jan 2015. http://cds.cern.ch/record/1985255
208. A. Stochino, B. Abbot, Y. Aso, M. Barton, A. Bertolini, V. Boschi, D. Coyne, et al., The Seismic Attenuation System (SAS) for the Advanced LIGO gravitational wave interferometric detectors. Nucl. Instr. Methods A **598**, 737–753 (2009). https://doi.org/10.1016/j.nima.2008.10.023
209. R. Amirikas, A. Bertolini, W. Bialowons, H. Ehrlichmann, Ground motion and comparison of various sites, in *Proc. 36th ICFA Advanced Beam Dynamics Workshop*, Kyoto, Japan, 17-21 October 2005 (2005)
210. C. Collette, K. Artoos, M. Guinchard, C. Hauviller, Seismic response of linear accelerators. Phys. Rev. Spec. Top., Accel. Beams **13**, 072801 (2010). https://doi.org/10.1103/PhysRevSTAB.13.072801
211. A. Seryi, Ground motion models for future linear colliders, in *Proc. EPAC 2000*, Vienna, Austria (2000). https://accelconf.web.cern.ch/accelconf/e00/PAPERS/THP6A13.pdf
212. G. Balik, B. Caron, D. Schulte, J. Snuverink, J. Pfingstner, Integrated simulation of ground motion mitigation, techniques for the future Compact Linear Collider (CLIC). Nucl. Instrum. Methods Phys. Res., Sect. A, Accel. Spectrom. Detect. Assoc. Equip. **700**, 163–170 (2012). https://doi.org/10.1016/j.nima.2012.10.031
213. J. Pfingstner, Mitigation of ground motion effects via feedback systems in the Compact Linear Collider. Phdthesis, Tech. University, Vienna (2013). Presented 13 March 2013. https://cds.cern.ch/record/1541276
214. B. Bolzon, Etude des vibrations et de la stabilisation à l'échelle sous-nanométrique des doublets finaux d'un collisionneur linéaire. PhD thesis, University of Savoie, Annecy-le-Vieux (2007). http://cdsweb.cern.ch/record/1100434/files/cer-002754217.pdf
215. J. Havskov, Overview of seismic arrays, in *Workshop: High Quality Seismic Stations and Networks for Small Budgets*. Volcan, Panama, 8–13 March 2004 (2004), pp. 8–13. https://slideplayer.com/slide/8754772/
216. Kinemetrics Inc. http://www.kinemetrics.com/
217. GURALP Systems Ltd. Product Catalogue. http://www.guralp.com/products
218. PMD Scientific Inc. http://www.eentec.com
219. Wilcoxon Sensing Technologies: Ultra-quiet, ultra low frequency seismic accelerometer. https://wilcoxon.com/wp-content/uploads/2017/09/731A-spec-98078D.pdf
220. A. Brazilai, Improving a geophone to produce an affordable broadband seismometer. PhD thesis, Stanford University (2000)

221. J. Frisch, E. Doyle, L. Eriksson, L. Hendrickson, T. Himel, T. Markiewicz, R. Partridge, Inertial sensor development for active vibration stabilization, in *Proceedings of the 2003 Particle Accelerator Conference, PAC2003*, Portland, USA (2003). https://doi.org/10.1109/PAC.2003.1288999
222. P. Novotny, B. Aimard, G. Balik, L. Brunetti, B. Caron, A. Gaddi, What is the best displacement transducer for a seismic sensor? in *IEEE Inertial Sensors and Systems 2017*, Hawaï, USA (2017). https://doi.org/10.1109/isiss.2017.7935672
223. Capacitive Displacement Sensors. http://www.capacitance-sensors.com/pdf/Cap_Sens_Web_PI_Capacitive_Displacement_Nanometrology_Capacitance_Gauge_Sensor_E.pdf
224. Magnescale Co. Ltd. http://www.mgscale.com/mgs/language/english/product/BH25.html
225. attocube systems. http://www.attocube.com/Specs_Sheets/Sen/IDS3010SMF.pdf
226. M. Pisani, A homodyne Michelson interferometer with sub-picometer resolution. Meas. Sci. Technol. **20**(8), 084008 (2009)
227. C. Collette, S. Janssens, P. Fernandez Carmona, K. Artoos, M. Guinchard, C. Hauviller, A. Preumont, Review: inertial sensors for low-frequency seismic vibration measurement review: inertial sensors for low frequency seismic vibration measurement. Bull. Seismol. Soc. Am. **102**(4), 1289 (2012). https://doi.org/10.1088/0957-0233/20/8/084008
228. S. Hellegouarch, L.F. Roza, K. Artoos, P. Lambert, C. Collette, Linear encoder based low frequency inertial sensor. Int. J. Optomechatron. **10**, 120–129 (2016). https://doi.org/10.1080/15599612.2016.1217109
229. B. Caron, G. Balik, L. Brunetti, A. Jeremie, Vibration control of the beam of the future linear collider. Control Eng. Pract. **20**, 236–247 (2012). https://doi.org/10.1016/j.conengprac.2011.11.001
230. N.D. Group, Next linear collider zeroth-order design report. Technical Report LBNL-5424. SLAC-R-474. UC-414. UCRL-ID-124161, SLAC, Stanford, CA, USA (1996). http://www.slac.stanford.edu/accel/nlc/zdr/
231. R.L. Breton, G. Deleglise, J. Allibe, A. Badel, G. Balik, B. Caron, A. Jeremie, J. Lottin, S. Vilalte, Nanometer scale active ground motion isolator. Sens. Actuators A **204**, 97–106 (2013). https://doi.org/10.1016/j.sna.2013.09.020
232. G. Balik, B. Aimard, L. Brunetti, B. Caron, Proof of concept of CLIC final focus quadrupoles stabilization, in *Proceedings of International Particle Accelerator Conference (IPAC 2017)*, Copenhagen, Denmark (2017). https://doi.org/10.18429/JACoW-IPAC2017-TUPAB001
233. A. Seryi, O. Napoly, Influence of ground motion on the time evolution of beams in linear colliders. Phys. Rev. E **53**, 5323–5337 (1996). https://doi.org/10.1103/PhysRevE.53.5323
234. K. Artoos, O. Capatina, C. Collette, M. Guinchard, C. Hauviller, M.V. Sylte, B. Bolzon, A. Jeremie, Ground vibration and coherence length measurements for the CLIC nano-stabilization studies, in *Proc. 23rd IEEE Particle Accelerator Conf.*, Vancouver, British Columbia, Canada, 4-8 May 2009 (2009), pp. 3636–3638. http://accelconf.web.cern.ch/accelconf/PAC2009/papers/th5rfp081.pdf
235. VIBRATIONS GROUND: Compilation of ground motion measurements. http://vibration.desy.de
236. J. Peterson, Observations and modeling of background seismic noise. Open-File Report 93-322, U. S. Geological Survey (1993). http://earthquake.usgs.gov/regional/asl/pubs/files/ofr93-322.pdf
237. M. Guinchard, M. Cabon, C. Charrondière, K. Develle, P. Fessia, L.L. Lacny, J.A. Osborne, L.S. Scislo, J. Wenninger, Investigation and estimation of the LHC magnet vibrations induced by HL-LHC civil engineering activities, in *Proc. 9th International Particle Accelerator Conference (IPAC'18)*, Vancouver, BC, Canada, April 29-May 4, 2018 (2018). https://doi.org/10.18429/JACoW-IPAC2018-WEPMF080
238. K. Artoos, C. Collette, F. Fernandez Carmona, M. Guinchard, C. Hauviller, et al., Compatibility and integration of a CLIC quadrupole nano-stabilization and positioning system in a large accelerator environment, in *Proc. 1st Int. Particle Accelerator Conf.*, Kyoto, Japan, 23-28 May 2010 (2010), pp. 2824–2826. http://accelconf.web.cern.ch/accelconf/IPAC10/papers/wepeb058.pdf
239. K. Artoos, C. Collette, M. Esposito, P. Fernandez Carmona, M. Guinchard, S. Janssens, R. Leuxe, M. Modena, R. Moron Ballester, M. Struik, C. Deleglise, A. Jeremie, Modal analysis and measurement of water induced vibrations on a CLIC main beam quadrupole prototype, in *Proc. 2nd International Particle Accelerator Conference (IPAC'11)*, San Sebastian, Spain, 4–9 September 2011 (2011). https://cds.cern.ch/record/1423008
240. B. Bolzon, J.P. Baud, G. Gaillard, N. Geffroy, A. Jeremie, Impact of flowing cooling water on the ATF2 final doublets vibrations. Technical Report ATF-09-01, KEK High Energy Accelerator Research Organization (2009). http://atf.kek.jp/collab/ap/library/internal-reports/ATF-09-01.pdf
241. Paul Scherrer Institute (PSI): SLS Building. https://www.psi.ch/sls/building
242. J. Pfingstner, K. Artoos, C. Charrondiere, S. Janssens, M. Patecki, Y. Renier, D. Schulte, R. Tomás, A. Jeremie, K. Kubo, S. Kuroda, T. Naito, T. Okugi, T. Tauchi, N. Terunuma, Mitigation of ground motion effects in linear accelerators via feed-forward control. Phys. Rev. Spec. Top., Accel. Beams **17**, 122801 (2014). https://doi.org/10.1103/PhysRevSTAB.17.122801
243. C. Collette, S. Janssens, K. Artoos, Review of active vibration isolation strategies. Rec. Pat. Mech. Eng. **4**, 212–219 (2011)
244. C. Collette, F. Matichard, Sensor fusion methods for high performance active vibration isolation systems. J. Sound Vib. **342**, 1–21 (2015). https://doi.org/10.1016/j.jsv.2015.01.006
245. C. Collette, K. Artoos, S. Janssens, C. Hauviller, Hard mounts for quadrupole nano-positioning in a linear collider, in *Proc. 12th International Conference on New Actuators ACTUATOR2010*, Bremen, Germany, 14-16 May 2010 (2010). http://cds.cern.ch/record/1297977
246. C. Collette, K. Artoos, A. Kuzmin, S. Janssens, M. Sylte, M. Guinchard, C. Hauviller, Active quadrupole stabilization for future linear particle colliders. Nucl. Instr. Methods A **621**, 71–78 (2010). https://doi.org/10.1016/j.nima.2010.05.020

247. M. Esposito, K. Artoos, P.F. Carmona, S. Janssens, R. Leuxe, Development of advanced mechanical systems for stabilization and nano-positioning of CLIC main beam quadrupoles, in *Proc. 12th International Workshop on Accelerator Alignment IWAA 2012*, Fermilab, USA, September 10 - 14 2012 (2012)
248. C. Collette, S. Janssens, K. Artoos, A. Kuzmin, P. Fernandez-Carmona, M. Guinchard, R. Leuxe, C. Hauviller, Nano-motion control of heavy quadrupoles for future particle colliders: an experimental validation. Nucl. Instrum. Methods Phys. Res. **643**, 95–101 (2011). https://doi.org/10.1016/j.nima.2011.04.028
249. G. Balik, B. Caron, B. Aimard, L. Brunetti, G. Deleglise, Vibration control using a dedicated inertial sensor. IEEE Sens. J. **18**, 428–435 (2018). https://doi.org/10.1109/jsen.2017.2768127
250. C. Collette, S. Janssens, D. Tshilumba, Control strategies for the final focus of future linear particle collider. Nucl. Instrum. Methods Phys. Res., Sect. A **684**, 7–17 (2012). https://doi.org/10.1016/j.nima.2012.04.090
251. J. Watchi, B. Ding, D. Tshilumba, K. Artoos, C. Collette, Coil-free active stabilisation of extended payloads with optical inertial sensors. Meas. Sci. Technol. **29**(5), 054005 (2018)
252. C. Collette, D. Tshilumba, L. Fueyo-Rosa, I. Romanescu, Conceptual design and scaled experimental validation of an actively damped carbon tie rods support system for the stabilization of future particle collider superstructures. Rev. Sci. Instrum. **84**(2), 023302 (2013). https://doi.org/10.1063/1.4789783
253. S. Janssens, K. Artoos, C. Collette, M. Esposito, P.F. Carmona, M. Guinchard, C. Hauviller, A. Kuzmin, R. Leuxe, R.M. Ballester, Stabilization and positioning of CLIC quadrupole magnets with sub-nanometre resolution, in *Proc. 7th Int. Conf. on Accelerator and Large Experimental Physics Control Systems ICALEPCS 2011*, Grenoble, France (2011). http://accelconf.web.cern.ch/AccelConf/icalepcs2011/papers/mommu005.pdf
254. J. Snuverink, K. Artoos, C. Collette, F. Duarte Ramos, A. Gaddi, et al., Status of ground motion mitigation techniques for CLIC, in *Proc. 2nd Int. Particle Accelerator Conf.*, San Sebastian, Spain, 4-9 September 2011 (2011), pp. 1048–1050. http://accelconf.web.cern.ch/accelconf/IPAC2011/papers/tupc023.pdf
255. I.R. Garcia, Calculation methodology and fabrication procedures for particle accelerator strip-line kickers: Application to the CTF3 combiner ring extraction kicker and tl2 tail clippers. PhD thesis, Industriales, December 2009 (2009). http://oa.upm.es/10818/
256. D. Alesini, S. Guiducci, F. Marcellini, P. Raimondi, Design, test, and operation of new tapered stripline injection kickers for the e+e− collider DAPHNE. Phys. Rev. Spec. Top., Accel. Beams **13** (2010). https://doi.org/10.1103/physrevstab.13.111002
257. T. Naito, S. Araki, H. Hayano, K. Kubo, S. Kuroda, N. Terunuma, T. Okugi, J. Urakawa, Multibunch beam extraction using the strip-line kicker at the KEK Accelerator Test Facility. Phys. Rev. Spec. Top., Accel. Beams **14**, 051002 (2011). https://doi.org/10.1103/PhysRevSTAB.14.051002
258. C. Belver-Aguilar, M.J. Barnes, L. Ducimetière, Review on the effects of characteristic impedance mismatching in a stripline kicker, in *Proc. of International Particle Accelerator Conference (IPAC'16)*, Busan, Korea, May 8-13, 2016 (2016). https://doi.org/10.18429/JACoW-IPAC2016-THPMW034
259. R. Apsimon, B. Balhan, M.J. Barnes, J. Borburgh, B. Goddard, Y. Papaphilippou, J.A. Uythoven, Optics and Protection of the Injection and Extraction Regions of the CLIC Damping Rings, in Proceedings of the 4th International Particle Accelerator Conference, IPAC 2013. http://accelconf.web.cern.ch/AccelConf/IPAC2013/papers/mopwo025.pdf
260. C. Belver-Aguilar, M.J. Barnes, Transient studies of the stripline kicker for beam extraction from CLIC damping rings, in *Proceedings, 5th International Beam Instrumentation Conference (IBIC 2016)*, Barcelona, Spain, September 11-15, 2016. https://doi.org/10.18429/JACoW-IBIC2016-MOPG05
261. J. Holma, M.J. Barnes, Prototype inductive adders with extremely flat-top output pulses for the compact linear collider at CERN, in *IEEE Transactions on Plasma Science*, pp. 1–11 (2018). https://doi.org/10.1109/TPS.2018.2836310
262. C. Belver-Aguilar, M.J. Barnes, Review of stripline beam impedance: application to the extraction kicker for the CLIC damping rings. J. Phys. Conf. Ser. **874**(1), 012074 (2017)
263. J. Holma, M.J. Barnes, S.J. Ovaska, Preliminary design of the pulse generator for the CLIC DR extraction system, in *Proceedings, 18th IEEE International Pulsed Power Conference (PPC11)*, Chicago, Illinois, USA, June 19-23, 2011 (2011), pp. 1353–1358. https://doi.org/10.1109/PPC.2011.6191614
264. J. Holma, M. Barnes, S.J. Ovaska, A Pulse Power Modulator with Extremely Flat-top Output Pulses for the Compact Linear Collider at CERN. PhD thesis, Aalto University, Finland. Presented 11 December 2015 (2015). https://cds.cern.ch/record/2130258
265. J. Holma, M.J. Barnes, A.F. Colomo, Demonstration of feasibility of the CLIC damping ring extraction kicker modulators, in *Proc. 9th International Particle Accelerator Conference (IPAC'18)*, Vancouver, BC, Canada, April 29–May 4 (2018). https://doi.org/10.18429/JACoW-IPAC2018-WEPMF077
266. J. Holma, M.J. Barnes, D. Woog, Measurements on 12.5 kV inductive adders with ±200ppm pulse flatness over 900 ns for CLIC damping ring kickers at CERN, in *2018 IEEE International Power Modulator and High Voltage Conference* (Jackson, Lake Lodge, USA, 2018)
267. K. Takayama, R.J. Briggs (eds.), *Induction Accelerators* (Springer, Germany, 2010)
268. E.G. Cook, F.V. Allen, E.M. Anaya, et al., Solid-State Modulator R&D at LLNL. Preprint UCRL-JC-149976. SLAC-WP-040, UCRL, Berkeley, USA (2002). Submitted to International Workshop on Recent Progress of Induction Accelerators, 29-31 October 2002, Tsukuba, Japan. https://e-reports-ext.llnl.gov/pdf/241699.pdf
269. M.J. Barnes, L. Ducimetiere, J. Holma, T. Kramer, A. Fowler, Inductive adders for replacing thyratron based modulators at CERN, in *Proc. EPE'15*, Geneva, Switzerland (2015). https://doi.org/10.1109/epe.2015.7309160

270. D. Woog, M.J. Barnes, J. Holma, T. Kramer, Prototype Inductive Adder for the Proton Synchrotron at CERN (2018). https://indico.cern.ch/event/707078/contributions/2902147
271. T. Kramer, M.J. Barnes, W. Bartmann, F. Burkart, L. Ducimetière, B. Goddard, V. Senaj, T. Stadlbauer, D. Woog, D. Barna, Consideration for the injection and extraction kicker systems of a 100 TeV centre-of-mass FCC-hh collider, in *Proceedings of the 7th International Particle Accelerator Conference (IPAC 2016)*, Busan, Korea, May 8-13 (2016). https://doi.org/10.18429/JACoW-IPAC2016-THPOR049
272. D. Woog, M.J. Barnes, A.F. Colomo, J. Holma, T. Kramer, First prototype inductive adder for the FCC injection, in *Proc. 9th International Particle Accelerator Conference (IPAC'18)*, Vancouver, BC, Canada, April 29–May 4 (2018). https://doi.org/10.18429/JACoW-IPAC2018-WEPMF076
273. M. Modena, A. Bartalesi, J. Garcia Perez, R. Leuxe, G. Perrin-Bonnet, C. Petrone, M. Struik, A. Vorozhtsov, Performances of the main beam quadrupole Type1 prototypes for CLIC. IEEE Trans. Appl. Supercond. **24**(CERN–ACC–2014–0028), 4002504–4 (2014)
274. B.J.A. Shepherd, J. Clarke, A. Bartalesi, M. Modena, M. Struik, N. Collomb, Prototype adjustable permanent magnet quadrupoles for CLIC, in *4th International Particle Accelerator Conference*, Shanghai, China, 12–17 May 2013 (2013), p. 3. https://cds.cern.ch/record/2010980
275. B. Shepherd, J. Clarke, P. Wadhwa, A. Bartalesi, M. Modena, M. Struik, N. Collomb, Design and measurement of a low-energy tunable permanent magnet quadrupole prototype, in *5th International Particle Accelerator Conference*, vol. TUPRO113, Dresden, Germany, 15–20 Jun 2014 (2014), p. 3. https://cds.cern.ch/record/2003133
276. B. Shepherd, J. Clarke, N. Collomb, Permanent magnet quadrupoles for the CLIC drive beam decelerator. Technical Report CERN-OPEN-2012-018. CLIC-Note-940, CERN, Geneva, July 2012 (2012). https://cds.cern.ch/record/1461571
277. B. Shepherd, Radiation damage to permanent magnet materials: a survey of experimental results. Technical Report CERN-ACC-2018-0029. CLIC-Note-1079, CERN, Geneva, May 2018 (2018). https://cds.cern.ch/record/2642418
278. M. Modena, R. Leuxe, M. Struik, Results on ultra-precise magnet yoke sectors assembly tests. IEEE Trans. Appl. Supercond. **24**, 9001304–4 (2014). https://doi.org/10.1109/TASC.2013.2288422
279. M. Modena, Cost estimate for clic normal-conducting magnets. Technical report, CERN (2012). https://edms.cern.ch/document/1117083/2
280. A. Vorozhtsov, M. Modena, D. Tommasini, Design and manufacture of a hybrid final focus quadrupole model for CLIC. IEEE Trans. Appl. Supercond. **22**(3), 4000604–4000604 (2012). https://doi.org/10.1109/tasc.2011.2182023
281. M. Modena, A. Aloev, H. Garcia, L. Gatignon, R. Tomás, Considerations for a QD0 with hybrid technology in ILC, in *Proc. of 5th International Particle Accelerator Conference (IPAC 2014)*, Dresden, Germany (2014). http://jacow.org/IPAC2014/papers/tupme006.pdf
282. D. Schoerling, Superconducting wiggler magnets for beam-emittance damping rings. Phdthesis. T.U. Bergakademie Freiberg (2012). Presented 19 Mar 2012. https://cds.cern.ch/record/1435176
283. L.G. Fajardo, F. Antoniou, A. Bernhard, P. Ferracin, J. Mazet, S. Papadopoulou, Y. Papaphilippou, J.C. Pérez, D. Schoerling, Design of Nb3Sn wiggler magnets for the compact linear collider and manufacturing of a five-coil prototype. IEEE Trans. Appl. Supercond. **26**(4), 4100506 (2016). https://doi.org/10.1109/TASC.2016.2517938
284. A. Bernhard, E. Huttel, P. Peiffer, A. Bragin, N. Mezentsev, V. Syrovatin, K. Zolotarev, P. Ferracin, D. Schoerling, Preparations for beam tests of a CLIC damping wiggler prototype at ANKA, in *Proceedings, 4th International Particle Accelerator Conference (IPAC 2013)*, Shanghai, China (2013). http://accelconf.web.cern.ch/AccelConf/IPAC2013/papers/tupme005.pdf
285. Y. Ivanyushenkov, K. Harkay, M. Abliz, Development and operating experience of a short-period superconducting undulator at the advanced photon source. Phys. Rev. Spec. Top., Accel. Beams **18**, 040703 (2015). https://doi.org/10.1103/PhysRevSTAB.18.040703
286. A.V. Bragin, A. Bernhard, S. Casalbuoni, L.G. Fajardo, P. Ferracin, A. Grau, Y.A. Gusev, S. Hillenbrand, S.V. Khrushchev, I.V. Poletaev, V.A. Shkaruba, D. Schoerling, V.M. Syrovatin, O.A. Tarasenko, V.M. Tsukanov, A.A. Volkov, K.V. Zolotarev, N.A. Mezentsev, Test results of the CLIC damping wiggler prototype. IEEE Trans. Appl. Supercond. **26**(4), 1–4 (2016). https://doi.org/10.1109/TASC.2016.2516341
287. B. Frammery, The LHC control system, in *Proc. 10th Int. Conf. on Accelerator and Large Experimental Physics Control Systems (ICALEPCS)*, Geneva, Switzerland, 10–14 October 2005 (2005). https://accelconf.web.cern.ch/ica05/proceedings/pdf/I1_001.pdf
288. G. Apollinari, I. Béjar Alonso, O. Brüning, M. Lamont, L. Rossi, *High-Luminosity Large Hadron Collider (HL-LHC): Preliminary Design Report*. CERN Yellow Reports: Monographs (CERN, Geneva, 2015). https://doi.org/10.5170/CERN-2015-005
289. G. Daniluk, E. Gousiou, Plans at CERN for electronics and communication in the distributed I/O tier, in Proc. of International Conference on Accelerator and Large Experimental Control Systems (ICALEPCS'17), Barcelona, Spain, pp. 1552–1556. https://doi.org/10.18429/JACoW-ICALEPCS2017-THPHA071
290. G. Daniluk, E. Gousiou, FMC nanoFIP. https://www.ohwr.org/projects/fmc-nanofip/wiki
291. E. Rubiola, *Phase Noise and Frequency Stability in Oscillators*. The Cambridge RF and Microwave Engineering Series (Cambridge University Press, UK, 2009). https://doi.org/10.1017/CBO9780511812798. ISBN 9780511812798
292. E. Jensen, Drive beam RF system, in *CLIC09 Workshop*, 12-16 October 2009 (CERN, 2009)
293. T. Lefevre, Progress on instrumentation, in *International Workshop on Linear Colliders 2010 (ECFA-CLIC-ILC Joint Meeting)*, Geneva, Switzerland, 18-22 October 2010 (2010). https://espace.cern.ch/LC2010/default.aspx

294. D. Schulte, Concept of MB-DB phase alignment and status of solutions, in *International Workshop on Linear Colliders 2010 (ECFA-CLIC-ILC Joint Meeting)*, Geneva, Switzerland, 18-22 October 2010 (2010)
295. F. Loehl, Linac timing, synchronization and active stabilization, in *Proc. 2nd Int. Particle Accelerator Conf.*, San Sebastian, Spain 4-9 September 2011, (2011), pp. 1381–1383. http://accelconf.web.cern.ch/accelconf/PAC2011/papers/weoan2.pdf
296. A. Ferrari, P.R. Sala, A. Fassò, J. Ranft, Fluka: a multi-particle transport code. Technical Report SLAC-R-773. CERN-2005-010. INFN-TC-2005-11, SLAC, Stanford, CA, USA (2005). http://www.slac.stanford.edu/cgi-wrap/getdoc/slac-r-773.pdf
297. D. Schulte, Study of Electromagnetic and Hadronic Background in the Interaction Region of the TESLA Collider. PhD thesis, Hamburg University, Hamburg (1997). http://cdsweb.cern.ch/record/331845/files/shulte.pdf. TESLA-97-08
298. R.V. Servranckx, K.L. Brown, L. Schachinger, D. Douglas, Users Guide to the Program DIMAD. Technical Report SLAC-R-285, SLAC, Stanford, CA, USA (1990). http://www.slac.stanford.edu/cgi-wrap/getdoc/slac-r-285.pdf
299. ANSYS - Simulation Driven Product Development - V. 12.1. http://www.ansys.com
300. N. Phinney, N. Toge, N. Walker, ILC Reference Design Report Volume 3. Accelerator. Technical report, December 2007 (2007). http://cds.cern.ch/record/1075836
301. C. Adolphsen, M. Barone, B. Barish, K. Buesser, P. Burrows, J. Carwardine, J. Clark, H. Mainaud Durand, G. Dugan, E. Elsen, et al., *The International Linear Collider Technical Design Report - Volume 3.II: Accelerator Baseline Design* (2013)
302. Swiss Index of Producer and Import Prices (2025). Last accessed 19 March 2025. https://www.bfs.admin.ch/bfs/fr/home/statistiques/prix/prix-production-prix-importation.html
303. V. Makinen, Cost study of machining clex / td 26 cc sic disk. Technical report, CERN (2013). https://edms.cern.ch/document/1298800/1
304. S. Pittet, Main beam powering strategy. Technical report, CERN (2025). https://edms.cern.ch/document/1060595/3
305. P. Lebrun, P. Garbincius, Assessing risk in costing high-energy accelerators: from existing projects to the future linear collider, in *Proceedings of IPAC 2010*, Kyoto, Japan (2011). https://cds.cern.ch/record/1341567
306. T. Roser, R. Brinkmann, S. Cousineau, D. Denisov, S. Gessner, S. Gourlay, P. Lebrun, M. Narain, K. Oide, T. Raubenheimer, J. Seeman, V. Shiltsev, J. Strait, M. Turner, L.-T. Wang, On the feasibility of future colliders: report of the snowmass'21 implementation task force. J. Instrum. **18**(05), 05018 (2023). https://doi.org/10.1088/1748-0221/18/05/p05018
307. A. Gaddi, D. Dannheim, CLIC Detector Power Requirements. https://cds.cern.ch/record/1602917
308. C. Prasse, et al., Energy Load and Cost Analysis. https://edms.cern.ch/document/2065162/1
309. S. Evans, et al., Life Cycle Assessment, comparative environmental footprint for future linear colliders CLIC and ILC (2023). https://edms.cern.ch/document/2917948/1
310. S. Evans, et al., Life Cycle Assessment, comparative environmental footprint for future linear colliders CLIC and ILC, whole accelerator. (2025). In preparation
311. M. Diomede, et al., RF design of the X-band linac for the EuPRAXIA@SPARC_LAB project, in *Proceedings of IPAC 2018*, Vancouver, BC, Canada (2018), pp. 4422–4425. https://doi.org/10.18429/JACoW-IPAC2018-THPMK058
312. (2018). CompactLight Project. Last accessed 14 December 2018. http://www.compactlight.eu/
313. Smart*Light: a Dutch Table-top Synchrotron Light Source. Last accessed 14 December 2018 (2018). https://www.knaw.nl/shared/resources/adviezen/EervolKNAWAgendaSmartLight.pdf
314. Y. Thiery, J. Gao, J. LeDuff, Design studies for a high current bunching system for CLIC Test Facility (CTF3) drive beam, in *Proc. XX Intl. Linac Conf.*, Monterey, CA, USA, 21-25 August 2000 (2000), pp. 95–97. http://epaper.kek.jp/l00/papers/MOB01.pdf
315. P. Urschuetz, H.H. Braun, G. Carron, R. Corsini, S. Doebert, T. Lefevre, G. McMonagle, J. Mourier, F.A. Tecker, L. Thorndahl, C. Welsch, Beam dynamics studies and emittance optimization in the CTF3 linac at CERN, in *Proc. 10th European Particle Accelerator Conf.*, Edinburgh, Scotland, UK, 26-30 June 2006 (2006), pp. 795–797. http://accelconf.web.cern.ch/AccelConf/e06/PAPERS/MOPLS101.PDF
316. P. Urschuetz, H.H. Braun, G. Carron, R. Corsini, S. Doebert, T. Lefevre, G. McMonagle, J. Mourier, F.A. Tecker, L. Thorndahl, C. Welsch, Beam dynamics and first operation of the sub-harmonic bunching system in the CTF3 injector, in *Proc. 10th European Particle Accelerator Conf.*, Edinburgh, Scotland, UK, 26-30 June 2006 (2006), pp. 798–800. https://cds.cern.ch/record/972321
317. E. Jensen, CTF3 Drive Beam accelerating structures, in *Proceedings, 21st International Linac Conference, Linac 2002*, Gyeongju, South Korea, August 19-23, 2002 (2002), pp. 34–36. http://cds.cern.ch/record/581340
318. R. Corsini, H.-H. Braun, G. Carron, O. Forstner, G. Geschonke, A.E. Jensen, L. Rinolfi, D. Schulte, F. Tecker, L. Thorndahl, et al., First full beam loading operation with the CTF3 linac, in *Proc. 9th European Particle Accelerator Conf.*, Lucerne, Switzerland, 5-9 July 2004 (2004), pp. 39–41. http://accelconf.web.cern.ch/accelconf/e04/PAPERS/MOOCH02.PDF
319. P. Urschuetz, Efficient long-pulse fully loaded CTF3 linac operation, in *Proc. Linear Accelerator Conf. (LINAC2006)*, Knoxville, Tennessee, USA (2006), pp. 31–33. http://accelconf.web.cern.ch/AccelConf/l06/PAPERS/MOP002.PDF
320. D. Alesini, C. Biscari, A. Chigo, F. Marcellini, Beam instability induced by RF deflectors in the combiner ring of the CLIC test facility and mitigation by damped deflecting structures. Phys. Rev. Spec. Top., Accel. Beams **14**, 022001 (2011). https://doi.org/10.1103/PhysRevSTAB.14.022001
321. R. Corsini, CTF3 status and plans. ICFA Beam Dyn. Newsl. **62**, 165 (2013)

322. D. Schulte, A. Andersson, S. Bettoni, R. Corsini, A. Dubrorsky, et al., Status of the CLIC phase and amplitude stabilization concept, in *Proc. XXV Linear Accelerator Conf.*, Tsukuba, Japan, 12–17 September 2010 (2010), pp. 103–105. http://accelconf.web.cern.ch/accelconf/LINAC2010/papers/mop024.pdf
323. G. Sterbini, Beam current stability in CTF3, in *Presented at the International Workshop on Future Linear Colliders*, Geneva, Switzerland (2010). http://agenda.linearcollider.org/event/4507/contributions/17550
324. P.K. Skowronski, Status and plans for completion of the experimental programme of the CLIC Test Facility CTF3, in *Proc. of International Particle Accelerator Conference (IPAC'16)*, Busan, Korea, May 8-13 (2016), pp. 3347–3350. https://doi.org/10.18429/JACoW-IPAC2016-THPMB046
325. J. Roberts, P. Burrows, G.B. Christian, C. Perry, A. Andersson, R. Corsini, P.K. Skowroński, A. Ghigo, F. Marcellini, Demonstration of CLIC level phase stability using a high bandwidth, low latency drive beam phase feedforward system at the CLIC Test Facility CTF3, in *Proc. of International Particle Accelerator Conference (IPAC'16)*, Busan, Korea, May 8-13 (2016), pp. 2677–2680. https://doi.org/10.18429/JACoW-IPAC2016-WEPOR006
326. J. Roberts, P. Skowronski, P.N. Burrows, G.B. Christian, R. Corsini, A. Ghigo, F. Marcellini, C. Perry, Stabilization of the arrival time of a relativistic electron beam to the 50 fs level (2018). https://doi.org/10.1103/PhysRevAccelBeams.21.011001
327. P.K. Skowronski, The CLIC feasibility demonstration in CTF3, in *Proc. of International Particle Accelerator Conference. IPAC 2011*, San Sebastian, Spain (2011), pp. 1042–1044. http://accelconf.web.cern.ch/AccelConf/IPAC2011/papers/tupc021.pdf
328. I. Syratchev, High power operation with beam of a CLIC PETS equipped with on/off mechanism, in *Proc. of International Particle Accelerator Conference. IPAC 2012*, New Orleans, Louisiana, USA (2012), pp. 1852–1854. http://accelconf.web.cern.ch/AccelConf/IPAC2012/papers/tuppr019.pdf
329. R.L. Lillestoel, *Power Production Experiments at the Test Beam Line in the CLIC Test Facility 3. Phdthesis* (Norwegian University of Science and Technology, Trondheim, Norway, 2010). Presented 21 Dec 2010. https://cds.cern.ch/record/1392630
330. F. Peauger, D. Bogard, G. Cheymol, P. Contrepois, et al., Status of the CTF3 probe beam linac CALIFES, in *Proc. XXIV Linear Accelerator Conf.*, Victoria, British Columbia, Canada, 29 September - 3 October 2008 (2008), pp. 389–391. http://accelconf.web.cern.ch/accelconf/LINAC08/papers/tup004.pdf
331. A. Palaia, M. Jacewicz, R. Ruber, V. Ziemann, W. Farabolini, Effects of RF breakdown on the beam in the Compact Linear Collider prototype accelerator structure. https://doi.org/10.1103/PhysRevSTAB.16.081004. http://arxiv.org/abs/1301.4673v2
332. S. Döbert, N. Chritin, B. Cadilhon, B. Cassany, J. Gardelle, K. Pepitone, Design of a high average current electron source for the CLIC drive beam injector, in *Proceedings, 27th Linear Accelerator Conference, LINAC2014*, Geneva, Switzerland, August 31–September 5, 2014 (2014), p. 030. http://jacow.org/LINAC2014/papers/tupp030.pdf
333. K. Pepitone, B. Cassany, S. Doebert, J. Gardelle, L. Garolfi, Operation of a high-current drive beam electron gun prototype for the compact linear collider. Rev. Sci. Instrum. **91**, 093302 (2020). https://doi.org/10.1063/5.0013144
334. G. White, R. Ainsworth, T. Akagi, J. Alabau-Gonzalvo, D. Angal-Kalinin, S. Araki, A. Aryshev, S. Bai, P. Bambade, D. Bett, et al., Experimental validation of a novel compact focusing scheme for future energy-frontier linear lepton colliders. Phys. Rev. Lett. **112**(3), 034802 (2014). https://doi.org/10.1103/PhysRevLett.112.034802
335. P. Bambade, Y. Renier, S. Bai, H. Braun, J.P. Delahaye, E. Marin, D. Schulte, R. Tomás, F. Zimmermann, J. Gao, D. Wang, X. Zhu, Y. Honda, S. Kuroda, T. Okugi, T. Tauchi, N. Terunuma, J. Urakawa, A. Seryi, G. White, M. Woodley, D. Angal-Kalinin, J. Jones, A. Scarfe, ATF2 ultra-low IP betas proposal (CERN-ATS-2009-092. CLIC-Note-792), 4 (2009)
336. M. Patecki, D. Bett, E. Marin, F. Plassard, R. Tomas, K. Kubo, S. Kuroda, T. Naito, T. Okugi, T. Tauchi, N. Terunuma, Probing half beta*optics in the Accelerator Test Facility 2. Phys. Rev. Accel. Beams **19** (2016). https://doi.org/10.1103/physrevaccelbeams.19.101001
337. V. Cilento, First explorations of crystal focusing for CLIC/ATF2, in *Proc. LCWS 2017*, Strasbourg, France (2017). https://agenda.linearcollider.org/event/7645/contributions/40182/contribution.pdf
338. H.G. Morales, R. Tomas Garcia, Final-focus systems for multi-TeV linear colliders. Phys. Rev. Spec. Top., Accel. Beams **17**, 101001 (2014). https://doi.org/10.1103/PhysRevSTAB.17.101001
339. M. Masuzawa, QEA magnet measurements at KEK and comparison with IHEP results, in *11th ATF2 Project Meeting* (2011). http://ilcagenda.linearcollider.org/conferenceDisplay.py?confId=4904
340. T. Okugi, S. Araki, P. Bambade, K. Kubo, S. Kurado, M. Masuzawa, E. Marin, T. Naito, T. Tauchi, N. Terunuma, R. Tomas, J. Urakawa, G. White, M. Woodley, Linear and second order optics corrections for the KEK Accelerator Test Facility final focus beam line **17** (2014). https://doi.org/10.1103/physrevstab.17.023501
341. E. Marin Lacoma, Design and higher order optimisation of final focus systems for linear colliders. Phdthesis, UNIVERSITAT POLITECNICA DE CATALUNYA (U.P.C) (2012). Presented 21 December 2012 https://cds.cern.ch/record/1504285
342. E. Marin, R. Tomas, P. Bambade, K. Kubo, T. Okugi, T. Tauchi, N. Terunuma, J. Urakawa, A. Seryi, G.R. White, M. Woodley, Design and high order optimization of the Accelerator Test Facility lattices. Phys. Rev. Spec. Top., Accel. Beams **17** (2014). https://doi.org/10.1103/physrevstab.17.021002
343. M. Patecki, R. Tomas, Effects of quadrupole fringe fields in final focus systems for linear colliders. Phys. Rev. Spec. Top., Accel. Beams **17** (2014). https://doi.org/10.1103/physrevstab.17.101002
344. E. Marin, G. White, M. Woodley, K. Kubo, T. Okugi, T. Tauchi, J. Urakawa, R. Tomas, Design and high order optimization of the atf2 lattices (2013)

345. M. Modena, Procurement, measurement and installation of 2 octupoles for ATF, in *Presented in Linear Collider Workshop 2016*, Morioka, Japan (2016). https://agenda.linearcollider.org/event/7371/contributions/38030/
346. E. Marin, M. Modena, T. Tauchi, N. Terunuma, R. Tomas, G.R. White, Specifications of the octupole magnets required for the ATF2 ultra-low beta* lattice. Technical Report SLAC-TN-14-019, SLAC (2014). http://www.slac.stanford.edu/cgi-wrap/getdoc/slac-tn-14-019.pdf
347. F. Plassard, Ultra-low beta-y* tuning study at ATF2 using octupoles, in *Presented in CLIC Workshop 2018* (CERN, Switzerland, 2018). https://indico.cern.ch/event/656356/contributions/2832987/
348. R. Yang, A. Pastushenko, A. Aryshev, M. Bergamaschi, V. Cilento, A. Faus-Golfe, M. Fukuda, P. Korysko, K. Kubo, S. Kuroda, T. Naito, T. Okugi, F. Plassard, N. Terunuma, R. Tomás, Tuning the ultralow β^* optics at the kek accelerator test facility 2. Phys. Rev. Accel. Beams **23**, 071003 (2020). https://doi.org/10.1103/PhysRevAccelBeams.23.071003
349. R. Yang, A. Pastushenko, V. Cilento, K. Kubo, T. Naito, T. Okugi, N. Terunuma, R. Tomás, Momentum bandwidth of the kek accelerator test facility 2. Phys. Rev. Accel. Beams **24**, 051001 (2021). https://doi.org/10.1103/PhysRevAccelBeams.24.051001
350. D.R. Bett, C. Charrondiere, M. Patecki, J. Pfingstner, D. Schulte, R. Tomas, A. Jeremie, K. Kubo, S. Kuroda, T. Naito, T. Okugi, T. Tauchi, N. Terunuma, P.N. Burrows, G.B. Christian, C. Perry, Compensation of orbit distortion due to quadrupole motion using feed-forward control at KEK ATF. Nucl. Instrum. Methods Phys. Res., Sect. A, Accel. Spectrom. Detect. Assoc. Equip. **895**, 10–18 (2018). https://doi.org/10.1016/j.nima.2018.03.037
351. P. Korysko, Orbit effects with beam intensity, in *CLIC Workshop 2018* (CERN, Switzerland, 2018). https://indico.cern.ch/event/656356/contributions/2832989/
352. P. Korysko, P.N. Burrows, A. Latina, A. Faus-Golfe, Wakefield effects and mitigation techniques for nanobeam production at the kek accelerator test facility 2. Phys. Rev. Accel. Beams **23**, 121004 (2020). https://doi.org/10.1103/PhysRevAccelBeams.23.121004
353. A. Latina, E. Adli, N. Fuster-Martínez, J. Pfingstner, D. Schulte, J. Snuverink, Tests of wakefield-free steering at ATF2, in *6th International Particle Accelerator Conference* (2015), p. 059. https://doi.org/10.18429/JACoW-IPAC2015-MOPJE059
354. T.O. Raubenheimer, Estimates of emittance dilution and stability in high-energy linear accelerators. Phys. Rev. Spec. Top., Accel. Beams **3**, 121002 (2000). https://doi.org/10.1103/PhysRevSTAB.3.121002
355. T.O. Raubenheimer, R.D. Ruth, A dispersion-free trajectory correction technique for linear colliders. Nucl. Instrum. Methods Phys. Res. **302**, 191–208 (1991). https://doi.org/10.1016/0168-9002(91)90403-d
356. P. Eliasson, D. Schulte, Design of main linac emittance tuning bumps for the compact linear collider and the international linear collider. Phys. Rev. Spec. Top., Accel. Beams **11**, 011002 (2008). https://doi.org/10.1103/PhysRevSTAB.11.011002
357. E. Adli, D. Schulte, Beam-based alignment for the CLIC decelerator, in *Proc. 11th European Particle Accelerator Conf*, Genoa, Italy, 23–27 June 2008 (2008), pp. 547–549. https://cds.cern.ch/record/1122730
358. A. Grudiev, W. Wuensch, Design of the CLIC main linac accelerating structure for CLIC conceptual design report, in *Proc. XXV Linear Accelerator Conf.*, Tsukuba, Japan, 12–17 September 2010 (2010), pp. 211–213. http://accelconf.web.cern.ch/accelconf/LINAC2010/papers/mop068.pdf
359. PLACET: (Program for Linear Accelerator Correction and Efficiency Tests). https://clicsw.web.cern.ch/clicsw
360. J. Pfingstner, A. Latina, Feasibility study of system identification of orbit response matrices at facet. Technical Report CERN-OPEN-2012-020. CLIC-Note-947, CERN, Geneva, July 2012 (2012). https://cds.cern.ch/record/1472967
361. W. Bruns, The GdfidL Electromagnetic Field Simulator. http://www.gdfidl.de
362. H. Zha, A. Latina, A. Grudiev, G.D. Michele, A. Solodko, W. Wuensch, D. Schulte, E. Adli, N. Lipkowitz, G.S. Yocky, Beam-based measurements of long-range transverse wakefields in the Compact Linear Collider main-linac accelerating structure. Phys. Rev. Accel. Beams **19** (2016). https://doi.org/10.1103/physrevaccelbeams.19.011001
363. A. Grudiev, S. Calatroni, W. Wuensch, New local field quantity describing the high gradient limit of accelerating structures. Phys. Rev. Spec. Top., Accel. Beams **12**, 102001 (2009). https://doi.org/10.1103/PhysRevSTAB.12.102001
364. J. Paszkiewicz, A. Grudiev, W. Wuensch, Local power coupling as a predictor of high-gradient breakdown performance (2022). https://arxiv.org/abs/2209.15291
365. W. Wuensch, S. Calatroni, F. Djurabekova, A. Kyritsakis, Y. Ashkenazy, Fundamental mechanisms of high-electric-field vacuum arc initiation (2025). https://arxiv.org/abs/2502.03967
366. A. Vnuchenko, D. Esperante Pereira, B. Gimeno Martinez, S. Benedetti, N. Catalan Lasheras, M. Garlasch, A. Grudiev, G. McMonagle, S. Pitman, I. Syratchev, M. Timmins, R. Wegner, B. Woolley, W. Wuensch, A. Faus Golfe, High-gradient testing of an *s*-band, normal-conducting low phase velocity accelerating structure. Phys. Rev. Accel. Beams **23**, 084801 (2020). https://doi.org/10.1103/PhysRevAccelBeams.23.084801
367. P. Craievich, M. Bopp, H.-H. Braun, A. Citterio, R. Fortunati, R. Ganter, T. Kleeb, F. Marcellini, M. Pedrozzi, E. Prat, S. Reiche, K. Rolli, R. Sieber, A. Grudiev, W.L. Millar, N. Catalan-Lasheras, G. McMonagle, S. Pitman, V.d.P. Romano, K.T. Szypula, W. Wuensch, B. Marchetti, R. Assmann, F. Christie, B. Conrad, R. D'Arcy, M. Foese, P.G. Caminal, M. Hoffmann, M. Huening, R. Jonas, O. Krebs, S. Lederer, D. Marx, J. Osterhoff, M. Reukauff, H. Schlarb, S. Schreiber, G. Tews, M. Vogt, A.d.Z. Wagner, S. Wesch, Novel x-band transverse deflection structure with variable polarization. Phys. Rev. Accel. Beams **23**, 112001 (2020). https://doi.org/10.1103/PhysRevAccelBeams.23.112001
368. B. Woolley, G. Burt, A.C. Dexter, R. Peacock, W.L. Millar, N. Catalan Lasheras, A. Degiovanni, A. Grudiev, G. Mcmonagle, I. Syratchev, W. Wuensch, E. Rodriguez Castro, J. Giner Navarro, High-gradient behavior of a dipole-mode rf structure. Phys. Rev. Accel. Beams **23**, 122002 (2020). https://doi.org/10.1103/PhysRevAccelBeams.23.122002

369. T. Argyropoulos, N. Catalan-Lasheras, A. Grudiev, G. Mcmonagle, E. Rodriguez-Castro, I. Syrachev, R. Wegner, B. Woolley, W. Wuensch, H. Zha, V. Dolgashev, G. Bowden, A. Haase, T.G. Lucas, M. Volpi, D. Esperante-Pereira, R. Rajamäki, Design, fabrication, and high-gradient testing of an x-band, traveling-wave accelerating structure milled from copper halves. Phys. Rev. Accel. Beams **21**, 061001 (2018). https://doi.org/10.1103/PhysRevAccelBeams.21.061001
370. A. Degiovanni, W. Wuensch, J. Giner Navarro, Comparison of the conditioning of high gradient accelerating structures. Phys. Rev. Accel. Beams **19**, 032001 (2016). https://doi.org/10.1103/PhysRevAccelBeams.19.032001
371. X. Wu, J. Shi, H. Chen, J. Shao, T. Abe, T. Higo, S. Matsumoto, W. Wuensch, High-gradient breakdown studies of an x-band compact linear collider prototype structure. Phys. Rev. Accel. Beams **20**, 052001 (2017). https://doi.org/10.1103/PhysRevAccelBeams.20.052001
372. W.L. Millar, et al., High-power test of two prototype X-band accelerating structures based on SwissFEL fabrication technology. IEEE Trans. Nucl. Sci. **70**(1), 1–19 (2023). https://doi.org/10.1109/TNS.2022.3230567
373. X. Wu, M.J. Boronat Arévalo, A. Castilla, N. Catalán Lasheras, A.V. Edwards, A. Grudiev, G. McMonagle, W.L. Millar, I. Syratchev, W. Wuensch, High-gradient breakdown studies of an X-band accelerating structure operated in the reversed taper direction, in *JACoW IPAC* 2021, 1543–1546 (2021). https://doi.org/10.18429/JACoW-IPAC2021-TUPAB076
374. D. Banon Caballero, et al., Dark current analysis at CERN's X-band facility, in *10th International Particle Accelerator Conference* (2019), p. 059. https://doi.org/10.18429/JACoW-IPAC2019-WEPRB059
375. J. Paszkiewicz, P. Burrows, W. Wuensch, Spatially resolved dark current in high gradient traveling wave structures, in *10th International Particle Accelerator Conference* (2019), p. 062. https://doi.org/10.18429/JACoW-IPAC2019-WEPRB062
376. A. Vnuchenko, et al., High gradient performance of an S-band backward traveling wave accelerating structure for medical hadron therapy accelerators, in *9th International Particle Accelerator Conference* (2018). https://doi.org/10.18429/JACoW-IPAC2018-MOPML043
377. R. Zennaro, et al., High power tests of a prototype X-band accelerating structure for CLIC, in *JACoW* IPAC2017, 4318–4320 (2017). https://doi.org/10.18429/JACoW-IPAC2017-THPIK097
378. W. Wuensch, High-gradient RF development and applications, in *28th International Linear Accelerator Conference* (2017), pp. 2–04. https://doi.org/10.18429/JACoW-LINAC2016-TU2A04
379. E. Senes, T. Argyropoulos, F. Tecker, W. Wuensch, Beam-loading effect on breakdown rate in high-gradient accelerating cavities: an experiment at the compact linear collider test facility at cern. Phys. Rev. Accel. Beams **21**, 102001 (2018). https://doi.org/10.1103/PhysRevAccelBeams.21.102001
380. In: Low Emittance Rings Workshop Series (2010, 2011, 2013, 2014, 2015, 2016, 2018)
381. J. Guo, T.O. Raubenheimer, Low emittance e−/e+ storage ring using bending magnets with longitudinal gradient (2002)
382. R. Nagaoka, A.F. Wrulich, Emittance minimisation with longitudinal dipole field variation. Nucl. Instrum. Methods Phys. Res., Sect. A, Accel. Spectrom. Detect. Assoc. Equip. **575**(3), 292–304 (2007). https://doi.org/10.1016/j.nima.2007.02.086
383. C.-X. Wang, Minimum emittance in storage rings with uniform or nonuniform dipoles. Phys. Rev. Spec. Top., Accel. Beams **12**, 061001 (2009). https://doi.org/10.1103/PhysRevSTAB.12.061001
384. C.-X. Wang, Y. Wang, Y. Peng, Optimal dipole-field profiles for emittance reduction in storage rings. Phys. Rev. Spec. Top., Accel. Beams **14**, 034001 (2011). https://doi.org/10.1103/PhysRevSTAB.14.034001
385. H. Braun, E.B. Levichev, Y. Papaphilippou, S. Siniatkin, K. Zolotarev, Alternative design of the CLIC damping ring lattice. Technical Report CERN-OPEN-2011-016. CLIC-Note-849, CERN (2010). https://cdsweb.cern.ch/record/1347751/files/CERN-OPEN-2011-016.pdf
386. J. Snuverink, W. Herr, C. Jach, J.B. Jeanneret, D. Schulte, F. Stulle, Impact of dynamic magnetic fields on the CLIC main beam, in *Proc. IPAC'10* (2010). http://cds.cern.ch/record/1271359
387. E. Marín, B. Heilig, J. Pfingstner, D. Schulte, Impact of dynamical stray fields on CLIC, in *Proceedings, 8th International Particle Accelerator Conference (IPAC 2017)*, Copenhagen, Denmark, May 14–19, 2017 (2017), p. 077. https://doi.org/10.18429/JACoW-IPAC2017-MOPIK077
388. C. Gohil, D. Schulte, P.N. Burrows, Stray magnetic field tolerances for the 380 GeV clic design. Technical Report CERN-ACC-2018-0052. CLIC-Note-1139, CERN, Geneva, November 2018 (2018). https://cds.cern.ch/record/2649488
389. A. Latina, E. Adli, H. Burkhardt, G. Rumolo, D. Schulte, R. Tomas, Y. Renier, Recent improvements in the tracking code PLACET, in *Proc. 11th European Particle Accelerator Conf.*, Genoa, Italy, 23-27 June 2008 (2008), pp. 1750–1752. http://accelconf.web.cern.ch/accelconf/e08/papers/tupp094.pdf
390. B. Heilig, C. Beggan, J. Lichtenberger, Natural sources of geomagnetic field variations. Technical Report CERN-ACC-2018-0033. CLIC-Note-1083, CERN, Geneva, October 2018 (2018). http://cds.cern.ch/record/2643499
391. W. Wuensch. To be published
392. D.A. Constable, A.Y. Baikov, G. Burt, R.D. Kowalczyk, I. Syratchev, High Efficiency Klystrons Using the COM Bunching Technique (2017) pp. 1–3. https://cds.cern.ch/record/2287334
393. P. Wang, H. Zha, I. Syratchev, J. Shi, H. Chen, RF design of a pulse compressor with correction cavity chain for klystron-based Compact Linear Collider. Phys. Rev. Accel. Beams **20**(11), 112001 (2017). https://doi.org/10.1103/PhysRevAccelBeams.20.112001
394. K.S. Yu, Pulse shape correction for RF pulse compression system, in *Proc. of EPAC 1992*, Berlin, Germany (1992)
395. R. Zennaro, M. Bopp, A. Citterio, R. Reiser, T. Stapf, C-band rf pulse compressor for swissfel, in *Proceedings, 4th International Particle Accelerator Conference (IPAC 2013)*, Shanghai, China, May 12–17, 2013, p. 059. http://JACoW.org/IPAC2013/papers/wepfi059.pdf

396. P. Wang, M.J. Capstick, N. Catalan Lasheras, S. Doebert, A. Grudiev, C. Rossi, P. Morales Sanchez, I. Syratchev, X. Wu, Design of the RF waveguide network for the klystron-based CLIC main linac RF Module. Technical report, CERN, Geneva (2024). https://cds.cern.ch/record/2893943
397. P. Wang, A. Grudiev, B. Riffaud, E. Berthome, F. Motschmann, I. Syratchev, K. Scibor, L. Giordanino, N. Catalan Lasheras, P. Morales Sanchez, Design, fabrication and RF measurements of the storage and correction cavity prototypes of the RF pulse compression system for the klystron-based CLIC main linac. Technical report, CERN, Geneva (2024). https://cds.cern.ch/record/2912954
398. Y. Jiang, H. Zha, P. Wang, J. Shi, H. Chen, W.L. Millar, I. Syratchev, Demonstration of a cavity-based pulse compression system for pulse shape correction. Phys. Rev. Accel. Beams **22**(8), 082001 (2019). https://doi.org/10.1103/PhysRevAccelBeams.22.082001
399. W. Wuensch, et al., Experience operating an X-band high-power test stand at CERN, in *Proceedings, 5th International Particle Accelerator Conference (IPAC 2014)*, Dresden, Germany, June 15–20, 2014 (2014), p. 016. https://doi.org/10.18429/JACoW-IPAC2014-WEPME016. http://jacow.org/IPAC2014/papers/wepme016.pdf
400. N. Catalán Lasheras, et al., Commissioning of xbox-3: a very high capacity X-band test stand, in *Proceedings, 28th International Linear Accelerator Conference (LINAC16)*, East Lansing, Michigan, September 25–30, 2016 (2017), p. 047. https://doi.org/10.18429/JACoW-LINAC2016-TUPLR047
401. D. Sprehn, A 12 GHz 50 MW klystron for support of accelerator research, in *Proc. of the International Particle Accelerator Conference (IPAC'10)*, Kyoto, Japan (2010). http://inspirehep.net/record/869227/files/slac-pub-14377.pdf
402. A.Y. Baikov, C. Marrelli, I. Syratchev, Toward high-power klystrons with RF power conversion efficiency on the order of 90%. IEEE Trans. Electron Devices **62**(10), 3406–3412 (2015). https://doi.org/10.1109/TED.2015.2464096

Affiliations

[1] CERN, Geneva, 1211, Switzerland
[2] Department of Physics, University of Oslo, Oslo, 0316, Norway
[3] Elettra-Sincrotrone Trieste S.C.p.A, AREA Science Park, Basovizza, Trieste, 34149, Italy
[4] John Adams Institute, Department of Physics, University of Oxford, Oxford, UK
[5] IN2P3, IJCLab, Paris-Saclay University, Orsay, 91400, France
[6] University of Glasgow, Glasgow, Scotland, UK
[7] High Energy Accelerator Research Organization, KEK, Tsukuba, Japan
[8] Raymond & Beverly Sackler School of Physics & Astronomy, Tel Aviv University, Tel Aviv, Israel
[9] SLAC National Accelerator Laboratory, Menlo Park, USA
[10] National Centre for Physics, Islamabad, Pakistan
[11] Helsinki Institute of Physics, University of Helsinki, Helsinki, Finland
[12] Present address: SolidWatts, Pully, Switzerland
[13] LAPP, Université de Savoie, IN2P3/CNRS, Annecy, France
[14] DESY, Zeuthen, Germany
[15] Ankara University, Ankara, Türkiye
[16] INFN e Laboratori Nazionali di Frascati, Frascati, Italy
[17] National Technical University of Athens, Athens, Greece
[18] King Abdulaziz City for Science and Technology, Riyadh, Saudi Arabia
[19] Université Paris-Saclay, CNRS, IJCLab, Orsay, France
[20] The John Adams Institute for Accelerator Science, Royal Holloway, University of London, Egham, UK
[21] Instituto de Física Corpuscular (CSIC-UV), Valencia, Spain
[22] University of Antananarivo, Antananarivo, Madagascar
[23] Lancaster University, Lancaster, UK
[24] The Cockcroft Institute, Keckwick Ln, Daresbury, UK
[25] Racah Institute of Physics, Hebrew University of Jerusalem, Jerusalem, Israel
[26] STFC Daresbury Laboratory, Warrington, UK
[27] Monash University, Melbourne, Australia
[28] Institute of Applied Physics, National Academy of Sciences of Ukraine, Sumy, Ukraine
[29] CELLS-ALBA, Barcelona, Spain
[30] Karlsruhe Institute of Technology (KIT), Karlsruhe, Germany
[31] John Adams Institute, University of Oxford, Oxford, UK
[32] Paul Scherrer Institute PSI, Villigen, Switzerland
[33] Present address: Diamond Light Source, Harwell, UK
[34] Thomas Jefferson National Accelerator Facility, Newport News, USA
[35] University of Saskatchewan, Saskatoon, Canada

[36] University of Manchester, Manchester, UK
[37] IFCA, CSIC-Universidad de Cantabria, Santander, Spain
[38] Vinča Institute of Nuclear Sciences, University of Belgrade, Belgrade, Serbia
[39] Institute of Nuclear Physics PAN, Krakow, Poland
[40] Uppsala University, Uppsala, Sweden
[41] University of Liverpool, Liverpool, UK
[42] Present address: STFC Daresbury Laboratory, Daresbury, UK
[43] CEA, Gif-sur-Yvette, France
[44] Argonne National Laboratory, Argonne, USA
[45] Tsinghua University, Beijing, China
[46] The School of Particles and Accelerators, Institute for Research in Fundamental Sciences, Tehran, Iran
[47] Department of Physics, Abant İzzet Baysal University, Bolu, Türkiye
[48] Department of Physics, University of Helsinki, Helsinki, Finland
[49] Centro de Investigaciones Energéticas, Medioambientales y Tecnológicas (CIEMAT), Madrid, Spain
[50] Shanghai Institute of Applied Physics, Chinese Academy of Sciences, Shanghai, China
[51] AGH University of Krakow, Krakow, Poland
[52] University of Melbourne, Melbourne, Australia
[53] University of Bristol, Bristol, UK
[54] Nikhef, Amsterdam, The Netherlands
[55] Present address: University of Bonn, Bonn, Germany
[56] Shandong University, Jinan, China
[57] HUN-REN Institute of Earth Physics and Space Science, Sopron, Hungary
[58] SpaceLab, Obuda University, Budapest, Hungary
[59] Imperial College London, London, UK
[60] European Spallation Source ERIC, Lund, Sweden
[61] Faculty of Physics, University of Warsaw, Warsaw, Poland
[62] ETIT, Karlsruhe Institute of Technology, Karlsruhe, Germany
[63] University of Tartu, Tartu, Estonia
[64] Present address: SolidWatts, Pully, Switzerland
[65] University of Bergen, Bergen, Norway
[66] ETH Zurich, Zurich, Switzerland
[67] Nuclear Research Centre-Negev, Beer Sheva, Israel
[68] DESY, Hamburg, Germany
[69] Eindhoven University of Technology, Eindhoven, The Netherlands
[70] University of Edinburgh, Edinburgh, UK
[71] Present address: DESY, Hamburg, Germany
[72] Omer Halis Demir University, Nigde, Türkiye
[73] LAL, Orsay, France
[74] Present address: Johannes-Gutenberg University, Mainz, Germany
[75] EPFL, Lausanne, Switzerland
[76] Present address: Faculty of Nuclear Sciences and Physical Engineering, CTU, Prague, Czech Republic
[77] Present address: Institute of Physics, Academy of Sciences, Prague, Czech Republic
[78] Sapienza Universita, INFN, Rome, Italy
[79] Aarhus University, Aarhus, Denmark
[80] Département de Physique Nucléaire et Corpusculaire (DPNC), Université de Genève, Geneva, Switzerland
[81] University of Birmingham, Birmingham, UK